Instituto Carlos I de Física Teórica y Computacional
y Depto. de Electromagnetismo y Física de la Materia
Universidad de Granada

# Some Aspects on Dynamics of Nonequilibrium Systems

## Metastability, Avalanches, Phase Separation, Absorbing States and Heat Conduction

PABLO HURTADO FERNÁNDEZ

Ph.D. THESIS
Advisor: Prof. J. Marro Borau
Granada, November 6$^{th}$, 2002

*To Ana*

# Contents

# List of Figures

# List of Tables

# Chapter 1

# Introduction

The beauty of Physics underlies on the striking simplicity of its fundamental laws. Maxwell equations, Hamiltonian mechanics, Einstein and Schrödinger equations, can each be expressed in a few lines. Not only the laws of Physics, but also the philosophic ideas behind these laws are simple. Everything is simple, except the world these laws intend to describe.[1] Nature is complex at all levels. Think for instance about a living organism (say yourself). You are ultimately made of many elementary particles, whose behavior can be accurately described within the framework of the Standard Model. However, we do not understand at all how the collective dynamics of such a large set of (quantum) particles can give rise to the amazing phenomenon of life. The whole does not behave as a simple superposition of its parts.

Complexity arises due to the non-trivial underlying structure of all natural systems, and the non-linear interactions among their constituents. The obvious question now is: how the complex world emerges from the simple laws of Physics?. The search for an answer to this question was the seed that gave rise to the development of Statistical Mechanics during the second half of XIX century and the beginning of XX century. In a general sense, Statistical Mechanics is a branch of Physics aimed to describe the macroscopic (complex) properties of matter from the interactions between its microscopic constituents. The most successful achievement of Statistical Mechanics is Ensemble Theory[2], which yields the connection between the microscopic fundamental physics and the macroscopic behavior of equilibrium systems. An isolated system which shows no hysteresis and reaches a steady state is said to stay at equilibrium.[3] Starting from a few basic postulates, Ensemble Theory provides us with a well-defined "canonical" formalism in order to obtain the stable equilibrium properties of macroscopic matter.[82] In particular, it allows us to understand how complex situations, as for instance phase transitions, arise in many-body interacting systems.

However, most of the systems we find in Nature are out of equilibrium: they are open, hysteretic systems, subject to thermal or energetic gradients, mass and/or energy fluxes, which suffer the action of external agents, or are

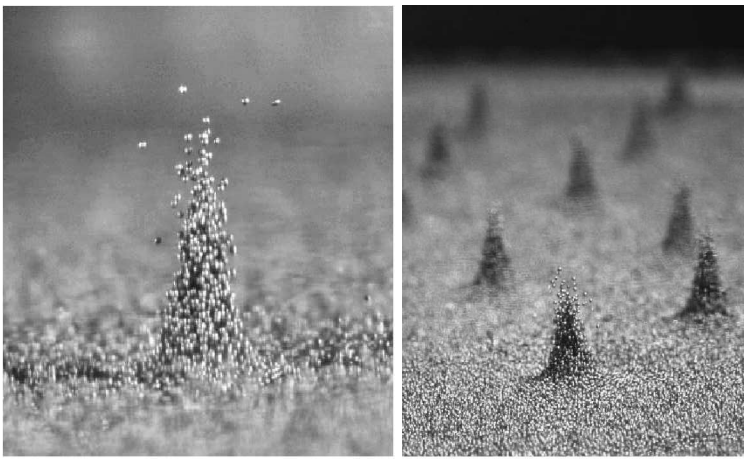

Figure 1.1: *Complexity in Nature:* pattern formation in vertically vibrated granular materials. In particular, here we observe localized wave structures called *oscillons*.[4]

subject to several sources of non-thermal noise. Think again about yourself: can you feel your breath?. This is a pure non-equilibrium process, where a flux of air from the external medium towards your lungs appears due to a pressure gradient. Nonequilibrium processes are also essential for cell functioning, brain processing, etc. What is more intriguing, all living organisms are nonequilibrium structures: nonequilibrium conditions are essential for life. On the other hand, nonequilibrium structures appear at all scales. For instance, the Sun exhibits temperature gradients, mass and energy transport, convection, etc. On the opposite limit one finds for example magnetic nanoparticles, where quantum tunneling acts as a non-thermal noise source inducing nonequilibrium conditions, or turbulent fluids. Nature abounds in such examples. In fact, non-equilibrium phenomena are the rule, being equilibrium systems a rather unlikely exception. It seems that nonequilibrium is a fundamental ingredient for the observed structure in Nature. As in equilibrium systems, those systems out of equilibrium also show instabilities which give rise to spatio-temporal patterns, dissipative structures, self-organization, time oscillations, spontaneous symmetry-breaking, etc., all of them commonly observed in Nature. All these instabilities are generally known as *nonequilibrium phase transitions*, and their properties are much richer than in equilibrium systems.

However, we are still lacking a general theory, equivalent to Statistical Mechanics for equilibrium systems, which allows us to classify and understand systems far from equilibrium, connecting their macroscopic phenomenology with their microscopic properties. In general, we only have at our disposal a set of *ad hoc* theoretical approximations which describe in a partial and incomplete manner the physics governing these systems. Hence nonequilibrium systems constitute a challenge for theoretical physicists, besides being very in-

teresting from the practical point of view due to their ubiquity in Nature. The simplest situation in a nonequilibrium system is that of a steady state. In this case, the properties of the system do not depend on time, thus simplifying the analysis. Nonequilibrium steady states (NESS) have been studied in depth during the last 20 years,[34] finding that their properties are much richer than those for equilibrium steady states. In general NESS do not obey the Boltzmann distribution. Moreover, they are not unique for a given system and fixed parameters, depending on the specific dynamics and the previous history of the system. On the other hand, the dynamics of nonequilibrium systems has been poorly studied.

> *The study of the dynamical properties of some nonequilibrium systems is the aim of this thesis.*

Many of the most interesting dynamic phenomena in complex systems are usually related to the transformation of one phase into another. Think for instance on the evolution from a uniform mixture of chemical constituents to a phase-separated pattern of precipitates. Other examples are the evolution from a disordered phase to an ordered one, or the exit from a metastable phase towards the truly stable one, etc. These transformations are not abrupt, but they involve a temporal (and usually inhomogeneous) evolution. The mechanisms behind these dynamical processes often involve the minimization of certain *privileged* fundamental observables -as the free energy in equilibrium systems- which contain the information about the system state at any time, and shed light on the relevant ingredients we must take into account to build up a theoretical description of the process. These dynamic transformations involve many features commonly observed in Nature: pattern formation and morphogenesis[5, 6], avalanche-like dynamics and self-organization[102], etc.

The dynamic evolution between two different phases is a nonequilibrium process since the system is not in a steady state. If the system under study is isolated and shows no hysteresis, we know that the steady state it will finally reach is an equilibrium state.[3] In this case the evolution between different phases, in spite of being a nonequilibrium process, can be understood and described using (equilibrium) Statistical Mechanics. This is the case of metastability and phase separation in equilibrium systems, which are described using appropriate extensions of the equilibrium free energy. We are interested in this thesis in dynamic processes in systems which asymptotically converge towards a NESS. These systems are essentially far from equilibrium (even in the steady state) and hence cannot be described by (equilibrium) Statistical Mechanics.

In addition to the phase-transformation dynamic processes described above, there are some dynamic phenomena in nonequilibrium systems which have no equilibrium counterparts. For instance, this is the case of systems suffering a dynamic phase transition between an active phase, characterized by the existence of non-trivial dynamics, and an absorbing phase, where the system is frozen, without any dynamics and hence no chance of escape. Another example is that of heat conduction, where a temperature gradient induces a steady energy flow from the hot reservoir to the cold one.

The study of dynamic phenomena in nonequilibrium systems and the underlying mechanisms driving these processes yields much information about the relevant observables which define the system evolution. Such observation, together with the comparison to similar results in equilibrium systems, help us in the search of a general theory for nonequilibrium systems (which should describe equilibrium systems as a limiting case).

In general, the study of the dynamic and/or static properties of real systems with many degrees of freedom is a formidably complicated task. Hence, approaching the study of these systems from first principles is not usually feasible in practice. For this reason we must study simplified models of reality that, while capturing the fundamental ingredients of real systems, are much more easily tractable. Usually these models are defined on a lattice, instead of being defined on the continuous space, and the interactions among their constituents are modeled in a very simple way. The obvious question now is: what do these models have to do with real systems?. In order to answer this question we must introduce the concept of *universality*, which is one of the most important philosophic ideas of modern physics. This concept is based on the observation that disparate systems often display strikingly similar features and behavior. It is observed in Nature that the large scale structure and behavior of a system do not depend on its microscopic details, but only on the fundamental features defining the system, as for instance dimensionality, symmetries, conservation laws, range of forces, kind of order parameter, etc. In this way all systems sharing the same essential features exhibit the same kind of behavior, in spite of being apparently very different (say a lattice gas and a saturated real vapor). Therefore these systems exhibit universal behavior[1]. This universal behavior allows us to design *minimal* models of reality that capture all the relevant ingredients of real systems, while they *maximally* simplify the microscopic irrelevant details. The universality property guarantees that the behavior of the system is not sensitive to the microscopic details, and hence that our results for the oversimplified model will also describe the behavior of the real system, provided that both systems share the same fundamental features. As an example, think for a while on the Navier-Stokes equation, which describes the macroscopic behavior of a incredibly large set of different fluids.[8] This equation is a simplified model of real fluids, based on several symmetries and conservation laws, which describes the macroscopic behavior of fluids with different compositions, interatomic forces, molecular weights, etc., but which share some fundamental features as mass and energy conservation, dimensionality, etc.

In spite of being oversimplified versions of real systems, the models we are going to study in this thesis exhibit a highly non-trivial and complicated

[1] In particular, universality appears in second order phase transitions. There the correlation length diverges, so that all scales are equally relevant and the microscopic details are no longer important. All systems sharing the same values for the critical exponents associated to a critical point belong to the same *universality class*. In a similar way, *dynamic universality classes* can be defined which include systems sharing the same dynamic exponents.[7] However, in this chapter we are presenting the concept of universality from a wider point of view, not only restricted to critical phenomena.

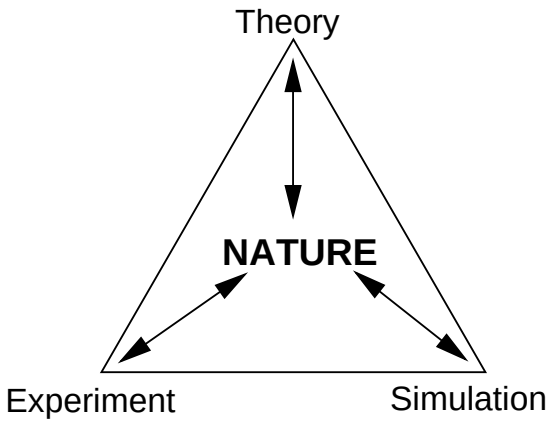


Figure 1.2: *Physics research:* The three ways of doing physics research nowadays. All three are complementary.[9]

behavior. For this reason we must use computer simulations in order to investigate such systems in detail, in addition to approximate theoretical tools. Computers allow us to simulate systems which would be intractable in other way. In addition, simulations help us to obtain the intuition we need in order to solve and understand the behavior of complex many-body systems. Historically, Physics has been called *natural philosophy*, since the research was only done via purely theoretical (i.e. philosophical) investigations. Eventually the experimental method was accepted as a second way of doing physics research, although it is limited by the scientists ability to design the appropriate experiments, prepare the system and accurately measure the desired magnitudes. Nowadays computer simulations have become a third way of doing physics research, yielding a new perspective. Sometimes computer simulations provide the theoretical basis we need in order to understand some experimental results, and other times simulations serve as *experiments* to which compare a theory. In any case, simulations complement the classical theoretical and experimental approaches to Nature.

The most used simulation method in this thesis will be the Monte Carlo method, although we will also implement other methods, as the Molecular Dynamics one. Monte Carlo method is very useful when studying the temporal evolution of models which have no deterministic dynamics (in the sense of Newton equations) but are subject to stochastic dynamics. In practice it is usually not possible to make a 100% atomistic description of the system we want to model. Roughly speaking, we do not need (and we are not able) to take into account the individual quark behavior when modeling a macroscopic material. On the contrary, one builds up a coarse-grained description of the system, taking into account only the relevant variables for the problem under study (say spins in a magnetic material), and letting the fast degrees of freedom that we

forget about in our coarse-grained description to act as a heat bath, thus inducing stochastic transitions on the relevant degrees of freedom. This method makes use of a sequence of pseudo-random numbers (this is the reason why it is called *Monte Carlo*).[9] On the other hand, the Molecular Dynamics method is based on the numerical integration of Newton equations of motion.

As we said before, the objective of this thesis is to study the dynamics of some nonequilibrium systems. In particular, we will pay attention to *metastability* and *avalanches* in a nonequilibrium ferromagnetic spin system, *phase segregation* in a driven (anisotropic) lattice gas, phase transitions in a system with *(super)absorbing states*, and *heat conduction* in a one-dimensional particle system. In this way we want to cover a wide variety of dynamic phenomena appearing in nonequilibrium systems. Of course, the list is not complete, lacking some fundamental phenomena, as for instance hydrodynamics. However, and in spite of the heterogeneity of this thesis, we think that the studied systems and processes yield a comprehensive overview of the effects that nonequilibrium conditions induce on dynamic phenomena in complex systems. The thesis is divided into two parts. The first part, which comprises chapters 2, 3, 4, 5 and 6, is devoted to the study of metastability (chapters 3, 4 and 5) and avalanches (chapter 6) in a nonequilibrium ferromagnetic spin model. The second part of this work is devoted to the study of anisotropic phase separation (chapter 7), systems with superabsorbing states (chapter 8), and heat conduction and Fourier's law (chapter 9).

Metastability is a crucial concept in many branches of Science. It has been observed in fluids, plasmas, quantum field theory, superconductors and superfluids, magnetic systems, atmospheric dynamics, cosmology, etc. It usually determines the system behavior. In particular, we are interested in metastability in nonequilibrium systems with short range interactions. In this way we study here metastability in a nonequilibrium ferromagnetic spin model, which is relevant for the problem posed by magnetic storage of information. On the other hand, from the theoretical point of view, studying metastability in this impure ferromagnet will allow us to investigate the existence of a nonequilibrium potential, equivalent to the equilibrium free energy, which controls the exit from the metastable state.

In this way, in **chapter 2** we motivate the study of metastability in nonequilibrium systems, presenting the ferromagnetic model we will investigate in the first part of this work. We also discuss some of the properties that characterize this model, paying special attention to the way in which nonequilibrium conditions enter the model definition.

In **chapter 3** we perform a mean field study of the metastability phenomenon. In particular we apply the Pair Approximation[51] to our model in order to obtain its static and dynamic properties. This study uncovers very interesting properties related to the non-linear interplay between the thermal noise and the non-thermal fluctuations induced by the nonequilibrium conditions.

**Chapter 4** is devoted to the study of the properties of the interface in the nonequilibrium model. The inhomogeneous character of the metastable-stable transition implies that the interface between the metastable and stable phases

plays a determining role in this process. In this chapter we generalize the Solid-On-Solid approximation of Burton, Cabrera and Frank[59] for an equilibrium discrete interface in order to take into account the effect induced by nonequilibrium conditions. This generalization is based on the concept of effective temperature. We find very interesting results at low temperatures showing, for instance, that the nonequilibrium surface tension converges to zero in this limit. We also study in this chapter the shape of a spin droplet using the Wulff construction[68].

In **chapter 5** we extend the equilibrium nucleation theory[26] to the nonequilibrium system, hypothesizing the existence of a nonequilibrium potential, similar in form to the equilibrium free energy, which controls the exit from the metastable state. Applying the results obtained in chapters 3 and 4 for the bulk and interfacial properties, we find surprising results for the metastable-state mean lifetime, the critical droplet size, the domain wall velocity and the metastable-stable transition morphology in the nonequilibrium case, which are fully confirmed via Monte Carlo simulations. In addition to its theoretical importance, these results may be technologically relevant.

In **chapter 6** we observe that under the combined action of both free boundaries and nonequilibrium conditions, the evolution from the metastable phase towards the stable one proceeds through well-defined avalanches. These avalanches are shown to follow power-law, i.e. scale free distributions. However, a detailed study reveals that this scale free behavior is a consequence of a finite superposition of well-defined, gap-separated typical scales, instead of being a consequence of any underlying critical point. The excellent comparison of our results with some Barkhausen experiments led us to suspect that Barkhausen Noise in particular, and $1/f$ noise in general, might also come from a superposition of elementary events.

**Chaper 7** is devoted to the study of phase separation in nonequilibrium anisotropic lattice gases. Phase separation appears in system with conserved number of particles. It is a dynamic process which has been largely studied in equilibrium systems. In addition to theoretically challenging, the details are of great practical importance. However, as we previously discussed, most systems in Nature are out of equilibrium. Therefore, extending the concepts involved in the phase separation process to more realistic situations is very interesting. This is the case, for example, for mixtures under a shear flow, whose study has attracted considerable attention.[128]-[132] Hence in this chapter we study anisotropic phase separation in a driven lattice gas. We propose a cluster effective diffusion theory in order to explain the late stage coarsening in this system. This theory describes correctly the grain growth process and the different growth regimes found during the evolution. In addition, we also demonstrate dynamical scaling of the structure factor, and generalize Porod's law to anisotropic systems. Finally we also study the dynamics of a continuous field equation, showing qualitatively its validity to describe the dynamics of the microscopic model.

In **chapter 8** we study a system showing a phase transition between an active phase, characterized by a nontrivial dynamics, and an absorbing phase,

which is completely frozen. In this sense this is a *dynamic phase transition*. There are many examples in Nature of systems with absorbing states and absorbing phase transitions: chemical reactions in autocatalytic reaction-diffusion systems and heterogeneous catalysis models, problems related with directed percolation, fire and epidemic spreading, etc. Absorbing states appear in situations where certain observable can proliferate or die, but never generate spontaneously. In this way the essential physics comes from the competition between the growth and dead of the relevant observable. There are two main universality classes in systems with absorbing states: the directed percolation (DP) universality class, and the multiplicative noise universality class. In this chapter we study how a new, hidden symmetry in a system with absorbing states (known as Lipowski model[176, 179]), namely the presence of the so-called *superabsorbing states*, is relevant at the critical point, thus defining a new scaling behavior.

In **chapter 9** we study heat conduction and Fourier's law in a one-dimensional particle model. Heat conduction is just one particular aspect of transport phenomena, which are dynamic processes that appear ubiquitously in Nature. Some classical examples are heat and mass transport in fluids, diffusion, electric conduction, stellar convection, etc. In spite of being very important, their microscopic understanding is far from clear. In particular, in this chapter we want to investigate the microscopic basis of heat conduction. Therefore we present computer simulation results for a chain of hard-point particles with alternating masses subject to a temperature gradient. We find, performing different, complementary numerical analysis, that the system obeys Fourier's law at the Thermodynamic Limit. This result is against the actual belief that one-dimensional systems with momentum conservative dynamics and non-zero pressure have an infinite thermal conductivity.[196] It seems that thermal resistivity occurs in our system due to a cooperative behavior in which light particles tend to absorb much more energy than heavier ones.

Finally, in **chapter 10** we present our conclusions, summing up the results obtained along this work and pointing out the possible research lines to follow in order to continue these investigations.

In what follows we summarize the original contributions contained in this thesis:

- In chapter 3 we calculate in mean field approximation and using computer simulations the *intrinsic coercive field*, $h^*$, associated to the nonequilibrium spin model. We show that the behavior of $h^*$ for strong nonequilibrium conditions signals the existence of a non-linear cooperative effect between the thermal noise and the nonequilibrium fluctuations, which involve the disappearance of metastable states at low temperatures, as opposed to what happens in equilibrium systems.

- In chapter 3 we also present a natural way to introduce fluctuations in a dynamic mean field theory. This method allows us to study the dynamics of the metastable-stable transition in mean field approximation.

- In chapter 4 we generalize the Solid-On-Solid approximation[59] in order to investigate the effects that nonequilibrium conditions induce on the system interface. This generalization, based on the concept of effective temperature, accurately describes the properties of the nonequilibrium model interface.

- In chapter 5 we introduce a hypothesis about the existence of a nonequilibrium potential, equivalent to the equilibrium free energy, which controls the exit from the metastable state. This hypothesis allows us to properly describe the nonequilibrium metastable-stable transition.

- In chapter 6 we measure scale free avalanches, and identify their origin, which is based on a finite superposition of avalanches with well-defined typical scales. Comparing our results with some Barkhausen experiments, we are able to propose a new explanation for Barkhausen Noise in particular and the ubiquitous $1/f$ Noise in general.

- We propose in chapter 7 a cluster effective diffusion theory in order to explain coarsening in the driven lattice gas, based on two different types of monomer events. In the same way, we demonstrate dynamical scaling of the structure factor, and generalize Porod's law to anisotropic systems. We also study the dynamics of a field theoretical equation whose dynamical properties have never been studied.

- In chapter 8 we identify the presence of superabsorbing sites as a new relevant symmetry in systems suffering absorbing phase transitions. In this way we define a novel scaling behavior.

- Finally, in chapter 9 we propose a new cooperative mechanism which gives rise to normal thermal conductivity in one-dimensional particle systems.

# Part I

# Metastability and Avalanches in Ferromagnetic Systems under Nonequilibrium Conditions

# Chapter 2

# Motivation and Model Definition

## 2.1 Introduction

The concept of metaestability is a cornerstone in many different branches of Science. In spite of its importance, it is very difficult to obtain a precise and general definition for it. The British Encyclopedia defines a metastable state in the following way: *in Physics and Chemestry, a metastable state is a particular excited state of an atom, nucleus or other system, such that its lifetime is larger than that of usual excited states, but generally lower than that of the ground state, which is often stable. A metastable state can be then considered as a temporal energetic trap or an intermediate stable state*. This definition, in spite of its ambiguity, captures the essence of what a metastable state is: it is a local, non-global stable state since the system finally evolves towards the ground state[1], but it is also a state very similar to the stable one, due to the long time the system spends wandering around it. There are many other different definitions of metastability in literature, some of them much more precise from the mathematical point of view, although they are always restricted to particular systems. For instance, we should say that a metastable state in Equilibrium Thermodynamics corresponds to a local, not global free energy minimum.

Metastability is observed in fluids, solids, plasmas and many other systems, and it usually determines their behavior. The metastability phenomenon is often related to the existence of an underlying first order phase transition. A prototypical example is that of supercooled water: if we slowly cool down a glass of water, in such a way that the final temperature is slightly below the solidification point, water will remain liquid. This supercooled liquid is in a metastable state: although the true stable state for this temperature is the crys-

[1]This is not strictly true. There are metastable states with infinite lifetime in systems subject to long range interactions. This problem points out, once more, the difficulties found in order to establish a precise definition of metastability.

tallized one, an energy barrier exists that prevents water crystallization (the system is confined in an *energetic trap*). If we add to the system a sufficient amount of energy from the outside in order to overcome the energy barrier (for instance, hitting softly the glass), the system will evolve from the metastable state to the stable one through the *nucleation* of crystals of the stable phase inside the metastable bulk.[10] The processes of energetic *activation* and *nucleation* here illustrated are crucial in order to understand how a generic system is able to exit the metastable state and to evolve to the true stable state.

There are many other systems which show metastability. In fact, metastability is observed from the smallest scales in the Universe to the largest ones. For instance, if the Higgs boson mass is as small as suggested by the latest experiments, this should point out that the Standar Model ground state, called *vacuum* in Quantum Field Theory, is metastable, instead of being a true stable state. This observation allows us to give a lower bound for the Higgs boson mass, since the metastable vacuum must have a long lifetime compared to the age of the Universe.[11] Moreover, some works have recently appear that speculate with the possibility that heavy ion collisions at the Relativistic Heavy Ion Collider in the Brookhaven National Laboratory (U.S.A.) should trigger a transition towards the true Standar Model vacuum.[12] Such transition would imply an apocalyptic disaster[2]. Metastability is also observed in quark/gluon plasma[13], systems showing superconductivity and superfluidity[14], electronic circuits[15], globular proteins[16], magnetic systems[17], climatic models [18], black holes and protoneutronic stars[19], cosmology[20], etc. A better microscopic understanding of this ubiquitous phenomenon is then of great theoretical and technological interest, besides a formidable mathematical challenge.

A problem of particular importance is that posed by magnetic storage of information, which is intimately related with metastability. A magnetic material is usually divided into magnetic monodomains. In order to store information on this material, we magnetize each individual domain using a strong magnetic field. In this way, each domain exhibits a well defined magnetization in the direction of the local applied field, thus defining a bit of information. A main concern is to retain the individual domain orientations for as long as possible in the presence of weak arbitrarily-oriented external magnetic fields, in order to keep unaltered the stored information. The interaction with these weak external fields often produces metastable states in the domains. The resistance of stored information depends on the properties of these metastable states, including the details of their decay.

In general, complex systems have many degrees of freedom which make very complicated any first-principles theoretical approach to their behavior. In particular, this is the case for the aforementioned magnetic systems, where there is a macroscopic number of magnetic moments or spins which interact among them and with an external magnetic field. Therefore, we are forced to

[2]Fortunately, the probability of such catastrophic scenario is estimated to be negligible, although non vanishing ...

study simplified models of real systems that, while capturing their relevant ingredients, are much more easily tractable. There has been in last decades a huge amount of works studying the problem of metastability in lattice models of classical spins. The most studied model has been the Ising model in one, two and three dimensions.[21, 81] The general interest in this model is two-fold. On one hand, it captures many of the fundamental features of a wide class of real systems. On the other hand, many of its equilibrium properties are analytically known in one and two dimensions[22]. This fact makes much more easy any theoretical approach to the properties of this model. In this way, continuous theories based on nucleation mechanisms have been proposed which successfully describe the evolution from the metastable state to the stable one.[23] Also the problem of metastability in the low temperature limit has been exactly resolved.[24] These theoretical results have been checked many times via computer simulations.[25, 26] Very interesting analytical and computational results have been obtained, showing the existence of different parameter space regions in finite systems, each one characterized by a typical metastable-stable transition morphology.[26] Likewise, the effects that open borders[27, 28], quenched impurities[29] and demagnetizing fields[30] have on the properties of metastable states in these systems have also been investigated.

With some exceptions[31], most works on metastability in magnetic systems have been limited to equilibrium models. For these models, the equilibrium Statistical Mechanics of Boltzmann, Gibbs, Einstein, etc. yields a clear-cut connection between microscopic and macroscopic Physics in terms of the partition function.[2] In this way, steady states in equilibrium systems are characterized by the Boltzmann distribution, $Z^{-1}\exp(-\beta E)$, where $\beta$ is the inverse temperature, $E$ is the state energy and the normalization constant $Z$ is the system's partition function. Although metastability is a dynamic phenomenon not included in the Gibbs formalism,[27] so successful on the other hand when describing equilibrium states, it is possible to understand such phenomenon extending dynamically the Gibbs theory using the thermodynamic potentials defined in this equilibrium theory and its connection with the microscopic parameters that characterize the system. In this way, nucleation theory, which correctly describes metastability in systems near a first order phase transition, is based on the concept of free energy of a droplet of the stable phase. This magnitude is an heterogeneous extension of the thermodynamic potential associated to the canonical partition function in an equilibrium system.

However, most of the systems we find in Nature are out of equilibrium: they are open systems, subject to thermal or energetic gradients, mass and/or energy currents, which suffer the action of external agents, or are subject to several sources of non-thermal noise. As an example, it has been observed that some properties of metastable states in certain mesoscopic magnetic particles are highly affected by quantum tunneling of individual spins, which is a pure nonequilibrium process since it breaks detailed balance.[32] Furthermore, there are nonequilibrium lattice spin models which reproduce these results.[31] For nonequilibrium systems there is no theory equivalent to equilibrium Statistical Mechanics that connects their microscopic properties with their macroscopic

phenomenology. If we want to understand metastability in real (i.e., nonequilibrium) systems we must study simplified nonequilibrium models. On the other hand, and from a theoretical point of view, the study of metastability in nonequilibrium systems will allow us, comparing with the well-established equilibrium results, to understand how nonequilibrium conditions affect a dynamic process like metastability. This comparison will also allow us to study the changes that the nucleation process suffers under nonequilibrium conditions, as well as the possible existence of some functional, similar to the equilibrium free energy, which controls the relaxation from the metastable state.

In the following chapters we are going to study metastability in magnetic thin films under nonequilibrium conditions. On the analogy of equilibrium systems, it seems sensible to model these magnetic systems using a bidimensional kinetic Ising lattice with nearest neighbor interactions and periodic boundary conditions. In addition, we will consider a (very) weak random dynamic perturbation competing with the usual thermal spin flip process. It has been shown that the presence of this weak perturbation could explain some intriguing properties, as for instance the non-vanishing value of magnetic viscosity in the low temperature limit, of some real magnetic materials.[31, 32] The impurity makes the system to reach asymptotically a nonequilibrium steady state. That is, we assume that a principal role of the microscopic disorder which is generally present in actual specimens consists in modifying the dynamics -in a way similar to that of an external non-Hamiltonian agent.[51]

It is observed that, under the action of the dynamic perturbation and a weak magnetic field oriented opposite to the initial magnetization, the system's demagnetization process from the initial metastable state to the true stable one proceeds through the nucleation of one or several critical droplets of the stable phase in the metastable bulk, as observed in equilibrium systems. Although, oppositely to what happens in equilibrium, we cannot properly define here any free energy functional that controls the demagnetization process, we can however hypothesize the existence of some nonequilibrium potential, similar to the equilibrium free energy, where two terms compete. On one hand, there is a surface term, which hinders the growth of the stable phase droplet. On the other hand, there is a bulk term, which favours its growth. If this hypothesis is correct (as we will see later on) we should expect a good description of the metastable-stable transition in terms of this nonequilibrium potential once we understand the bulk and interfacial properties of our model under the action of the nonequilibrium random perturbation. With this aim we will propose in the following chapters approximate theories to study the effect of the dynamic random perturbation on the system's bulk and interface. As a result, we will conclude that the bulk exhibits a very interesting non-linear cooperative phenomenon between the thermal noise and the non-thermal (nonequilibrium) fluctuations when subject to strong nonequilibrium conditions, although bulk properties are qualitatively similar in both the equilibrium and weak nonequilibrium cases. On the other hand, the interfacial properties in the nonequilibrium system change in a fundamental way. In particular, we will observe that while the surface tension in the equilibrium system monotonically grows

as temperature decreases, the surface tension in the nonequilibrium case exhibits a maximum for a given temperature, decreasing for smaller temperatures. Using this result, and the hypothesis of existence of a nonequilibrium potential that controls the metastable-stable transition, we are able to develop a nonequilibrium nucleation theory analogous to the equilibrium one. However, the results obtained from this nonequilibrium theory are surprising, since the nonequilibrium conditions imply a completely different behavior of the system at low temperatures, as compared with the equilibrium one. We observe that metastability tends to disappear at low temperatures. Even existing, the metastable lifetime reaches a maximum for a given temperature, decreasing if we further decrease the temperature. These results point out that the general belief which states that in order to prolong the lifetime of a metastable state we must cool the system is not true if the system is subject to any random perturbation as the one we implement (perturbation which, on the other hand, is usually present in real systems -quantum tunneling, external noises, etc.-). Moreover, our theory predicts the existence of a low temperature phase where the system demagnetizes through the nucleation of multiple stable phase critical droplets, as opposed to equilibrium systems, which demagnetize through the nucleation of a single critical droplet at low temperatures.[26] All our theoretical results are compared with extensive Monte Carlo simulations, showing very good agreement.

This and the following chapters are organized as follows. In section 2.2 of the present chapter we describe the model in detail, summarizing some of its properties. We also briefly explain in this section the computational scheme used in our simulations. Chapter 3 is devoted to a first order dynamic mean field approximation. This approximation, also called Pair Approximation or Bethe-Peierls Dynamic Approximation, will allow us for a first theoretical approach to the problem of metastability. In Chapter 4 we study the properties of the interface in the nonequilibrium model. In order to do so we generalize the Solid-on-Solid Approximation for discrete interfaces to take into account the effects that nonequilibrium conditions induce on the interfacial properties. Finally, in Chapter 5 we propose a nonequilibrium Nucleation Theory for the nonequilibrium model, formally similar to that of equilibrium systems, but where we introduce the results obtained for the bulk and interfacial properties affected by nonequilibrium conditions. In this chapter we also present our conclusions about the problem of metastability in nonequilibrium systems, paying some attention to practical applications of our results and possible experimental implications.

## 2.2 The Model

In the following chapters we are going to study a bidimensional kinetic Ising model with periodic boundary conditions and subject to a dynamic random perturbation. The two-dimensional Ising model[33] is defined on a square lattice of side L. On each lattice node a spin variable is defined, $s_i$, with $i \in [1, N]$,

$N = L^2$. Each spin can take two different values: $s_i = +1$ (up spin) o $s_i = -1$ (down spin). The system is characterized by the Hamiltonian,

$$\mathcal{H}(\mathbf{s}) = -J \sum_{\langle i,j \rangle} s_i s_j - h \sum_{i=1}^{N} s_i \tag{2.1}$$

where $J > 0$ is the (ferromagnetic) coupling constant, $\mathbf{s} \equiv \{s_i, i = 1, \ldots, N\}$ is the system's configuration, and $h$ is an external magnetic field. The first sum runs over all nearest neighbor pairs, $\langle i, j \rangle$, while the second sum runs over all spins. We endow this kinetic model with a dynamics determined by the stochastic master equation,[37]

$$\frac{dP(\mathbf{s};t)}{dt} = \sum_{\mathbf{s}'} \left[ \omega(\mathbf{s}' \to \mathbf{s}) P(\mathbf{s}';t) - \omega(\mathbf{s} \to \mathbf{s}') P(\mathbf{s};t) \right] \tag{2.2}$$

where $\mathbf{s}$ and $\mathbf{s}'$ are system's configurations, $P(\mathbf{s};t)$ is the probability of finding the system in a configuration $\mathbf{s}$ at time $t$, and $\omega(\mathbf{s} \to \mathbf{s}')$ is the probability per unit time (or transition rate) for a transition from configuration $\mathbf{s}$ to $\mathbf{s}'$. In order to complete the definition of the model, we must precise the transition rate $\omega(\mathbf{s} \to \mathbf{s}')$. In our case we assume that the system evolves due to the superposition of two "canonical" dynamics. That is, we choose the transition rate to be,

$$\omega(\mathbf{s} \to \mathbf{s}^i) = p + (1-p) \frac{e^{-\beta \Delta \mathcal{H}_i}}{1 + e^{-\beta \Delta \mathcal{H}_i}} \tag{2.3}$$

(*Glauber dynamics*). Here $\mathbf{s}^i$ stands for the configuration $\mathbf{s}$ after flipping the spin at node $i$, $\beta = 1/k_B T$ is the inverse temperature, $k_B$ is the Boltzmann constant, and $\Delta \mathcal{H}_i \equiv \mathcal{H}(\mathbf{s}^i) - \mathcal{H}(\mathbf{s})$. We only allow single spin flip transitions between configurations. In what follows we fix Boltzmann constant to unity, $k_B = 1$.

One can interprete the above dynamical rule as describing a spin flip process under the action of two competing heat baths: with probability $p$ the spin flip is performed completely at random, independently of any energetic consideration (we can interpret in this case that $\mathbf{s}$ is in contact with a heat bath at *infinite* temperature), while the spin flip is performed at temperature $T$ with probability $(1-p)$ .

The dynamics we have chosen is a particular case of the general group of competitive dynamics.[34] Let's suppose we have two different dynamics $\omega_1$ and $\omega_2$ which independently satisfy detailed balance,

$$\frac{\omega_j(\mathbf{s} \to \mathbf{s}')}{\omega_j(\mathbf{s}' \to \mathbf{s})} = e^{-\beta \Delta \mathcal{H}} \tag{2.4}$$

where $j = 1, 2$ and in this case $\Delta \mathcal{H} = \mathcal{H}(\mathbf{s}') - \mathcal{H}(\mathbf{s})$. The detailed balance condition ensures that the stationary state under the action of one of these dynamics will be described by a Boltzmann distribution. That is, in the stationary state the probability of finding the system in a configuration $\mathbf{s}$, $P_{st}(\mathbf{s})$, will be proportional to $\exp[-\mathcal{H}(\mathbf{s})/T]$ (remember we fixed $k_B = 1$). Hence, the detailed

balance condition for the transition rate is sufficient, although not necessary, in order to make the system converge asymptotically to an equilibrium stationary state. This is the case for dynamics $\omega_1$ and $\omega_2$ independently. However, if the stationary state to which dynamics $\omega_1$ drives the system is different from the stationary state associated to dynamics $\omega_2$ (for instance, if both dynamics work at different temperature), any competitive dynamics of the form $p\omega_1 + (1-p)\omega_2$ with $0 < p < 1$ will produce in the system what is called in literature *dynamical frustration*, and the competition between both dynamics generically drives the system towards a nonequilibrium steady state[3].

As can be deduced from (2.3), in our case we have chosen $\omega_1 = 2\omega(\beta_1\Delta\mathcal{H})$ and $\omega_2 = \omega(\beta_2\Delta\mathcal{H})$, where $\omega(\beta\Delta\mathcal{H}) = \exp(-\beta\Delta\mathcal{H})/[1+\exp(-\beta\Delta\mathcal{H})]$ is the Glauber transition rate, with $\beta_1 = 0$ and $\beta_2 = \beta \equiv 1/T$, and where only transitions between configurations which differ in a single spin are allowed. This is only one of infinite possibilities when constructing a competing dynamics from two canonical dynamics driving independently the system towards equilibrium. In principle, any of these infinite possibilities should be equally valid in order to investigate how nonequilibrium conditions affect the properties of metastable states in Ising-like systems. However, if we want to predict properties of real magnetic systems, we then have to choose carefully the dynamics. Thus, Glauber dynamics, used here in our definition of $\omega$, can be derived from first principles for a system of $\frac{1}{2}$-spin fermionic quantum particles, each one subject to its own thermal bath.[38] On the other hand, the weak dynamic perturbation parameterized by $p$ emulates in some sense the effect of quantum tunneling of individual spins in real magnetic systems. The existence of this small $p \neq 0$ allows the spins to flip independently of any energetic constraint imposed by their surroundings with a (very) low probability. This is roughly what quantum tunneling produces in real spins: the spin is able to flip by *tunneling* through the energy barrier which impedes its classical flipping, i.e., independently of this energy barrier. We also can interpret in a more general way the dynamic random perturbation parameterized by $p$ as a generic source of disorder and randomness, i.e. as a simplified representation of the impure dynamic behavior typical of real systems.[31]

For $p = 0$, the dynamics (2.3) corresponds to the canonical Ising case which converges asymptotically towards a Gibbs equilibrium state at temperature $T$ and energy $\mathcal{H}$. In this case the model for $h = 0$ exhibits a second order phase transition at a critical temperature $T = T_c \approx 2.2691J \equiv T_{ons}$.[22] The critical exponents associated to this phase transition define the Ising universality class. This universality class is one of the most robust, and all phase transitions in monocomponent systems with up-down symmetry and without any extra symmetry or conservation law (model A in the Hohenberg-Halperin classification[39]) belong to this universality class. For $p \neq 0$ the conflict in (2.3) impedes canonical equilibrium, and as we mentioned above the system then

[3]This is true except for some (in principle) nonequilibrium systems which can be mapped, under specific circumstances, to equilibrium systems with effective parameters. For these *special* systems we can write an effective Hamiltonian in such a way that the competing dynamics $p\omega_1 + (1-p)\omega_2$ verify detailed balance with respect to this effective Hamiltonian.[35, 36]

evolves towards a nonequilibrium steady state whose nature essentially differs from a Gibbs state at temperature $T$. The system now, and always for $h = 0$, exhibits a second order phase transition at a critical temperature $T_c(p) < T_{ons}$ for small enough values of $p$. This critical point disappears for values of $p$ above certain critical value $p_c$ defined by the condition $T_c(p_c) = 0$ (for more details, see next chapter). In general, critical phenomena in models with competition of dynamics have been studied as a paradigm of nonequilibrium phase transitions. In particular, it has been proved for Ising-like models with dynamics of the type $p\omega(T_1) + (1-p)\omega(T_2)$ where two different temperatures $T_1$ and $T_2$ compete, and where $\omega(T)$ is an equilibrium dynamics at temperature $T$, that the critical point observed at $T_{1,c}(p, T_2)$ belongs to the Ising universality class.[40, 41] Notice that our model is just a particular realization of a system under competition of temperatures.

In order to study metastability in our model, we initialize the system in a state with all spins up, i.e. $s_i = +1 \ \forall i \in [1, N]$, under a weak magnetic field which favours the opposite orientation, $h = -0.1$ (we will keep constant this magnetic field during our study). In what follows we will study several different values of temperature $T$ and dynamic perturbation $p$, such that the system is always in the ordered phase (i.e. below the critical point). Under these conditions the initial state is metastable, and it eventually will decay towards the truly stable state, which in this case is a negative magnetization state, $m \equiv N^{-1} \sum_i s_i < 0$. In principle we could use a classic Monte Carlo scheme[42] in order to simulate such system. However, as a consequence of the strong local stability that characterizes metastable states, the time the system needs to exit the metastable state and to evolve towards the stable one can be as long as $\tau \sim 10^{40}$ Monte Carlo Steps per spin at low temperatures. A Monte Carlo Step per spin corresponds to a spin flip trial of all the spins in the lattice on the average (from now on we will denote this temporal unit as MCSS). In general, for Ising spins interacting with a phonon bath, a MCSS corresponds roughly with a physical time of the order of the inverse phonon frequency, which is approximately $10^{-13}$ seconds.[43] If we suppose for a while that the classic Monte Carlo algorithm is able to execute a spin flip trial after every tic of the CPU clock (which has an approximate period of $10^{-9}$ seconds), we should wait for low temperatures a time of order $N \times 10^{31}$ seconds in order to observe the metastable-stable transition ($N$ is the number of spins in the lattice). This time is fairly larger than the age of the Universe. Hence, we need to use advanced, faster-than-real-time algorithms in order to simulate the behavior of these systems. This is the case for the *Monte Carlo with Absorbing Markov Chains algorithms*, generically known as MCAMC algorithms.[43] They are *rejection-free* algorithms, based on the *n-fold way* algorithm[44], that without changing the system dynamics (they only rewrite in an efficient way the classic Monte Carlo algorithm) are many order of magnitude faster than standard algorithms. However, for low temperatures and weak magnetic fields, even MCAMC algorithms are not efficient for the metastability problem. Hence we have to implement, together with MCAMC algorithms, the so-called *slow forcing approximation*.[45] In this approximation the system is forced to evolve to-

wards the stable state using a moving magnetization wall. That is, we define an upper bound for magnetization, which depends on time, $m_{lim}(t) = 1 - \phi t$, and we force the system magnetization to stay at any time below this magnetization threshold. Although this constraint clearly modifies the dynamics, it has been proved that a slow forcing limit exists for $\phi$[45], in such a way that in this limit all observables are independent of the forcing, while the simulation is still significatively accelerated as compared to the system without forcing. In Appendix A we explain in detail the MCAMC algorithms and the slow forcing approximation.

# Chapter 3

# Mean Field Approximation to the Problem of Metastability

## 3.1 Introduction

In this chapter we study the problem of metastability in the nonequilibrium magnetic system taking as starting point a first order dynamic mean field approximation. This approach is a generalization for the study of dynamic problems of Kikuchi's method[49] known as *Cluster Variation Method*. This method has been reformulated for the study of some nonequilibrium systems by Dickman and other authors[50, 51], with the name of Pair Approximation. In this chapter we will formulate in a first step the pair approximation applied to our model. Later on we will use this approximation to obtain information about the static properties that characterize the system. Finally, we will study the dynamics of the system using the mean field theory.

## 3.2 Formulation of the Pair Approximation

The approximation we describe here, following reference [34], is a mean field approximation as far as it neglects correlations actually present in the system, and it builds, using this assumption, a set of equations for averaged observables which describe the dynamical and statical behavior of the system.

As we saw in section 2.2, our system is defined on a square lattice $\Lambda = \{1, \ldots, L\}^2 \subset \mathbb{Z}^2$. A state in the system is described by a configuration vector $\mathbf{s} = \{s_i, i = 1, \ldots, N\}$, where $s_i$ is the spin variable associated to lattice site $i$, and $N = L^2$ is the number of spins in the system. The dynamics is given by the master equation,

$$\frac{dP(\mathbf{s};t)}{dt} = \sum_{i\in\Lambda} \left[\omega(\mathbf{s}^i \to \mathbf{s})P(\mathbf{s}^i;t) - \omega(\mathbf{s} \to \mathbf{s}^i)P(\mathbf{s};t)\right] \tag{3.1}$$

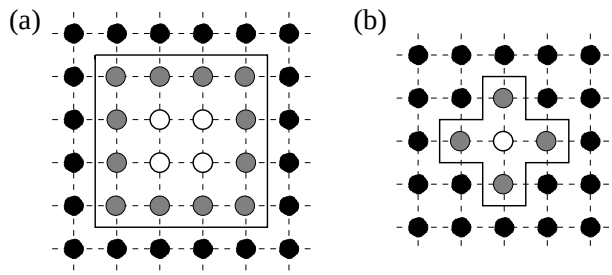


Figure 3.1: Different examples of spin domains, each one characterized by a different kind of partition $\mathbb{P}(\Lambda)$. External spins are coloured in black, surface spins are gray, and internal spins are white.

where $P(\mathbf{s};t)$ is the probability of finding the system in a state $\mathbf{s}$ for time $t$, $\omega(\mathbf{s} \to \mathbf{s}^i)$ is the transition rate between states $\mathbf{s}$ and $\mathbf{s}^i$, and $\mathbf{s}^i$ is a configuration exactly equal to $\mathbf{s}$ but with the spin at position $i$ overturned. Our dynamics only allows transitions between configurations which differ in the state of a single spin. Let's assume now that we perform a partition $\mathbb{P}$ of the lattice $\Lambda$, in such a way that domains $q_j$ resulting from this partition will verify the following restrictions: $q_j \in \mathbb{P}(\Lambda)$ such that $q_j \cap q_{j'} = \varnothing$ if $j \neq j'$ and $\bigcup_j q_j = \Lambda$. Subindex $j$ indicates the domain lattice position. Given a domain $q_j$, its surface $\mathcal{S}_j$ is formed by all spins in the domain which have some nearest neighbor outside the domain. Equivalently, the domain's interior, $\mathcal{I}_j$, is formed by all spins in the domain whose nearest neighbor spins are also inside the domain.[1] Thus $q_j = \mathcal{I}_j \cup \mathcal{S}_j$. Fig. 3.1 shows an example. Let's assume now that we have a local observable $A(\mathbf{s}_{q_j};j)$ which exclusively depends on spins belonging to domain $q_j$ (we denote these spins as $\mathbf{s}_{q_j}$). The average of this observable at time $t$ is,

$$\langle A(j)\rangle_t = \sum_{\mathbf{s}} A(\mathbf{s}_{q_j};j)P(\mathbf{s};t) \tag{3.2}$$

If we derive with respect to time this expression, and make use of eq. (3.1), we obtain a temporal evolution equation for the average,

$$\frac{d\langle A(j)\rangle_t}{dt} = \sum_{\mathbf{s}} \sum_{i\in\Lambda} \Big[\omega(\mathbf{s}^i \to \mathbf{s})P(\mathbf{s}^i;t)A(\mathbf{s}_{q_j};j) - \omega(\mathbf{s} \to \mathbf{s}^i)P(\mathbf{s};t)A(\mathbf{s}_{q_j};j)\Big] \tag{3.3}$$

Now if we make a variable change in the first term of right hand side in this equation, $\mathbf{s}^i \to \mathbf{s}_c$ (which implies $\mathbf{s} \to \mathbf{s}_c^i$) and we notice that the index in the sum over configurations is a dumb index (that is, it does not matter whether to sum over configurations $\mathbf{s}_c^i$ or sum over configurations $\mathbf{s}_c$, since we go over *all*

[1] A more general definition of the domain's interior and surface can be written using the transition rates. The domain spins whose flipping probability depends on spins outside the domain define the domain's surface. The interior is defined via $\mathcal{I}_j = q_j - \mathcal{S}_j$. However, for our particular system, where the spin flipping probability depends on the value of the spin and its four nearest neighbors (see eq. (2.3)), this general definition reduces to the one expressed in the main text.

configurations), we can write in a compact way,

$$\frac{d\langle A(j)\rangle_t}{dt} = \sum_{\mathbf{s}} \sum_{i\in q_j} \Delta A(\mathbf{s}_{q_j}; j; i)\omega(\mathbf{s} \to \mathbf{s}^i)P(\mathbf{s}; t) \tag{3.4}$$

where we define,

$$\Delta A(\mathbf{s}_{q_j}; j; i) = A(\mathbf{s}^i_{q_j}; j) - A(\mathbf{s}_{q_j}; j) \tag{3.5}$$

and where the sum over $i \in \Lambda$ is now a sum over $i \in q_j$ since $\Delta A(\mathbf{s}_{q_j}; j; i) = 0$ if the spin at position $i$ is outside the domain $q_j$. We can rewrite eq. (3.4) taking into account the definition of surface and interior of domain $q_j$,

$$\begin{aligned}\frac{d\langle A(j)\rangle_t}{dt} &= \sum_{\mathbf{s}_{q_j}} \sum_{i\in\mathcal{I}_j} \Delta A(\mathbf{s}_{q_j}; j; i)\omega(\mathbf{s}_{q_j} \to \mathbf{s}^i_{q_j})Q(\mathbf{s}_{q_j}; t) \\ &+ \sum_{\mathbf{s}} \sum_{i\in\mathcal{S}_j} \Delta A(\mathbf{s}_{q_j}; j; i)\omega(\mathbf{s} \to \mathbf{s}^i)P(\mathbf{s}; t)\end{aligned} \tag{3.6}$$

where we have defined the projected probability,

$$Q(\mathbf{s}_{q_j}; t) = \sum_{\mathbf{s}-\mathbf{s}_{q_j}} P(\mathbf{s}; t) \tag{3.7}$$

which is the probability of finding domain $q_j$ in a configuration $\mathbf{s}_{q_j}$ at time $t$. When we write $\omega(\mathbf{s}_{q_j} \to \mathbf{s}^i_{q_j})$ in the first term of right hand side in eq. (3.6) we want to stress the fact that the probability of flipping a spin in the domain's interior depends exclusively on the spins belonging to this domain.

The steps performed up to now do not involve approximations. As a first approximation, we assume from now on that our system is *homogeneous*, i.e. its properties do not depend on the selected point in the system. Hence $\langle A(j)\rangle \equiv \langle A\rangle$, $q_j \equiv q$, $\mathcal{I}_j \equiv \mathcal{I}$ and $\mathcal{S}_j \equiv \mathcal{S}$. Equivalently, we suppose that the partition is regular, so all domains are topologically identical. On the other hand, eq. (3.6) shows two well-differentiated terms. The first one only depends on what happens in the domain interior, while the second one involves the domain's surface, couples the domain dynamics with its surroundings, and makes the problem unapproachable in practice. Our second approximation consists in neglecting the surface term in this equation. This approximation involves[34] that the domain is *kinetically isolated* from the exterior: the domain's exterior part does not induce any *net* variation on the local observables defined inside the domain.[2] Thus we are neglecting in practice correlations longer than the domain size. Under both *homogeneity* and *kinetic isolation* approximations, the equation we must study reduces to,

$$\frac{d\langle A\rangle_t}{dt} = \sum_{\mathbf{s}_q} \sum_{i\in\mathcal{I}} \Delta A(\mathbf{s}_q; i)\omega(\mathbf{s}_q \to \mathbf{s}^i_q)Q(\mathbf{s}_{q_j}; t) \tag{3.8}$$

[2]Notice that this approximation is exact for equilibrium systems due to the detailed balance condition.

In order to go on, we must know the expression for the projected probability $Q(\mathbf{s}_q;t)$. It is known that this probability can be written as[34],

$$Q(\mathbf{s}_q;t) = 1 + \langle s\rangle_t \sum_{i\in q} s_i + \sum_{i,j\in q} \langle s_i s_j\rangle_t s_i s_j + \ldots + \langle \prod_{i\in q} s_i\rangle_t \prod_{i\in q} s_i \tag{3.9}$$

This formula involves $n$-body correlation functions. In order to be coherent with the kinetic isolation approximation, which neglects long range correlations, we express the probability $Q(\mathbf{s}_q;t)$ as a function of a reduced number of correlation functions. In particular, our third approximation consists in expressing all correlations as functions of magnetization $\langle s\rangle$ and the nearest neighbors correlation function, $\langle s_i s_j\rangle$, with $i$ and $j$ nearest neighbors sites inside the domain. This is equivalent to writing $Q(\mathbf{s}_q;t)$ as a function of $\rho(+,+)$, $\rho(-,-)$ and $\rho(+,-)$, where $\rho(s,s')$ is the density of $(s,s')$ nearest neighbors pairs, and as a function of the density of up spins, $\rho(+)$. We only have to define now the domain $q$ that we are going to use in our study. Since we only take into account nearest neighbors correlations, we must choose a domain with only one spin in its interior, and $2d$ spins (the nearest neighbors of the interior spin) on the surface, being $d$ the system dimension (in our particular case, $d = 2$). Fig. 3.1.b shows an example of this domain type.

The probability of finding this domain in a configuration defined by a central spin $s$ and $n$ up nearest neighbors can be easily written,

$$Q(\mathbf{s}_q;t) \equiv Q(s,n) = Deg(n)\rho(s)\rho(+|s)^n \rho(-|s)^{2d-n} \tag{3.10}$$

where $Deg(n)$, which is the number of domain configurations that are compatible with a central spin $s$ and $n$ up nearest neighbors, is given by the combinatoric number $\binom{2d}{n}$. $\rho(s)$ is the probability of finding a central spin in state $s$, and $\rho(\pm|s)$ is the conditional probability of finding a neighboring spin in state $\pm$ given that the central spin is in state $s$. Since,

$$\rho(\pm|s) = \frac{\rho(\pm,s)}{\rho(s)} \tag{3.11}$$

where $\rho(\pm,s)$ is the probability of finding a nearest neighbor pair in a state $(\pm,s)$, we can write,

$$Q(s,n) = \binom{2d}{n} \rho(s)^{1-2d} \rho(+,s)^n \rho(-,s)^{2d-n} \tag{3.12}$$

In order to simplify the equations, we use the following notation,

$$\begin{aligned} \rho(+) &\equiv x \\ \rho(-) &\equiv 1-x \\ \rho(+,+) &\equiv z \\ \rho(+,-) &\equiv v = \rho(-,+) \\ \rho(-,-) &\equiv w \end{aligned} \tag{3.13}$$

Taking into account that $v = x - z$ and $w = 1 + z - 2x$, we finally write,

$$\begin{aligned} Q(+,n) &= \binom{2d}{n} x^{1-2d} z^n (x-z)^{2d-n} \\ Q(-,n) &= \binom{2d}{n} (1-x)^{1-2d} (x-z)^n (1+z-2x)^{2d-n} \end{aligned} \tag{3.14}$$

Inserting these formulas into eq. (3.8) we arrive to the basic equation in Pair Approximation,

$$\begin{aligned} \frac{d\langle A\rangle_t}{dt} &= \sum_{n=0}^{2d} \binom{2d}{n} \Big[ \Delta A(+,n) x^{1-2d} z^n (x-z)^{2d-n} \omega(+,n) \\ &- \Delta A(-,n)(1-x)^{1-2d}(x-z)^n (1+z-2x)^{2d-n} \omega(-,n) \Big] \end{aligned} \tag{3.15}$$

We must notice that, since the domain state $\mathbf{s}_q$ is defined by the pair $(s,n)$, we have modified our notation in such a way that $\Delta A(\mathbf{s}_q; i) \equiv \Delta A(s,n)$ and $\omega(\mathbf{s}_q \to \mathbf{s}_q^i) \equiv \omega(s,n)$. Here we also assume that the transition rate depends only on the value of the central spin, $s$, and the number of up nearest neighbors of this spin, $n$. This is true in our particular model, where transitions rates are local.

From eq. (3.15) we can study the dynamics of any local observable in the system at a first order mean field approximation level. However, in order to do so we must know the temporal dependence of both $x \equiv \rho(+)$ and $z \equiv \rho(+,+)$. With this aim in mind we apply eq. (3.15) to both $x$ and $z$. Thus we must write down two local microscopic observables, $A_1(s,n)$ and $A_2(s,n)$, such that their configurational averages correspond to $x$ and $z$, respectively. We can check that these observables are,

$$\begin{aligned} A_1(s,n) &= \frac{1+s}{2} \\ A_2(s,n) &= \frac{n}{2d} \times \frac{1+s}{2} \end{aligned} \tag{3.16}$$

Hence, $\langle A_1(s,n)\rangle = x$ and $\langle A_2(s,n)\rangle = z$. From these expressions we can see that $\Delta A_1(s,n) = -s$ and $\Delta A_2(s,n) = -sn/2d$. Applying eq. (3.15) to both observables we find,

$$\begin{aligned} \frac{dx}{dt} &= -\sum_{n=0}^{2d} \binom{2d}{n} \Big[ x^{1-2d} z^n (x-z)^{2d-n} \omega(+,n) \\ &- (1-x)^{1-2d}(x-z)^n (1+z-2x)^{2d-n} \omega(-,n) \Big] \end{aligned} \tag{3.17}$$

$$\begin{aligned} \frac{dz}{dt} &= -\frac{1}{2d} \sum_{n=0}^{2d} \binom{2d}{n} n \Big[ x^{1-2d} z^n (x-z)^{2d-n} \omega(+,n) \\ &- (1-x)^{1-2d}(x-z)^n (1+z-2x)^{2d-n} \omega(-,n) \Big] \end{aligned} \tag{3.18}$$

These two equations are the basic equations in Pair Approximation. Hence, once defined the transition rate $\omega(s,n)$ (see eq. (2.3)), the general working method thus consists in calculating both $x(t)$ and $z(t)$ using the above equations, and using eq. (3.15) and the results for $x(t)$ and $z(t)$ calculate any other local magnitude.

## 3.3 Static Properties

In a first step we want to study the stationary solutions of eqs. (3.17) and (3.18) as well as their stability for the nonequilibrium ferromagnetic system. We have two non-linear coupled differential equations,

$$\begin{aligned} \frac{dx}{dt} &= F_1(x,z) \\ \frac{dz}{dt} &= F_2(x,z) \end{aligned} \tag{3.19}$$

where $F_1(x,z)$ and $F_2(x,z)$ are defined by eqs. (3.17) and (3.18), respectively, once we include in these equations the explicit form of the transition rate, eq. (2.3). This dynamics only depends on the energy increment $\Delta\mathcal{H}$ due to a spin change. Since the energy of the system is defined via the Ising Hamiltonian, eq. (2.1), if we flip a spin $s$ with $n$ up nearest neighbors, then $\Delta\mathcal{H}(s,n) = 2s[2J(n-d)+h]$, so the transition rate can be written as,

$$\omega(s,n) = p + (1-p)\frac{e^{-2s[2J(n-d)+h]}}{1+e^{-2s[2J(n-d)+h]}} \tag{3.20}$$

Once we specify the dynamics, the stationary solutions of the previous coupled set of equations, $x_{st}$ and $z_{st}$, are the solutions of the system,

$$F_1(x_{st},z_{st}) = 0 \qquad , \qquad F_2(x_{st},z_{st}) = 0 \tag{3.21}$$

Both stable and metastable states in a generic system are *locally stable* under small perturbations. Hence we are interested in locally stable stationary solutions of this set of equations. We must give a local stability criterion. In order to build such criterion, let's study what happens if we slightly perturb the steady solutions, that is, $x = x_{st} + \epsilon_x$ and $z = z_{st} + \epsilon_z$, where $\epsilon_x$ and $\epsilon_z$ are very small. From eqs. (3.19), taking into account the stationarity condition, eq. (3.21), a expanding to first order as a function of $\epsilon_x$ and $\epsilon_z$, we find,

$$\begin{aligned} \frac{d\epsilon_x}{dt} &= \left(\frac{\partial F_1}{\partial x}\right)_{st}\epsilon_x + \left(\frac{\partial F_1}{\partial z}\right)_{st}\epsilon_z + \mathcal{O}(\epsilon_x^2, \epsilon_z^2, \epsilon_x\epsilon_z) \\ \frac{d\epsilon_z}{dt} &= \left(\frac{\partial F_2}{\partial x}\right)_{st}\epsilon_x + \left(\frac{\partial F_2}{\partial z}\right)_{st}\epsilon_z + \mathcal{O}(\epsilon_x^2, \epsilon_z^2, \epsilon_x\epsilon_z) \end{aligned} \tag{3.22}$$

We can write this set of equation in matrix form,

$$\frac{d}{dt}\begin{pmatrix} \epsilon_x \\ \epsilon_z \end{pmatrix} \approx \begin{pmatrix} (\frac{\partial F_1}{\partial x})_{st} & (\frac{\partial F_1}{\partial z})_{st} \\ (\frac{\partial F_2}{\partial x})_{st} & (\frac{\partial F_2}{\partial z})_{st} \end{pmatrix} \begin{pmatrix} \epsilon_x \\ \epsilon_z \end{pmatrix} \tag{3.23}$$

This system can be solved in a standard way, getting,

$$\epsilon_x \approx \epsilon_x^0 e^{\lambda t} \qquad , \qquad \epsilon_z \approx \epsilon_z^0 e^{\lambda t} \tag{3.24}$$

where $\epsilon_x^0$ and $\epsilon_z^0$ are constants determined by initial conditions, and $\lambda$ is determined by the solutions of the equation,

$$\begin{vmatrix} (\frac{\partial F_1}{\partial x})_{st} - \lambda & (\frac{\partial F_1}{\partial z})_{st} \\ (\frac{\partial F_2}{\partial x})_{st} & (\frac{\partial F_2}{\partial z})_{st} - \lambda \end{vmatrix} = 0 \tag{3.25}$$

This equation for the determinant is reduced to a second order polynomial equation for $\lambda$, with two solutions $\lambda_+$ and $\lambda_-$. From eq. (3.24) it is obvious that the steady solutions $x_{st}$ and $z_{st}$ will be locally stable if the real parts of both $\lambda_+$ and $\lambda_-$ are negative, since in this way we ensure that the perturbation will disappear in the limit $t \to \infty$. The real parts of both $\lambda_+$ and $\lambda_-$ will be negative if the following condition is fulfilled,

$$\begin{aligned} &\left(\frac{\partial F_1}{\partial x}\right)_{st} + \left(\frac{\partial F_2}{\partial z}\right)_{st} < 0 \\ &\left(\frac{\partial F_1}{\partial x}\right)_{st}\left(\frac{\partial F_2}{\partial z}\right)_{st} - \left(\frac{\partial F_1}{\partial z}\right)_{st}\left(\frac{\partial F_2}{\partial x}\right)_{st} > 0 \end{aligned} \tag{3.26}$$

This criterion, known as Hurwitz criterion[52], states the necessary and sufficient conditions that a steady solution of our set of non-linear differential equations must fulfill in order to be locally stable under small perturbations.

### 3.3.1 Phase Diagram

We are also interested in simple necessary (although not sufficient) conditions that locally stable steady states must fulfill. For instance, if we perturb the stationary state by only varying $x$ and keeping untouched $z$, that is, $x = x_{st} + \epsilon_x$ and $z = z_{st}$, we arrive to the following solution once we apply the previous stability analysis,

$$\epsilon_x \approx \epsilon_x^0 e^{t(\frac{\partial F_1}{\partial x})_{st}} \tag{3.27}$$

so the steady state defined by $(x_{st}, z_{st})$ can be locally stable only if $(\frac{\partial F_1}{\partial x})_{st} < 0$. It will be unstable if this derivative is larger than zero. The condition

$$\left(\frac{\partial F_1(x,z)}{\partial x}\right)_{st} = 0 \tag{3.28}$$

defines a point $(x_{st}^c, z_{st}^c)$ of incipient instability or marginal stability which signals the presence of an underlying critical point or second order phase transition for $h = 0$ between a disordered phase and an ordered phase.[34] Just at this critical point we have $x_{st}^c = \frac{1}{2}$, since it separates an ordered phase with non vanishing spontaneous magnetization from a disordered phase with zero

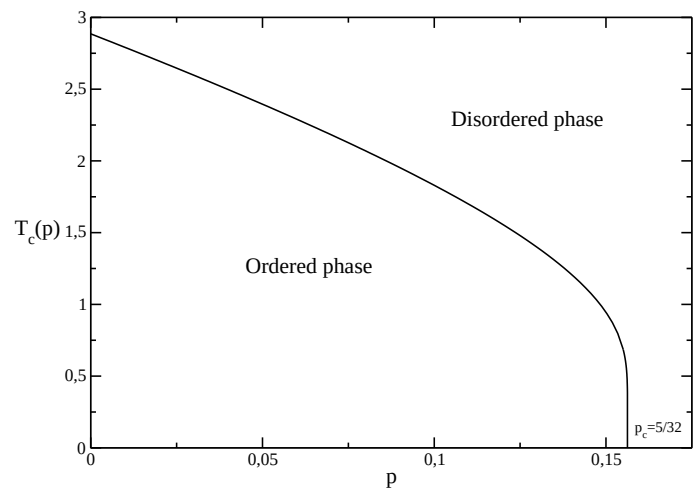


Figure 3.2: Critical temperature for the nonequilibrium ferromagnetic system as a function of $p$ in Pair Approximation.

spontaneous magnetization. This observation trivially implies $z \equiv \rho(+,+) = \rho(-,-) \equiv (1+z-2x)$ at the critical point. We also have $z^c_{st} = \frac{1}{3}$ at the critical point.[53] Using these values for $x^c_{st}$ y $z^c_{st}$ in eq. (3.28) once we substitute there the explicit form of $F_1(x,z)$, eq. (3.17), and solving for temperatures, we find,

$$\frac{T_c(p)}{J} = \frac{-4}{\ln\left[-\frac{1}{2}+\frac{3}{4}\sqrt{\frac{1-4p}{1-p}}\right]} \tag{3.29}$$

This equation yields the critical temperature for the nonequilibrium model in first order mean field approximation as a function of parameter $p$, which characterizes the dynamic nonequilibrium perturbation present in the system. We can also arrive to this expression from eqs. (3.26), which define the general stability criterion, applying the marginal stability condition. Fig. 3.2 shows $T_c(p)$ as a function of $p$. For $p = 0$ the critical temperature $T_c(p)$ is just the Bethe temperature, $T_{Bethe}/J \approx 2.8854$, to be compared with the exact critical value for $p = 0$, which is the Onsager temperature, $T_{ons}/J \approx 2.2691$. For each value of $p$, temperature $T_c(p)$ signals the border, always in mean field approximation, between the ordered phase at low temperatures ($T < T_c(p)$) and the disordered phase at higher temperatures ($T > T_c(p)$). There is a critical value of $p$, $p_c$, such that for larger values of $p$ there is no ordered phase for any temperature. This value $p_c$ can be obtained from the condition $T_c(p_c) = 0$, yielding $p_c = \frac{5}{32} = 0.15625$. On the other hand, the phase transition we obtain in mean field approximation belongs to the mean field universality class, as expected, on the contrary to the real nonequilibrium system, which as we said in Chapter 2 belongs to the Ising universality class. Such discrepancy is due to the absence of fluctuations in our mean field approximation.

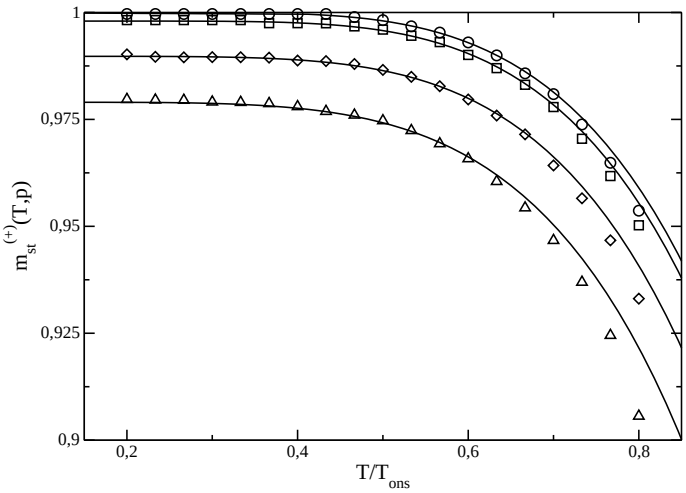


Figure 3.3: Locally stable steady state magnetization as a function of temperature (in units of Onsager temperature) for different values of $p$ and for $h = 0$. In particular, from top to bottom, $p = 0$, $0.001$, $0.005$ and $0.01$. Points are results obtained from Monte Carlo simulations for a system with $L = 53$. Continuous lines are the solutions in Pair Approximation. Error bars in computational results are much smaller than the symbol sizes.

### 3.3.2 Stable and Metastable States

After this brief parenthesis about the model critical behavior, we turn back to study its locally stable steady states in the ordered phase. These stationary states $(x_{st}, z_{st})$ will be given by solutions of the set of non-linear differential equations (3.21), subject to the Hurwitz local stability condition, eqs. (3.26). Unfortunately, the non-linearity of the set of eqs. (3.21) impedes any analytical solution, so we have to turn to numerical solutions.

In a first step we center our attention on the study of stationarity for zero magnetic field, $h = 0$. In this case, the system exhibits up-down symmetry, so we will have two symmetrical branches of solutions in the ordered phase, one of positive magnetization and another one with negative magnetization. Moreover, we can prove for $h = 0$ that if the pair $(x_{st}, z_{st})$ is a locally stable steady solution of the set of eqs. (3.21), then the pair $(1 - x_{st}, 1 + z_{st} - 2x_{st})$ is also a locally stable steady solution. If we solve the set of eqs. (3.21) using standard numerical techniques[54] and we keep only those solutions which fulfill Hurwitz criterion, we finally obtain the results shown in Fig. 3.3. There we compare the theoretical predictions for the positive magnetization branch with results obtained from Monte Carlo simulations for different values of the dynamic random perturbation $p$. The agreement between theory and computational results is excellent for low and intermediate temperatures for all studied values of $p$, failing gradually as we approach the critical temperature. Furthermore, the differences between theory and simulations begin to be relevant for

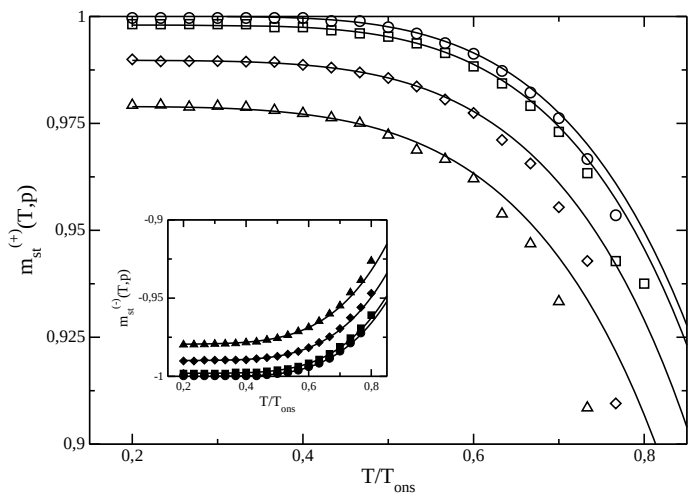


Figure 3.4: Magnetization of the locally stable steady state of positive magnetization as a function of temperature (in units of Onsager temperature) for different values of $p$ and $h = -0.1$. From top to bottom, $p = 0$, $p = 0.001$, $p = 0.005$ and $p = 0.01$. Points are results obtained from Monte Carlo simulations for a system of size $L = 53$. The continuous lines are Pair Approximation solutions. Error bars associated to computational results are much smaller than symbol sizes. In the inset we show the results for the negative magnetization branch.

temperatures higher than a 75% of the critical temperature for each case. Such inaccuracy of Pair Approximation for temperatures close enough to the critical one was expected a priori, since mean field theory neglects long range correlations, which on the other hand gradually arise as we approach the critical region. Fig. 3.3 shows also that, as we increase $p$ for a fixed temperature, the system's magnetization decrease in absolute value. Therefore, an increase of $p$ is equivalent to an increase of disorder in the system. On the other hand, the qualitative form of the curve $m_{st}^{(+)}(T, p)$ does not change for $p \neq 0$ as compared to the equilibrium system ($p = 0$).

The Monte Carlo simulations whose results are shown in Fig. 3.3 have been performed for a system with size $L = 53$, subject to periodic boundary conditions (we use the same boundary conditions in all simulations within this chapter), with $h = 0$ and different values of $T$ and $p$. In order to measure the magnetization of the positive magnetization steady state, we put the system in an initial state with all spins up. We let evolve this state with the dynamics (2.3) for certain values of $T$ and $p$. After some relaxation time, the systems starts fluctuating around the steady state. We then measure magnetization at temporal intervals $\Delta t$ larger than the correlation time, and we average over different measurements. The error associated to this average is the standard statistical error. A second method to measure the stationary state magnetization is based on the stable phase growth and shrinkage rates, which we will

define later on in this chapter. Both methods yield equivalent results.

We also can study the steady states for $h < 0$. In particular, here we study the case $h = -0.1$. As opposed to the $h = 0$ case, here there is no up-down symmetry since the magnetic field favours the negative orientation of spins. Therefore the negative and positive magnetization branches are now different. Moreover, the locally stable steady state with positive magnetization is now metastable. Numerically solving the set of eqs. (3.21) subject to the conditions (3.26) we obtain the results shown in Fig. 3.4. In this figure we also show results from simulations analogous to the ones described above, but with $h = -0.1$, and where the initial state is defined with all spins up (down) if we want to measure the positive (negative) magnetization branch. Comparatively, these results are very similar to the results obtained for $h = 0$.

### 3.3.3 Hysteresis and the Intrinsic Coercive Field

An interesting question consists in knowing what happen to locally stable steady states as we change the magnetic field. In order to answer this question we numerically solve again the set of eqs. (3.21) subject to Hurwitz conditions for fixed temperature and dynamic random perturbation $p$, varying the magnetic field between $h = -1$ and $h = +1$. In particular, Fig. 3.5 shows the result for $T = 0.7T_{ons}$ and $p = 0.005$. This curve forms what is generally known as a hysteresis loop. Hysteresis is a property of many systems near a first order critical point, and it is intimately related to metastability. A system is said to exhibit *hysteresis* if its properties depend on its previous history. Thus systems showing hysteresis are systems with *memory*. In our case, as can be seen in Fig. 3.5 for fixed $T$ and $p$ and for a fixed magnetic field in the interval $[-h^*(T,p), h^*(T,p)]$, the system properties (represented this time by the magnetization) depend on whether the system evolved along the positive or the negative magnetization branch, i.e. they depend on the previous system history. As we can see in Fig. 3.5, this dependence on previous history is clearly due to metastability, i.e. locally stable steady states with magnetization opposed to the magnetic field.

There is a magnetic field $h^*(T,p)$ such that for all $|h| > h^*(T,p)$ metastable states disappear. This magnetic field $h^*(T,p)$ is known as *intrinsic coercive field*[3]. As we increase the absolute value of the field, metastable states get weaker and weaker. The reason underlies on the increase of the transition rate for spins in the metastable phase as we increase the magnetic field strength, see eq. (3.20). Thus there is a value of the magnetic field for which the metastable state is no longer metastable and transforms into an unstable state. In order to study this item more carefully, let's suppose that we are able to simplify eqs. (3.19) in

[3]The intrinsic coercive field $h^*$ is defined in a precise manner as the magnetic field for which magnetization is zero in a hysteresis loop. In our case, the hysteresis loop goes discontinuously from positive to negative magnetization (and vice versa) when the metastable state disappears, so we can say that magnetization *discontinuously* crosses $m = 0$ at $h = h^*$.[55]

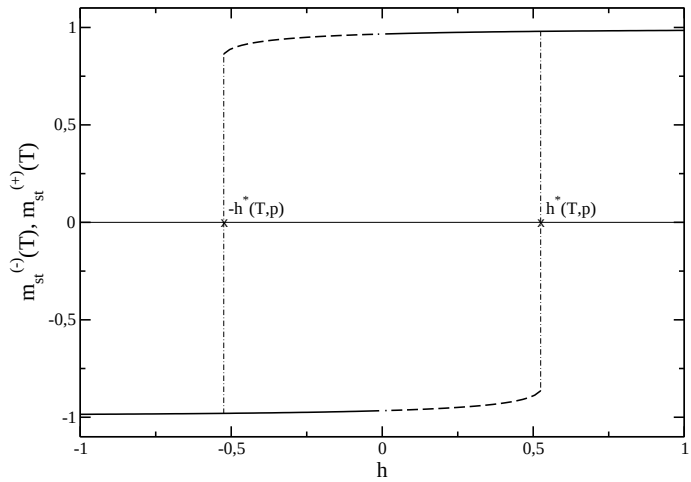


Figure 3.5: Locally stable steady state magnetization for both magnetization branches as a function of magnetic field $h$ for fixed $T = 0.7T_{ons}$ and $p = 0.005$. The continuous line represents stable states, the dashed line represents metastable states, and the dot-dashed line signals the discontinuous transition where metastable states disappear. This discontinuity appears for a magnetic field $h^*(T, p)$.

such a way that we know $z = z(x)$. Now we can rewrite eq. (3.17) as,

$$\frac{dx}{dt} = -\frac{\delta V(x)}{\delta x} \tag{3.30}$$

where $V(x)$ is a (nonequilibrium) potential which controls the system evolution. Fig. 3.6 shows a schematic plot of this potential for the ordered phase at fixed temperature and $p$, and for several negative magnetic fields of increasing absolute value. As we can see, the effect of the magnetic field is to attenuate the local minimum associated to the metastable state. For magnetic fields $|h| < h^*(T, p)$ this local minimum, although attenuated, exists. However, for magnetic fields $|h| > h^*(T, p)$ the metastable minimum disappears, and so the metastable state. Therefore, for $|h| > h^*(T, p)$ the set of eqs. (3.21) has only one solution, with magnetization sign equal to that of the applied field.

In order to calculate $h^*(T, p)$ let's study how a metastable state changes under small perturbations of magnetic field. Let's assume then that $(x_{st}^{h_0}, z_{st}^{h_0})$ is a locally stable stationary state for parameters $T$, $p$ and $h_0$, with magnetization opposed to the external magnetic field. If we slightly perturb this magnetic field, $h = h_0 + \delta h$, also the locally stable stationary solution will be modified, $x_{st}^{h} = x_{st}^{h_0} + \epsilon_x$ and $z_{st}^{h} = z_{st}^{h_0} + \epsilon_z$. We can write,

$$\begin{aligned} \frac{dx_{st}^{h}}{dt} &= F_1(x_{st}^{h}, z_{st}^{h}; h) \approx F_1(x_{st}^{h_0}, z_{st}^{h_0}; h_0) + \frac{\partial F_1}{\partial x}(x_{st}^{h_0}, z_{st}^{h_0}; h_0)\epsilon_x \\ &+ \frac{\partial F_1}{\partial z}(x_{st}^{h_0}, z_{st}^{h_0}; h_0)\epsilon_z + \frac{\partial F_1}{\partial h}(x_{st}^{h_0}, z_{st}^{h_0}; h_0)\delta h \end{aligned} \tag{3.31}$$

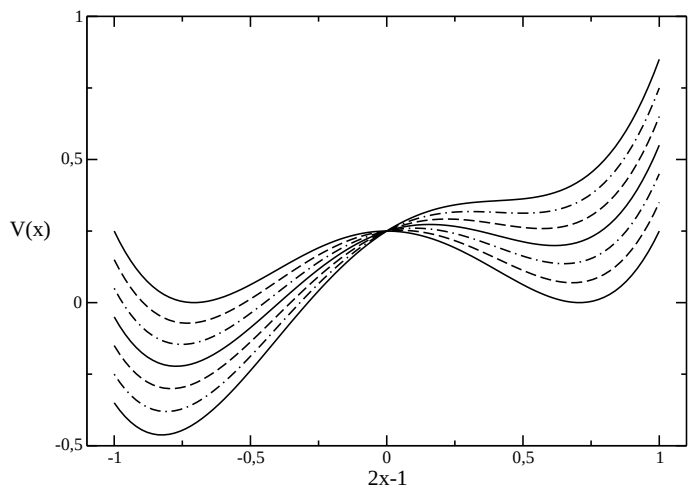


Figure 3.6: Schematic plot of the potential $V(x)$ defined in the main text, for fixed temperature and $p$, and for several different values of magnetic field $h < 0$. Notice that the local minimum in the positive magnetization branch is attenuated as $|h|$ increases, up to its disappearance for large enough values of $|h|$.

where we have specified the magnetic field dependence. Due to the steadiness of the initial state, $F_1(x_{st}^{h_0}, z_{st}^{h_0}; h_0) = 0$, and since $(x_{st}^{h}, z_{st}^{h})$ is also a steady state, we have that $\frac{dx_{st}^{h}}{dt} = 0$. Hence,

$$\frac{\partial F_1}{\partial x}(x_{st}^{h_0}, z_{st}^{h_0}; h_0)\epsilon_x + \frac{\partial F_1}{\partial z}(x_{st}^{h_0}, z_{st}^{h_0}; h_0)\epsilon_z = -\frac{\partial F_1}{\partial h}(x_{st}^{h_0}, z_{st}^{h_0}; h_0)\delta h \tag{3.32}$$

In a similar way we can calculate the perturbation that $z_{st}^{h}$ suffers,

$$\frac{\partial F_2}{\partial x}(x_{st}^{h_0}, z_{st}^{h_0}; h_0)\epsilon_x + \frac{\partial F_2}{\partial z}(x_{st}^{h_0}, z_{st}^{h_0}; h_0)\epsilon_z = -\frac{\partial F_2}{\partial h}(x_{st}^{h_0}, z_{st}^{h_0}; h_0)\delta h \tag{3.33}$$

Solving the linear system formed by eqs. (3.32) and (3.33) for $\epsilon_x$ we obtain,

$$\epsilon_x = \left[\frac{\frac{\partial F_2}{\partial h}\frac{\partial F_1}{\partial z} - \frac{\partial F_1}{\partial h}\frac{\partial F_2}{\partial z}}{\frac{\partial F_1}{\partial x}\frac{\partial F_2}{\partial z} - \frac{\partial F_2}{\partial x}\frac{\partial F_1}{\partial z}}\right]_{x_{st}^{h_0}, z_{st}^{h_0}, h_0, T, p} \delta h \tag{3.34}$$

This equation says that the metastable state magnetization response after a small variation of the magnetic field is proportional to such perturbation in a first approximation. However, the magnetization response will be divergent when,

$$\left[\frac{\partial F_1}{\partial x}\frac{\partial F_2}{\partial z} - \frac{\partial F_2}{\partial x}\frac{\partial F_1}{\partial z}\right]_{x_{st}^{h_0}, z_{st}^{h_0}, h_0, T, p} = 0 \tag{3.35}$$

When this condition holds, there will be a discontinuity in the metastable magnetization as a function of $h$. For fixed $T$ and $p$ we thus identify the magnetic field $h_0$ for which condition (3.35) is fulfilled as the *intrinsic coercive field*,

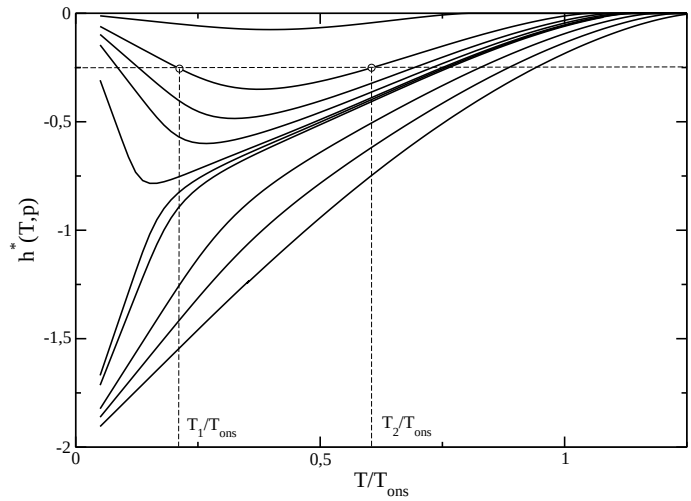


Figure 3.7: Intrinsic coercive field, $h^*(T,p)$, as a function of temperature for different values of $p$. From bottom to top, $p = 0$, $0.01$, $0.02$, $0.03$, $0.031$, $0.032$, $0.035$, $0.04$, $0.05$ and $0.1$. Notice that the qualitative change of behavior in the low temperature limit appears for $p \in (0.031, 0.032)$. Here we also show, for $h = -0.25$, the temperatures $T_1 < T_2$ such that for $T_1 < T < T_2$ there are metastable states for $p = 0.05$.

$h^*(T,p)$. Unfortunately, we cannot analytically calculate $h^*(T,p)$, since we do not explicitely know the metastable solutions $x_{st}^{h_0}$ and $z_{st}^{h_0}$. Solving again the problem with standard numerical methods, we obtain the results shown in Fig. 3.7. There we plot $h^*(T,p)$ as a function of temperature for different values of the nonequilibrium parameter $p$. The first conclusion we draw from this family of curves is the existence of two different low temperature limits for $h^*(T,p)$, depending on the value of $p$. For small enough values of $p$ (including the equilibrium case, $p = 0$), the curve $h^*(T,p)$ extrapolates towards $-2$ in the limit $T \to 0$. In particular this is true for $p \in [0, 0.031]$ (see Fig. 3.7). On the contrary, for large enough values of $p$, namely $p \in [0.032, \frac{5}{32})$, the curve $h^*(T,p)$ extrapolates towards $0$ in the limit $T \to 0$. There is a critical value for $p$, that we estimate here to be $\pi_c \approx 0.0315$, which separates both types of asymptotic behaviors. As we said before, the intrinsic coercive field $h^*(T,p)$ signals the magnetic field strength above which there are no metastable states. As we see in Fig. 3.7, for $p < \pi_c$ the behavior of $h^*(T,p)$ for the nonequilibrium system is qualitatively similar to that of the equilibrium one: $|h^*(T, p < \pi_c)|$ is a monotonously decreasing function of $T$. Therefore, for $p < \pi_c$, if we cool the system we need a stronger magnetic field in order to *destroy* the metastable state. This result agree with intuition. In a metastable state there are two competing processes: a net tendency of the system to line up in the direction of the field, and a net tendency in order to maintain the spin order, i.e. in order to keep all spins oriented in the same direction (whatever this direction is). A metastable state survives a long time because the tendency towards main-

taining the order in the system overcomes the tendency to line up along the field direction. Both the temperature $T$ and the nonequilibrium parameter $p$ are ingredients which introduce disorder in the system. Hence if we drop temperature, since in this way order grows in the system, we would expect in this phenomenologic picture that the magnetic field needed in order to *destroy* the metastable state should be stronger, as we effectively check for $p < \pi_c$. In the same way, as $p$ is increased, disorder grows in the system, so $|h^*(T,p)|$ must decrease for a fixed temperature, as we again observe.

On the contrary, for $p > \pi_c$ the system exhibits an unexpected behavior, difficult to understand using the above phenomenologic picture. Let's assume we fix the magnetic field to be $h = -0.25$ and the nonequilibrium parameter to be $p = 0.05 > \pi_c$. As we can see in Fig. 3.7, we can define two different temperatures, $T_1 < T_2$, such that if $T < T_1$ or $T > T_2$ the system does not show metastable states, while metastable states do exist if temperature lies in the interval $T \in (T_1, T_2)$. The fact that $h^*(T,p)$ extrapolates to zero in the low temperature limit for $p = 0.05 > \pi_c$ points out that the nonequilibrium parameter $p = 0.05$, which is the relevant source of disorder and randomness in the low temperature limit, takes a value in this case large enough in order to *destroy* on its own any metastable state. In principle, following the above phenomenologic picture, we would say that increasing in this case temperature the metastable state should not ever exist, because we add disorder to the system. However, we observe that a regime of intermediate temperatures exists, $T \in (T_1, T_2)$, where metastable states emerge. This observation involves the presence of a *non-linear cooperative phenomenon* between the thermal noise (parameterized by $T$) and the non-thermal fluctuation source (parameterized by $p$): although both noises add independently disorder to the system, which involves the attenuation or even the destruction of the existing metastable states, the combination of both noise sources, parameterized in the dynamics (2.3), not always implies a larger disorder, giving rise to regions in parameter space $(T,p)$ where there are no metastable states for low and high temperatures, existing however metastability for intermediate temperatures. This counter-intuitive behavior resembles in some sense the behavior of some systems under the action of multiplicative noise, as for instance the annealed Ising model[57], where a disordered phase exists for low and high temperatures, but there is an ordered phase for intermediate temperatures.[58]

### 3.3.4 Intrinsic Coercive Field from Monte Carlo Simulations: Stable Phase Growth and Shrinkage Rates

Now we want to check our theoretical predictions via computer simulations, so we need to discern when the system exhibits a metastable state. In order to establish a criterion, we must introduce the concept of spin class (see Appendix A). For a spin $s$ in the lattice, the spin class to which this spin belongs to is defined once we know the spin orientation, $s = +1$ or $s = -1$, and its number of up nearest neighbors, $n \in [0,4]$. Therefore, for the two-dimensional isotropic

| Class | Central spin | Number of up neighbors | $\Delta\mathcal{H}$ |
|---|---|---|---|
| 1 | +1 | 4 | 8J+2h |
| 2 | +1 | 3 | 4J+2h |
| 3 | +1 | 2 | 2h |
| 4 | +1 | 1 | -4J+2h |
| 5 | +1 | 0 | -8J+2h |
| 6 | -1 | 4 | -8J-2h |
| 7 | -1 | 3 | -4J-2h |
| 8 | -1 | 2 | -2h |
| 9 | -1 | 1 | 4J-2h |
| 10 | -1 | 0 | 8J-2h |

Table 3.1: Spin classes for the two-dimensional isotropic Ising model with periodic boundary conditions. The last column shows the energy increment involved by a spin flip for each class.

Ising model subject to periodic boundary conditions there are 10 different spin classes, schematized in Table 3.1. All spins belonging to the same spin class involve the same energy increment $\Delta\mathcal{H}(s,n)$ when flipped (see Table 3.1), so the transition rate for a spin to flip depends exclusively on the spin class $i \in [1,10]$ to which the spin belongs to, $\omega_i \equiv \omega(s,n)$, see eq. (3.20). If $n_k(m)$ is the number of spins in the system that belong to class $k$ when the system has magnetization $m$, then $n_k(m)\omega_k$ will be the number of spins in class $k$ which flip per unit time when we have $n_{up} = N(1+m)/2$ up spins. Since in our convention (see Table 3.1) all classes $k \in [1,5]$ are characterized by a central spin with $s = +1$ and $n = 4, 3, \ldots, 0$ up nearest neighbors, the number of up spins which flip per unit time when magnetization is $m$ will be,

$$g(m) = \sum_{k=1}^{5} n_k(m)\omega_k \tag{3.36}$$

This observable is the growth rate of the negative magnetization phase, and it depends on system's magnetization. In a similar way, we define the shrinkage rate of the negative magnetization phase as,

$$s(m) = \sum_{k=6}^{10} n_k(m)\omega_k \tag{3.37}$$

Now $s(m)$ is the number of down spins which flip per unit time when system's magnetization is $m$. Since we are studying a system subject to a negative magnetic field, we will name $g(m)$ and $s(m)$ *stable phase growth and shrinkage rates*, respectively.[46]

If we have a state with magnetization $m$, the rate of change of magnetization will be,

$$\frac{dm}{dt} = \frac{2}{N}\big[s(m) - g(m)\big] \tag{3.38}$$

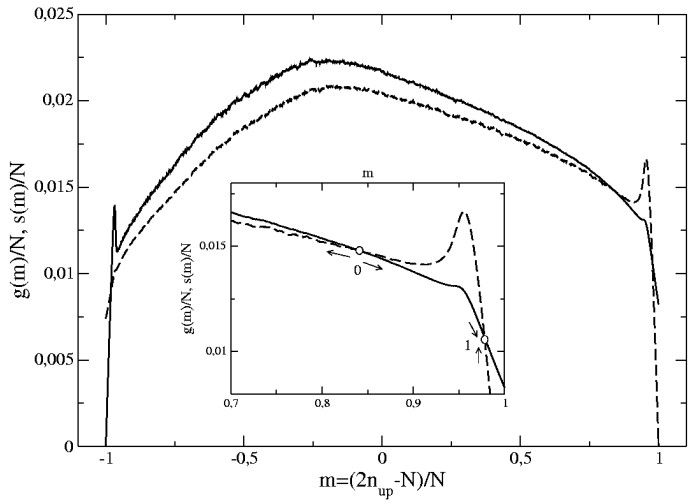


Figure 3.8: Growth and shrinkage probabilities of the stable phase, $g(m)/N$ and $s(m)/N$ respectively, for a system of size $L = 53$, with $T = 0.6T_{ons}$, $p = 0.005$ and $h = -0.1$. The continuous line represents $g(m)/N$, while the dashed line represents $s(m)/N$. The inset shows a detail of the positive magnetization region.

Thus the system will show steady states for $g(m) = s(m)$. Fig. 3.8 shows $g(m)/N$ and $s(m)/N$ as measured in a system with size $L = 53$, temperature $T = 0.6T_{ons}$, $p = 0.005$ and $h = -0.1$, after averaging over 1000 different demagnetization experiments. These demagnetization experiments begin with all spins up (such state is metastable for the studied parameters) and finish once the negative magnetization stable state has been reached. As we can see in Fig. 3.8, there are three points where the curves $g(m)$ and $s(m)$ intersect one each other. Two of this intersection points appear in the positive magnetization region, and the third one appears in the negative magnetization region. The points where $g(m) = s(m)$ indicate steady states of the real system, whose magnetization can be deduced from the intersection abscissa. Let's denote these magnetization values as $m_{-1}$, $m_0$ and $m_1$, being $m_{-1}$ the magnetization of the intersection point in the negative magnetization region, $m_0$ the magnetization of the intermediate intersection point, and $m_1$ the largest intersection point magnetization. In order to discern local stability, let's study what happen if we slightly perturb the magnetization in these steady states. If we perturb for instance the steady state with the largest intersection point magnetization, $m_1$, in such a way that the final state has magnetization $m = m_1 + \delta m$, we can see that if $\delta m > 0$ then $g(m_1 + \delta m) > s(m_1 + \delta m)$, while $g(m_1 + \delta m) < s(m_1 + \delta m)$ if $\delta m < 0$. In both cases, as indicated by eq. (3.38), the system tends to counteract the perturbation, coming back to the stationary state. Hence the stationary state with the largest magnetization, $m_1$, is locally stable under small perturbations. The arrows in the inset of Fig. 3.8 represent the tendency of the system immediately after the perturbation. We find something analogous

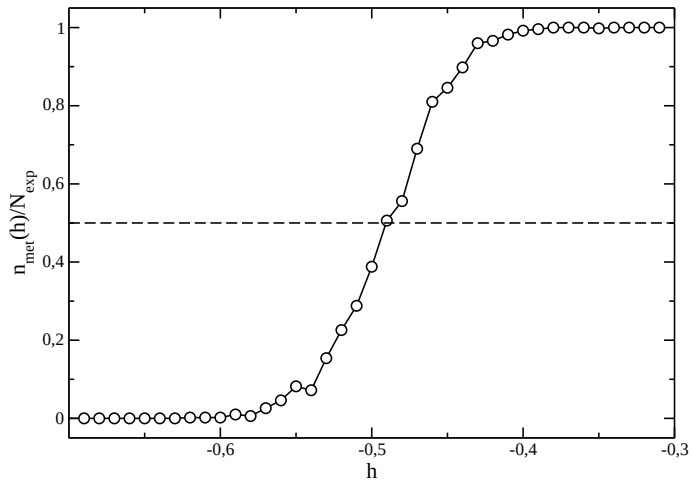


Figure 3.9: Probability of finding a metastable state, as defined in the main text, as a function of magnetic field $h < 0$ for a system of size $L = 53$, with temperature $T = 0.7T_{ons}$ and $p = 0$, where we have performed $N_{exp} = 500$ demagnetization experiments for each value of $h$. Error bars are smaller than symbol sizes.

for the steady state with negative magnetization, $m_{-1}$, i.e. it is locally stable. Therefore the stationary state represented by $m_1$ signals the metastable state, while the stationary state $m_{-1}$ signals the stable state in this case (remember $h < 0$). The steady state $m_0$ is unstable under small perturbations, as can be easily derived using the above arguments. This stationary state signals the separation point between the region where the stable phase tends to disappear ($m > m_0$), and the region where the stable phase tends to grow ($m < m_0$). As we will see in forthcoming chapters, this point defines the critical fluctuation needed in order to exit the metastable state. This critical fluctuation is the magnitude that controls the demagnetization process. Finally, we want to point out that measuring $g(m)$ y $s(m)$ in particular experiments, extracting the stable and metastable state magnetizations, $m_{-1}$ and $m_1$ respectively, and averaging such measures over many different experiments, we can obtain a measure of the average stable and metastable state magnetizations. This measure compares perfectly with the previously presented results (see Fig. 3.3 and 3.4, and complementary discussion).

It is clear from the previous discussion that if there is a magnetization interval inside the metastable region (in our case, the positive magnetization region) where $s(m) > g(m)$, that is, where the stable phase shrinkage rate is larger than its growth rate, then a metastable state will exists. On the other hand, when $|h| > h^*(T, p)$ the metastable state will not exist. In this case it is observed that the curve $s(m)$ does not intersect $g(m)$ in the positive magnetization region. Hence the existence or absence of intersection between $s(m)$ and $g(m)$ in the positive magnetization region (for $h < 0$) allows us to decide whether the sys-

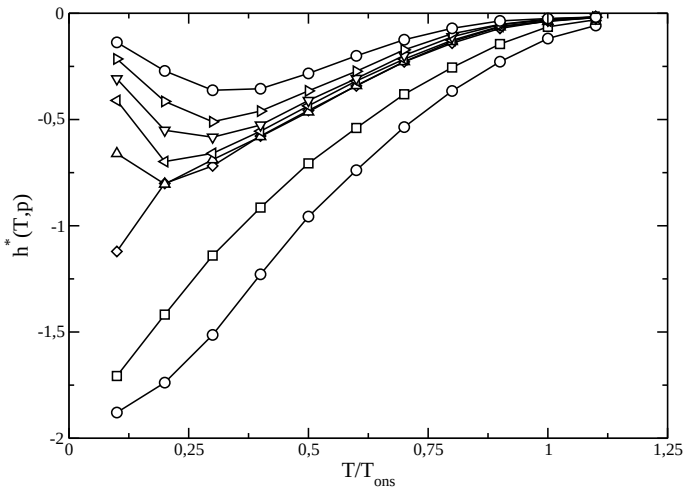


Figure 3.10: Monte Carlo results for the intrinsic coercive field, $h^*(T, p)$, as a function of temperature for different values of $p$. In particular, from bottom to top, $p = 0$, 0.01, 0.03, 0.0305, 0.0320, 0.0350, 0.04 and 0.05. Notice the change of asymptotic behavior in the low temperature limit for $p \in (0.03, 0.0305)$. This figure is to be compared with Fig. 3.7.

tem exhibits a metastable state or not. In the above discussion we have treated all states with the same magnetization as an single state. However, there are many different microscopic states in the system which are compatible with a fixed magnetization. These states may exhibit very different properties. In particular, the rates $g(m)$ y $s(m)$ depend not only on magnetization, but on the population of all the spin classes. Thus, for a fixed set of parameters $T$, $p$ and $h < 0$, we can have experiments where $s(m)$ and $g(m)$ intersect one each other in the positive magnetization region, and for the same parameters we can observe other experiments where they do not intersect. Therefore, instead of speaking about the existence or absence of a metastable state, we must speak about the *probability* of existence of a metastable state. In this way we can define a method to measure the intrinsic coercive field $h^*(T, p)$ in Monte Carlo simulations. For a fixed set of parameters $T$, $p$ and $h < 0$, we perform $N_{exp}$ different demagnetization experiments, starting from a state with all spins up. We measure on each experiment the stable phase growth and shrinkage rates, $g(m)$ and $s(m)$ respectively, as a function of magnetization. If $n_{met}$ of those $N_{exp}$ experiments are such that $g(m)$ and $s(m)$ intersect one each other in the positive magnetization region, we can define the probability of existence of a metastable state as $n_{met}(T, p, h)/N_{exp}$. If we repeat such process for fixed values of temperature $T$ and nonequilibrium perturbation $p$, varying the magnetic field in a wide interval, we obtain the results shown in Fig. 3.9. Here we observe that the metastable state existence probability abruptly changes from $+1$ to $0$ in a narrow magnetic field interval. Therefore we define in this case the in-

trinsic coercive field, $h^*(T, p)$, for fixed $T$ and $p$, as the magnetic field for which $n_{met}(T, p, h^*)/N_{exp} = 0.5$.

Fig. 3.10 shows $h^*(T, p)$, as measured from Monte Carlo simulations using the above explained method, as a function of temperature for a system size $L = 53$, and for varying values of $p$. Comparing this figure with Fig. 3.7, we observe that Monte Carlo results confirm both qualitatively and quantitatively[4] the theoretical predictions based on Pair Approximation. In this way we observe that the low temperature asymptotic behavior of $h^*(T, p)$ depends on the nonequilibrium parameter $p$. There is a critical value $\pi_c$ for $p$ which separates both asymptotic behaviors. We estimate from Monte Carlo simulations $\pi_c^{MC} \approx 0.03025$ (see Fig. 3.10). This critical value has to be compared with the result derived from Pair Approximation, $\pi_c^{pair} \approx 0.0315$. Hence we confirm that the system exhibits, as we discussed in the previous section, a non-linear cooperative phenomenon between the thermal noise, parameterized by $T$, and the non-thermal noise, parameterized by $p$, for $p > \pi_c$, in such a way that there are no metastable states for low and high temperatures, but there is an intermediate temperature region where metastable states emerge due to the non-linear coupling between both noises.

## 3.4 Dynamics of Metastable States in Mean Field Approximation

In the previous section we have studied the *static* properties of our metastable system. These static properties are related to the properties of the nonequilibrium potential, defined by eq. (3.30), which controls the system behavior, see Fig. 3.6. In particular, we have calculated the local extrema positions, and their local stability against small perturbations. Finally, we have investigated the intrinsic coercive magnetic field. These static investigations give us a good picture of the nonequilibrium potential shape for different values of temperature $T$, nonequilibrium perturbation $p$ and magnetic field $h$.

However, the metastability phenomenon is, as we discussed in Chapter 2, a *dynamical* process where the system, after wandering a long time around the metastable state, *evolves* towards the globally stable state. Therefore we are also interested in understanding the properties of this evolution, the processes which give rise to the metastable-stable transition, and the role played by nonequilibrium conditions in the system behavior. We also want to characterize the system dynamics with observables that, as the metastable state lifetime, define the typical temporal scales of the process.

Due to the successful description that we have obtained from the dynamic mean field approximation for the static properties of the system, it seems sensible to derive also the system dynamic properties using this approximation.

[4] At the quantitative level, Monte Carlo results match rather well with the theoretical predictions, although we observe, as expected, some systematic deviations for temperatures close enough to the critical one.

However, this methodology faces up to a fundamental problem, implicit in the structure of the mean field approximation. In the previous section we affirmed that, in mean field theory, all locally stable steady states with positive magnetization are metastable for $h < 0$. However, we can trivially prove that once the set of non-linear differential equations (3.19) reaches a steady state, it *never* evolves to any other state. This fact does not fit with the definition we gave in Chapter 2 for a metastable state, where we identified as a key feature of such state its transient character, i.e. a metastable state finally evolves towards the truly stable state. The reason why mean field theory fails when describing the exit from a metastable state underlies in one of the basic hypothesis assumed in this approximation: the suppression of fluctuations. The real system, once situated in the metastable region, *fluctuates* around the metastable state, due to the presence of noise in the system (in our case, noise has thermal -T- and non-thermal -p- origin). These fluctuations temporarily separate the system from the metastable state, although it rapidly reacts coming back to the metastable state. However, the *existence* of such fluctuations implies a non vanishing probability for one of these fluctuations to have a large enough amplitude in order to allow the system to overcomes the energy barrier which separates the metastable state from the stable one. That is, fluctuations constitute the origin of the metastable-stable transition, so a theory which neglects fluctuations cannot properly describe this dynamical process.

Hence, in order to theoretically investigate the dynamical aspects associated to metastability in our system using mean field theory, we must generalize the Pair Approximation in order to include the effect of fluctuations. In order to do so, let's remember one of the two basic equations in our approximation, namely eq. (3.17),

$$\begin{aligned} \frac{dx}{dt} &= -\sum_{n=0}^{2d}\binom{2d}{n}\Big[x^{1-2d}z^n(x-z)^{2d-n}\omega(+,n) \\ &- (1-x)^{1-2d}(x-z)^n(1+z-2x)^{2d-n}\omega(-,n)\Big] \end{aligned} \tag{3.39}$$

This equation describes the time evolution of the probability of finding an up spin in the system, $x \equiv \rho(+)$, as a function of both $x$ and $z$, where $z$ is the probability of finding a $(+,+)$ nearest neighbor pair. Let's remember now that the magnitudes,

$$\begin{aligned} Q(+,n) &\equiv \binom{2d}{n}x^{1-2d}z^n(x-z)^{2d-n} \\ &= \binom{2d}{n}\rho(+)\rho(+|+)^n\rho(-|+)^{2d-n} \\ Q(-,n) &\equiv \binom{2d}{n}(1-x)^{1-2d}(x-z)^n(1+z-2x)^{2d-n} \\ &= \binom{2d}{n}\rho(-)\rho(+|-)^n\rho(-|-)^{2d-n} \end{aligned} \tag{3.40}$$

defined in eq. (3.12) and entering eq. (3.39), are the probabilities of finding a spin in state up or down, respectively, and with $n$ up nearest neighbors. In the previous section we have specified that the spin class to which a spin belongs to is defined by the spin orientation and by its number of up nearest neighbors. Therefore, the magnitude $Q(s,n)$, which we define in mean field theory for our particular choice of the domain topology, is the probability of finding a spin in the system belonging to a spin class defined by the pair $(s,n)$. For instance, $Q(+,4)$ is the probability (in mean field approximation) of finding a spin in the system belonging to the first spin class, as defined in our convention, see Table 3.1. Although it is not clearly stated in our notation, we must notice that $Q(s,n)$ depends on $x$ and $z$, see eqs. (3.40).

Once we have identified the magnitudes $Q(s,n)$ as the population densities for each spin class in Pair Approximation, we can trivially write down the stable phase growth and shrinkage probabilities, $\tilde{g}(x,z)$ and $\tilde{s}(x,z)$ respectively, in this approximation,

$$\begin{aligned}
\tilde{g}(x,z) &\equiv \sum_{n=0}^{2d} Q_{x,z}(+,n)\omega(+,n) \\
&= \sum_{n=0}^{2d} \binom{2d}{n} x^{1-2d} z^n (x-z)^{2d-n} \omega(+,n) \\
\tilde{s}(x,z) &\equiv \sum_{n=0}^{2d} Q_{x,z}(-,n)\omega(-,n) \\
&= \sum_{n=0}^{2d} \binom{2d}{n} (1-x)^{1-2d} (x-z)^n (1+z-2x)^{2d-n} \omega(-,n) \qquad (3.41)
\end{aligned}$$

where we have stressed when using the notation $Q_{x,z}(s,n)$ the dependence of the spin class population densities on $x$ and $z$. Now we can write eq. (3.39) as,

$$\frac{dx}{dt} = \tilde{s}(x,z) - \tilde{g}(x,z) \qquad (3.42)$$

which is formally equivalent to eq. (3.38), taking into account that we spoke there about stable phase growth and shrinkage *rates*, and here we speak about stable phase growth and shrinkage *probabilities*.

This reformulation of some of the Pair Approximation original equations in terms of spin class population densities will allow us to introduce fluctuations in the system in a very natural way. Other methods which introduce fluctuations in mean field theories have been proposed in the literature[56], although these methods need additional assumptions. In order to implement fluctuations in mean field theory, let's have a look on the real system evolution. In our model, each spin in the lattice belongs to one of 10 possible spin classes. As the stochastic dynamics flips the spins, the population of the different spin classes changes. Moreover, as we explain in Appendix A, the population of the different classes is the magnitude which defines, together with the microscopic dynamics of the system, the stochastic jumps in system's phase space. Our mean

field theory yields an approximation for the spin class population densities for each value of $x$ and $z$. Hence, in order to include fluctuations in our mean field theory we only have to build a stochastic process similar to the one observed in the real system, but where instead of using the spin class population densities obtained from simulations, we will use the spin class population densities derived from mean field theory. This process will give rise to *stochastic* trajectories in the mean field phase space, defined by $(x, z)$, which will include fluctuations around the average behavior equivalent to those observed in the real system.

Let's assume now that we want to study the system dynamics in mean field approximation for temperature $T$, nonequilibrium perturbation $p$, and magnetic field $h < 0$. The algorithm we use in order to study the demagnetization process is the following[5],

1. We put the mean field system in an initial state defined by $x = 1 = z$. This initial state is equivalent to a state with all spins up.
2. For those values of $x$ and $z$ we evaluate the spin class population densities for all the classes, $Q_{x,z}(s, n)$, using eqs. (3.40).
3. We calculate the time $\Delta t$ the system spends in the current state $(x, z)$ before going to some other state (see Appendix A). This time depends exclusively on the current state. We increment time, $t \to t + \Delta t$.
4. We randomly select one of the possible spin classes with probability proportional to the spin class flip probabilities, $Q_{x,z}(s, n) \times \omega(s, n)$. This spin class is defined by the pair $(s, n)$, where $s = \pm 1$ and $n = 0, \ldots, 4$.
5. We actualize the variables $x$ and $z$, in such a way that $x \to x + \delta x(s)$ and $z \to z + \delta z(s, n)$.
6. We come back to point 2 until we reach the stable state.

The increments $\delta x(s)$ and $\delta z(s, n)$ obviously depend on the chosen spin class in order to actualize the system. Thus, if we choose class 1, characterized by a central spin $s = +1$ and $n = 4$ up nearest neighbors (see Table 3.1), we know that $x$, which is the probability of finding an up spin in the system, will decrease in an amount $1/N$ when we flip a spin in this spin class, where $N$ plays the role of the number of spins in the system. On the other hand, if we choose class 7, characterized by a down central spin and $n = 3$ up nearest neighbors, now $x$ will increase up to $x + 1/N$. Therefore, the increment induced on $x$ only depends on the values of the central spin which defines each class, and not on the number of up nearest neighbors. Thus we can write, for a fixed selected spin class characterized by a central spin $s$,

$$\delta x(s) = -\frac{s}{N} \tag{3.43}$$

[5]This algorithm is based on the s-1 MCAMC algorithm explained in Appendix A. In general, MCAMC algorithms, when applied to the real system, are exact reformulations of the standard Monte Carlo algorithm, although they are much more efficient since they are rejection-free. The philosophy used by these algorithms, based on the different spin class populations, allows us to write down a mean field stochastic dynamics from our theory, as we show in the main text.

In order to calculate the modification that the variable $z$ suffers after one step, $\delta z(s, n)$, let's assume again that we choose class 1 to actualize the system, where we already know that $s = +1$ and $n = 4$. Variable $z$ is the probability of finding a $(+, +)$ pair in the system, $\rho(+, +)$. Each spin in class 1 contributes to $z$ with $n = 4$ different $(+, +)$ nearest neighbors pairs. The total number of pairs in a system with N spins and dimension $d$ is $dN$. Hence when we flip a spin in class 1, the variable $z$ has to decrease in an amount $4/dN$. In general we can write,

$$\delta z(s, n) = -\frac{sn}{dN} \tag{3.44}$$

With eqs. (3.43) and (3.44) we completely define the mean field stochastic dynamics previously explained. We have checked that this stochastic dynamics yields the same results for the static properties of the system that we found using Pair Approximation in the previous section. On the other hand, this method allows us to obtain the dependence of $z$ on $x$ for any $x \in [0, 1]$, $z = z(x)$, for any parameter space point $(T, p, h)$. This was not possible numerically integrating the set of eqs. (3.17) and (3.18), due to the presence of multiple stationary states. In particular, once we obtain the dependence $z(x)$, we can compare the stable phase growth and shrinkage probabilities calculated using the mean field stochastic dynamics, ecs. (3.41), with the computational results for these observables. Fig. 3.11 shows this comparison. We use there the parameters $T = 0.6T_{ons}$, $p = 0.005$ and $h = -0.1$ for a system size $L = 53$, i.e. $N = 2809$ spins. These parameters were also used in Fig. 3.8.

We observe in this figure that, while the comparison between the computational results and the mean field stochastic dynamics prediction is remarkably good in the relatively narrow magnetization intervals $m \in [-1, m_{-1}]$ and $m \in [m_1, 1]$ (we defined $m_1$ and $m_{-1}$ in the previous section), this comparison turns over disastrous for magnetizations in the interval $m \in (m_{-1}, m_1)$. In particular, the values $m_{-1}$ and $m_1$ derived from the mean field stochastic dynamics nicely agree with the stable and metastable state magnetizations measured in the real system.

The stable phase growth and shrinkage probabilities, $g(m)/N$ y $s(m)/N$ respectively, are the most relevant observables in the metastable-stable transition. They determine most of the properties of this dynamic process between the metastable state $(m_1)$ and the stable one $(m_{-1})$. For instance, we can calculate the metastable state lifetime from these probabilities (see Appendix A). Therefore, the discrepancies between the theoretical prediction for both probabilities (based on the mean field stochastic dynamics approximation) and the measured values for $g(m)/N$ y $s(m)/N$ in the interval $m \in (m_{-1}, m_1)$ points out that our theoretical approximation, in spite of taking into account fluctuations, is not able to describe the dynamics of the metastable state demagnetization process.

The key question now is: Why does the extended mean field approximation fail when describing the dynamics of the demagnetization process ?. The answer to this question underlies again in one of the basic hypothesis of mean field approximation: the hypothesis of *homogeneity*. During the formulation of

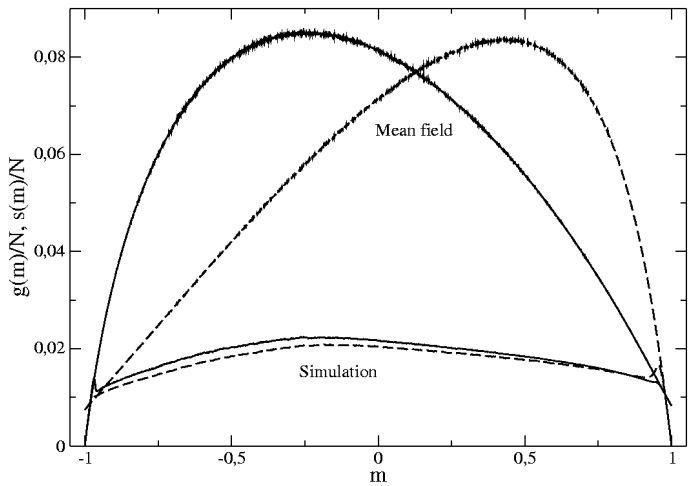


Figure 3.11: Comparison of stable phase growth and shrinkage probabilities, $g(m)/N$ and $s(m)/N$ respectively, as obtained from mean field stochastic dynamics (pair of curves with larger amplitude) and from Monte Carlo simulations of the real system. The continuous line represents $g(m)/N$ in both cases, while the dashed line represents $s(m)/N$. The parameters are $T = 0.6T_{ons}$, $p = 0.005$ and $h = -0.1$, for a system size $L = 53$, i.e. $N = 2809$ spins. These parameters are the same than those used in Fig. 3.8. Notice that $m = 2x - 1$.

Pair Approximation (see section 3.2) we assumed two basic hypothesis: homogeneity and kinetic isolation[6]. The kinetic isolation hypothesis involved neglecting long range correlations. Although these long range correlations are generally relevant to understand the global behavior of the system, we can neglect them for temperatures far away the critical one, as in our case. On the other hand, the homogeneity hypothesis involved the assumption that the properties of the system did not depend on the position in the system. However, the metastable-stable dynamic transition is a highly inhomogeneous phenomenon: fluctuations present in the system give rise to small *droplets* of the stable phase inside the metastable bulk. These compact droplets appear instead of non-compact fluctuations because compact fluctuations minimize in some sense the surface-volume ratio, and hence they are energetically favoured. These localized droplets constitute an inhomogeneity not taken into account in our mean field theory. If one (or several) of these droplets reaches a size large enough such that the system is able to overcome the energy barrier which separates the metastable state from the stable one, then the system will rapidly evolve towards the stable state. When we impose homogeneity in mean field theory, we force the system to behave coherently, that is, all spins in the system behave in the same way. Therefore, the fluctuations we have included in the theory via the mean field stochastic dynamics approach, de-

[6]We have to add a third hypothesis, namely suppression of fluctuations.

scribed above, are *coherent*, non-compact fluctuations, and hence energetically punished. This is the reason why we observe that it is much more difficult for the system to exit the metastable well in mean field approximation than for the real system[7]. In particular, it is observed in Fig. 3.11 that the area delimited by the curve $[s(m) - g(m)]/N$ between the points $m_0$ and $m_1$, which is in some sense a measure of the strength of the metastable state, is much larger in mean field approximation than for the real system. On the other hand, our mean field theory describes in a proper way the static properties of both the stable and metastable states because these states are homogeneous, i.e. without any *preferred* point.

The above discussion implies that we need to build a inhomogeneous theory, based on the picture of nucleation of stable phase compact droplets in the metastable bulk, in order to understand the dynamic properties of the metastable system. This theory was formulated long ago for equilibrium systems [23, 26], and it is based on the free energy of one of these droplets. This droplet free energy can be written as the competition of two different terms. On one hand, there is a volume term, related to the properties of the pure homogeneous phase which constitutes the droplet, i.e. the stable phase. On the other hand, there is a surface term, related to the interface separating the stable phase inside the droplet from the metastable phase that surrounds it. This term is associated with the inhomogeneity which characterize the metastable-stable transition. In previous sections we have studied the properties of both pure homogeneous phases (the metastable and the stable phases) for our nonequilibrium system. If we want to build a droplet theory valid for the nonequilibrium ferromagnetic system we must understand also the system interfacial properties, which will characterize the inhomogeneous, surface term which determines, in competition with the volume term, the droplet properties. Therefore, our aim in the next chapter consists in studying the interface in our model[8].

## 3.5 Conclusion

In this chapter we have studied both the static and dynamic properties of metastable states in the nonequilibrium ferromagnetic model using a first order dynamic mean field approximation.

In particular, we have applied the so-called Pair Approximation[50, 51], a dynamic analogous of the equilibrium Bethe-Peierls Approximation, to the problem of metastability in our lattice spin system. This theory is based on a

[7]In practice, in order to perform the simulation with mean field stochastic dynamics we must implement the slow forcing approximation (see Appendix A). In this way we are able to exit the metastable state.

[8]This last section, devoted to the investigation of the system dynamics in mean field approximation, can be thought as a waste of time, since it was obvious from the very beginning that the homogeneity hypothesis in mean field theory should impede any realistic description of the dynamics. However, apart from the pedagogical value of the discussion, in this section we have presented a novel method to include fluctuations in mean field theory in a natural way, which may be very useful in other kind of problems where the system is homogeneous.

mean field approximation for the master equation governing the system dynamics, once this stochastic equation is reduced to local observables. The approximation is developed using three fundamental hypothesis. In a first step, it neglects all fluctuations in the system, so in this approach we only study the *average* behavior of local observables. On the other hand, this theory also neglects long range correlations. In particular, we only have into account nearest neighbor correlations (this is why this approximation is termed *first order*). The last hypothesis assumes that the system is homogeneous, which implies that all points in the lattice behave in the same way, independently from their positions.

Taking into account these hypothesis, and taking as starting point the master equation, we obtain two coupled non-linear differential equations for the dynamics of $x$, the probability of finding an up spin in the system, and $z$, the probability of finding a $(+,+)$ nearest neighbors pair in the system. We obtain numerically the locally stable steady solutions of this set of differential equations, both for zero magnetic field and $h < 0$. For $h = 0$ we obtain theoretical predictions for the stationary state magnetization as a function of temperature for different values of $p$. These predictions perfectly compare with Monte Carlo results in the low and intermediate temperature regime, although some differences between theory and simulation appear for temperatures near to the critical one, $T_c(p)$, since for these temperatures long range correlations become important. As the value of the nonequilibrium perturbation $p$ is increased, the stationary state magnetization decreases in magnitude for $h = 0$ for a fixed temperature, although the qualitative shape of curves $m_s^{(\pm)}(T,p)$ is similar to those of the equilibrium system. The critical temperature $T_c(p)$ signals a second order phase transition in the nonequilibrium systems between a disordered phase for high temperatures and an ordered phase for low temperatures. Applying the marginal stability condition to the dynamic equations, we are able to extract the phase diagram in first order mean field approximation for the nonequilibrium model. The phase diagram yields the critical temperature $T_c(p)$ as a function of the nonequilibrium parameter $p$. The ordered phase disappears for all temperatures when $p > p_c$, where $p_c = \frac{5}{32}$ in this approximation. Finally, for the locally stable steady magnetization for $h < 0$ we obtain qualitatively similar results as compared with the $h = 0$ case, although now the up-down symmetry which held for $h = 0$ breaks up. The comparison of predicted curves with Monte Carlo results for both magnetization branches for $h < 0$ is also excellent.

On the other hand, the system exhibits hysteresis due to the existence of metastable states. This implies that the system keeps memory of the past evolution history. In particular, using mean field approximation we calculate the intrinsic coercive field $h^*(T,p)$, defined in this case as the magnetic field for which the metastable state becomes unstable. We observe that $h^*(T,p)$ shows two different kinds of asymptotic behaviors in the low temperature limit, which depend on the value of $p$. There is a critical value for $p$, $\pi_c \approx 0.0315$, which separates both behaviors. For $p < \pi_c$ the intrinsic coercive field $h^*(T,p)$ increases

in magnitude as temperature decreases, in the same way that in equilibrium systems. However, for $p > \pi_c$ we predict that the intrinsic coercive field converges towards zero in the limit $T \to 0$, showing a maximum in magnitude for certain intermediate temperature. This involves the existence of a *non-linear cooperative phenomenon* between the thermal noise (parameterized by $T$) and the non-thermal noise (parameterized by $p$): although both noise sources independently add disorder to the system, which implies the attenuation, or even destruction of existing metastable states, the combination of both noises parameterized in the microscopic dynamics does not always involves a larger disorder, giving rise to parameter space regions where there are no metastable states for low and high temperatures, but metastable states appear for intermediate temperatures. This theoretical prediction based on the mean field approximation is fully confirmed via Monte Carlo simulations.

Finally, apart from the mean field investigations on the static properties of both stable and metastable states in the system, summarized in previous paragraphs, we have also attempted a description of the dynamics of the metastable-stable transition using Pair Approximation. However, one of the basic hypothesis in this approximation, namely the hypothesis of suppression of fluctuations, impedes any realistic description of this dynamic process using Pair Approximation. The reason underlies in that fluctuations constitute the basic mechanism which gives rise to the metastable-stable transition. Therefore, in order to describe the metastable state demagnetization process, we relax the above hypothesis, including fluctuations in the dynamic mean field theory. This can be done in a natural way using the concepts of stable phase growth and shrinkage rates, observables which are defined in a simple manner in our approximation, and the philosophy underlying MCAMC algorithms (see Appendix A). In this way we write a *mean field stochastic dynamics*, which includes fluctuations in a natural way. From this extended theory we predict the dynamic (and static) properties of the system. However, while the static results obtained from the mean field stochastic dynamics are equivalent to those obtained in Pair Approximation and reproduce the measured properties in Monte Carlo simulations, the results on the dynamics of the metastable-stable transition are remarkably different from those obtained in simulations. This discrepancy is due to the failure of another basic hypothesis of mean field approximation: the homogeneity hypothesis. This hypothesis implies that the exit from the metastable state in the mean field stochastic dynamics approximation is produced by *coherent* fluctuations of all spins in the system, which are energetically punished. The metastable demagnetization process in the real system is, on the other hand, a highly inhomogeneous process, where one or several stable phase droplets nucleate in the metastable bulk, since these compact structures minimize the system free energy for a fixed magnetization. Thus, in order to understand the dynamics of the metastable-stable transition we must therefore write an inhomogeneous theory where the interface plays a very important role. This inhomogeneous theory, based on the droplet picture, will be developed in Chapter 5. However, in order to write such theory for the nonequilibrium system, we must first understand the interfacial properties in

the model, since they will play a fundamental role in the droplet nucleation process. We study this problem in the next chapter.

# Chapter 4

# Interfacial Properties

## 4.1 Introduction

In the previous chapter we have inferred the need of an inhomogeneous description, based on the picture of droplets of the stable phase nucleating in the metastable bulk, in order to describe properly the dynamics of the metastable-stable transition in the nonequilibrium ferromagnetic system. One of the fundamental features characterizing the inhomogeneity in this process is the presence of interfaces separating the metastable phase from the stable one. Thereby, we must study the properties of an interface in the classic spin system under nonequilibrium conditions in order to develop an inhomogeneous theory that explains the dynamics of the demagnetization process from the metastable state.

We devote this chapter to the study of the interfacial properties of the nonequilibrium spin model. In particular, we are going to pay attention to both the microscopic properties of the interface and its surface tension. With this aim in mind we will first describe the Solid-On-Solid (SOS) approximation, first formulated by Burton, Cabrera and Frank[59]. This approximation studies the interfacial properties in the Ising model for zero magnetic field, and it is based on a microscopic description of the interface. In spite of the approximate character of this theory, the predictions derived from it nicely reproduce the properties of the equilibrium interface. Afterwards we will present a generalization of SOS approximation which will allow us to study and predict the properties of the interface in our nonequilibrium spin model. Finally, using the results obtained via the generalized SOS theory, we will study the shape of a spin droplet in the nonequilibrium system. This shape can be derived once we know the interface surface tension using Wulff construction[68].

## 4.2 The Solid-On-Solid Approximation

The Solid-On-Solid approximation (see ref. [59]) describes the interface in a bidimensional equilibrium Ising model for zero magnetic field, $h = 0$, using a simple picture where the interface is an *univaluated* function. If we have, as in our case, a square lattice, the interface is completely defined by a set of integer height values, $y_x$, with $x = 0, \ldots, L$, as Fig. 4.1.a shows. If $\mathbf{y} = \{y_i, i = 0, \ldots, L\}$ is a configuration of the interface, the energy associated to this configuration is,

$$\mathcal{H}_I(\mathbf{y}) = 2J \sum_{i=1}^{L} (1 + |y_i - y_{i-1}|) \tag{4.1}$$

where J is the spin coupling constant in Ising model (see eq. (2.1)). If we compare this Hamiltonian $\mathcal{H}_I$ with the original equilibrium Ising Hamiltonian, eq. (2.1), for zero magnetic field, $h = 0$, we observe that $\mathcal{H}_I(\mathbf{y})$ is just the energy contributed by all $(+,-)$ spin pairs forming the interface to the total Ising configuration energy. Since in the ferromagnetic Ising model spins tend to align with their nearest neighbor spins, we can say that a $(+,-)$ spin pair constitutes a *broken bond*. The energy cost of a broken bond in the Ising model is just 2J, so the Hamiltonian $\mathcal{H}_I$ is just the energy associated to all the broken bonds which define the interface.

Let's introduce now the canonical ensemble for this model, which consists in all possible interfacial configurations in a system with length L and with boundary conditions specified by $y_L - y_0 = \mathcal{Y} \equiv L \tan\phi$, where $\phi$ is the angle formed by the interface and the $\hat{x}$ axis. The associated partition function will be given by,

$$\mathcal{Z}(L, \phi) = \sum_{\mathbf{y}} e^{-\beta \mathcal{H}_I(\mathbf{y})} \delta\big[(y_N - y_0) - \mathcal{Y}\big] \tag{4.2}$$

where $\beta$ is the inverse temperature, and $\delta(t)$ is the Kronecker Delta function ($\delta(t) = 1$ if $t = 0$ and $\delta(t) = 0$ otherwise). The corresponding free energy per site is defined using the following limit,

$$\sigma_{pr}(\phi) = \lim_{L\to\infty} -\frac{1}{\beta L} \ln \mathcal{Z}(L, \phi) \tag{4.3}$$

This free energy is known as the projected surface tension[60]. The surface tension, which is the free energy per unit length, can be written as,

$$\sigma(\phi) = |\cos\phi| \;\; \sigma_{pr}(\phi) \tag{4.4}$$

Due to the boundary conditions, mathematically expressed via the Kronecker Delta function that appears in eq. (4.2), it is not possible to perform the sum needed to calculate the canonical partition function. In order to perform the calculation we introduce a new ensemble, conjugated to the previous one, where instead of fixing the height values at the borders (that is, instead of fixing the angle $\phi$ formed between the interface and the $\hat{x}$ axis), we fix a new

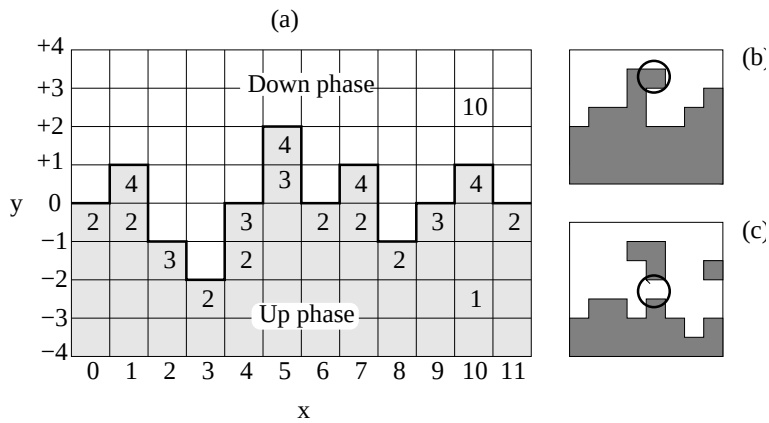


Figure 4.1: (a) Schematic representation of a SOS interface between an up spin phase and a down spin phase. In this case $L = 11$. The numbers inside the spins indicate the spin class to which they belong to (see Table 3.1). Notice that interfacial spins belong to classes 2, 3 and 4. (b) Example of configuration with overhangs, which is forbidden in SOS approximation. The marked spin involves a multivaluated interface for that $x$ coordinate. (c) Schematic representation of an interface close to interact with bulk fluctuations. These kind of configurations are also forbidden in SOS approximation.

thermodynamic parameter, $\gamma(\phi)$[1]. If we define the *step variables* $\delta_i = y_i - y_{i-1}$, we can write the Hamiltonian for an interface with a configuration $\delta = \{\delta_i, i = 1, \ldots, L\}$ as $\mathcal{H}_I(\delta) = 2J \sum_{i=1}^{L} (1 + |\delta_i|)$. Thus boundary conditions, defined by $y_L - y_0 = \mathcal{Y}$, can be expressed now as $\sum_{i=1}^{L} \delta_i = \mathcal{Y}$. The partition function for the new ensemble is,

$$\mathcal{Z}_2(L, \gamma) = \sum_{\delta} e^{-\beta \mathcal{H}_I(\delta)} e^{\gamma(\phi) \sum_{i=1}^{L} \delta_i} \tag{4.5}$$

where the new thermodynamic parameter $\gamma(\phi)$ is just the Lagrange multiplier which keeps the *average* step variable in a $x$ independent value, that is, $\langle \delta_i \rangle = \tan \phi$ for all $i \in [1, L]$.[61] If we use in eq. (4.5) the previously derived expression for $\mathcal{H}_I(\delta)$, we obtain,

$$\mathcal{Z}_2(L, \gamma) = e^{-2\beta J L} [z(\gamma)]^L \tag{4.6}$$

where $z(\gamma)$ is the partition function for a single step,

$$z(\gamma) = \sum_{\delta=-\infty}^{\infty} e^{-2\beta J |\delta|} e^{\gamma(\phi)\delta} = \frac{1 - X^2}{1 + X^2 - 2X \cosh \gamma(\phi)} \tag{4.7}$$

[1]This is similar to what happens when we introduce the macrocanonical ensemble in gases. While the thermodynamic parameters in the canonical ensemble for gases are $(T, V, N)$, in the macrocanonical ensemble we introduce a new thermodynamic parameter, namely the chemical potential $\mu$, which substitutes the number of particles $N$, which is not fixed now in this new ensemble. The thermodynamic potentials derived from both ensembles are related via a Legendre transform based on the thermodynamic parameters $\mu$ and $N$.

and where we have used the notation $X \equiv e^{-2\beta J}$. It is obvious from eq. (4.6) that in SOS approximation the different step variables $\delta_i$ are supposed to be statistically independent among them. We could also derive this idea from the additive character of the Hamiltonian $\mathcal{H}_I$ once written in terms of the step variables. In order to calculate the $\phi$ dependence of the Lagrange multiplier $\gamma(\phi)$, we use the condition $\langle\delta\rangle = \tan\phi$. The probability of finding a step with size $\delta$ in the new ensemble is (see the previous equation),

$$p(\delta) = \frac{1}{z(\gamma)} X^{|\delta|} e^{\gamma(\phi)\delta} \tag{4.8}$$

We thus can write,

$$\langle\delta\rangle = \frac{\partial \ln z(\gamma)}{\partial\gamma} = \tan\phi \tag{4.9}$$

where we use the single step partition function as a moment generating function. From this equality we find,

$$\begin{aligned} e^{\gamma(\phi)} &= \frac{(1+X^2)\tan\phi + R(\phi)}{2X(\tan\phi+1)} \\ e^{-\gamma(\phi)} &= \frac{(1+X^2)\tan\phi - R(\phi)}{2X(\tan\phi-1)} \end{aligned} \tag{4.10}$$

where $R(\phi) = [(1-X^2)^2\tan^2\phi + 4X^2]^{1/2}$. Substituting these expressions in eq. (4.7) we arrive to,

$$z(\phi) = \frac{(1-X^2)(1-\tan^2\phi)}{1+X^2-R(\phi)} \tag{4.11}$$

The thermodynamic potential associated to this second ensemble can be written as a function of $\phi$ in the following way,

$$\begin{aligned} \varphi(\phi) &\equiv \lim_{L\to\infty} -\frac{1}{\beta L}\ln \mathcal{Z}_2[L,\gamma(\phi)] \\ &= -\frac{1}{\beta}\ln\Big[X\frac{(1-X^2)(1-\tan^2\phi)}{1+X^2-R(\phi)}\Big] \end{aligned} \tag{4.12}$$

This thermodynamic potential is related to the projected surface tension, eq. (4.3), via a Legendre transform which involves the thermodynamic variables $\tan\phi$ and $\gamma$. If we perform such Legendre transform, and obtain from the so-calculated $\sigma_{pr}(\phi)$ the surface tension, we find,

$$\begin{aligned} \sigma_{SOS}(\phi;T) &= |\cos\phi|\Big\{-T\ln\Big[X\frac{(1-X^2)(1-\tan^2\phi)}{1+X^2-R(\phi)}\Big] \\ &\quad +T\tan\phi\ln\Big[\frac{(1+X^2)\tan\phi+R(\phi)}{2X(\tan\phi+1)}\Big]\Big\} \end{aligned} \tag{4.13}$$

where we have used that $\beta = 1/T$, with $T$ the system temperature. The subindex *SOS* included in our notation for the surface tension, $\sigma_{SOS}(\phi;T)$, points out

that this is the solution in Solid-On-Solid approximation. This theory is approximate in several ways. First, as we said before, the SOS approximation neglects correlations between neighboring step variables $\delta_i$. On the other hand, when we assume that the interface is univaluated we are neglecting the possible presence of *overhangs*. These overhangs give rise to non-analytic regions in the interface of the real Ising model, since for a fixed $x$ coordinate there are several different values of the height $y(x)$. Fig. 4.1.b shows an example of overhang. Furthermore, the SOS approximation also neglects all possible interactions between the interface and the fluctuations or droplets appearing in the bulk. Fig. 4.1.c shows an example of this possible interaction. Therefore it is surprising that, in spite of these approximations, the surface tension derived in SOS approximation, eq. (4.13), reproduces the known exact result for $\phi = 0$ [62], and yields a very good approximation for $|\phi| \leq \pi/4$.[63] For values of $|\phi|$ larger that $\pi/4$ is more reasonable to use the SOS approximation taking as reference frame the $\hat{y}$ axis instead of the $\hat{x}$ axis.

## 4.3 Generalization of the Solid-On-Solid Approximation for an Interface under Nonequilibrium Conditions

In this section we want to generalize the SOS approximation to our nonequilibrium model. In order to perform such extension of the equilibrium interfacial theory we must understand deeply, in a first step, the effects that the nonequilibrium random perturbation $p$ induces on the system.

### 4.3.1 Effective Temperature

Our starting point to do that is the microscopic dynamics we have imposed to the system. The transition rate in the model, eq. (2.3), is,

$$\omega(s,n) = p + (1-p)\frac{e^{-\beta\Delta\mathcal{H}(s,n)}}{1+e^{-\beta\Delta\mathcal{H}(s,n)}} \tag{4.14}$$

This dynamics, which we called Glauber dynamics, is local as far as it depends exclusively on the spin $s$ we are trying to flip, and on the number of its up nearest neighbor spins, $n$, through the energy increment involved in the transition, $\Delta\mathcal{H}(s,n)$. As we discussed before, there are many other different competing dynamics. One of the most used dynamics in literature because of its appropriate features is Metropolis dynamics,

$$\omega(s,n) = p + (1-p)\min[1, e^{-\beta\Delta\mathcal{H}(s,n)}] \tag{4.15}$$

This dynamics is a bit faster than Glauber dynamics, although the qualitative results derived using Metropolis dynamics to study metastability in the

nonequilibrium system are very similar to those obtained with Glauber dynamics. In order to analyze the effect that the nonequilibrium dynamic perturbation induces on the system behavior, it is appropriate to work initially using Metropolis dynamics instead of the original Glauber dynamics due to technical details which will be clear later on in this section. The results we obtain are apparently independent of this detail.

Dynamics as those written in eqs. (4.14) and (4.15), where two canonical rates working at different temperatures compete, generically drive the system towards a nonequilibrium steady state. We could think however that we can map this a priori nonequilibrium system to an equilibrium system with effective parameters. The transition rate should verify now the detailed balance condition, eq. (2.4), for these effective parameters. In particular, for competing temperatures, we could think of mapping the nonequilibrium system to an equilibrium model with certain *effective temperature*. In order to calculate this effective temperature we use eq. (4.15). Thus we want to write the transition rate (4.15) as $\min[1, e^{-\beta_{eff}\Delta\mathcal{H}(s,n)}]$, which is a dynamics driving the system towards an equilibrium steady state at inverse temperature $\beta_{eff}$. For $\Delta\mathcal{H}(s,n) > 0$,

$$p + (1-p)e^{-\beta\Delta\mathcal{H}(s,n)} \equiv e^{-\beta_{eff}\Delta\mathcal{H}(s,n)} \tag{4.16}$$

where $\beta_{eff} = 1/T_{eff}$, being $T_{eff}$ the effective temperature. From this equation we obtain an expression for the effective temperature, as deduced from Metropolis rate, for $\Delta\mathcal{H}(s,n) > 0$,

$$T_{eff}^{(s,n)}(p) = \frac{-\Delta\mathcal{H}(s,n)}{\ln\left[p + (1-p)e^{-\beta\Delta\mathcal{H}(s,n)}\right]} \tag{4.17}$$

For $\Delta\mathcal{H}(s,n) \leq 0$ we have that $T_{eff}^{(s,n)} = T$. The effective temperature defined in this way is not unique for a system with $p \neq 0$, because it clearly depends on the spin class to which the flipping spin belongs to through the energy increment $\Delta\mathcal{H}(s,n)$ involved in this transition, for $\Delta\mathcal{H}(s,n) > 0$. All spins in the same spin class share the same energy increment $\Delta\mathcal{H}(s,n)$ when flipped. Hence, all spins in the same spin class suffer the same effective temperature. However, for $0 < p < 1$ this effective temperature varies depending on the chosen spin class. In the limit $p = 0$ the effective temperature defined in (4.17) reduces to the usual temperature, $T$.

First, the fact that the effective temperature depends on $\Delta\mathcal{H}(s,n)$ points out that we cannot exactly map the nonequilibrium system to an equilibrium model with well-defined effective temperature. On the other hand, the dependence of $T_{eff}^{(s,n)}$ on the energy increment (that is, on the spin class to which the chosen spin belongs to) will allow us to obtain a clear physical picture of the effect that the nonequilibrium parameter $p$ induces on system's dynamics. Fig. 4.2 shows the effective temperature for each spin class, as defined from Metropolis dynamics, see eq. (4.17), for a system with temperature $T = 0.5T_{ons}$ and $p = 0.01$ (the magnetic field $h$ is always zero in this section), taking into account that the energy increment associated to each class

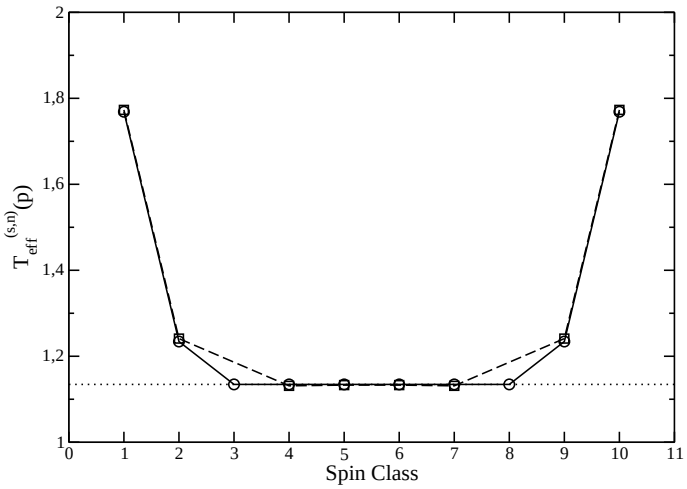


Figure 4.2: Effective temperature $T_{eff}^{(s,n)}$ as a function of the spin class $i \in [1, 10]$ as obtained from Metropolis dynamics (◯) and from Glauber dynamics (□), for a system with $T = 0.5T_{ons}$ and $p = 0.01$ ($h = 0$ always in this section). Notice that $T_{eff}^{(s,n)}$ is not defined for spin classes 3 and 8 (both corresponding with $\Delta\mathcal{H}(s, n) = 0$) for Glauber dynamics. The dotted line corresponds to the system temperature, $T$.

is $\Delta\mathcal{H}(s, n) = 2s[2J(n - d) + h]$. In this figure we observe that the effective temperature curve is fully symmetrical for up and down spins: that is, spin classes 1 and 10 suffer the same effective temperature, and the same happens for spin classes 2 and 9, 3 and 8, 4 and 7, 5 and 6. On the other hand, we see that *more ordered* spin classes, i.e. spin classes characterized by a larger number of nearest neighbor spins pointing in the same direction that the central spin, suffer a higher effective temperature. Thus, classes 1 and 10, where all four nearest neighbor spins point in the same direction than the central spin, are subject to the highest effective temperature. This observation is compatible with intuition. As we have explained before, the presence of the nonequilibrium perturbation $p$ implies that, with a very small probability, spins in the system are able to flip independently from energetic restrictions imposed by the interaction with their nearest neighbors. The larger is the number of nearest neighbors pointing in the same direction than the central spin, the larger is the energy barrier that is *violated* when flipping such central spin independently from any energetic constraint. Hence, if we interpret the effect of the nonequilibrium parameter $p$ in terms of an effective temperature, it is obvious the need of a larger effective temperature in order to overcome higher energy barriers. Therefore we would a priori expect that the larger is the local order that a spin feels, the larger is the effective temperature this spin suffers. This is in fact what we have obtained in the above calculation.

The effective temperature can be also defined using Glauber dynamics, eq. (4.14), in a way similar to the one followed when using Metropolis dynamics,

eq. (4.17). However, the definition of effective temperature based on Glauber dynamics shows a singularity for $\Delta\mathcal{H}(s,n) = 0$, that is, for spin classes 3 and 8, so using this definition in theoretical analysis is not suitable. Fig. 4.2 also shows the effective temperature as obtained from Glauber dynamics. The effective temperature obtained from Metropolis dynamics is almost indistinguishable from the one obtained via Glauber dynamics, and it does not show any singularity for $\Delta\mathcal{H}(s,n) = 0$. This is the reason why we have used from the very beginning Metropolis dynamics to define the effective temperature, instead of using Glauber dynamics.

### 4.3.2 Statistical Weight Associated to a Broken Bond in the Nonequilibrium Interface

Coming back to the interface problem, we observe in Fig. 4.1.a that the spins that define the interface belong to different spin classes. If we fix our attention on the up phase interfacial spins[2], they belong to spin classes 2, 3 and 4. Spins in classes 1 and 5 cannot never belong to the interface. Spins in class 1 are typical of the up phase bulk, and spins in class 5 are isolated up spins in the down phase bulk. If we call $T_{eff}^{(i)}$ the effective temperature associated to class $i \in [1, 10]$, then we have spins in the interface that suffer effective temperatures $T_{eff}^{(2)} \geq T_{eff}^{(3)} \geq T_{eff}^{(4)}$ if they belong to classes 2, 3 and 4, respectively.

One of the central magnitudes in the Solid-On-Solid approximation for the equilibrium system ($p = 0$) is $X \equiv e^{-2\beta J}$, which is the probabilistic weight associated to a broken bond in the interface. Thus the probability of finding a step of height $\delta$ in the interface is proportional to $X^{|\delta|}$, see eq. (4.8). Using the concept of effective temperature previously introduced, we can assume that the probabilistic weight associated to a broken bond in the nonequilibrium system ($p \neq 0$) will depend on the spin class to which the interfacial spin whose bond is broken belongs to through the effective temperature associated to this spin class. If this spin belongs to class $i$, we denote this statistical weight as $X_i$. Hence we can write in this picture $X_i = e^{-2\beta_{eff}^{(i)} J}$, where $\beta_{eff}^{(i)} = 1/T_{eff}^{(i)}$, being $T_{eff}^{(i)}$ the effective temperature associated to the class $i$ to which the interfacial spin whose bond is broken belongs to. That is, we assume that each spin class $i$ behaves as an equilibrium system at effective temperature $T_{eff}^{(i)}$, so the probabilistic weight associated to a broken bond in class $i$ is just the Boltzmann factor associated to this broken bond at temperature $T_{eff}^{(i)}$, $X_i = e^{-2\beta_{eff}^{(i)} J}$. Moreover, we assume now that, as a first approximation, the probabilistic weight associated to an interfacial broken bond in the system with $p \neq 0$ will be given by the following average,

$$X_p = \Pi_2(T,p)X_2 + \Pi_3(T,p)X_3 + \Pi_4(T,p)X_4 \tag{4.18}$$

[2]In order to define the interface we must center our attention on all up interfacial spins, *or* on all down interfacial spins. In this case we choose the up interfacial spins.

where $\Pi_i(T,p)$ is the probability of finding an interfacial spin belonging to class $i$, and where $X_i$ is the statistical weight for a broken bond associated to class $i$, as we said before. This last assumption constitutes a mean field approximation, because we neglect the effect derived from presence of different spin classes in the interface, with different associated statistical weights $X_i$ for each broken bond. Instead we average such effect, building an average probabilistic weight $X_p$, identical for all broken bonds in the interface and independent of the spin class. Since all interfacial spins in the up phase belong to classes 2, 3 and 4, it is obvious that the following normalization condition holds,

$$\Pi_2(T,p) + \Pi_3(T,p) + \Pi_4(T,p) = 1 \tag{4.19}$$

$X_p$ is our approximation for the statistical weight associated to a broken bond in the nonequilibrium interface. In order to generalize the SOS approximation to the system with $p \neq 0$, we only have to substitute in the results obtained in the previous section the variable $X$ for the new generalized probabilistic weight $X_p$. Thus, for the nonequilibrium system, the probability of finding a step in the interface with magnitude $\delta$ is,

$$p_p(\delta) = \frac{1}{z_p(\gamma_p)} X_p^{|\delta|} e^{\gamma_p(\phi)\delta} \tag{4.20}$$

where now $z_p(\gamma_p)$ and $\gamma_p(\phi)$ are the corresponding generalized versions, substituting $X$ for $X_p$, of the partition function associated to a single step and the thermodynamic parameter conjugated to the interface slope, respectively. In the same way, the generalized surface tension is now,

$$\begin{aligned} \sigma_{SOS}^{(p)}(\phi;T,p) &= |\cos\phi| \Big\{ -T \ln \Big[ X_p \frac{(1-X_p^2)(1-\tan^2\phi)}{1+X_p^2-R_p(\phi)} \Big] \\ &\quad + T \tan\phi \ln \Big[ \frac{(1+X_p^2)\tan\phi + R_p(\phi)}{2X_p(\tan\phi+1)} \Big] \Big\} \end{aligned} \tag{4.21}$$

where $R_p(\phi) = [(1-X_p^2)^2 \tan^2\phi + 4X_p^2]^{1/2}$. In order to find the explicit form of all these magnitudes we only have to evaluate the probabilities $\Pi_i(T,p)$ of finding an interfacial spin in class $i$.

### 4.3.3 Population of Interfacial Spin Classes

In order to explicitely calculate the probabilities $\Pi_i(T,p)$ we must introduce the two-body probability function $p(\delta,\epsilon)$, which yields the probability that a step variable in the interface takes a value $\delta$ and its right neighbor step variable takes a value $\epsilon$. Indeed, coming back to Fig. 4.1.a, we observe there that, for a fixed spin column, we know how many interfacial spins associated to this column belong to each spin class once we know the value of the left and right step variables associated to that interfacial spin column, $\delta$ and $\epsilon$ respectively. Thus, for instance, if we have a spin column where $\delta = +2$ and $\epsilon = -2$ (see column 5

| Notation | Configuration | Step variables | $p(\delta, \epsilon)$ |
|---|---|---|---|
| A | 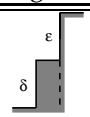  | $\delta > 0, \epsilon > 0$ | $[Y^{\delta+\epsilon} X_3^2 X_8 X_2^{\delta-1} X_9^{\epsilon-1}]/\mathcal{Q}$ |
| B |   | $\delta > 0, \epsilon = 0$ | $[Y^{\delta} X_2^{\delta-1} X_3^2]/\mathcal{Q}$ |
| C |   | $\delta > 0, \epsilon < 0$ | $[Y^{\delta+\epsilon} X_4^3 X_3^{2(\alpha-1)} X_2^{\lambda-\alpha}]/\mathcal{Q}$ |
| D |   | $\delta = 0, \epsilon > 0$ | $[Y^{\epsilon} X_8^2 X_9^{\epsilon-1}]/\mathcal{Q}$ |
| E |   | $\delta = 0, \epsilon = 0$ | $X_2/\mathcal{Q}$ |
| F |   | $\delta = 0, \epsilon < 0$ | $[Y^{\epsilon} X_3^2 X_2^{\lvert\epsilon\rvert-1}]/\mathcal{Q}$ |
| G | 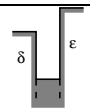  | $\delta < 0, \epsilon > 0$ | $[Y^{\delta+\epsilon} X_7^3 X_8^{2(\alpha-1)} X_9^{\lambda-\alpha}]/\mathcal{Q}$ |
| H |   | $\delta < 0, \epsilon = 0$ | $[Y^{\delta} X_8^2 X_9^{\lvert\delta\rvert-1}]/\mathcal{Q}$ |
| I | 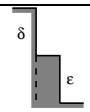  | $\delta < 0, \epsilon < 0$ | $[Y^{\delta+\epsilon} X_3^2 X_8 X_2^{\lvert\epsilon\rvert-1} X_9^{\lvert\delta\rvert-1}]/\mathcal{Q}$ |

Table 4.1: In this table we present the 9 different typical configurations of an interfacial spin column in the SOS approximation. These typical configurations are defined by the sign of the left step, $\delta$, and the sign of the right step, $\epsilon$. The first column shows the notation we use for each typical configuration. The second column shows a schematic graphical representation for each typical configuration. The third column presents the characteristic values of $\delta$ and $\epsilon$ for each case. Finally, the fourth column shows the two-body probability $p(\delta, \epsilon)$ of finding each typical configuration. Notice that $Y = e^{\gamma_p(\phi)}$ and $X_i = e^{-2J\beta_{eff}^{(i)}}$. In some cases we have to define $\alpha = \min(|\delta|, |\epsilon|)$ and $\lambda = \max(|\delta|, |\epsilon|)$.

in Fig. 4.1.a) we know that, given the total number $\delta = +2$ of interfacial spins associated to this column, there is one in class 4 and another one in class 3. On the other hand, if we have $\delta = -2$ and $\epsilon = +1$ (see column 6 in Fig. 4.1.a) we find only one interfacial spin associated to this column, and it belongs to class 2. In general, we have 9 different typical configurations for an interfacial spin column in the generalized SOS approximation, as shown in Table 4.1. These 9 typical configurations come from the possible sign combinations between $\delta$ and $\epsilon$, taking zero into account. Any interface in SOS approximation can be constructed from these 9 typical column configurations.

Let's assume for a while that we have one of the previous typical configurations with $\delta = +2$ y $\epsilon = +2$, as the one found in column 4 in Fig. 4.1.a. This configuration corresponds to a configuration type A (see Table 4.1). This spin column formed by up and down spins in contact with the interface and flanked by a step $\delta = +2$ to the left and a step $\epsilon = +2$ to the right is composed by one spin in class 2, one spin in class 3, one spin in class 8 and one spin in class 9. Therefore there are 5 broken bonds which define this interfacial column: one of these broken bonds belongs to the spin in class 2, two of them belong to the spin in class 3, another one belongs to the spin in class 8 and the last one belongs to the spin in class 9. The probabilistic weights associated to these broken bonds will be, respectively, $X_2$, $X_3^2$, $X_8$ y $X_9$. We assume now that the probability of finding this configuration will be $p(\delta = +2, \epsilon = +2) \propto Y^4 X_2 X_3^2 X_8 X_9$, where $Y = e^{\gamma_p(\phi)}$ is the factor associated to the thermodynamic parameter $\gamma_p(\phi)$, which fixes the average interface's slope. In general, for a configuration type A, we have,

$$p(\delta > 0, \epsilon > 0) = \frac{1}{\mathcal{Q}}[Y^{\delta+\epsilon} X_3^2 X_8 X_2^{\delta-1} X_9^{\epsilon-1}] \tag{4.22}$$

where $\mathcal{Q}$ is the associated normalization factor, which will be calculated later on.

Let's assume now that we have a configuration type C, with $\delta > 0$ and $\epsilon < 0$. If we define in this case $\alpha = \min(|\delta|, |\epsilon|)$ and $\lambda = \max(|\delta|, |\epsilon|)$, we have $\lambda$ interfacial spins associated to this spin column type C: $\lambda - \alpha$ of those interfacial spins are in class 2, each one with one associated broken bond, $\alpha - 1$ of those interfacial spins are in class 3, each one with two associated broken bonds, and finally one of those $\lambda$ interfacial spins belongs to class 4, and it has three broken bonds. Hence the probability $p(\delta, \epsilon)$ of finding an interfacial column with $\delta > 0$ and $\epsilon < 0$ is,

$$p(\delta > 0, \epsilon < 0) = \frac{1}{\mathcal{Q}}[Y^{\delta+\epsilon} X_4^3 X_3^{2(\alpha-1)} X_2^{\lambda-\alpha}] \tag{4.23}$$

In the same way we can build the probability $p(\delta, \epsilon)$ for the rest of typical configurations (see Table 4.1). In the limit where the nonequilibrium dynamic perturbation is zero, $p = 0$, i.e. for the equilibrium system, where the effective temperature $T_{eff}^{(i)}$ associated to class $i$ reduces to the usual temperature $T$, we have that $X_i(p = 0) = X$, so the two-body probability function reduces to $p(\delta, \epsilon) = p(\delta)p(\epsilon)$ for $p = 0$, being $p(x)$ the probability of finding a step variable of magnitude $x$ in the equilibrium SOS approximation, see eq. (4.8). The

two-body probability function $p(\delta, \epsilon)$ factorizes in the limit $p = 0$ as a consequence of the statistical independence of neighboring steps in the equilibrium SOS approximation. However, for $p \neq 0$, although the two-body probability function $p(\delta, \epsilon)$ is written as the product of the probabilistic weights for the different broken bonds associated to the different spin classes, $X_i$, such probability $p(\delta, \epsilon)$ includes nontrivial correlations, since the classes to which interfacial spins belong to depend strongly on the relative signs of $\delta$ and $\epsilon$. In this sense the use of $p(\delta, \epsilon)$ is beyond the SOS approximation for $p \neq 0$, where it is assumed no correlations between neighboring steps.

The normalization constant $\mathcal{Q}$ associated to the two-body probability function $p(\delta, \epsilon)$ can be calculated from the normalization condition,

$$\sum_{\delta,\epsilon=-\infty}^{+\infty} p(\delta, \epsilon) = 1 \tag{4.24}$$

The double sum in $\delta$ and $\epsilon$ must be divided depending on the sign of both step variables, $\delta < 0$, $\delta = 0$ and $\delta > 0$, and in the same way for $\epsilon$, yielding 9 different sums where the probabilities of each column configuration type enter (see Table 4.1). Taking into account the geometric sum, we obtain,

$$\begin{aligned}
\mathcal{Q} &= \frac{X_3^3 Y^2}{(1-X_2Y)^2} + 2\frac{X_3^2 Y}{1-X_2Y} + \frac{X_4^3}{(1-X_3^2X_2^{-1}Y^{-1})(1-X_2Y)} \\
&- \frac{X_4^3X_3^2X_2^{-1}Y^{-1}}{(1-X_3^2X_2^{-1}Y^{-1})(1-X_3^2)} + \frac{X_4^3X_2Y^{-1}}{(1-X_2Y^{-1})(1-X_3^2)} + X_2 \\
&+ 2\frac{X_3^2Y^{-1}}{1-X_2Y^{-1}} + \frac{X_4^3}{(1-X_3^2X_2^{-1}Y)(1-X_2Y^{-1})} + \frac{X_3^3Y^{-2}}{(1-X_2Y^{-1})^2} \\
&- \frac{X_4^3X_3^2X_2^{-1}Y}{(1-X_3^2X_2^{-1}Y)(1-X_3^2)} + \frac{X_4^3X_2Y}{(1-X_2Y)(1-X_3^2)}
\end{aligned} \tag{4.25}$$

where we remind that $X_2 = e^{-2J\beta_{eff}^{(2)}}$, $X_3 = e^{-2J\beta_{eff}^{(3)}}$, $X_4 = e^{-2J\beta_{eff}^{(4)}}$ and $Y = e^{\gamma_p(\phi)}$. In order to write the above formula we have taken into account that $X_9 = X_2$, $X_8 = X_3$ and $X_7 = X_4$.

Once we have calculated the two-body probability functions $p(\delta, \epsilon)$, it is easy to evaluate the probability $\Pi_i(T, p)$ of finding an interfacial spin in class $i$. We assume for an interface in the SOS approximation that the probability of finding an interfacial spin in class $i$ is equal to the probability of finding a spin of an interfacial spin column in class $i$. Assuming the last statement we neglect correlations between neighboring spin columns, following the Solid-On-Solid spirit. Therefore, the probability of finding an interfacial spin belonging to class $i \in [2, 4]$ is,

$$\Pi_i = \sum_{\delta,\epsilon=-\infty}^{+\infty} \pi_i(\delta, \epsilon) p(\delta, \epsilon) \tag{4.26}$$

where $\pi_i(\delta, \epsilon)$ is the probability of finding a spin belonging to class $i$ in an interfacial spin column characterized by the pair of steps $(\delta, \epsilon)$, and where we

| Notation | $n_2(\delta,\epsilon)$ | $n_3(\delta,\epsilon)$ | $n_4(\delta,\epsilon)$ | $N(\delta,\epsilon)$ |
|---|---|---|---|---|
| A | $\delta-1$ | 1 | 0 | $\delta$ |
| B | $\delta-1$ | 1 | 0 | $\delta$ |
| C | $\lambda-\alpha$ | $\alpha-1$ | 1 | $\lambda$ |
| D | 1 | 0 | 0 | 1 |
| E | 1 | 0 | 0 | 1 |
| F | $\lvert\epsilon\rvert-1$ | 1 | 0 | $\lvert\epsilon\rvert$ |
| G | 1 | 0 | 0 | 1 |
| H | 1 | 0 | 0 | 1 |
| I | $\lvert\epsilon\rvert-1$ | 1 | 0 | $\lvert\epsilon\rvert$ |

Table 4.2: In this table we show the populations $n_i(\delta,\epsilon)$ for each interfacial class, $i = 2,3,4$, for each one of the column configuration types summarized in Table 4.1. Thus, in the second column we write the number of spins in class 2 for each column configuration type, in the third column we write the number of spins in class 3, and in the fourth column, the number of spins in class 4. The last column shows the total number of interfacial (up) spins associated to each column configuration type, $N(\delta,\epsilon)$. The first column yields the notation for each type. Remember that $\alpha = \min(|\delta|,|\epsilon|)$ and $\lambda = \max(|\delta|,|\epsilon|)$.

have not written explicitely the dependence on temperature $T$ and nonequilibrium perturbation $p$. In general, we can write,

$$\pi_i(\delta,\epsilon) = \frac{n_i(\delta,\epsilon)}{N(\delta,\epsilon)} \tag{4.27}$$

$n_i(\delta,\epsilon)$ is the number of spins belonging to class $i$ in an interfacial spin column characterized by $(\delta,\epsilon)$, and $N(\delta,\epsilon)$ is the total number of interfacial spins associated to such spin column. Table 4.2 shows $n_i(\delta,\epsilon)$ and $N(\delta,\epsilon)$ for the different column configuration types. Thus, for instance, for a column type A with $\delta,\epsilon > 0$, we have $N(\delta > 0, \epsilon > 0) = \delta$ (up) interfacial spins, from which $\delta - 1$ belong to class 2, and one belongs to class 3. Hence, in this case, $\pi_2(\delta > 0, \epsilon > 0) = (\delta-1)/\delta$, $\pi_3(\delta > 0, \epsilon > 0) = 1/\delta$ and $\pi_4(\delta > 0, \epsilon > 0) = 0$. For a column type C, where $\delta > 0$ and $\epsilon < 0$, we must define the magnitudes $\alpha = \min(|\delta|,|\epsilon|)$ and $\lambda = \max(|\delta|,|\epsilon|)$. There are $\lambda$ (up) interfacial spins, from which $\lambda - \alpha$ belong to class 2, $\alpha - 1$ belong to class 3 and only one belongs to class 4. Therefore $\pi_2(\delta > 0, \epsilon < 0) = (\lambda-\alpha)/\lambda$, $\pi_3(\delta > 0, \epsilon < 0) = (\alpha-1)/\lambda$ and $\pi_4(\delta > 0, \epsilon < 0) = 1/\lambda$. The rest of probabilities $\pi_i(\delta,\epsilon)$ are defined in the same way from the different entries in Table 4.2.

In order to calculate the probabilities $\Pi_i(T,p)$ we must perform the sums involved in eq. (4.26). We need the classic results for the geometric sum and series to perform such sums, as well as some results derived from them taking into account the linear behavior of both the derivative and the Riemann

integral operators,

$$\sum_{k=0}^{\infty} x^k = \frac{1}{1-x} \quad , \quad |x| < 1 \tag{4.28}$$

$$\sum_{k=0}^{n} x^k = \frac{1-x^{n+1}}{1-x} \quad , \quad x \neq 1 \tag{4.29}$$

$$\sum_{k=1}^{\infty} \frac{x^k}{k} = \ln(\frac{1}{1-x}) \quad , \quad |x| < 1 \tag{4.30}$$

$$\sum_{k=1}^{n} \frac{x^k}{k} = \ln(\frac{1}{1-x}) - \int_0^x dy \frac{y^n}{1-y} \quad , \quad |x| < 1 \tag{4.31}$$

$$\sum_{k=1}^{\infty} kx^k = \frac{x}{(1-x)^2} \quad , \quad |x| < 1 \tag{4.32}$$

$$\sum_{k=1}^{n} kx^k = \frac{x(1-x^n)}{(1-x)^2} - \frac{nx^{n+1}}{1-x} \quad , \quad x \neq 1 \tag{4.33}$$

Using these equalities we find the desired results for the probabilities $\Pi_i(T,p)$. In particular, we obtain for $\Pi_2(T,p)$ the following result,

$$\begin{aligned}
\Pi_2 = \frac{1}{\mathcal{Q}}\Big\{ & \frac{X_3^3Y^2}{(1-X_2Y)^2} - \frac{X_3^3X_2^{-1}Y}{1-X_2Y}\ln\big(\frac{1}{1-X_2Y}\big) + \frac{X_3^2Y}{1-X_2Y} \\
- & \frac{X_3^2}{X_2}\ln\big(\frac{1}{1-X_2Y}\big) + \frac{X_4^3}{(1-X_3^2X_2^{-1}Y^{-1})(1-X_2Y)} \\
+ & \frac{X_4^3X_2^{-1}Y^{-1}}{(1-X_3^2X_2^{-1}Y^{-1})^2}\ln\big(\frac{1-X_2Y}{1-X_3^2}\big) - \frac{X_4^3X_2X_3^{-2}Y^{-1}}{1-X_2Y^{-1}} \\
+ & \frac{X_4^3X_2X_3^{-2}Y^{-1}}{(1-X_2Y^{-1})(1-X_3^2X_2^{-1}Y)} + \frac{X_3^2Y}{1-X_2Y} + X_2 \\
+ & \frac{X_4^3X_2^{-1}Y}{(1-X_3^2X_2^{-1}Y)^2}\ln\big(\frac{1-X_2Y^{-1}}{1-X_3^2}\big) + \frac{X_3^2Y^{-1}}{1-X_2Y^{-1}} \\
- & \frac{X_3^2}{X_2}\ln\big(\frac{1}{1-X_2Y^{-1}}\big) + \frac{X_4^3}{(1-X_3^2X_2^{-1}Y)(1-X_2Y^{-1})} \\
- & \frac{X_4^3X_3^2X_2^{-1}Y}{(1-X_3^2X_2^{-1}Y)(1-X_3^2)} + \frac{X_4^3X_2Y}{(1-X_2Y)(1-X_3^2)} \\
+ & \frac{X_3^2Y^{-1}}{1-X_2Y^{-1}} + \frac{X_3^3Y^{-2}}{(1-X_2Y^{-1})^2} - \frac{X_3^3X_2^{-1}Y^{-1}}{1-X_2Y^{-1}}\ln\big(\frac{1}{1-X_2Y^{-1}}\big)\Big\}
\end{aligned} \tag{4.34}$$

In the same way we can calculate $\Pi_4(T,p)$, obtaining,

$$\begin{aligned}\Pi_4 &= \frac{1}{\mathcal{Q}}\Big\{\frac{X_4^3X_2^{-1}Y^{-1}}{1-X_3^2X_2^{-1}Y^{-1}}\ln\big(\frac{1}{1-X_2Y}\big)-\frac{X_4^3X_2^{-1}Y^{-1}}{1-X_3^2X_2^{-1}Y^{-1}}\ln\big(\frac{1}{1-X_3^2}\big)\\ &+ \frac{X_4^3X_2^{-1}Y}{1-X_3^2X_2^{-1}Y}\ln\big(\frac{1}{1-X_2Y^{-1}}\big)-\frac{X_4^3X_3^{-2}}{1-X_3^2X_2^{-1}Y}\ln\big(\frac{1}{1-X_3^2}\big)\Big\} \qquad (4.35)\end{aligned}$$

In order to obtain $\Pi_3$ we only have to apply the normalization condition, eq. (4.19), which in this case implies $\Pi_3 = 1 - \Pi_2 - \Pi_4$. The details about the calculation of the probabilities $\Pi_i$ are exposed in Appendix B, where we write down in particular the detailed calculation for $\Pi_2$.

At this point we must notice that the probabilities $\Pi_i(T,p)$ depend in principle on the thermodynamic parameter $\gamma_p(\phi)$ (remember that $Y = e^{\gamma_p(\phi)}$), and via this parameter they implicitly depend on the average interface slope, $\tan\phi$. Hence we must use the notation $\Pi_i[T,p,\gamma_p(\phi)]$. On the other hand, this dependence was expected, since the interfacial spin distribution among the different classes strongly depends on the typical values of the step variables $\delta$ and $\epsilon$ for each column, and these values depend on the average interface slope. Hence $X_p$ will depend on the parameter $\gamma_p(\phi)$ due to the explicit dependence of $\Pi_i[T,p,\gamma_p(\phi)]$ on such parameter, and it will be impossible to extract the explicit relation between the thermodynamic parameter $\gamma_p(\phi)$ and the interface slope, $\tan\phi$, on the contrary to what happened in the equilibrium case, where we calculated this explicit relation through eq. (4.9). However, we need to know the properties of the interface, i.e. its microscopic structure, codified in the probability function $p_p(\delta)$, and its macroscopic structure, codified in the surface tension, $\sigma_{SOS}^{(p)}$, as a function of the angle $\phi$ formed between the interface and the $\hat{x}$ axis. This knowledge will give us the possibility of studying the properties and the shape of a spin droplet, which is one of the fundamental objects needed to write a nucleation theory for metastability (see next chapter). Therefore we must make an additional approximation at this stage. This approximation consists in assuming that the probabilities $\Pi_i$ of finding an interfacial spin belonging to class $i$ do not depend on the angle $\phi$ formed between the interface and the $\hat{x}$ axis. These probabilities $\Pi_i$ enter the definition of the statistical weight for an interfacial broken bond in the generalized SOS approximation, $X_p$. Thus we assume that the probabilities $\Pi_i$ are the ones we have obtained previously, see eqs. (4.34) and (4.35), particularized to an interface forming an angle $\phi = 0$ with the $\hat{x}$ axis. In this case we will have $Y = e^{\gamma_p(\phi)} = 1$ in the definition of the probabilities $\Pi_i$, so all the dependence on $\gamma_p(\phi)$ disappears inside $X_p$. The dependence on the interface slope enters the theory through the statistical weight $Y^{\gamma_p(\phi)\delta}$ that appears in the probability $p_p(\delta)$ of finding a step of size $\delta$ in the nonequilibrium interface, see eq. (4.20). In this way we build in a simple way a generalization of the original SOS approximation through the definition of a new probabilistic weight associated to an interfacial broken bond, $X_p$, which exclusively depends on the temperature $T$ and the nonequilibrium perturbation $p$. This generalized theory keeps the elegant and simple structure of the original SOS approximation.

## 4.4 Properties of the Nonequilibrium Interface

Once we have completed the generalization of SOS approximation to take into account the nonequilibrium character of our interface, the next step consists in verifying the predictions of this theory.

### 4.4.1 Interfacial Microscopic Structure

In a first step, we wonder about the interfacial microscopic structure. Here the extended theory predicts that the probability of finding a step in the interface with size $\delta$ is given by eq. (4.20), where $X_p$ is, as we know, the probabilistic weight associated to an interfacial broken bond. In order to check this prediction, we perform Monte Carlo simulations of the model interface, paying special attention to its microscopic structure. To do that we define the system on a rectangular lattice with shape $L_\perp \times L_\parallel$, where $L_\perp$ is the lattice size in the direction perpendicular to the interface, and $L_\parallel$ is the lattice size in the direction of the interface. The initial condition for the simulation consists in a stripe formed by up spins which completely filles the first $Ł_\perp/2$ rows of the system, and a second stripe formed by down spins filling the remainder of the system. In this way the initial configuration exhibits a linear interface in the $\hat{x}$ direction between a phase with spins up (bottom) and a phase with spins down (top). Boundary conditions are periodic in the direction of the interface, and open in the direction perpendicular to the interface. Thus spins in column 1, $(i, 1)$ with $i \in [1, L_\perp]$, have as left neighbors the corresponding spins in column $L_\parallel$, $(i, L_\parallel)$, and reversely. The open boundary conditions in the direction perpendicular to the interface involve that spins in the first row, $(1, j)$ with $j \in [1, L_\parallel]$, do not have down neighbors, and spins in the last row, $(L_\perp, j)$, do not have up neighbors.

In order to completely define the system to simulate, we must implement Glauber dynamics, previously defined in eq. (2.3). However we are only interested in computationally studying the interfacial structure. Thus we must eliminate the possible interaction between the interface and the fluctuations present in the bulk. Moreover, the Solid-On-Solid approximation (both the equilibrium one and our generalization) assumes that the interface does not interact with the bulk. Hence in order to properly compare the theoretical results with the computational ones we must suppress bulk dynamics, eliminating in this way the presence of bulk fluctuations. We can do that in practice making zero the transition rates for spins belonging to both spin classes 1 and 10, which are the spins that initially form the bulk. In this way the bulk remains frozen, fluctuation-free during the whole simulation process, thus preventing the interference of bulk fluctuations on the interface properties. However, we can wonder about the effect that these bulk fluctuations involve on interfacial properties. In order to investigate this effect, we have also simulated the interface using the *full* Glauber dynamics, i.e. including bulk dynamics. We observe that bulk fluctuations are not relevant for the interfacial properties as far as we are well below the critical temperature, where fluctuations of all scales appear in the system. Since we are interested in the properties of the interface at tem-

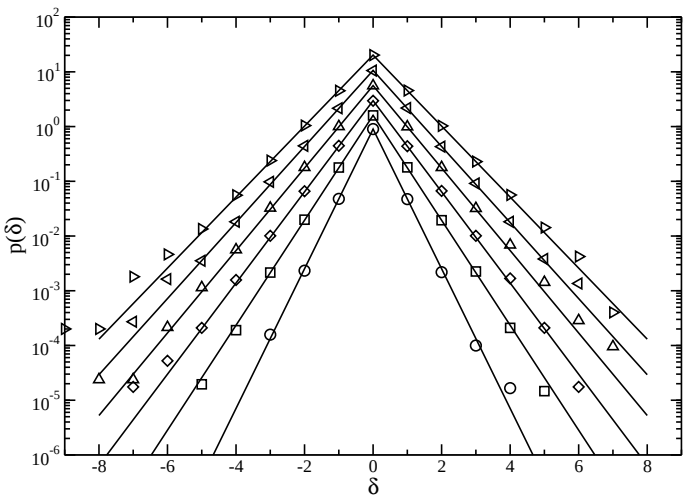


Figure 4.3: Probability of finding in the interface a step with size $\delta$, $p_p(\delta)$, for a system size $L_\perp \times L_\parallel = 128 \times 256$ at temperature $T = 0.3T_{ons}$ and several different values of the nonequilibrium perturbation $p$. Namely, from bottom to top, $p = 0, 0.01, 0.02, 0.03, 0.04$ and $0.05$. For the shake of clarity the curves has been shifted a factor $2^i$, $i \in [0, 5]$ in the vertical direction, where $i = 100 \times p$.

peratures far away the critical one, $T_c(p)$, the suppression of bulk dynamics will not influence our results for the interface.

For the fixed initial condition, and using the *trunked* Glauber dynamics, the system rapidly evolves from the initial state with a completely flat interface towards a stationary state characterized by a rough non-trivial interface configuration. Such configuration is defined by the step variables vector $\delta = \{\delta_i, i = 1, L_\parallel\}$[3], where $\delta_i = y_i - y_{i-1}$, being $y_i$ the height of the interface for the spin column $i$. In order to measure the probability $p_p(\delta)$ we wait until the interface reaches the steady state. For a fixed interfacial configuration we measure the step sizes $\delta_i$ using an algorithm for microscopic interfacial recognition[65]. From those values $\delta_i$ we accumulate the histogram $p_p(\delta)$. However, as opposed to the SOS approximation, the real model shows correlations between close steps, parameterized by certain typical correlation length $\xi$. In order to build the histogram $p_p(\delta)$ we must use statistically independent measures of the step variable $\delta$. Therefore for a fixed interfacial configuration we measure step variables separated by a distance larger that $\xi$, so in this way we ensure the statistical independence of measures. In our case we sample the interfacial configuration extracting measures of $\delta$ separated by a distance $2\xi$. In order to accumulate enough statistics we let the system evolve in time,

[3]When we characterize an interfacial configuration in the real system via the step variables vector $\delta$ we are neglecting the presence of overhangs (see Fig. 4.1.b) in this interface. In fact it is observed that the presence of overhangs in the interface affects very weakly its properties, at least for temperatures well below the critical one.

repeating the histogram measurement process for $p_p(\delta)$ at time intervals $\Delta t$ larger than the typical correlation time in the interface (again, in order to ensure statistical independence of data). The results of such measurements are shown in Fig. 4.3, where we observe the probability of finding a step with size $\delta$ in the interface, $p_p(\delta)$, for a system size $L_\perp \times L_\parallel = 128 \times 256$ and a temperature $T = 0.3T_{ons}$ with different values of $p \in [0, 0.05]$. The interface we have studied was parallel to the $\hat{x}$ axis, so $\phi = 0$. As we can observe in this figure, the distribution $p_p(\delta)$ is a decreasing exponential of $|\delta|$. Furthermore, as we increase the nonequilibrium parameter $p$, the probability of finding larger step sizes increases, as expected. Fig. 4.3 also shows, for comparison, the theoretical prediction based on the generalized SOS approximation for $p_p(\delta)$, eq. (4.20) (notice that here we have $Y = 1$ because $\phi = 0$). As we see, the agreement between theory and simulations is nearly perfect for all studied values of $p$. This agreement points out that the generalized SOS approximation, based on the concept of effective temperature, correctly reproduces the microscopic features of the interface subject to nonequilibrium conditions. We have also studied the microscopic properties of the interface for other temperature values below the critical temperature, $T_c(p)$, always finding a very good agreement between theory and simulations. On the other hand, we have investigated the differences that the presence of overhangs and the interaction between the interface and the bulk induce in our computational results. We conclude that, as far as we are well below the critical region, the extended SOS approximation describes very well the observed real interface structure (including overhangs and bulk dynamics).

### 4.4.2 Interfacial Macroscopic Properties

We next pay attention to the macroscopic properties of the interface, codified in the surface tension, $\sigma^{(p)}_{SOS}(\phi; T, p)$. Fig. 4.4 shows $\sigma^{(p)}_{SOS}(\phi = 0; T, p)$, as defined in eq. (4.21), as a function of temperature for different values of the nonequilibrium parameter $p$. These curves show the theoretical prediction for the surface tension in the real system. The first conclusion derived from this figure is the fundamental difference between the surface tension for the equilibrium system ($p = 0$) and that for the nonequilibrium system ($p \neq 0$) in the low temperature limit. We can observe in Fig. 4.4 that for $p = 0$ the surface tension grows monotonously as temperature decreases, converging towards 2 in the low temperature limit. However, for any $p \neq 0$ we observe that the surface tension exhibits a maximum for certain temperature, $T_{max}$. For $T < T_{max}$ the surface tension decreases as temperature decreases, while for $T > T_{max}$ the surface tension increases as temperature decreases. Moreover, $\sigma^{(p)}_{SOS}(\phi = 0; T, p)$ linearly converges towards 0 in the limit $T \to 0$ for $p \neq 0$. As we will see in the next chapter, this fundamental difference in the macroscopic properties of the interface will involve very important differences in the properties of metastable states in the nonequilibrium system as compared to the equilibrium one in the low temperature region.

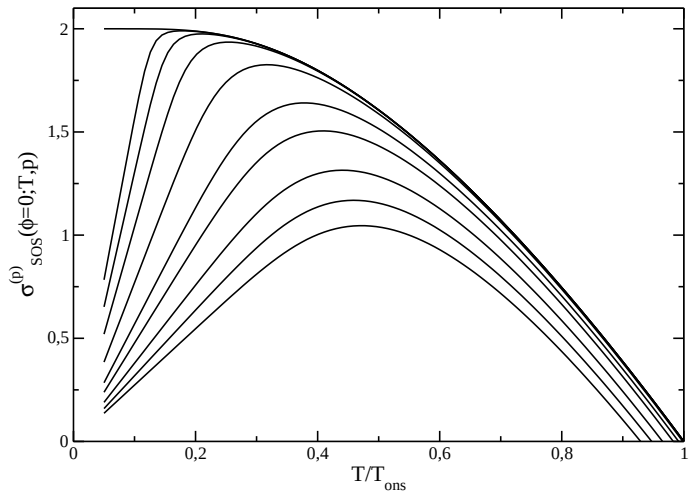


Figure 4.4: Surface tension $\sigma^{(p)}_{SOS}(\phi = 0; T, p)$ as a function of temperature for different values of $p$, as derived from the generalized SOS approximation for an interface parallel to the $\hat{x}$ axis. In particular, from top to bottom, $p = 0$, $10^{-6}$, $10^{-5}$, $10^{-4}$, $10^{-3}$, $5 \times 10^{-3}$, $10^{-2}$, $2 \times 10^{-2}$, $3 \times 10^{-2}$ and $4 \times 10^{-2}$. Notice that for any $p \neq 0$ the surface tension shows a maximum for certain temperature, and it converges towards zero for smaller temperatures.

Let's rewrite $X_p$ in order to understand why this unexpected behavior emerges for the nonequilibrium system. As we know, $X_p$ is the statistical weight associated to a interfacial broken bond in the generalized SOS approximation. In the limit $p = 0$, the weight $X_p$ converges to $X = e^{-2J\beta}$, where $\beta$ is the system's inverse temperature. Comparatively, for $p \neq 0$ we can write $X_p$ as,

$$X_p \equiv e^{-2J\beta^I_{eff}} \tag{4.36}$$

where $\beta^I_{eff} \equiv 1/T^I_{eff}$. The previous equation defines the interface effective temperature, $T^I_{eff}$. In some sense this interface effective temperature yields the average of the effective temperatures associated to the different spin classes in the interface, taking into account the classes relative populations. In the limit $p = 0$ it is evident that the interface effective temperature, $T^I_{eff}$, reduces to the usual temperature, $T$. However, for any $p \neq 0$ both temperatures defer. Fig. 4.5 shows the interface effective temperature, as defined in eq. (4.36), as a function of $T$ for different values of $p$. The behavior of $T^I_{eff}(T)$ shown in Fig. 4.5 helps us to understand the novel behavior of surface tension for low temperatures in the nonequilibrium model. First we observe that for a fixed value of $p$ the relation between $T^I_{eff}$ and $T$ is linear for high temperatures. That is, in the high temperature limit, where the thermal noise ($T$) dominates over the non-thermal noise ($p$), the interface effective temperature is completely coupled to the system's temperature. In this limit the effect induced by $p$ reduces to a slight increase of the interface effective temperature as compared to the system's temperature.

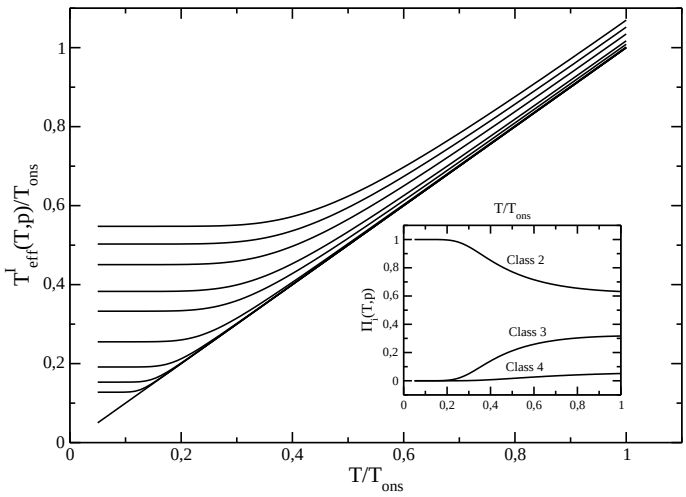


Figure 4.5: The main plot shows the interface effective temperature, $T^I_{eff}$, obtained from our generalized SOS approximation, as a function of system's temperature, $T$, for varying $p$. From bottom to top $p = 0, 10^{-6}, 10^{-5}, 10^{-4}, 10^{-3}, 5\times10^{-3}, 10^{-2}, 2\times10^{-2}, 3\times10^{-2}$ and $4\times10^{-2}$. The inset shows the probabilities $\Pi_i(T,p)$ of finding an interfacial spin belonging to class $i$ as a function of temperature for $p = 0.01$. Notice that for low temperatures almost all spins belong to class 2.

However, in the low temperature limit the noise with non-thermal origin dominates, so the interface effective temperature $T^I_{eff}$ completely decouples from the system's thermodynamic temperature, $T$, converging to a constant nonzero value, see Fig. 4.5. This low temperature limit for the interface effective temperature can be easily calculated, taking into account that, as shown in the inset of Fig. 4.5, almost all interfacial spins belong to class 2 in this limit and for moderate values of $p$. Therefore $T^I_{eff}$ converges towards $T^{(2)}_{eff}(T=0)$ in the limit $T \to 0$, where $T^{(2)}_{eff}(T=0)$ is the effective temperature associated to class 2 for $T = 0$. Hence,

$$\lim_{T\to 0} T^I_{eff}(T,p) \approx T^{(2)}_{eff}(T=0,p) = \frac{-4}{\ln(p)} > 0 \tag{4.37}$$

Thus the interface suffers a nonzero effective temperature, independent of $T$, at low temperatures due to the non-thermal noise. Hence the statistical weight $X_p$ converges to a nonzero and constant value for $T \to 0$, so the surface tension, which is directly proportional to $T$, converges linearly towards zero in this limit.

The next logical step should be the measurement of surface tension in Monte Carlo simulations for the interface of the discrete model, in order to compare these computational results with the theoretical predictions. However, we do not know how to define in the system a thermodynamic potential as the surface tension from the microscopic point of view, because the system is out of

equilibrium. Moreover, if we could microscopically define such potential, we still would have to face the additional problem of its explicit measurement. This problem comes from the need of a dense sampling of the complete system's phase space in order to obtain a reliable measurement of surface tension. The system presents many degrees of freedom, so its phase space is incredibly huge. Therefore any feasible Monte Carlo simulation only samples a small region of this phase space, which implies an incorrect measurement of surface tension[4]. As an alternative option, we can evaluate physical observables easy to define and measure from the microscopic point of view, which have a direct and simple relation with surface tension. This is the case for the size of the critical droplet appearing when studying the problem of metastability in the ferromagnetic nonequilibrium system. As we explained in previous sections, when the system is in a metastable state (for instance, a state with positive magnetization in the ordered phase subject to a weak negative magnetic field) it eventually evolves from the metastable phase towards the truly stable state. This transition proceeds through the nucleation of a droplet of the stable phase in the metastable bulk. Small stable phase droplets tend to disappear, while large enough droplets tend to grow. There is a critical size separating both tendencies, which is the critical droplet size. The critical droplet controls the demagnetization process. Generalizing the results obtained for equilibrium systems, we observe (see next chapter) that the critical droplet size is proportional to the surface tension in the model for zero magnetic field. Thus, measuring the critical droplet size and comparing these measurements with the predictions based on the generalized SOS approximation result for the surface tension, $\sigma^{(p)}_{SOS}(\phi = 0; T, p)$, we will be able to quantify in an indirect way the agreement between the prediction for the nonequilibrium surface tension and this observable in the real system. Fig. 5.2 in next chapter shows the computational results for the critical droplet size as a function of temperature for different values of $p$, and the corresponding theoretical predictions based on the surface tension $\sigma^{(p)}_{SOS}(\phi = 0; T, p)$. As we can see in this figure, the agreement between theory and simulations is rather good. Apart from the quantitative agreement, which is very good taking into account the approximate character of the theory, it is remarkable that the predictions perfectly reproduce the existence of a maximum in the critical droplet size as a function of temperature for any $p \neq 0$. This maximum is directly related to the maximum observed for the surface tension in the nonequilibrium model.

Therefore we conclude that, from both the microscopic -$p_p(\delta)$- and the macroscopic -$\sigma^{(p)}_{SOS}(\phi; T, p)$- point of view, the generalized SOS approximation that we have derived in this chapter for the interface in the nonequilibrium magnetic system correctly explains the properties of such interface, both qualitatively and quantitatively. This agreement between theory and simulations will allow us to deduce in the next section some properties for a spin droplet. These properties will be very useful when trying to study and understand the dy-

[4]Nowadays there are some methods which allow to calculate thermodynamic potentials as the free energy of a complex system.[66]

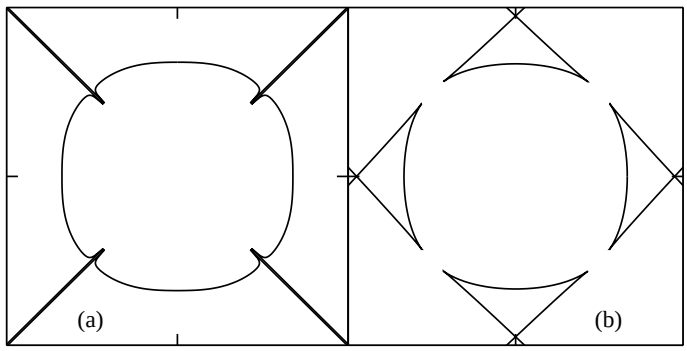


Figure 4.6: (a) Polar plot of the surface tension as obtained in the generalized SOS approximation, $\sigma^{(p)}_{SOS}(\phi)$, for temperature $T = 0.3T_{ons}$ and $p = 0.01$. Notice the underlying symmetry of surface tension, and the presence of singularities for angles $\phi = (2n+1)\pi/4$, with $n = 0, \ldots, 3$; (b) Polar plot of the droplet radius $R(\theta)$ derived from the surface tension plotted in (a) using the Wulff construction. The singularities in $\sigma^{(p)}_{SOS}(\phi)$ involve angular regions where $R(\theta)$ is not defined.

namic properties of metastable states in the ferromagnetic nonequilibrium system.

## 4.5 Shape and Form Factor of a Spin Droplet using Wulff Construction

In the previous section we have developed a theoretical approximation, based on the Solid-On-Solid approximation by Burton, Cabrera and Frank[59]. It has allowed us to calculate the surface tension associated to the interface in the ferromagnetic system under nonequilibrium conditions. In this section we want to use the results obtained in the previous section in order to calculate the shape of a spin droplet and the associated form factor.

### 4.5.1 The Wulff Construction

As we have stated above several times, the process of demagnetization from a metastable state in our system takes place through the nucleation of one or several droplets of the stable phase in the metastable bulk. In order to understand and analyze the nucleation and consequent growth of these droplets we need to know in detail their shape. In general, the equilibrium shape of these droplets is determined by minimization of the associated total surface tension for a fixed volume. For isotropic systems this process yields a droplet with spherical shape (circular in two dimensions). However, when the surface tension depends, as in our case, on the orientation of the interface with respect to certain privileged axis, the shape of the droplet will adjust to take advan-

tage of the low free energy cost of certain interface orientations, and this shape will minimize interface orientations with high free energy cost. This mechanism gives rise to droplets with typical crystal-like shape, which will depend on temperature and other system parameters.[67]

In our case we know the surface tension $\sigma^{(p)}_{SOS}(\phi)$ for all possible interface orientations, parameterized by the angle $\phi$. Hence the Wulff construction[68] will allow us to obtain the equilibrium droplet shape. This construction can be summarized as follows: through each point of the polar curve $\sigma^{(p)}_{SOS}(\phi)$, with $\phi \in [0, 2\pi]$, we draw a line perpendicular to the radius linking such point with the center. The interior envelope of all these perpendicular lines determines $R(\theta)$, which is the droplet radius in polar coordinates. Mathematically speaking, the equilibrium shape $R(\theta)$ can be calculated parametrically[69],

$$\begin{aligned} R(\theta) &= R_0\sqrt{x^2(\phi) + y^2(\phi)} \\ x(\phi) &= (\cos\phi)\sigma^{(p)}_{SOS}(\phi) - (\sin\phi)\frac{d\sigma^{(p)}_{SOS}(\phi)}{d\phi} \\ y(\phi) &= (\sin\phi)\sigma^{(p)}_{SOS}(\phi) + (\cos\phi)\frac{d\sigma^{(p)}_{SOS}(\phi)}{d\phi} \\ \tan\theta &= \frac{y(\phi)}{x(\phi)} \end{aligned} \tag{4.38}$$

where $R_0$ is just a constant that fixes the droplet radius, and $\sigma^{(p)}_{SOS}(\phi)$ is the surface tension derived from the SOS approximation generalized to the nonequilibrium case, eq. (4.21). In fact, in order to define the surface tension $\sigma^{(p)}_{SOS}(\phi)$ for angles outside the interval $\phi \in [-\pi/4, \pi/4]$ we use the symmetry that $\sigma^{(p)}_{SOS}(\phi)$ exhibits. As we previously discussed, in order to study the surface tension of an interface forming an angle $|\phi| > \pi/4$ with the $\hat{x}$ axis, it is convenient to change the reference axis to be the $\hat{y}$ axis. Thus if we suppose for instance that $\pi/4 < \phi < \pi/2$, we have that $\sigma^{(p)}_{SOS}(\phi) = \sigma^{(p)}_{SOS}(\pi/2 - \phi)$, where now $0 < \pi/2 - \phi < \pi/4$. In the same way we can extend using equivalent symmetry arguments the definition of $\sigma^{(p)}_{SOS}(\phi)$ to the whole circumference, $\phi \in [0, 2\pi]$.

The surface tension $\sigma^{(p)}_{SOS}(\phi)$, as defined in the generalized SOS approximation, eq. (4.21), and once extended by symmetry over the whole circumference, has a fundamental problem, because it is singular for angles $\phi = (2n+1)\pi/4$, with $n = 0, \ldots, 3$. Fig. 4.6.a shows a polar plot of $\sigma^{(p)}_{SOS}(\phi)$ for temperature $T = 0.3T_{ons}$ and $p = 0.01$. In this figure we observe the aforementioned singularities. These singularities found in $\sigma^{(p)}_{SOS}(\phi)$ induce the appearance of angular regions where the droplet radius, $R(\theta)$, obtained from the Wulff construction, eqs. (4.38), is not defined, see Fig. 4.6.b. These undefined regions in $R(\theta)$ constitute an important objection in our investigation, because one of the principal aims in this section consists in calculating the so-called form factor, $\Omega_d(T, p)$, which is the constant that relates the droplet radius $\mathcal{R}$ (to be defined later on)

and the droplet volume. Thus $V = \Omega_d(T, p)\mathcal{R}^d$, where $d$ is the system dimension. The so-defined form factor is an important magnitude in order to write a nucleation theory which correctly describes the dynamics of the nonequilibrium metastable-stable transition. To calculate $\Omega_d(T, p)$ we need to evaluate the droplet shape, parameterized by $R(\theta)$, for all values of $\theta$. Hence we must regularize in some sense the function $R(\theta)$ obtained from the generalized SOS approximation, in order to define this function over the whole circumference.

### 4.5.2 Analytic Continuation of the Radial Function

In order to regularize $R(\theta)$ in the undefined angular regions, we propose an analytical continuation of the radial function $R(\theta)$ inside such regions. We denote this analytical continuation as $R^{(c)}(\theta)$. In particular, we analytically continue the radial function using a second order polynomial, $R^{(c)}(\theta) = a\theta^2 + b\theta + c$. In order to fix the three free coefficients in this polynomial we need three different conditions for it. In a first step, we notice that the angular symmetry that surface tension exhibits is inherited by the radial function $R(\theta)$, as can be observed in Fig. 4.6. This symmetry implies that the analytical continuation of the radial function must fulfill,

$$\frac{dR^{(c)}(\theta)}{d\theta}|_{\theta=\pi/4} = 0 \tag{4.39}$$

since we expect that $R^{(c)}(\pi/4 + \epsilon) = R^{(c)}(\pi/4 - \epsilon)$. This equation provides the first condition on $R^{(c)}(\theta)$. The other two conditions are obtained requiring continuity and analyticity to the analytic continuation. Hence, if $\theta^*$ is the angle where the connection between the radial function $R(\theta)$ and its analytical continuation $R^{(c)}(\theta)$ takes place, the continuity and analyticity conditions reduce respectively to,

$$R^{(c)}(\theta)|_{\theta=\theta^*} = R(\theta)|_{\theta=\theta^*} \tag{4.40}$$

$$\frac{dR^{(c)}(\theta)}{d\theta}|_{\theta=\theta^*} = \frac{dR(\theta)}{d\theta}|_{\theta=\theta^*} \tag{4.41}$$

Using these three conditions we are able to obtain the coefficients $a$, $b$ and $c$ which appear in the definition of the analytical continuation $R^{(c)}(\theta)$ as a function of the connection angle $\theta^*$ and the values that $R(\theta)$ and its derivative take for such connection angle. The only remaining problem is the determination of $\theta^*$. However, it is easy to solve such problem, because the nature of the singularity in the surface tension is such that it gives rise to a discontinuous change in the derivative of $R(\theta)$ for certain angle $\theta^*$, as observed in Fig. 4.6.b. This angle $\theta^*$ where the derivative of $R(\theta)$ is discontinuous signals the angle where the undefined region for $R(\theta)$ begins. Therefore we define this angle (see Fig. 4.6.b) as the connection angle $\theta^*$. This connection angle can be calculated numerically in a simple way[5]. In this way we are able to continue analytically

[5]For high temperatures, the influence of the singularity appearing for the surface tension ex-

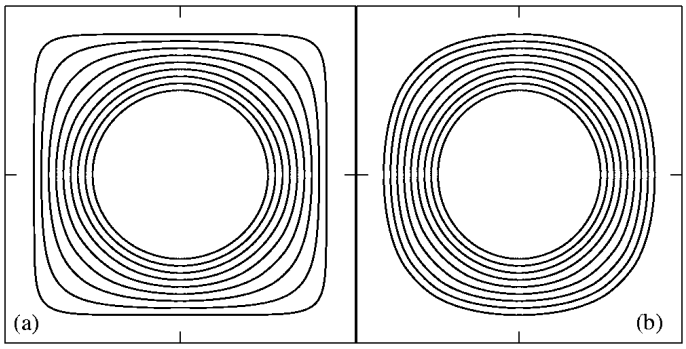


Figure 4.7: (a) Shape of a spin droplet for the equilibrium system ($p = 0$), and several different temperatures. In particular, from outside to inside, $T/T_{ons} = 0.1$, $0.2$, $0.3$, $0.4$, $0.5$, $0.6$, $0.7$, $0.8$ and $0.9$. For the shake of clarity we have rescaled the droplet radius depending on temperature; (b) The same than in (a), but for the nonequilibrium model, with $p = 0.01$.

the radial function $R(\theta)$ in a safe manner. We only have to apply the analytical continuation once, inside the angular interval $\theta \in [0, \pi/4]$, due to the angular symmetry exhibited by the radial function (inherited from the angular symmetry shown by the surface tension). The remainder of the analytically extended angular function is defined by symmetry taking as starting point this small angular interval.

Using this analytical continuation technique we obtain the shape of a spin droplet for the nonequilibrium ferromagnetic model. Fig. 4.7 shows the shape of such droplet for different temperatures, for an equilibrium system (with $p = 0$) and for a nonequilibrium one, with $p = 0.01$. We observe for $p = 0$ that the shape of the droplet tends to be a square at low temperatures, while for high temperatures we recover the circular shape associated to a bidimensional isotropic system. Thus for high temperatures the observed differences in the surface tension for different orientations are very small as compared to thermal energy, so in practice the interface does not feel the existence of privileged interface orientations. This process gives rise to the observed isotropy. On the contrary, for low temperatures, the differences observed in the surface tension for different interface orientations are very important as compared to thermal energy, so interface orientations not parallel to the privileged axes are highly punished. An important detail is that for temperatures of the order of $T = 0.5T_{ons}$ the spin droplet shape is already almost circular for $p = 0$. This property points out that effective isotropy appears at not very high tempera-

tends to certain interval around it. Hence the radial function feels the singularity before it reaches the angular undefined region. In these cases we can get rid of the region where $R(\theta)$ *feels* the singularity by performing the analytical continuation for a connection angle previous to the angle defined by the discontinuous change in the derivative of $R(\theta)$. This new connection angle is detected looking for the angle where the angular derivative of $R(\theta)$ becomes negative, since such condition points out that the effect of the singularity is becoming relevant.

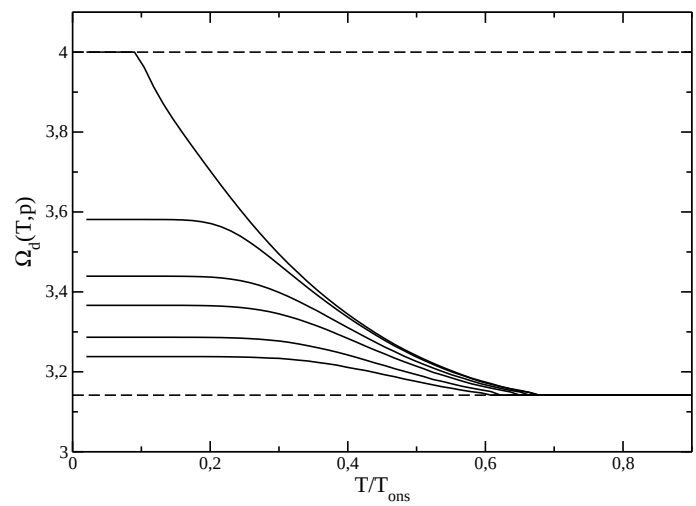


Figure 4.8: Form factor $\Omega_d(T,p)$ as a function of temperature for different values of $p$. In particular, from top to bottom, $p = 0$, $0.001$, $0.005$, $0.01$, $0.02$ and $0.03$. The upper dotted line signals $\Omega_d = 4$, while the lower dotted line signals $\Omega_d = \pi$.

tures. Fig. 4.7.b shows the shape of a spin droplet for different temperatures, but now for the nonequilibrium system with $p = 0.01$. Equivalently to what we observed in the equilibrium system ($p = 0$), the droplet for high enough temperatures takes circular (isotropic) shape. However, for low temperatures we observe that its shape converges towards an intermediate structure between a circle and a square, where the underlying lattice anisotropy is reflected only partially. In order to understand this difference between the equilibrium system ($p = 0$) and the nonequilibrium one ($p \neq 0$) we must recall the concept of interface effective temperature, $T^I_{eff}(T,p)$, see eq. (4.36). In the previous section we observed that for $p \neq 0$ the interface effective temperature converged towards a nonzero value in the limit $T \to 0$, see Fig. 4.5. Therefore, taking into account this interface effective temperature picture, we would expect that in this low temperature limit for $p \neq 0$ the shape of the droplet should not depend on system's temperature. Instead we would expect this shape to converge towards a structure similar to that observed in the equilibrium system for a temperature approximately equal to the interface effective temperature. This is so because the shape of the droplet is exclusively defined by the interfacial properties. In fact, such independence of the shape of the droplet on system's temperature is what we exactly observe for low temperatures, see Fig. 4.7.b.

### 4.5.3 Droplet Form Factor

Our last objective in this section consists in calculating the form factor, $\Omega_d(T,p)$, which relates the droplet radius, $\mathcal{R}$, with its volume, $V = \Omega_d(T,p)\mathcal{R}^d$. In order to calculate $\Omega_d(T,p)$ we need to precisely define the droplet radius, $\mathcal{R}$,

which is a typical length scale which characterizes the droplet size. In this case we choose the droplet radius $\mathcal{R}$ to be the radial function $R(\theta)$ for $\theta = 0$, i.e. $\mathcal{R} \equiv R(\theta = 0)$. In this way in the high temperature limit, where the droplet is circular, the droplet radius $\mathcal{R}$ will coincide with the circle radius, while in the low temperature limit, where the droplet is a square (for $p = 0$), the radius $\mathcal{R}$ will be $\ell/2$, where $\ell$ is the square side. The droplet volume is defined by the following radial integral for a bidimensional system,

$$V = \Omega_d(T, p)\mathcal{R}^d = 8\int_0^{\pi/4} d\theta \int_0^{R(\theta)} r dr \tag{4.42}$$

so the form factor is calculated from,

$$\Omega_d(T, p) = 4\int_0^{\pi/4} d\theta \left[\frac{R(\theta)}{R(0)}\right]^2 \tag{4.43}$$

Numerically solving the previous integral using the analytically extended radial function we obtain the results plotted in Fig. 4.8. In this figure we show the form factor $\Omega_d(T, p)$ as a function of temperature for different values of $p$. For $p = 0$ the form factor smoothly evolves from $\Omega_d = 4$ for low temperatures to $\Omega_d = \pi$ for high temperatures. The value $\Omega_d = 4$ is typical of square droplets, where $V = 4 \times (\ell/2)^2 = \ell^2$. On the other hand, the value $\Omega_d = \pi$ is typical of circular droplets, where $V = \pi\mathcal{R}^2$. As we see in Fig. 4.8, for $p \neq 0$ the form factor for low temperature converges towards a value smaller than 4. This fact confirms the above phenomenologic observation, deduced from the droplet shape for $p \neq 0$. The results derived in this section, and in particular those related to the form factor $\Omega_d(T, p)$, will be be very useful in the next chapter, where we will formulate a nucleation theory to explain the dynamics of the metastable-stable transition in the ferromagnetic system subject to nonequilibrium conditions.

## 4.6 Conclusion

In this chapter we have studied both theoretically and computationally the microscopic and macroscopic properties of an interface in the nonequilibrium model. In order to do so we have generalized the SOS approximation first introduced by Burton, Cabrera and Frank[59] for a discrete interface in an equilibrium spin system.

This theoretical approximation for the equilibrium system describes the structure of the interface from a microscopic point of view using three basic hypothesis. On one hand, it neglects the presence of overhangs in the interface. Moreover, the approximation does not take into account the possible interactions between the interface and bulk fluctuations. Finally, it assumes that the different step variables defining the interface are uncorrelated. In spite of these three hypothesis, the SOS approximation for the equilibrium system correctly predicts the microscopic and macroscopic interfacial structure. In particular, it

predicts a surface tension for the equilibrium system which coincides with the known exact result obtained for the two dimensional Ising model for an angle $\phi = 0$, and it is a very good approximation for nonzero angles.

The generalized SOS approximation for $p \neq 0$ is based on the concept of *effective temperature*. That is, the effect induced by the nonequilibrium perturbation $p$ on the system can be re-interpreted in terms of an effective temperature. We calculate that the higher is the order to which a spin is subject (i.e. the larger is the number of neighboring spins pointing in the same direction that the given spin), the higher is the effective temperature this spin suffers for $p \neq 0$. The interface is composed by spins belonging to different classes (i.e. spins subject to different degrees of order), which, consistently, suffer different effective temperatures. The central magnitude in the equilibrium SOS approximation is the probabilistic weight or Boltzmann factor associated to an interfacial broken bond, $X = e^{-2J\beta}$. In order to build the SOS approximation for $p \neq 0$ we generalize this statistical weight, denoted now as $X_p$, taking into account the effective temperature of the different spin classes. To do that we perform an average over the statistical weights associated to the different spin classes (each class having its own well defined effective temperature) using in this average the population densities for each interfacial spin class. We have calculated these population densities using two-body probability functions.

We obtain from this generalization predictions for the microscopic structure of the interface . These predictions are codified in the probability function $p_p(\delta)$, which is the probability of finding a step of size $\delta$ in the nonequilibrium interface. The comparison between the theoretical prediction for $p_p(\delta)$ and Monte Carlo results for the real system is excellent. This agreement supports the validity of our approach for $p \neq 0$.

On the other hand, we obtain the surface tension of the interface for $p \neq 0$ using the extended theory. This surface tension exhibits an unexpected behavior for the nonequilibrium system as compared to the equilibrium one. In particular, we observe that, while the equilibrium surface tension monotonously increases as we decrease temperature, for the nonequilibrium model the surface tension $\sigma_{SOS}^{(p)}$ shows a maximum for certain temperature, converging linearly towards zero for lower temperature. In order to understand this behavior it is necessary to turn again to the concept of effective temperature. Thus we can define a global effective temperature for the interface. We observe for $p \neq 0$ that, while for high temperatures the interface effective temperature, $T_{eff}^{I}$, is totally coupled to the system's temperature, in the $T \to 0$ limit $T_{eff}^{I}$ completely decouples from $T$, converging towards a constant, nonzero value, which involves that surface tension converges towards zero for at low temperature for $p \neq 0$. Unfortunately, we cannot check this result through direct simulations for the surface tension. However, as we will describe in the next chapter, there are certain observables, as the critical droplet size (to be defined later on), which are directly related to the surface tension. As we will see, the theoretical predictions derived for this observable, based on the results for the surface tension of the nonequilibrium interface, $p \neq 0$, nicely reproduce the

measurements obtained via Monte Carlo simulations. The unexpected behavior of the surface tension for $p \neq 0$ will be crucial for the properties of the metastable-stable transition, to be discussed in next chapter.

Finally, we have obtained the shape of a spin droplet in the nonequilibrium system from the surface tension we have derived in the generalized SOS approximation, using the Wulff construction[68]. On one hand, we observe that for the equilibrium model the droplet shape varies continuously from a square at low temperatures to a circle at high temperatures. On the contrary, for the nonequilibrium system we obtain a droplet shape that, although it is circular for high temperature, in the low temperature limit it converges towards an intermediate shape which is not a square, but partially exhibits the anisotropy inherited from the underlying lattice. We have numerically calculated the form factor $\Omega_d$ associated to the droplet, confirming that while for $p = 0$ the form factor varies from $\Omega_d = 4$ to $\Omega_d = \pi$, for $p \neq 0$ the form factor converges towards a constant value $\Omega_d \in (\pi, 4)$ for low temperatures.

The results obtained in this chapter on the effect of the nonequilibrium conditions on the interfacial properties are not only relevant for the study of metastability, but they are also important for the study of many systems where one of the fundamental ingredients consists in a nonequilibrium interface.

# Chapter 5

# Nucleation Theory for the Study of Metastability

## 5.1 Introduction

In this chapter we want to extend the nucleation theory, already developed for equilibrium spin systems[26, 71], to our nonequilibrium system subject to a magnetic field. Nucleation theory explains in a detailed way the (highly inhomogeneous) processes which make a ferromagnetic system to evolve from a metastable state to the corresponding stable state. This theory is based on the concepts of stable phase spin droplet and free energy cost of such droplet. In this chapter we will present in a first step the nucleation theory, as formulated for equilibrium magnetic systems. Once we understand the foundations of this theoretical approximation, we will extend such theory to the nonequilibrium system. This extension will provide us with a good approximation for the dynamics of the metastable-stable transition in this case. Finally we will analyze the effects that nonequilibrium conditions involve on the properties of such transition.

## 5.2 Nucleation Theory for Equilibrium Magnetic Systems

In what follows we describe, following in part reference [26], the foundations of nucleation theory as applied to our system when $p = 0$, i.e. for the equilibrium case.[26, 71] The Hamiltonian of this system is that of eq. (2.1), and the implemented dynamics is given by the Glauber rate, eq. (2.3), once we fix $p = 0$. An initial state with all spins up subject to a weak negative magnetic field for a temperature below the critical temperature, $T_{ons}$, is a metastable state. As we have explained in previous chapters, a system in a metastable state eventually evolves towards the truly stable one. This evolution proceeds through the

nucleation of one or several droplets of the stable phase (down spins) in the metastable bulk (up spins). We could think of other different ways in order to evolve from the metastable phase to the stable one. For instance, we could hypothesize that the metastable-stable transition happens due to the *coherent* rotation of all spins in the system[1]. However, except for some marginal, sharply-defined cases, the free energy cost of such coherent rotation is prohibitive (see section 3.4), so this mechanism is not observed in practice. The same argument helps us to understand why the system nucleates droplets: these compact configurations minimize in some way the free energy of the system for a fixed magnetization, so they are observed with high probability during the metastable state demagnetization process.

The process of nucleation and growth of a droplet is controlled by two different, competing terms.[26] On one hand we have a bulk term, related to the droplet volume, which favours the droplet growth, because the droplet belongs to the stable phase, favoured by the magnetic field. On the other hand there is a surface term, which impedes the droplet growth due to the free energy cost of the interface between the stable and metastable phases (the droplet bulk and the rest of the system, respectively). Due to the competition between these two terms, it is observed that small droplets, where the surface term dominates over the bulk term, tend to shrink, while droplets with size larger than certain threshold size tend to grow (in this case, the bulk term dominates). The droplet size that separates both typical behaviors is called critical droplet size, $\mathcal{R}_c$. This observable, $\mathcal{R}_c$, yields a typical length scale for the metastable-stable transition. However, there are other different, well-defined typical length scales in the system. For instance, we have also the lattice spacing $a$, the typical correlation lengths of both the stable and metastable phases, $\xi_s$ and $\xi_{ms}$ respectively, the radius $\mathcal{R}_0$ up to which a droplet can grow before interacting with another droplet (we name this radius $\mathcal{R}_0$ the *mean droplet separation*), and the system size, $L$. However, only three of these six typical length scales will be relevant to our problem. The lattice spacing is fixed to unity in this study, $a = 1$. On the other hand, the typical correlation lengths $\xi_s$ and $\xi_{ms}$ will always be much smaller than the remaining length scales, since we are interested in temperatures well below the critical one, so both correlation lengths will be irrelevant for the investigation. Hence all characteristic processes related to metastability in the equilibrium system will be a consequence of the interplay among the three relevant length scales for this problem, namely $\mathcal{R}_c$, $\mathcal{R}_0$ and $L$.

Let's assume that we have a stable phase droplet with radius $R$ in a system at temperature $T$ in equilibrium, $p = 0$. The droplet volume is $V(R) = \Omega_d(T)R^d$, where $\Omega_d(T)$ is the form factor defined in section 4.5. The free energy associated to this droplet can be written as[26],

$$F(R) = d\Omega_d R^{d-1}\sigma_0 - \Omega_d R^d \Delta \tag{5.1}$$

where $\Delta$ is the free energy density difference between the metastable and sta-

[1] In fact, the Neél-Brown theory[70], which is aimed to explain the process of demagnetization in metastable magnetic particles, is based on the concept of coherent rotation of spins.

ble phases, and $d\Omega_d R^{d-1}$ is the surface associated to a droplet with volume $\Omega_d R^d$. The factor $\sigma_0$ is the surface tension (or interfacial free energy per unit length) along a primitive lattice vector (i.e. for an angle $\phi = 0$ between the interface and one of the reference axis). We exactly know the surface tension $\sigma(\phi)$ for zero magnetic field in equilibrium. The solution obtained from the Solid-On-Solid approximation for the surface tension reproduces the exactly known result for $\phi = 0$.[63] In principle, we could expect that $\sigma_0$ depends on the magnetic field. However, many different studies based on analytic series expansions[72], transfer matrix calculations[73] and Monte Carlo simulations[74] point out that the surface tension $\sigma_0$ entering the droplet free energy cost is the equilibrium surface tension for *zero* magnetic field. Hence we will use from now on the notation $\sigma_0(T)$ to emphasize the independence of this term on the magnetic field.

In eq. (5.1) we observe the competence between the surface term, which impedes the droplet growth, and the bulk term, which favours it. Since the system attempts to minimize the free energy, in order to determine the critical droplet radius $\mathcal{R}_c$, which separates the growth tendency from the shrinkage tendency we only have to find the maximum of the droplet free energy with respect to droplet radius. In this way we obtain,[71]

$$\mathcal{R}_c(T) = \frac{(d-1)\sigma_0(T)}{\Delta} \approx \frac{(d-1)\sigma_0(T)}{2m_s(T)|h|} \tag{5.2}$$

where he have substituted $\Delta \approx 2m_s(T)|h|$, with $h$ the magnetic field and $m_s(T)$ the equilibrium spontaneous magnetization (defined positive).

In order to understand the previous approximation for the free energy density difference between the metastable and stable phases, $\Delta$, we start from the definition of free energy, $F = -k_B T \ln \mathcal{Z}(T)$, where $k_B$ is the Boltzmann constant, which we fix to unity already in Chapter 2, and where $\mathcal{Z}(T)$ is the canonical partition function,

$$\mathcal{Z}(T) = \sum_{\mathbf{s}} e^{-\beta \mathcal{H}(\mathbf{s})} \tag{5.3}$$

Here $\mathcal{H}(\mathbf{s})$ is the energy associated to a spin configuration $\mathbf{s}$ in the equilibrium system, eq. (2.1). In the low temperature limit, the only states with relevant statistical weight (Boltzmann factor) are the stable and metastable states, $e^{-\beta\mathcal{H}_s}$ and $e^{-\beta\mathcal{H}_{ms}}$. Hence, in this very low temperatures limit the free energy associated to a metastable state will be approximately the energy associated to such state, $F_{ms}(T<<) \approx \mathcal{H}_{ms}$, and equivalently for the stable state, $F_s(T<<) \approx \mathcal{H}_s$. In this limit the metastable state will be given by a configuration where practically all spins are up, while in the stable state almost all spins will be down. The system Hamiltonian was $\mathcal{H}(\mathbf{s}) = -J\sum_{\langle i,j\rangle} s_i s_j - h\sum_i s_i$. For $T \to 0$ the exchange term will be approximately $\sum_{\langle i,j\rangle} s_i s_j \approx 2N$, where $2N$ is the number of neighbor spin pairs in the system. Hence we can write $N\Delta = F_{ms} - F_s \approx \mathcal{H}_{ms} - \mathcal{H}_s \approx Nh[m_s(T,h) - m_{ms}(T,h)]$, where $m_s(T,h)$ and $m_{ms}(T,h)$ are the stable and metastable magnetizations, respectively, $m = N^{-1}\sum_i s_i$. For weak magnetic fields we have $|m_s(T,h)| \approx |m_{ms}(T,h)| \approx m_s(T,h=0)$, so, if we

define $m_s(T) \equiv m_s(T, h = 0)$, we finally arrive to $\Delta \approx 2m_s(T)|h|$. This approximation is expected to remain valid even for temperatures near the critical one, although we have derived it in the low temperature limit.[72]

The free energy cost associated to the critical droplet is,

$$F_c(\mathcal{R}_c) = \Omega_d(T)\sigma_0(T)\mathcal{R}_c^{d-1} = \sigma_0(T)\frac{V_c}{\mathcal{R}_c} \tag{5.4}$$

where $V_c \equiv \Omega_d \mathcal{R}_c^d$ is the critical droplet volume. The nucleation rate $I(T, h)$ per unit time and volume, which is the probability per unit time and volume of nucleating a critical droplet in the system, can be determined from $F_c(\mathcal{R}_c)$ using the Arrhenius law[23, 75],

$$I(T, h) = A(T)|h|^{b+c}e^{-\frac{F_c}{T}} \approx A(T)|h|^{b+c}e^{-\frac{\sigma_0 V_c}{\mathcal{R}_c T}} \tag{5.5}$$

The function $A(T)$ is non-universal, the exponent $b$ is an universal exponent related to the Goldstone modes present on the droplet surface[76], and the exponent $c$ yields the dependence of the *kinetic prefactor* on the magnetic field[75], being the only part of $I(T, h)$ which can explicitely depend on the specific spin dynamics. In particular, for a bidimensional system there are many numerical evidences pointing out that $b = 1$, as predicted via field theory[76], while the value of $c$ changes between $c \approx 1$ for sequential dynamics and $c \approx 2$ for random dynamics.[26]

The nucleation rate $I(T, h)$ yields the rate at which the critical droplet nucleates in the system. Using the information codified in eq. (5.5), and once we determine the mean droplet separation, $\mathcal{R}_0$, and its associated time scale, $t_0$, which is the time the droplet needs in order to radially grow a distance $\mathcal{R}_0$, we will be able to calculate the metastable state mean lifetime using Avrami law[23, 78]. In order to calculate $\mathcal{R}_0$ and $t_0$ we need to know the radial growth velocity for a stable phase droplet, $v_\perp$. This growth velocity can be determined using the Allen-Cahn approximation[23]. This approximation is based on a phenomenologic motion equation written using thermodynamic arguments, which linearly relates the rate of change of the local order parameter, which in our case is the magnetization $m(\vec{r})$, to the local thermodynamic force,

$$\frac{dm(\vec{r})}{dt} = -\Gamma' \frac{\delta F}{\delta m(\vec{r})} \tag{5.6}$$

From this equation, assuming that the free energy functional $F$ has a shape similar to that of the asymmetrical Ginzburg-Landau functional[77], and assuming that the droplet has a spherical shape, we find the following result for the radial growth velocity of a stable phase droplet in Allen-Cahn approximation[23],

$$v_\perp = (d-1)\Gamma\left(\frac{1}{\mathcal{R}_c} - \frac{1}{R}\right) \underset{R\to\infty}{\longrightarrow} \frac{(d-1)\Gamma}{\mathcal{R}_c} \equiv v_0 \tag{5.7}$$

where the constant $\Gamma$ depends on the particular implemented dynamics. We can approximate $v_\perp \approx v_0$ always that, as in our case, $\mathcal{R}_0 \gg \mathcal{R}_c$, so from now on we take $v_0$ as the radial growth velocity.

It is obvious that $\mathcal{R}_0 = v_0 t_0$, since $t_0$ is the time the droplet needs to radially grow a distance $\mathcal{R}_0$. On the other hand, we also know that $\mathcal{R}_0^d t_0 I = 1$, since, by definition of both magnitudes $\mathcal{R}_0$ and $t_0$, the probability of finding a droplet nucleating a volume $\mathcal{R}_0^d$ in a time $t_0$ is equal to unity. From these two relations we arrive to,

$$t_0(T,h) = (v_0^d I)^{-\frac{1}{d+1}} = B(T)|h|^{-\frac{b+c+d}{d+1}} e^{\frac{\Xi(T)}{|h|^{d-1}}} \tag{5.8}$$

$$\mathcal{R}_0(T,h) = v_0 t_0 = C(T)|h|^{-\frac{b+c-1}{d+1}} e^{\frac{\Xi(T)}{|h|^{d-1}}} \tag{5.9}$$

where we have defined the function $\Xi(T)$ as,

$$\Xi(T) = \frac{1}{d+1}\Omega_d(T)\Big(\frac{d-1}{2m_s(T)}\Big)^{d-1}\frac{\sigma_0^d(T)}{T} \tag{5.10}$$

and where both amplitudes are written in the following way,

$$B(T) = \Big(\frac{2\Gamma m_s(T)}{(d-1)\sigma_0(T)}\Big)^{\frac{-d}{d+1}} A(T)^{-\frac{1}{d+1}} \tag{5.11}$$

$$C(T) = \frac{2\Gamma m_s(T)}{(d-1)\sigma_0(T)} B(T) \tag{5.12}$$

In the above equations we have carefully specified that $\Xi(T)$, and the amplitudes $B(T)$ and $C(T)$, do depend exclusively on temperature. We must notice that the amplitudes $B(T)$ and $C(T)$ inherit the non-universal character of $A(T)$.

We can calculate the metastable state lifetime using the results obtained up to now. In general, this lifetime is defined as the average first passage time (in Monte Carlo Steps per spin, MCSS) to certain stable phase volume fraction. The stable phase volume fraction at time $t$, $\Phi_s(t)$, is defined as the number of spins in the stable phase divided by the total number of spins, $N$. We hence can interpret $\Phi_s(t)$ as the probability, at time $t$, that a spin already belongs to the stable phase. In order to calculate $\Phi_s(t)$ it is convenient, on the other hand, to ask the opposite question: for a fixed point $O$ in the system, which is the probability $P$ that the point $O$ does not belong to the stable phase at time $t$ ?. In order to calculate such probability, we know that a droplet of the stable phase will reach the point $O$ before a time $t$ if the following conditions are fulfilled:

- The droplet nucleates a distance $r'$ away the point $O$ such that $0 \leq r' \leq v_0 t$.
- The time $t'$ which signals the beginning of the nucleation event must fulfill $0 \leq t' \leq t - \frac{r'}{v_0}$.

Since the nucleation rate $I(T,h)$ is the probability of nucleating a droplet per unit time and volume, the probability $P$ that point $O$ has not been reached by the stable phase at time $t$ can be written as,

$$P = \prod_{\substack{0 \leq r' \leq v_0 t \\ 0 \leq t' \leq t - \frac{r'}{v_0}}} \left[1 - I(T,h) d\vec{r}' dt'\right] \tag{5.13}$$

We have that $e^{-Id\vec{r}'dt'} = 1 - Id\vec{r}'dt'$, and since the product is continuous, we can write in general, for a d-dimensional system,

$$P = \exp\Big[-I(T,h)\int_0^{v_0 t} dr' d\Omega_d r'^{d-1}\int_0^{t-\frac{r'}{v_0}} dt'\Big] = e^{-\frac{\Omega_d}{d+1}\left(\frac{t}{t_0}\right)^{d+1}} \tag{5.14}$$

Hence, the probability that the point O belongs to the stable phase at time t, i.e. the stable phase volume fraction at time t, will be given by $\Phi_s(t) = 1 - P$. The last equality constitutes the Avrami's law.[78] From this equation we can obtain the time the system needs to nucleate for first time certain stable phase volume fraction $\Phi_s$,

$$\tau(\Phi_s) = t_0(T,h)\Big[\frac{d+1}{\Omega_d(T)}\ln\big(\frac{1}{1-\Phi_s}\big)\Big]^{\frac{1}{d+1}} \tag{5.15}$$

This equation yields the mean lifetime of the metastable state as a function of the nucleated volume fraction of the stable phase that we fix as threshold for its measure, for an equilibrium ferromagnetic system of *infinite* size. We must take into account that we have assumed that the positions of the (possibly overlapping) growing droplets are uncorrelated when constructing the probability P. This *ideal gas* hypothesis will be valid when the total volume fraction occupied by the droplets is small enough, so we can neglect correlations among them. This is the case in our study, due to the weakness of the magnetic field. For strong magnetic fields the picture of localized nucleating droplets is no longer valid in order to explain the exit from the metastable state. The metastable-stable transition is then observed to proceed via long-wavelength unstable modes reminiscent of spinodal decomposition.[26]

## 5.3 Extension of Nucleation Theory to Nonequilibrium Ferromagnetic Systems

In the previous section we have presented nucleation theory, which explains the dynamics of the metastable-stable transition for an equilibrium ferromagnetic system, based on the droplet picture. The central magnitude in this theory is the droplet free energy, eq. (5.1). From such observable we have calculated the critical droplet size, and using Arrhenius law, the nucleation rate, from which, applying Avrami's law, we obtained the mean lifetime of the metastable state.

In order to extend this theory to the nonequilibrium system ($p \neq 0$), we first have to write the *free energy cost* of a droplet in this case. However, here we face some fundamental problems, which impede any first-principles definition for the free energy in the nonequilibrium case. First, from a microscopic point of view, we do not know for $p \neq 0$ the stationary probability distribution $P(\mathbf{s})$ of finding the magnetic system in a steady configuration $\mathbf{s}$. This steady probability function is solution of the master equation, eq. (3.1), once applied

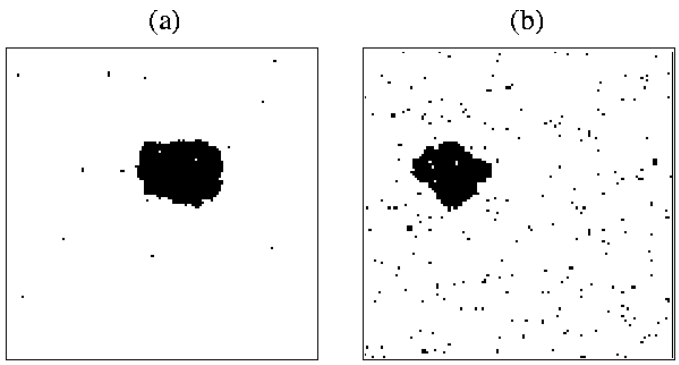


Figure 5.1: (a) Snapshot of the metastable-stable transition for a system with $T = 0.5T_{ons}$, $h = -0.1$, $p = 0$ (equilibrium system) and $L = 128$. In black, stable phase spins (down spins), while metastable phase spins (up spins) are in white. (b) The same than in (a), for the same magnetization, but for the nonequilibrium system, with $p = 0.01$.

the stationarity condition. Since detailed balance does not hold for $p \neq 0$, see eq. (2.4), the distribution $P(\mathbf{s})$ will be different from the Boltzmann distribution. Moreover, the system is open, subject to a continuous energy flux due to the nonequilibrium perturbation. We do not know how to precisely define the energy of this system. We also do not know how to construct any statistical ensemble in the nonequilibrium case, and we also do not know how to connect the microscopic properties of the system, which should be captured by those nonequilibrium statistical ensembles, with the system macroscopic behavior. Finally, there is not even an unique macroscopic theory, equivalent to equilibrium Thermodynamics, to connect with taking as a starting point the microscopic equations. This inexistent macroscopic theory ought to satisfactorily describe the macroscopic phenomena that appear in nonequilibrium systems[2]. All these facts force us to propose a phenomenologic approximation, not based on first principles, to the problem of the nonequilibrium *free energy* associated to a stable phase droplet in the system with $p \neq 0$.

### 5.3.1 Nonequilibrium Potential and Critical Droplet Size

Fig. 5.1.a shows a typical escape configuration from the metastable state in an equilibrium system, with $T = 0.5T_{ons}$, $h = -0.1$, $p = 0$ and $L = 128$, for certain fixed magnetization, while Fig. 5.1.b shows an escape configuration for an identical system, for the same magnetization, but with $p = 0.01$, i.e. under nonequilibrium conditions. Comparing both figures we realize that, in

[2]Irreversible Thermodynamics[79] is an extension of usual Thermodynamics, based on conservation and balance equations, the maximum entropy production postulate, and a series of phenomenological laws which postulate the proportionality among the fluxes and the thermodynamic forces (for more references, see Chapter 9 in this thesis). This macroscopic theory describes in a partial and approximate way some nonequilibrium situations, although it cannot be considered a complete macroscopic theory for nonequilibrium systems.

spite of the obvious differences due to the presence of the nonequilibrium perturbation, which introduces small fluctuations in the bulk, the picture based on a stable phase droplet which nucleates in the metastable bulk is still valid. Furthermore, we think that the shape and the growth of such droplet in the nonequilibrium system are again controlled by the competition between the droplet bulk, which favours the droplet growth, and the droplet surface, which hinders such growth. Therefore we observe that, although there are many fundamental problems in order to define from first principles a nonequilibrium potential which controls the exit from the metastable state for $p \neq 0$, it is possible to establish from a phenomenological level a formal equivalence between the equilibrium and nonequilibrium cases.

Taking into account this observation, we assume the existence of a nonequilibrium potential, $\mathcal{F}$, which controls the metastable-stable transition for the nonequilibrium system. We also assume that there are two different terms competing in $\mathcal{F}$: a surface term, which hinders the droplet growth process, and a bulk (or volume) term, which favours such growth. Moreover, we assume that this nonequilibrium potential for a stable phase droplet is *formally identical* to the free energy of a droplet in the equilibrium case, eq. (5.1), so for a droplet of size $R$,

$$\mathcal{F}(R) = d\Omega_d(T,p)R^{d-1}\sigma_0(T,p) - 2m_s(T,p)|h|\Omega_d(T,p)R^d \tag{5.16}$$

where now $\Omega_d(T,p)$ is the form factor associated to a droplet of the stable phase at temperature $T$ and nonequilibrium perturbation $p$, see Fig. 4.8, $\sigma_0(T,p)$ is the surface tension along one of the primitive lattice vectors for zero magnetic field and parameters $T$ and $p$, and $m_s(T,p)$ is the spontaneous magnetization for the nonequilibrium system (defined positive) at temperature $T$ and perturbation $p$. This phenomenologic hypothesis, which is not justified from a formal point of view, will be checked *a posteriori*, comparing the theoretical predictions derived from it with the results obtained from Monte Carlo simulations of the original model.

Although we do not have exact solutions for the observables $\Omega_d(T,p)$, $\sigma_0(T,p)$ and $m_s(T,p)$, we have developed in previous chapters good approximations for all of them. Thus, we take the spontaneous magnetization $m_s(T,p)$ as the steady solution for zero magnetic field of the set of eqs. (3.17)-(3.18) which we obtained in Pair Approximation, see section 3.2 and Fig. 3.3. We approximate $\sigma_0(T,p)$ using the expression we derived for the surface tension in the generalized SOS approximation (section 4.3), $\sigma^{(p)}_{SOS}(\phi;T,p)$ for an angle $\phi = 0$, which we denote as $\sigma^{(p)}_{SOS}(T) \equiv \sigma^{(p)}_{SOS}(\phi = 0;T,p)$, see eq. (4.21). The form factor $\Omega_d(T,p)$ has been calculated in section 4.5 using the generalized SOS result for the surface tension, see Fig. 4.8.

Using this information, and taking into account the form of the nonequilibrium potential for a stable phase droplet, the critical droplet size for $p \neq 0$ will be,

$$\mathcal{R}_c(T,p) = \frac{(d-1)\sigma^{(p)}_{SOS}(T)}{2m_s(T,p)|h|} \tag{5.17}$$

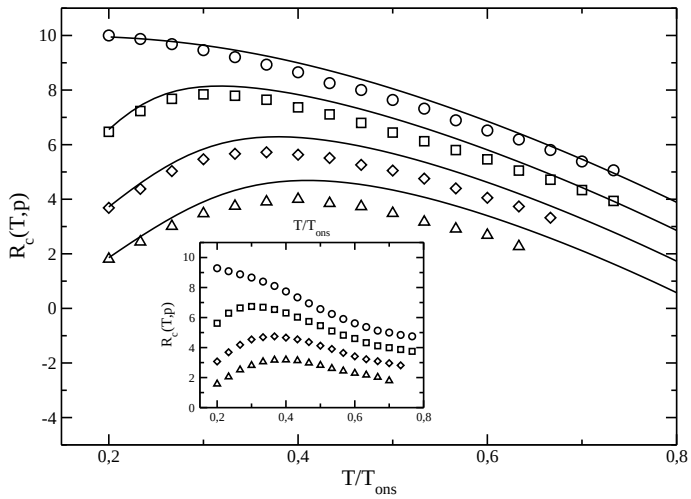


Figure 5.2: Critical droplet size, $\mathcal{R}_c$, as a function of temperature for different values of $p$, for a system size $L = 53$, with periodic boundary conditions and subject to a magnetic field $h = -0.1$. In particular, from top to bottom, $p = 0$(◯), $0.001$(□), $0.005$(◇) and $0.01$(△). The points are Monte Carlo results, measuring $\mathcal{R}_c(T, p)$ using the method based on the growth probability of an initial square droplet, after averaging over $N_{exp} = 1000$ experiments. Lines correspond to the theoretical prediction, eq. (5.17). For the shake of clarity, results for the $n$-th value of $p$, $n = 1, \ldots, 4$ (using the above order) have been shifted $(1 - n)$ units in the $\hat{y}$ axis. The inset shows Monte Carlo results for $\mathcal{R}_c$ as those plotted in the main graph, but here we measure $\mathcal{R}_c$ using the stable phase growth and shrinkage rates. Data here have been also shifted. In all cases error bars are smaller than the symbol sizes.

where the different magnitudes have been defined in the previous paragraph. Fig. 5.2 shows the theoretical prediction for the critical droplet size $\mathcal{R}_c(T, p)$ as a function of temperature for different values of $p$ and $h = -0.1$. This figure also shows the results of different Monte Carlo simulations for a system with size $L = 53$, with periodic boundary conditions and the same magnetic field. As we see there, the agreement between theory and Monte Carlo results is rather good. From the qualitative point of view, we observe that in the equilibrium system ($p = 0$) the critical droplet size grows monotonously as temperature decreases, converging towards a value $\mathcal{R}_c(T \to 0) \approx 1/|h| = 10$. On the other hand, for any $p \neq 0$ the critical droplet size depicts a maximum as a function of temperature, decreasing for lower temperatures. This non-monotonous behavior of $\mathcal{R}_c(T, p \neq 0)$ is clearly inherited from the non-monotonous behavior of the surface tension which we derived in the generalized SOS approximation for the nonequilibrium interface. Moreover, as we said previously, the good agreement shown in Fig. 5.2 verifies in an indirect way that the surface tension we derived in the generalized SOS approximation constitutes a good approximation for the nonequilibrium surface tension.

On the other hand, from the quantitative point of view, we observe that the theoretical predictions are very good for low enough temperatures, although they slightly overestimate the value of the measured $\mathcal{R}_c$ for larger temperatures, for any value of $p$. It is remarkable that this overestimation for $\mathcal{R}_c$ at high temperatures also appears for the equilibrium system, where $\sigma_{SOS}^{(p=0)}(T)$ perfectly reproduces the exact known result for the surface tension, and where $m_s(T, p = 0)$ yields values almost indistinguishable from the real ones. In this case the observed differences between theoretical predictions and computational results for the critical droplet size at high temperatures can be traced back to the lack of precision of the approximation $\Delta \approx 2m_s(T)|h|$ in this temperature regime. For $p \neq 0$ it is observed that the differences appearing between the measured critical droplet size and the one predicted by the nonequilibrium nucleation theory are similar to those observed in the equilibrium system, so again the approximation for the free energy density difference between the metastable and stable phases, $\Delta$, seems to be at the origin of the discrepancy. In spite of these slight differences, we can affirm that our theoretical approximation nicely reproduces the simulation results.

In order to obtain the critical droplet size from Monte Carlo simulations of the real system we have used two different methods which, as we can observe in Fig. 5.2, yield equivalent results. In a first method, we simulate a system with size $L$, with a total amount of $N = L^2$ spins, and subject to periodic boundary conditions. We initialize the system in a state with all spins up (i.e. in the metastable phase), except for a *square* droplet of down spins (stable phase spins) with side $2R$ which we situate on the lattice center. For this initial condition we let evolve the system under the usual Glauber dynamics, eq. (2.3), for fixed temperature $T$, nonequilibrium perturbation $p$ and magnetic field $h < 0$. The imposed initial condition is highly unstable. If the initial state converges as time goes on to a state with magnetization $m \approx +1$ (metastable state), then the initial droplet, with side $2R$, was subcritical (that is, for this droplet the surface term dominates over the bulk term, so it tends to shrink). This means that the radius $R$ of the initial droplet, defined as half of the square droplet side, is smaller than the critical droplet radius $\mathcal{R}_c(T, p, h)$ for these parameters. On the other hand, if the initial droplet grows until the system reaches a state with magnetization near $m \approx -1$ (stable state), the radius $R$ of the initial square droplet was larger than the critical droplet radius, so the initial droplet was supercritical (now the bulk term dominates over the interfacial one). Since the system is stochastic, the growth or shrinkage of a droplet depending on its size is not a deterministic process. Therefore we can define a function $P_{super}(R)$ which yields the probability that a (square) stable phase droplet with radius $R$ is supercritical. In our case, in order to evaluate such probability we perform $N_{exp}$ experiments as the above described, and we accumulate the number of times $n_{super}(R)$ that a droplet of size $R$ grows up to the stable state. In this case we have that $P_{super}(R) = n_{super}(R)/N_{exp}$. Fig. 5.3 shows the probability $P_{super}(R)$ for a system size $L = 53$, with periodic boundary conditions, at temperature $T = 0.4T_{ons}$, nonequilibrium parameter $p = 0$

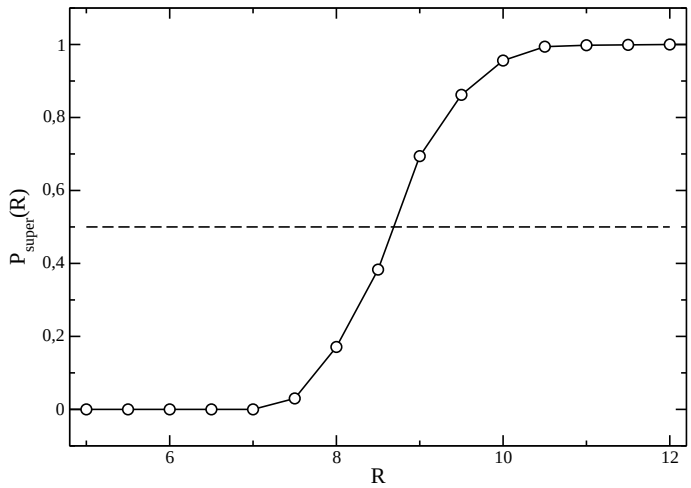


Figure 5.3: Probability that a initial (square) droplet with radius $R$ is supercritical, $P_{super}(R)$, as a function of $R$ for a system size $L = 53$, at temperature $T = 0.4T_{ons}$, $p = 0$, $h = -0.1$, once we collect $N_{exp} = 1000$ different experiments for each value of $R$.

and magnetic field $h = -0.1$, once we collect a total amount of $N_{exp} = 1000$ different experiments for each value of $R$. As expected, the function $P_{super}(R)$ abruptly changes from 0 to 1 in a narrow interval for the radius of the initial square droplet. Here we define the critical droplet radius $\mathcal{R}_c$ as the radius $R^*$ for which $P_{super}(R^*) = 0.5$.[3] Using this method we have obtained the results shown in the main plot in Fig. 5.2, after averaging over $N_{exp} = 1000$ different experiments.

The second method we previously referred to in order to measure $\mathcal{R}_c(T, p, h)$ is based on the stable phase growth and shrinkage rates, $g(m)$ and $s(m)$ respectively, defined in section 3.3, see eqs. (3.36) and (3.37) and complementary discussion. We said there that $g(m)$ was the number of spins in the system that change from the metastable phase to the stable one per unit time, when the system was in a state with magnetization $m$. Equivalently, $s(m)$ was the number of spins in the system that change from the stable phase to the metastable one per unit time, when the system magnetization is $m$. The rate of change associated to the order parameter was given by the difference $s(m) - g(m)$, see eq. (3.38), so stationary states was defined by the solutions of the equation $s(m) = g(m)$. We deduced that this equation has three different solutions for a system showing metastability, $m_1$, $m_0$ y $m_{-1}$, where $m_1$ and $m_{-1}$ were magnetizations near $+1$ and $-1$, respectively, and $m_0$ signaled a intermediate positive magnetization for $h < 0$ (see Fig. 3.8). While $m_1$ and $m_{-1}$ were locally

[3]Due to the discontinuous character of variable $R$, most of the times there is no sampled value $R^*$ such that $P_{super}(R^*) = 0.5$. In these cases it is necessary to perform a linear interpolation between the two values of the variable $R$ that flank the intersection point between the function $P_{super}(R)$ and the constant line $y = 0.5$ (see Fig. 5.3).

stable solutions which identified the metastable and stable states respectively, the solution $m_0$ was unstable against small perturbations. Moreover, we deduced that if $m > m_0$ the system rapidly evolves towards the metastable state, while if $m < m_0$ the system evolves towards the stable state. In this sense the magnetization $m_0$ signals a critical magnetization separating the region where the stable phase tends to shrink ($m > m_0$) from the region where the stable phase tends to grow ($m < m_0$). This concept is formally analogous to that of critical droplet. Furthermore, the magnetization $m_0$ signals the magnetization that the system exhibits when the critical droplet nucleates. As we will explain in the following, we are able to obtain the critical droplet size using this magnetization value, $m_0$, and the metastable state magnetization, $m_1$. We define $n_0^- = N(1 - m_0)/2$ as the number of down spins in the *critical* state characterized by $m_0$, where N is the total number of spins in the system. Equivalently, we define $n_1^- = N(1 - m_1)/2$ as the number of down spins in the metastable state. In the *critical* state we expect that $n_0^- = n_c^- + n_{bulk}^-$, where $n_c^-$ is the number of down spins belonging to the critical droplet, and $n_{bulk}^-$ is the number of down spins in the metastable phase bulk which has not been occupied by the critical droplet. We can assume that, as a first approximation, the density of down spins in the metastable bulk when we are in the *critical* state is equal to the density of down spins in the metastable state, which we define as $d_1^- = n_1^-/N$. In this case we have that $n_{bulk}^- = d_1^-(N - n_c^-)$, so,

$$n_c^- = \frac{n_0^- - n_1^-}{1 - \frac{n_1^-}{N}} \tag{5.18}$$

The variable $n_c^-$ yields the volume of the critical droplet. As a definition of the critical droplet size we choose,

$$\mathcal{R}_c \equiv \frac{\sqrt{n_c^-}}{2} \tag{5.19}$$

Thus measuring the magnetizations $m_0$ and $m_1$ for which the curves $g(m)$ and $s(m)$ intersect one each other, we can obtain a measure of the critical droplet size. In order to do so we perform a series of $N_{exp}$ experiments studying the demagnetization process from the metastable to the stable state. We measure in each experiment the rates $g(m)$ and $s(m)$. As we have already done in other simulations, we initialize the system in a state with all spins up under the action of a negative magnetic field. Such state is metastable, and the system eventually evolves up to the stable state. We measure the magnetizations $m_0$ and $m_1$ on each experiment, and we calculate from them the critical droplet size $\mathcal{R}_c$ defined in eq. (5.19). Finally, we average over the different experiments in order to obtain good statistics. In this way we have obtained the results shown in the inset of Fig. 5.2 for the critical droplet radius as a function of temperature for different values of $p$. These data have been obtained for a system size $L = 53$ with a magnetic field $h = -0.1$, and averaging over $N_{exp} = 1000$ different experiments.

If we compare the computational results obtained using both methods for the critical droplet size, we observe that these results are completely equivalent, up to a small amplitude factor, which varies slightly with the temperature and the nonequilibrium parameter $p$. In particular, the results for $\mathcal{R}_c$ obtained from the probability $P_{super}(R)$ of finding a supercritical square droplet with side $2R$ are slightly larger than the results obtained from the stable phase growth and shrinkage rates. In order to collapse both measures we must multiply the results obtained via the first method by a scaling factor of order $0.9$. On the other hand, these tiny global differences observed between both measures were expected due to the different influence of the form factor on each computational scheme. However, in spite of these small discrepancies, the results obtained from both measures depict the same behavior: $\mathcal{R}_c$ is monotonous in equilibrium, while $\mathcal{R}_c$ shows a maximum as a function of temperature for the nonequilibrium system. Finally, we must notice before going on that the two computational methods presented here in order to measure the critical droplet size will be valid always that the metastable-stable transition proceeds through the nucleation of a *single* critical droplet, and not for several critical droplets, as is observed in certain parameter space regions. However, for the parameters we study, the system usually decays through the nucleation of a single critical droplet (see next sections).

### 5.3.2 Radial Growth Velocity for a Stable Phase Droplet

In the following we study the radial growth velocity for a stable phase droplet in the nonequilibrium system. In equilibrium we deduced this velocity via the Allen-Cahn approximation. This approximation was based on a phenomenologic equation postulating the proportionality between the rate of change of the order parameter and the local thermodynamic force, eq. (5.6). This thermodynamic force is just the variation induced on the system free energy by a perturbation of the local magnetization, $\delta F/\delta m(\vec{r})$. For the nonequilibrium case we cannot properly define a free energy functional. However, if our postulate about the existence of a nonequilibrium potential for $p \neq 0$ similar to the free energy in the equilibrium system is correct, we can define the *thermodynamic* force the order parameter suffers in the same way, but now using the nonequilibrium potential $\mathcal{F}$ instead of the equilibrium free energy $F$. Furthermore, due to the similarities observed in the metastable-stable transition for both the equilibrium and nonequilibrium systems, we assume that the shape of the nonequilibrium potential matches in some sense that of the Ginzburg-Landau functional. Hence the same formal result we derived in equilibrium is assumed to be valid for $p \neq 0$,

$$v_0(T, p, h) = \frac{(d-1)\Gamma}{\mathcal{R}_c(T, p, h)} \tag{5.20}$$

where now $\mathcal{R}_c(T, p, h)$ is the critical droplet radius for the nonequilibrium system, see eq. (5.17).

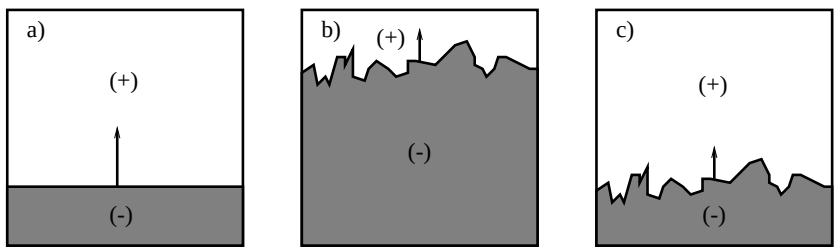


Figure 5.4: In $a)$ we show the initial configuration for the semi–infinite system defined in the text. In $b)$ we show a possible schematic configuration before we shift the lattice. The fraction of up spins in this configuration has decreased to a value close to $\alpha$. Finally, in $c)$ it is shown the final system configuration after the shift. We have added some new up spins to the top of the system, and some down spins from the bottom of the system have been removed.

In order to check this prediction about the interface velocity we perform Monte Carlo simulations. We then build a system with effective size $L \times \infty$. To do that in practice, we define the system in a square $L \times L$ lattice. We impose periodic boundary conditions in the horizontal direction ($\hat{x}$ axis), and open boundary conditions in the vertical one ($\hat{y}$ axis), forming in this way a cylinder with height $L$. All spins in the upper row are fixed in the up state, while all spins in the lower row are fixed in the down state. The initial configuration consists of a spin stripe of height $\alpha L$ where all spins are down, which fills the first $\alpha L$ rows, and a complementary stripe where all spins are up, which fills the remaining $(1-\alpha)L$ rows. We choose in this case $\alpha = 0.15$. The interface moves upwards for a negative magnetic field (i.e. the stable phase -down spins- grows at the expense of the metastable one -up spins). In order to emulate an infinite system in the interface movement direction, we shift the *observation window* as the interface advances, always keeping it inside the system. In practice we do that generating a new region with up spins in the upper part of the system as the interface advances, and eliminating an equivalent down spins region in the lower part of the system. In fact the shift is performed each time the fraction of up spins in the system is smaller than $\alpha$. The magnitude of the shift is such that once performed we approximately recover the fraction of up and down spins we had in the initial configuration, i.e. 15% of up spins and 85% of down spins. The choice $\alpha = 0.15$ allows the added up spins to relax towards the typical state of the metastable bulk for the studied parameters $T$, $p$ and $h$ before the interface reaches them (see figure 5.4). In order to measure the interface velocity we calculate the system magnetization $m(t)$ as a function of time, evaluating $m(t)$ without taking into account the variations in magnetization due to the added and removed spins in the upper and lower parts of the system respectively. The slope of $m(t)$ yields the interface velocity, $v_0(T, p, h)$.

We measure the interface velocity using this method for a system size $L = 128$ as a function of temperature for different values of $p$ with fixed $h = -0.1$. Fig. 5.5 shows the results of these measures. This figure also includes the pre-

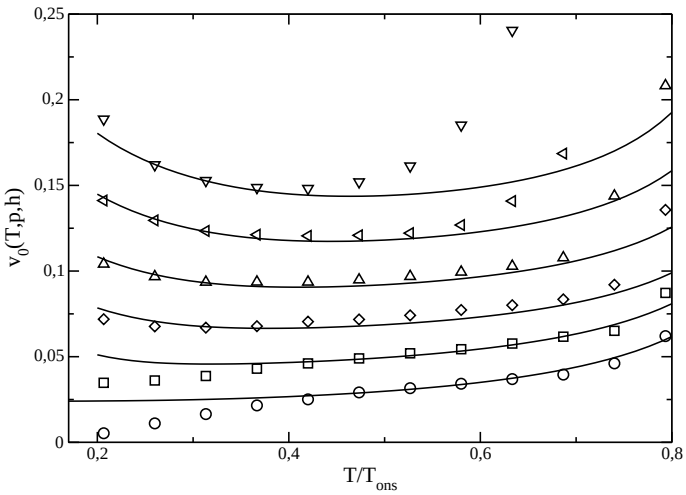


Figure 5.5: Monte Carlo results for the interface velocity as a function of temperature for different values of $p$, and $h = -0.1$. In particular, from bottom to top, $p = 0$, $0.001$, $0.005$, $0.01$, $0.02$ and $0.03$. Continuous lines are our theoretical prediction. The free parameter $\Gamma$ (see main text) is fixed in each case to yield the best fit, always obtaining $\Gamma \in [\frac{1}{5}, \frac{1}{4}]$. For the shake of clarity, if the integer $n = 1, \ldots, 6$ characterizes the curve position (its order from bottom to top), we have shifted the results for each $p$ an amount $(n-1) \times 0.02$ in the vertical axis. Error bars are smaller than symbol sizes.

dictions based on eq. (5.20), once we fix the only free parameter, $\Gamma$, to yield the best fit in each case (we obtain always $\Gamma \in [\frac{1}{5}, \frac{1}{4}]$). The theory reproduces rather well the Monte Carlo results for most of the values for $T$ and $p$. It is remarkable that for $p = 0$ (and very small values of $p$, say $p = 0.001$) the interface velocity prediction based on eq. (5.20) fails in the low temperature limit. This discrepancy is due to the underlying lattice anisotropy which induces effects that dominate the behavior of the system in the low temperature limit (remember the droplet shape in the low temperature limit for $p = 0$, Fig. 4.7.a). A continuous and macroscopic theory as the Allen-Cahn approximation, which is isotropic and does not take into account the lattice details, fails when describing the interface velocity at low temperatures. However this discrepancy is *healed* as the value of $p$ is increased, since the interface for $p \neq 0$ *feels* an effective temperature $T^{I}_{eff} > T$, eq. (4.36), due to the nonequilibrium perturbation, which is nonzero even in the low temperature limit. Hence the interface almost does not realize the presence of the underlying lattice for large enough $p \neq 0$, and so the continuous approximation remains valid.

On the other hand we also observe in Fig. 5.5 that the differences between the theoretical prediction for the interface velocity and the computational results grow as we approach the critical temperature $T_c(p)$. These differences are due to the interaction between the interface and bulk fluctuations, whose relative importance grows as we approach the critical point. Our theory does not

take into account such possible interaction. We can remove these differences in the high temperature limit eliminating the bulk dynamics, as we did when measuring the interface microscopic structure in the nonequilibrium system, see section 4.3 and Fig. 4.3. In this way we recover the agreement between the theory and the measured velocities for high temperatures.

It is remarkable that the interface velocity shows a minimum as a function of temperature for an intermediate temperature in the nonequilibrium system ($p \neq 0$), growing the interface velocity if we further decrease temperature, see Fig. 5.5. This surprising feature of the nonequilibrium system, measured in Monte Carlo simulations and compatible with our theory, points out that when there is non-thermal noise ($p$), a decrease of the thermal noise ($T$) when the system is at intermediate temperatures favours the interface advance. The origin of this property underlies again on the non-monotonous behavior of surface tension for $p \neq 0$, see Fig. 4.4.

### 5.3.3 Mean Lifetime for the Metastable State

The hypothesis of existence of a nonequilibrium potential $\mathcal{F}$, formally identical to the equilibrium free energy, which controls the dynamics of the metastable-stable transition for $p \neq 0$, has provided us with correct theoretical predictions for both the critical droplet size and the droplet radial growth velocity. Once we have derived these magnitudes we are able to study the metastable state mean lifetime for $p \neq 0$. In this case, the nucleation rate $I(T, p, h)$ can be written using Arrhenius law[23, 75] as,

$$I(T, p, h) = A(T, p)|h|^{b+c} e^{-\frac{\mathcal{F}_c(T,p,h)}{T}} \tag{5.21}$$

where $\mathcal{F}_c(T, p, h) = \mathcal{F}(R = \mathcal{R}_c)$, eq. (5.16). For the nonequilibrium system the non-universal amplitude factor $A(T, p)$ will depend not only on temperature, but generically also on $p$. We can calculate for $p \neq 0$, in an equivalent way as we did in equilibrium, the mean droplet separation $\mathcal{R}_0(T, p, h)$ and the time $t_0(T, p, h)$ a droplet needs to grow radially a distance $\mathcal{R}_0$ once we know the nucleation rate, obtaining,

$$t_0(T, p, h) = B(T, p)|h|^{-\frac{b+c+d}{d+1}} e^{\frac{\Xi(T,p)}{|h|^{d-1}}} \tag{5.22}$$

$$\mathcal{R}_0(T, p, h) = C(T, p)|h|^{-\frac{b+c-1}{d+1}} e^{\frac{\Xi(T,p)}{|h|^{d-1}}} \tag{5.23}$$

where now we define the function $\Xi(T, p)$ as,

$$\Xi(T, p) = \frac{1}{d+1}\Omega_d(T, p)\left(\frac{d-1}{2m_s(T, p)}\right)^{d-1} \frac{\left[\sigma^{(p)}_{SOS}(T)\right]^d}{T} \tag{5.24}$$

and where both amplitudes for the nonequilibrium system are written as,

$$B(T,p) = \Big(\frac{2\Gamma m_s(T,p)}{(d-1)\sigma_{SOS}^{(p)}(T)}\Big)^{\frac{-d}{d+1}} A(T,p)^{-\frac{1}{d+1}} \tag{5.25}$$

$$C(T,p) = \frac{2\Gamma m_s(T,p)}{(d-1)\sigma_{SOS}^{(p)}(T)} B(T,p) \tag{5.26}$$

These equations are structurally identical to those formulated for the equilibrium system, eqs. (5.8)-(5.12). The difference between these equations for $p \neq 0$ and their counterparts in equilibrium rests on the nonequilibrium generalized observables $\Omega_d(T,p)$, $m_s(T,p)$ and $\sigma_{SOS}^{(p)}(T)$. Using Avrami's law[23, 78] we can write the mean lifetime of the metastable state as a function of the stable phase volume fraction for $p \neq 0$,

$$\tau(\Phi_s;T,p,h) = t_0(T,p,h)\Big[\frac{d+1}{\Omega_d(T,p)} \ln\big(\frac{1}{1-\Phi_s}\big)\Big]^{\frac{1}{d+1}} \tag{5.27}$$

This equation yields the mean lifetime of a metastable state for a system with $p \neq 0$ and *infinite* size. However, the systems we study are always finite, with a typical size L. In this case the system will evolve from the metastable to the stable state nucleating one or several stable phase droplets (or via some other marginal mechanisms to be described later on), depending on the value of L and its relation to the other relevant length scales in the system, namely $\mathcal{R}_c(T,p,h)$ and $\mathcal{R}_0(T,p,h)$.

In general, the mean droplet separation $\mathcal{R}_0$ for intermediate values of the parameters (as the ones we are interested in) is much larger than the critical droplet size, $\mathcal{R}_c \ll \mathcal{R}_0$. In this case the picture based on nucleation of droplets is valid, because the droplet volume fraction is small enough so we can neglect correlations between droplets. For very strong magnetic fields (not studied in this thesis) the picture based on localized droplets is no longer valid, and now the system decays from the metastable state via long-wavelength Goldstone modes reminiscent of spinodal decomposition. The region of parameter space where the localized droplets picture is no longer valid is known as the Strong Field Region (SF)[26], and the magnetic field signaling the transition between the intermediate field region, where the metastable-stable transition proceed through the nucleation of one or several critical droplets, and the Strong Field Region is known as *Mean Field Spinodal Point*, $|h_{MFSP}|$.[26, 80]

We now assume a large system size, such that,

$$L \gg \mathcal{R}_0 \gg \mathcal{R}_c \tag{5.28}$$

In this case the system evolves from the metastable state to the stable one through the nucleation of many stable phase critical droplets. This region is known as *Multidroplet Region* (MD)[26]. In order to calculate the mean lifetime in this case, we perform a partition of the system in $(L/\mathcal{R}_0)^d$ cells of volume $\mathcal{R}_0^d$. Each cell decays from the metastable state to the stable one in an independent Poisson process of rate $\mathcal{R}_0 I = t_0^{-1}$. This rate is the probability per unit

time that a cell with volume $\mathcal{R}_0^d$ will decay to the stable phase. The stable phase volume fraction is in this case self-averaging, and hence $\Phi_s^{(i)}$ inside any cell $i$ coincides approximately with the total stable phase volume fraction of the system at any time. Therefore the mean lifetime of the metastable state will be in this case approximately equal to the result obtained for the infinite system,

$$\tau_{MD}(\Phi_s; T, p, h) = t_0(T, p, h)\Big[\frac{d+1}{\Omega_d(T,p)} \ln\big(\frac{1}{1-\Phi_s}\big)\Big]^{\frac{1}{d+1}} \tag{5.29}$$

This lifetime does no depend on system size $L$. Additionally, it can be shown that the relative standard deviation associated to the lifetime in region MD, $r_\tau$, is very small (this is also observed in SF region), so both regions (MD and SF) are termed *Deterministic Region* in literature[26].

For smaller system sizes, such that

$$\mathcal{R}_0 \gg L \gg \mathcal{R}_c \tag{5.30}$$

the random nucleation of a *single* stable phase critical droplet in a Poisson process of rate $L^d I$ is the rate-determining step in the metastable-stable transition. Therefore in this case a single stable phase droplet will nucleate and it will rapidly grow to cover the whole system much before any other critical droplet appears. The time the system needs to nucleate a critical droplet is much larger than the time this critical droplet needs to grow and cover the whole system. Hence we can approximate in this case the metastable state mean lifetime with $\tau_{SD} = (L^d I)^{-1}$, i.e.,

$$\tau_{SD}(T, p, h) = \frac{|h|^{-(b+c)}}{A(T,p)L^d} e^{\frac{\Xi(T,p)}{|h|^{d-1}}} \tag{5.31}$$

The parameter space region where the exit from the metastable state proceeds through the nucleation of a single droplet is called *Single Droplet Region* (SD)[26]. The mean lifetime in this region only exhibits a slight dependence on the threshold $\Phi_s$, since the time the system needs to nucleate a critical droplet is much larger than the time the droplet needs to grow and cover the whole system. On the other hand, in this case it can be shown that the relative standard deviation associated to the lifetime, $r_\tau$, is of order unity, so we call this region *Stochastic Region*[26].

The magnetic field which signals the transition between the Single Droplet Region (SD) and the Multidroplet Region (MD) is known as *Dynamic Spinodal Point*, $|h_{DSP}|$.[26, 80] This Dynamic Spinodal Point can be estimated from the condition $\mathcal{R}_0(T, p, h_{DSP}) \propto L$. Taking into account the expression derived for $\mathcal{R}_0$ in the nonequilibrium system, eq. (5.23), we have in the limit $h \to 0$ that the Dynamic Spinodal Point is given by,

$$|h_{DSP}| = \Big[\frac{\Xi(T,p)}{\ln(L)}\Big]^{\frac{1}{d-1}} \tag{5.32}$$

where the function $\Xi(T, p)$ is defined in eq. (5.24). $|h_{DSP}|$ converges towards zero in the limit $L \to \infty$, which involves that the only relevant process in this

large system size limit is that of nucleation of multiple droplets. However, this convergence is logarithmic, i.e. very slow, so the exit process from the metastable state via the nucleation of a single droplet of the stable phase will be measurably even for macroscopic systems. On the other hand, the Mean Field Spinodal Point, $|h_{MFSP}|$, which separates the MD and SF regions, can be roughly estimated from the condition $2\mathcal{R}_c \approx \xi_{ms}$, where $\xi_{ms}$ is the correlation length in the metastable phase.[26] When this condition holds, the correlation between droplets is relevant, so the description based on the droplet nucleation process is no longer valid. For temperatures well below the critical one, the correlation length $\xi_{ms}$ is small, of the same order of magnitude that the lattice spacing, so $\xi_{ms} \approx 1$. Using this observation in the above condition, we obtain the Mean Field Spinodal Point,

$$|h_{MFSP}| = \frac{(d-1)\sigma^{(p)}_{SOS}(T)}{m_s(T,p)} \tag{5.33}$$

Finally, there is a last possibility, captured by the condition,

$$\mathcal{R}_0 \gg \mathcal{R}_c \gg L \tag{5.34}$$

In this case the critical droplet size is larger than the system size, and the demagnetization process from the metastable state proceeds through the *coherent* rotation of all spins in the system. This mechanism is relevant only for very small system sizes and for very weak magnetic fields. The parameter space region where this mechanism is observed is known as the *Coexistence Region* (CE), and the magnetic field separating CE and SD regions is known as *Thermodynamic Spinodal Point*, $|h_{THSP}|$.[26]

The above analysis allows us to investigate the finite size effects which affect the properties of the mean lifetime of the metastable state in the nonequilibrium system. In the following we want to check these theoretical predictions using Monte Carlo simulations of the metastable-stable transition. We thus build a square system with size L, subject to periodic boundary conditions. We impose as initial condition a state with all spins up, in such a way that under the action of a negative magnetic field this initial state is metastable. We let evolve the system under these conditions using Glauber dynamics, eq. (2.3). The system rapidly evolves from the initial state to a state in the metastable region, with magnetization close to $+1$. After this fast initial relaxation, the system spends a long time wandering around the metastable state. Eventually it will nucleate one or several critical droplets of the stable phase (assuming our parameters are such that the system is in the SD or MD regions), which will grow rapidly making the system to evolve from the metastable state to the stable one, where it stays forever. We define the mean lifetime of the metastable state, $\tau(T, p, h)$, as the average first passage time (in Monte Carlo Steps per spin, MCSS) to $m = 0$. Hence in order to calculate the mean lifetime from our equations we must use $\Phi_s = 0.5$ due to this convention. In practice the metastable state lifetime can be a long as $10^{40}$ MCSS, so we need to use Monte Carlo with

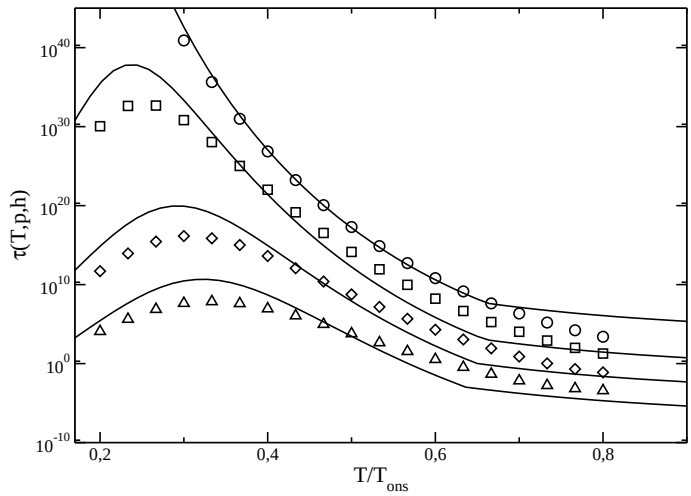


Figure 5.6: Semilogarithmic plot for the mean lifetime of the metastable state as a function of temperature for different values of $p$, as obtained in Monte Carlo simulations. We study here a system with size $L = 53$, subject to periodic boundary conditions and with $h = -0.1$, and we average over $N_{exp} = 1000$ independent runs. In particular, from top to bottom, $p = 0$(◯), $0.001$(□), $0.005$(◊) and $0.01$(△). The continuous lines are the theoretical predictions for each case. For the shake of clarity, we rescale the $n$-th curve (in the aforementioned order) by a factor $10^{-2(n-1)}$. Error bars are smaller than symbol sizes.

Absorbing Markov Chains (MCAMC) algorithms in order to perform the simulations. In particular, we have used the $s - 1$ MCAMC algorithm, together with the slow forcing approximation[4]. These advanced algorithms are presented in Appendix A. In order to improve our statistics for the lifetime, we simulate $N_{exp}$ different metastable state demagnetization experiment, averaging the lifetime over all them.

Fig. 5.6 shows the mean lifetime of the metastable state, as defined in the above paragraph, in semilog scale, as a function of temperature for different values of $p$, as measured in Monte Carlo simulations for a system with size $L = 53$, with $h = -0.1$ once we average over $N_{exp} = 1000$ different runs. This figure also shows the theoretical predictions, based on eqs. (5.29) and (5.31). For each temperature $T$ and nonequilibrium parameter $p$ ($h = -0.1$ is fixed) we evaluate whether the system is in the MD or SD regions calculating $\mathcal{R}_0(T, p, h)$ and comparing it with the system size $L$. Consequently we use expressions (5.29) or (5.31) to predict the lifetime. In practice we observe that most of the studied temperature interval in Fig. 5.6 lies on the SD region. The

[4]Whenever we apply the slow forcing approximation, we ensure that the forcing rate $\phi$ (see Appendix A) is slow enough so we have reached the slow forcing limit, where the measured observables do not depend on the applied forcing. Notice on the other hand that when we apply the slow forcing approximation, the metastable state mean lifetime is derived from the stable phase growth and shrinkage rates, see Appendix A.

only free parameters in our theory are the constant $\Gamma$ which related the radial growth velocity to the inverse of the critical droplet size, see eq. (5.20), and the non-universal amplitude factor $\mathcal{A}(T,p) \equiv A(T,p)|h|^{b+c}$ that appears in the nucleation rate $I(T,p,h)$, eq. (5.21). We fixed the constant $\Gamma$ in each case when we studied the radial growth velocity in the previous section, where we obtained $\Gamma \in [\frac{1}{5}, \frac{1}{4}]$ depending on the value of $p$. For the amplitude factor $\mathcal{A}(T,p)$ we assume that its temperature dependence is weak as compared to the exponential dependence on temperature which dominates the behavior of $I(T,p,h)$. Therefore we fix the value of $\mathcal{A}(T,p)$ to a constant which does not depend on temperature, $\mathcal{A}(p)$. For each $p$, $\mathcal{A}(p)$ is derived from the best fit between the theoretical prediction and computational results (notice that $\mathcal{A}(T,p) \approx \mathcal{A}(p)$ only produces a vertical shift, in semilogarithmic scale, in the mean lifetime curve).

As we can observe in Fig. 5.6, in the equilibrium system the mean lifetime grows monotonously as temperature decreases (moreover, $\tau(T,p=0,h)$ grows exponentially with $1/T$, as predicted by nucleation theory). However, the mean lifetime for $p \neq 0$ grows as temperature decreases, up to certain nonzero temperature $T^{(\tau)}_{max}(p,h)$ where the lifetime reaches a maximum, after which the lifetime change its tendency and decreases as temperature decreases. Hence we see that for any $p \neq 0$ the metastable state survives a maximum time for a nontrivial, nonzero temperature $T^{(\tau)}_{max}(p,h)$. Therefore if we need to maximally prolong the lifetime of a metastable state in a real magnetic thin film, which shows the kind of impure behavior parameterized by the nonequilibrium perturbation $p$ (think for instance of the problem posed by magnetic storage of information in technological applications), the most effective method will not consists in a *blind* decrease of temperature, but in the search of the temperature $T^{(\tau)}_{max}(p,h)$ for which the metastable states has the longest lifetime. On the other hand, the theoretical results for the lifetime reproduce rather well, at least from the qualitative and semi-quantitative point of view, the Monte Carlo results. The theory predicts a maximum in $\tau(T,p \neq 0,h)$ for certain nonzero temperature, which coincides with the one observed in simulations. This non-monotonous behavior of the mean lifetime is inherited again from the non-monotonous behavior of surface tension in the nonequilibrium system. Hence the interfacial properties of the system determine in a fundamental way the dynamical and statical processes related to metastability. On the other hand, from the quantitative point of view, our approximation for the lifetime of the metastable state for $p \neq 0$ differs somewhat from Monte Carlo results. In particular, we observe that although the general shape of the theoretical curves is similar to Monte Carlo curves, the theoretical curves are more steep than the computational results.

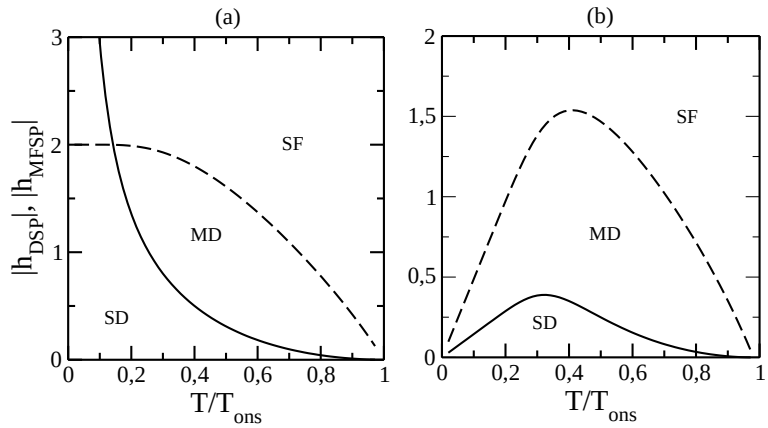


Figure 5.7: Dynamic Spinodal Point, $|h_{DSP}|(T, p)$, represented by a continuous line, and Mean Field Spinodal Point, $|h_{MFSP}|(T, p)$, represented by a dashed line, as a function of temperature for: (a) $p = 0$, and (b) $p = 0.01$. Notice the fundamental change in behavior for low temperatures when we compare the equilibrium case ($p = 0$) with the nonequilibrium one ($p \neq 0$).

### 5.3.4 Morphology of the Metastable-Stable Transition

An interesting question is to study the morphology of the metastable-stable transition as a function of the system parameters. This study will allow us to divide the parameter space in different regions, each one characterized by a well-defined typical morphology for the process of demagnetization of the metastable state. In order to characterize the different morphologies we study the Dynamic Spinodal Point, $|h_{DSP}|$, and the Mean Field Spinodal Point, $|h_{MFSP}|$, defined respectively in eqs. (5.32) and (5.33), as functions of temperature for different values of $p$. The field $|h_{DSP}|(T, p)$ separates the Single Droplet Region from the Multidroplet Region. Hence if $|h| < |h_{DSP}|$ the metastable-stable transition proceeds through the nucleation of a single droplet of the stable phase, while if $|h_{MFSP}| > |h| > |h_{DSP}|$ it proceeds through the nucleation of multiple droplets. On the other hand, the Mean Field Spinodal Point , $|h_{MFSP}|$, separates the Multidroplet Region from the Strong Field Region, where the nucleating droplet picture is no longer valid. The SF region is observed for $|h| > |h_{MFSP}|$.

Fig. 5.7.a shows the theoretical prediction for the fields $|h_{DSP}|(T, p)$ and $|h_{MFSP}|(T, p)$ as a function of temperature for a equilibrium system ($p = 0$) with size $L = 53$. The parameter space is divided in three different regions. The SD region, characterized by the nucleation of a single critical droplet, dominates the morphology of the metastable-stable transition for low temperatures in this case ($p = 0$). For intermediate temperatures, if the magnetic field is high enough, the metastable state demagnetization process proceeds through the nucleation of multiple critical droplets, which is the typical morphology of MD region. Finally, for very strong magnetic fields the metastable-stable tran-

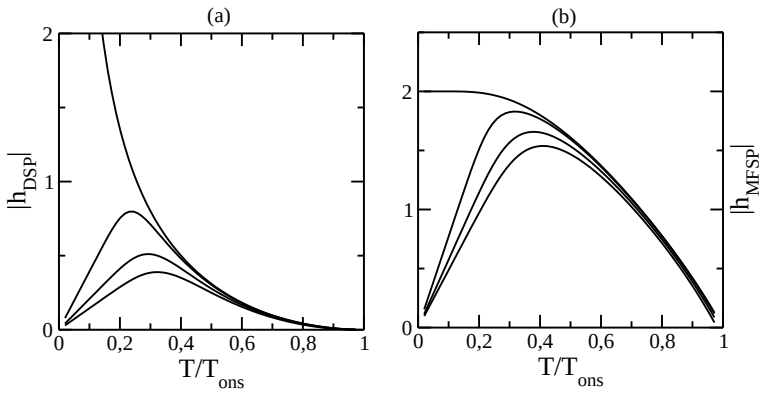


Figure 5.8: (a) $|h_{DSP}|(T, p)$ as a function of temperature for $L = 53$ and several different values of $p$. In particular, from top to bottom, $p = 0$, $0.001$, $0.005$ and $0.01$; (b) $|h_{MFSP}|(T, p)$ as a function of temperature for the same values of $p$. Notice the fundamental change of behavior in both $|h_{DSP}|(T, p)$ and $|h_{MFSP}|(T, p)$ in the low temperature limit for any $p \neq 0$ as compared to the equilibrium case.

sitions exhibits a morphology typical of SF region, where the concept of mutually independent nucleating droplets is not valid. These theoretical results about the morphology of the metastable-stable transition, first derived in refs. [26, 81], are perfectly verified in Monte Carlo simulations of the system with $p = 0$.[26, 81] Therefore, for a fixed (intermediate) magnetic field, the typical sequence of morphologies as temperature decreases from temperatures close to the critical one is SF→MD→SD.

Fig. 5.7.b shows the same results than Fig. 5.7.a but for a system with $p = 0.01$, i.e. under nonequilibrium conditions. As in equilibrium , the parameter space is divided in three different regions. However, for $p \neq 0$ there is a fundamental difference as compared to the equilibrium case: both $|h_{DSP}|(T, p)$ and $|h_{MFSP}|(T, p)$ converge towards zero in the low temperature limit for $p \neq 0$. This implies that the SD region does not dominates now at low temperatures. Instead, we observe that there is a region for intermediate temperatures and weak magnetic fields where the SD region determines the morphology of the metastable-stable transition. This region disappears if we excessively increase or *decrease* the temperature, appearing instead the MD region. Hence, for intermediate magnetic fields the characteristic morphology sequence in the metastable-stable transition will be SF→MD→SF as we decrease temperature from values near the critical one. For weak magnetic fields this sequence will be SF→MD→SD→MD→SF.

Fig. 5.8.a shows the theoretical prediction for the Dynamic Spinodal Point, $|h_{DSP}|(T, p)$, as a function of temperature for varying $p$ in a system with size $L = 53$. Apart from the fundamental change of behavior observed in $|h_{DSP}|(T, p)$ at low temperatures for $p \neq 0$, we observe that, as $p$ increases the SD region decreases, increasing the MD region. This behavior is easy to understand from a

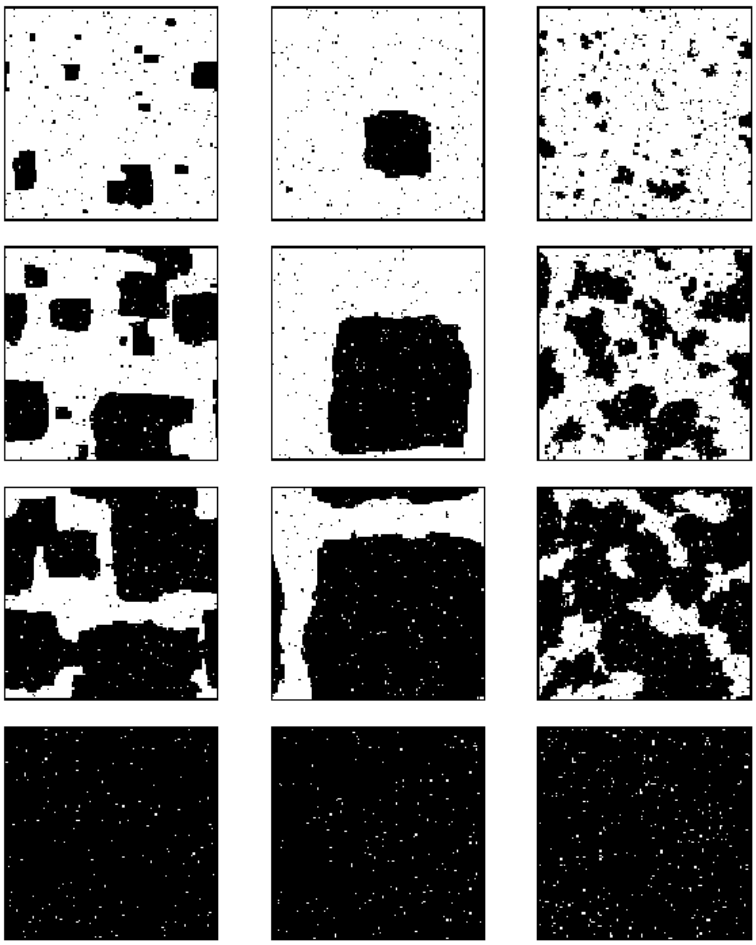

Figure 5.9: Snapshots of the metastable-stable transition for a system with size $L = 128$, with $p = 0.01$, $h = -0.25$ and temperatures $T = 0.1T_{ons}$ (left column), $T = 0.3T_{ons}$ (central column) and $T = 0.7T_{ons}$ (right column). The first row corresponds to a stable phase volume fraction $\Phi_s = 0.1$, the second one to $\Phi_s = 0.4$, the third one to $\Phi_s = 0.7$ and the last one tho the stable state for each temperature. Notice that, while for $T = 0.1T_{ons}$ and $T = 0.7T_{ons}$ the decay from the metastable state proceeds through the nucleation of multiple droplets, for the intermediate temperature $T = 0.3T_{ons}$ this transition proceeds through the nucleation of a single droplet, in total agreement with the theoretical predictions (see the main text).

phenomenologic point of view, because the nonequilibrium perturbation $p$ acts as a noise with non-thermal origin, affecting mainly the most ordered regions in the system (remember the definition of effective temperature in Chapter 4), so the presence of $p \neq 0$ favours the nucleation of new stable phase droplets in the metastable bulk, favouring in this way the MD morphology at the expense of the SD region. Analogously, Fig. 5.8.b shows the theoretical prediction for $|h_{MFSP}|(T, p)$ as a function of $T$ for varying $p$. We observe here that as we increase $p$, the SF region grows at the expense of the MD region.

Finally, if we take a constant magnetic field $h = -0.25$ in Fig. 5.7.b, where we plot $|h_{DSP}|(T, p)$ and $|h_{MFSP}|(T, p)$ as a function of $T$ for a system with $p = 0.01$ and $L = 53$, we observe that the theory points out that for a temperature $T = 0.1T_{ons}$ the morphology associated to the metastable-stable transition will be that of the MD region. For $T = 0.3T_{ons}$ this morphology will be the typical of SD region, while for $T = 0.7T_{ons}$ we again will recover the MD morphology. Fig. 5.9 shows a series of snapshots for the temporal evolution of a system with size $L = 128$,[5] with periodic boundary conditions and with a magnetic field $h = -0.25$, for $p = 0.01$ and temperatures $T = 0.1T_{ons}$, $0.3T_{ons}$ and $0.7T_{ons}$. It is remarkable that, in agreement with the theoretical predictions, the metastable-stable transition proceeds through the nucleation of multiple droplets for both $T = 0.1T_{ons}$ and $T = 0.7T_{ons}$, while it proceeds through the nucleation of a single droplet for the intermediate temperature $T = 0.3T_{ons}$. Therefore, the fundamental differences that the approximation predicts in the low temperature limit for the decay morphology between the equilibrium and the nonequilibrium cases are verified in Monte Carlo simulations.

## 5.4 Conclusion

In this chapter we have developed a nucleation theory for the nonequilibrium ferromagnetic system, in order to understand the dynamics of the metastable-stable transition in such system.

We have generalized the equilibrium nucleation theory[26, 71], based on a picture where stable phase droplets nucleate in the metastable bulk, in order to build the nonequilibrium dynamic theory. The central magnitude of nucleation theory is the free energy cost of a droplet of the stable phase with radius $R$. In our generalization we have hypothesized the existence of certain nonequilibrium potential $\mathcal{F}(R)$, which controls the exit from the metastable state, and plays in the system the same role than the droplet free energy in equilibrium. Moreover, we have proposed, based on phenomenological grounds, a particular expression for this nonequilibrium potential, which is *formally* identical to the droplet equilibrium free energy.

[5] The theoretical predictions about the morphology of the metastable-stable transition that we perform using the curves associated to a system with size $L = 53$ are almost identical to the predictions we would perform for a system size $L = 128$. This is so because the logarithmic dependence of $|h_{DSP}|(T, p)$ on the system size $L$ and the independence of $|h_{MFSP}|(T, p)$ on $L$. In Fig. 5.9 we use a system size $L = 128$ for the shake of clarity.

There are two competing terms in the nonequilibrium potential $\mathcal{F}(R)$: a volume term, which favours the droplet growth, and a surface term, which hinders such growth. The physical observables which determine the relative importance of both terms are $m_s(T,p)$, $\sigma_0(T,p)$ and $\Omega_d(T,p)$, where $m_s(T,p)$ is the spontaneous magnetization of the nonequilibrium system for zero magnetic field, $\sigma_0(T,p)$ is the surface tension along one of the primitive lattice vectors for $h = 0$, and $\Omega_d(T,p)$ is the form factor which relates the droplet volume to its radius, all these observables defined for temperature $T$ and nonequilibrium perturbation $p$. Although we do not know the exact expression for any of these observables when $p \neq 0$, we have obtained in previous chapters very good approximations to all of them.

We write a nucleation theory for $p \neq 0$ using all this information. From this theory we are able to correctly predict the behavior and the properties of fundamental observables associated to the dynamic problem of metastability. For instance, the extended nucleation theory precisely predicts the dependence on $T$ and $p$ of the critical droplet radius, $\mathcal{R}_c(T,p,h)$. In particular, we find that while the equilibrium system shows a critical droplet size which monotonously increases as temperature decreases, the critical droplet size for the nonequilibrium system ($p \neq 0$) exhibits a maximum as a function of temperature, which depends on $p$. In the same way, the generalized nucleation theory approximately predicts the growth velocity of a stable phase droplet under nonzero magnetic field, $v_0(T,p,h)$. We observe that for $p \neq 0$ this velocity shows a minimum for certain temperature, $T^{(v)}_{min}$, growing for $T < T^{(v)}_{min}$. The mean lifetime of the metastable state, defined as the average first passage time to a zero magnetization state, $\tau(T,p,h)$, is also correctly predicted by the theory. In the same way than for the previously discussed observables, the fundamental feature distinguishing the equilibrium and nonequilibrium cases is the fact that, for $p \neq 0$, the mean lifetime $\tau(T,p,h)$ is non-monotonous with temperature, showing a maximum for a given nonzero temperature $T^{(\tau)}_{max}$, while in the equilibrium case the lifetime grows monotonously as temperature decreases. Finally, the generalized theory also describes correctly the different typical morphologies which characterize the metastable-stable transition. The dominant typical morphology in the equilibrium system at low temperatures is that characterized by the nucleation of a single critical droplet, dominating at higher temperatures the nucleation of multiple droplets. For the nonequilibrium system this behavior enriches considerably. We observe for $p \neq 0$ that the morphology characterized by the nucleation of the single droplet dominates for intermediate temperatures, being the characteristic morphology for low and high temperatures that associated to the nucleation of multiple droplets. All the theoretical predictions have been checked in Monte Carlo simulations of the nonequilibrium system.

The generalized nucleation theory allows us to describe in an approximate manner the dynamics of the metastable-stable transition in the nonequilibrium ferromagnetic system. An important conclusion derived from this study is that the properties of the interface determine in a fundamental way the exit dynam-

ics from the metastable state. All the fundamental differences that we observe (and predict) in this dynamic process between the equilibrium and nonequilibrium cases can be easily understood once we know the properties of the interface for $p \neq 0$, which were studied in Chapter 4, and how they compare with the equilibrium interfacial properties. In particular, the non-monotonous behavior of surface tension as a function of temperature for $p \neq 0$ is inherited by all the observables associated to the metastable decay process, namely $\mathcal{R}_c$, $\nu_0$, $\tau$, $|h_{DSP}|$ and $|h_{MFSP}|$.

The extended nucleation theory is based on a phenomenologic, non-justified hypothesis which assumes the existence and the particular form of a nonequilibrium potential which controls the exit from the metastable state, in a similar way to that of the free energy in equilibrium. This hypothesis allows us to obtain many results about the dynamics of the metastable-stable transition, which correctly reproduce the behavior of the real system (as obtained from Monte Carlo simulations). The fundamental ingredient in this hypothesis consist in assuming that, similarly to what happens in equilibrium systems, the droplet dynamics is determined by the competition between the droplet bulk and its surface, in such a way that if we correctly capture the bulk and interfacial behavior we will be able to obtain much information about the metastable state demagnetization process. This observation, which yields very good results for the nonequilibrium ferromagnetic system here studied, may be generalizable to many other nonequilibrium systems showing metastability.

Finally, our results may also be relevant from the technological point of view. Think for a while on magnetic systems used for magnetic storage of information (previously discussed in Chapter 2). Such systems are magnetic thin films composed by many small monodomain ferromagnetic particles. These particles, for which Ising-like models are in some cases a good description, generally show an impure behavior related to the presence of lattice, bond and/or spin disorder, quantum tunneling, etc. Therefore we expect that our simplified nonequilibrium system will model adequately (at least in a first approximation) the behavior of these magnetic materials. On the other hand, a main concern in these magnetic systems is to retain for as long as possible the stored information. The information is stored in these systems magnetizing with a strong magnetic field the particular domains, defining in this way a bit of information for each magnetized particle. Due to the interaction with the external medium, the different particles suffer small random magnetic fields, which involve the eventual appearance of metastable states in such magnetic particles. The resistance of the stored information to these external perturbations strongly depends on the properties of the underlying metastable states, including the details of their decay. As we have derived in this chapter, the presence of impurities, parameterized in our model by the nonequilibrium perturbation $p$, affects in a fundamental way the properties of metastable states. In particular, if we want to prolong as much as possible the metastable state lifetime, we must not *blindly* decrease the system temperature, but we must look for the temperature $T_{max}^{(\tau)}$ for which the metastable state lifetime is maximum.

# Chapter 6

# Scale Free Avalanches during Decay from Metastable States in Impure Ferromagnetic Nanoparticles

## 6.1 Introduction

In previous chapters we have studied the problem of metastability in a nonequilibrium ferromagnetic system which we think correctly models the behavior of some real impure magnetic materials. We have developed a nonequilibrium nucleation theory which explains the dynamics of the metastable-stable transition in this system. This theory is based on a phenomenologic hypothesis about the existence of a nonequilibrium potential that controls the exit from the metastable state in a way similar to that of the free energy in equilibrium systems. Such nonequilibrium potential depends on the properties of both the bulk and the interface separating the stable phase from the metastable one. We have derived these properties using mean field-like approximations.

This theoretical and computational study has shown that the presence of nonequilibrium conditions considerably enriches the behavior of the system, mainly at low temperatures. In particular, we observe that the properties of metastable states strongly depend on the properties of the interface separating the metastable phase from the stable one. Thus, the non-monotonous behavior of surface tension as a function of temperature in the nonequilibrium model is inherited by most of the physical observables that characterize the dynamics of the metastable-stable transition, as for instance the metastable state mean lifetime $\tau$, the critical droplet size $\mathcal{R}_c$, etc.

As we have previously discussed, the results of this analysis, apart from their theoretical value, are relevant from the technological point of view. Con-

sider again the problem posed by magnetic storage of information. We already know that the resistance of stored information in magnetic recording media strongly depends on the properties of the underlying metastable states of the magnetic particles that compose such materials. Retaining the orientation of such domains for as long as possible is a main technological concern. Another principal aim during recording is to maximize the amount of information stored. This requires manufacturing very dense media which is also important for many other areas of present and emergent technologies.[83] One needs in practice to create and control fine grains, i.e., magnetic particles with *borders* whose size ranges from mesoscopic to atomic levels, namely, clusters of $10^4$ to $10^2$ spins, and even smaller ones. Though experimental techniques are already accurate for the purpose,[84, 85] the underlying physics is much less understood than for bulk properties. In particular, one cannot assume that such particles are neither *infinite* nor *pure.* That is, they have free borders, which results in a large surface/volume ratio inducing strong border effects, and impurities, which might dominate the behavior of near-microscopic particles; in fact, they are known to influence even macroscopic systems.

The effects that free borders induce on the properties of the metastable-stable transition have been already studied in equilibrium systems.[27, 28] In this case it is observed that the system evolves from the metastable state to the stable one through the *heterogeneous* nucleation of one or several critical droplets which always appear at the system's border.[27] That is, the free border acts as a droplet condenser. This is so because it is energetically favorable for the droplet to nucleate at the border. Apart from the observed heterogeneous nucleation, the properties of the metastable-stable transition in equilibrium ferromagnetic nanoparticles do not change qualitatively as compared to the periodic boundary conditions case.[28] In our nonequilibrium system we obtain similar results, namely heterogeneous nucleation and the same qualitative nucleation properties. However, it is very interesting to study the fluctuations or noise that the nonequilibrium system exhibits as it evolves towards the stable state subject to the combined action of free borders and the nonequilibrium perturbation. As we will describe below, the metastable-stable transition in this case proceeds through *avalanches*. These burst-like events, present in our model case, characterize the dynamics of an enormous amount of nonequilibrium complex systems.[102]

In general, noise in magnetic systems has been shown to be of major importance in many technological applications, [86, 87] as well as from the theoretical point of view[88]. The celebrated Barkhausen Noise, e.g. the magnetic noise by which a impure ferromagnet responds to a slowly varying magnetic field, has been profusely used as a non−invasive material characterization technique [87, 89]. The statistical properties of Barkhausen Noise are extremely sensitive to microstructural changes in the material, thus providing a sharp tool in order to characterize such system. Its applications include microstructure analysis, fatigue testing, measurement of fundamental properties of magnetic materials, stress analysis, etc. [87] Theoretically, systems exhibiting Barkhausen Noise have been studied as a paradigm of complex spatio-temporal extended sys-

tems showing generically scale invariance.[88, 90] Barkhausen systems show avalanche−like dynamics, where avalanches are scale-free. Furthermore, this property is found *naturally* in these magnetic materials, i.e. no fine tuning is needed in order to reach such scale invariant state.

Scale-free noise is observed ubiquitously in Nature,[91] and its origin still remains unknown. It receives the generic name of $1/f$ *noise*,[92] and Barkhausen Noise is just a particular realization. This name reflects the power law behavior of the fluctuation's power spectrum, which also involves a power law behavior for avalanche distributions. There are many natural systems (besides Barkhausen materials) which show $1/f$ noise. Some examples are: biological (e.g. human cognition [93]), economical (e.g. the number of stocks traded daily [94]) and social systems, earthquakes [95], superconductors [96], combustion, piles of rice [97] and sand [98], crumpling paper [99], music [100], etc. The *universality* of this phenomenon points out the existence of a common underlying mechanism present in all the above apparently unrelated situations. In recent years it has been claimed that a new idea, namely *Self Organized Criticality* (SOC) [101, 102], could be behind this universal, scale invariant phenomenon. Self-Organized Criticality is based on the idea that complex, scale-free behavior can develop *spontaneously* in many body systems whose dynamics is dominated by at least two very different time scales, and where metastability is observed.[102] In this picture, the system would evolve towards a *critical* state where avalanches of all scales appear. In particular, Barkhausen Noise has been thought as an experimental realization of SOC, thus provoking an active and excited research in this field. However, experimental works are not able to conclude on the underlying mechanism responsible of this $1/f$ noise. Furthermore, experimentalists cannot even affirm the existence of any underlying critical point[88], neither a plain old one nor a SOC one.

Summing up, the scenario to be investigated in this chapter involves the formation and evolution of a stable phase droplet inside the metastable parent phase in our nonequilibrium (i.e. impure) ferromagnetic system subject to free boundaries. Under the combined action of both the nonequilibrium perturbation and free boundaries, the formation of a nucleus of the stable phase turns out to proceed by avalanches. In addition to small events, which show up as a completely random, thermal effect (*extrinsic noise* [88]) having an exponential distribution, we describe well-defined *critical avalanches.* These are typically much larger than the extrinsic noise, while they *apparently* show no characteristic temporal and spatial scale. In particular, we find size and lifetime distributions that follow power laws, $P(\Delta_m) \sim \Delta_m^{-\tau}$ and $P(\Delta_t) \sim \Delta_t^{-\alpha}$ with $\tau \to 1.71(4)$ and $\alpha \to 2.25(3)$ for large enough systems. This holds up to an exponential cutoff which grows as a power law of system size. A detailed analysis of these scale free avalanches reveals that they are in fact the combined result of many avalanches of different well-defined *typical* size and duration. That is, the simplicity and versatility of our model system allows us to identify many different types of avalanches, each type characterized by a probability distribution with well defined typical size and duration, associated with a particular *curvature* of the domain wall. Due to free borders and the microscopic impurity the system

visits a broad range of domain wall configurations, and thus the combination of these avalanches generally results in a distribution which exhibits several decades of power law behavior and an exponential cutoff. However, this apparent scale-free behavior does not mean that avalanches are critical, in the sense of a second order phase transition where diverging correlation lengths appear. Instead, we find that avalanches in the magnetic nanoparticle have a large (but finite) number of different, gap-separated typical sizes and durations.

These observations led us to suspect that Barkhausen Noise, as defined above, might also come from the superposition of more elementary events. In fact, the $1/f$ noise behavior in this case is assumed to reflect topological rearrangements of domain walls,[104] which result in practice in a series of jumps between different metastable states, which is the basic process in our model. We strongly support this conjecture because our avalanche model reproduces many features previously observed in different experimental situations. For instance, the avalanche exponents we obtain are almost identical to those measured in some Barkhausen experiments [88], and our model system shows some properties, as for example *reproducibility* [105], observed in real magnetic materials. Up to now, theoretical explanations of Barkhausen Noise were based on the hypothesis of the existence of an underlying critical point, thus yielding the observed scale invariance. However, this assumption faces some fundamental problems, since experiments on Barkhausen Noise show no universality: experimental critical exponents are different for different conditions and materials, and expected universal observables in Barkhausen Noise are in practice very sensitive to microscopic details, which is against the concept of universality derived from a critical point. The conceptual framework we propose here for Barkhausen Noise solves this problem, since it does not imply the existence of an underlying critical point, and thus no universality is expected. The chances are that our observation that scale invariance originates in a combination of simple events, which we can prove in our model cases, is a general feature of similar phenomena in many complex systems [91].

The remainder of the chapter is organized as follows. In section 6.2 we briefly remind the model, introducing the free boundary conditions we use in this chapter. In section 6.3 we present our simulations, and the analysis of the avalanche distributions obtained. Section 6.4 is devoted to the search of an explanation for the observed behavior. Finally, in Section 6.5 we present the conclusions, paying special attention to the consequences derived from our results for the explanation of Barkhausen Noise in particular, and $1/f$ noise in general.

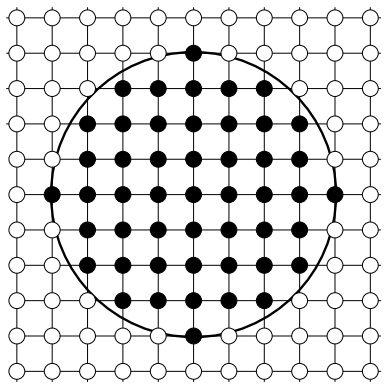

Figure 6.1: Schematic plot of the system subject to open circular boundary conditions. The spins are represented by black points. White points are empty nodes. Spins at the border nodes do not have nearest neighbor spins outside the circle.

## 6.2 The Magnetic Particle Model

In this chapter we consider a modification of the system studied in Chapters 2-5. This modification only involves a change on the implemented boundary conditions. The system is defined again on a two-dimensional square lattice, with binary spins $s_i = \pm 1$ on each node, $i \in [1, N]$. These spins interact among them and with an external magnetic field via the Ising Hamiltonian, eq. (2.1). We choose the transition rate to be the Glauber rate, defined in eq. (2.3). This rule describes a spin-flip mechanism under the action of two competing heat baths whose relative strength is characterized by the nonequilibrium parameter $p$, see eq. (2.3). For $p \neq 0$ the transition rate (2.3) asymptotically drives the system towards a nonequilibrium state, which essentially defers from the Gibbs (equilibrium) one.

Motivated by the experimental situation, we choose to study a finite, relatively small system subject to *open circular* boundary conditions. In order to implement these boundary conditions, we inscribe a circle of radius $R$ in the square lattice where the system is defined. Sites outside this circle do not belong to the system. In this way we define the free boundary: spins at the border sites inside the circle do not have nearest-neighbor spins outside the circle. Fig. 6.1 shows an example. The lattice is set initially with all spins up, $s_i = +1$ for $i = 1, ..., N$. Under a weak negative magnetic field, this ordered state is metastable, and it eventually decays to the stable state which, for low temperatures, corresponds to $m \equiv N^{-1} \sum_i s_i \simeq -1$. Investigating the influence of different boundary conditions on the relaxation, and how a small system compares with a macroscopic one, is a crucial issue when trying to understand better the behavior of particles of $\sim 10^3$ spins. For this reason we will also use other different boundary conditions (to be defined later), in order to understand the role played by the free boundary.

We mainly report here on a set of fixed values for the model parameters, namely, $J = 1$, $h = -0.1$, $T = 0.11T_{ons}$, and $p = 10^{-6}$, where $J$ is the (ferromagnetic) coupling constant, $h$ is the magnetic field, $T$ is the system temperature and $p$ is the nonequilibrium perturbation. This choice is dictated by simplicity and also because (after exploring the behavior for other cases) we came to the conclusion that this corresponds to an interesting region of the system parameter space. In fact, the field, which only aims to produce a convenient metastable situation, needs to be small —to avoid becoming a relevant parameter— but not too small that metastability lasts for a very long (unobservable) time. The restriction to this small value for $h$ also guarantees that the system is in a regime in which the decay is dominated by a single droplet (see section 5.3.4); otherwise a finite density of droplets, or even a more complex situation, may occur, as we have concluded in the previous chapter. The low value of $T$ allows for compact configurations, which are more convenient for analysis of clusters. Finally, our choice for $p$ corresponds to a *small enough* perturbation which induces interesting significant effects that are in fact comparable to the ones by other stochastic sources. In particular, a measure of the relative importance of the thermal ($T$) and non-thermal ($p$) noise sources can be obtained using the concept of interface effective temperature, $T^I_{eff}$, first introduced in section 4.4.2. For high temperatures, where the thermal noise dominates, $T^I_{eff}$ depends linearly on $T$, while for low temperatures, where the non-thermal noise source dominates, $T^I_{eff}$ is independent of $T$, converging to a nonzero value, see Fig. 4.5. For a fixed $p$ there is narrow range of temperatures where $T^I_{eff}$ changes its asymptotic tendency. In this temperature interval the relative importance of both noise sources is comparable. Hence the temperature $T = 0.11T_{ons}$ ensures for $p = 10^{-6}$ that both $T$ and $p$ have a comparable effect, see Fig. 4.5. For these values of the model parameters the system shows many metastable states between $m \approx +1$ and $m \approx -1$, which introduces interesting phenomena, as we will see below. Summing up, we believe that we are describing here typical behavior of our model, and the chances are that it can be observed in actual materials.

In spite of the free borders, which considerably accelerate the exit from the metastable state, the simulations reported here required in practice using the $s-1$ MCAMC algorithm[107, 44], together with the slow forcing approximation (see Appendix A).[45] We have checked that the results reported in this chapter do not depend on the implemented forcing.

## 6.3 Monte Carlo Results for Avalanche Statistics

We are concerned with demagnetization from an initial fully—ordered state with $m = +1$. This is subject to a negative (small) field, so that the system eventually relaxes towards the stable state with $m \approx -1$. The temporal relaxation typically shows three principal regimes (see Fig. 6.2):

1. After a very short transient time, $t_1$, the system reaches the metastable

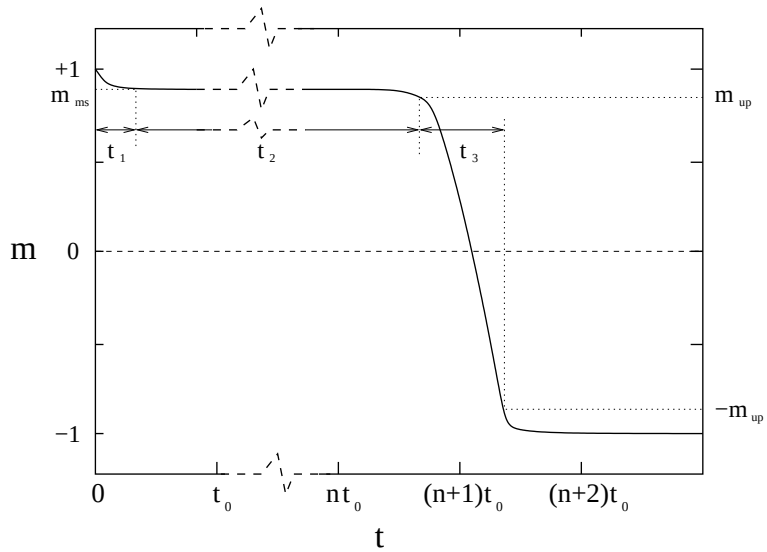


Figure 6.2: Sketch of a typical decay from a metastable state showing the different time regimes. Time units ($t_0$) are arbitrary. The threshold magnetizations, $m_{up}$ and $-m_{up}$, and the metastable magnetization, $m_{ms}$ are also shown. For the shake of clarity, time scales $t_1$, $t_2$ and $t_3$ have been plotted within the same order of magnitude, which is not the case in simulations and real systems.

state. The magnetization $m(t)$ is then observed to fluctuate, around its characteristic metastable value, $m_{ms}$, during a long time interval, $t_2$.

2. Suddenly at some time during such wandering, $m(t)$ decays in a time interval $t_3$ to a value near the stable magnetization, $m_{st}$. As we know this evolution proceeds through the nucleation of a critical droplet of the stable phase and its subsequent growth. Time scales are $t_1 << t_3 << t_2$. It turns out convenient to define the time $\tau_0$ at which this regime begins as the last time for which $m(t) = m_{up}$, where $m_{up} < m_{ms}$ is a given magnetization threshold set $m_{up} = 0.9$ here. We then define $t_3$ as the time interval between $\tau_0$ and the time at which $m(t) = -m_{up}$.

3. After this fast decay, $m(t)$ stays fluctuating around $m_{st}$.

As it is clear in Fig. 6.3, the relaxation of $m(t)$ occurs via a sequence of well−defined abrupt jumps. That is, when the system relaxation is observed after each MCSS, which corresponds to a 'macroscopic' time scale, strictly monotonic changes of $m(t)$ can be identified that we shall call *avalanches* in the following. One may think of other definitions of these avalanches, of course, so that we are somewhat arbitrary at this point, but we believe this does not significantly affect our results in this paper. Moreover, since our model system is subject to dynamical fluctuations, a clear−cut definition of avalanche is not

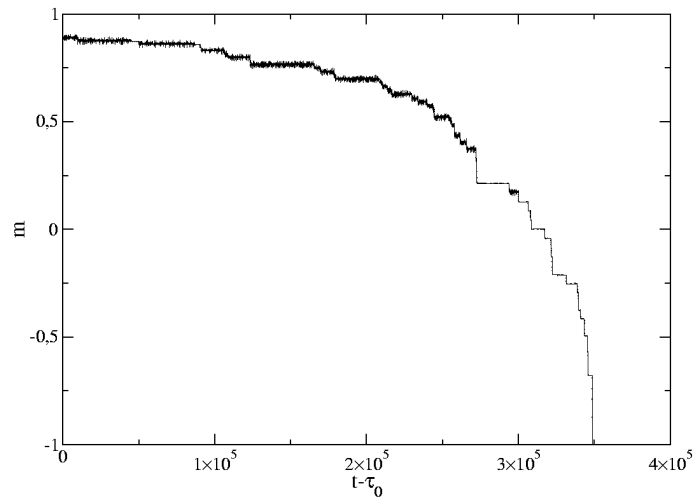


Figure 6.3: Decay from a metastable state for the circular system with radius $R = 30$, and the model parameters defined in the text. This figure corresponds to the $t_3$ region sketched in Fig. 6.2. The discrete, abrupt jumps in the magnetization (*avalanches*) are seen by direct inspection. Time is in units of MCSS (Monte Carlo Steps per Spin). Here $\tau_0$ is the time for which magnetization crosses the upper magnetization threshold $m_{up} = 0.9$. In this case $\tau_0 = t_1 + t_2 \sim 10^{30}$ MCSS, and notice that $t_3 \sim 3.5 \times 10^5$ MCSS.

possible, and thus this lack of precision will always exists. The important fact is that fluctuations on the microscopic, single−spin−flip scale are despised.

To be precise, consider the avalanche beginning at time $t_a$, when the system magnetization is $m(t_a)$, and finishing at $t_b$. We define its *size* and *lifetime* or *duration*, respectively, as $\Delta_m = |m(t_b) - m(t_a)|$ and $\Delta_t = |t_b - t_a|$. (We also studied $m(t_b) - m(t_a)$, i.e., positive and negative events. Such detail turns out to be irrelevant for the purposes here, however; in fact, large events cannot be positive in practice.). Alternatively, let us consider now the time evolution of the *activity*, defined as $A(t) = m(t+1) - m(t)$. It is just the magnetization change in an unit time (measured in MCSS). This observable is the analogous to voltage pulses observed in experiments on magnetic noise. [108, 109] An avalanche is thus comprised between two successive crossings of $A(t)$ with the origin. In this way, the avalanche size is proportional to the area below this curve, and its duration or lifetime is defined as the time interval between such crossings. Our interest is on the histograms $P(\Delta_m)$, $P(\Delta_t)$ and $P(\Delta_t|\Delta_m)$.

### 6.3.1 Global Avalanche Distributions

Fig. 6.4 shows, among other things, a semilog plot of $P(\Delta_m)$ for a circular nanoparticle with radius $R = 30$ (i.e. $N = 2828$ spins, as compared to $N \in [10^3, 10^4]$ spins in real magnetic nanoparticles), as obtained after performing $10^4$ different runs. Direct inspection of $P(\Delta_m)$ reveals the existence of two

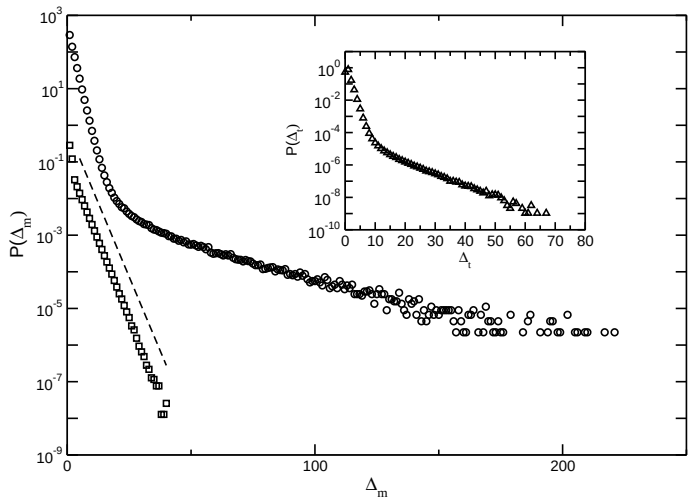


Figure 6.4: Here we show the avalanche size distribution for a circular magnetic nanoparticle of radius $R = 30$ (◯) and the same histogram for the semi–infinite system defined in the text (□). Results have been shifted in the vertical direction for the shake of clarity. The slope of the dashed line is a theoretical prediction for small avalanches. Notice the good accordance between theory and simulations. The inset shows the avalanche lifetime distribution for this circular particle.

well−defined different regimes: $(i)$ An exponential regime for small avalanches ($\Delta_m < 20$), $P(\Delta_m) \sim \exp(-\Delta_m/\bar{\Delta}_{small})$, where events have a typical size, namely $\bar{\Delta}_{small} \approx 1.4$, and $(ii)$ a second regime for larger avalanches with no easily identifiable distribution. In order to elucidate the nature of both regimes, and the physical origin of this crossover, we now introduce a modification of our model, where boundary effects are effectively absent.

Let us study again our system on the $L \times \infty$ square lattice we introduced in the previous chapter (see section 5.3.2 and Fig. 5.4) when studying the growth velocity of the interface. There we defined the system in a $L \times L$, with periodic boundary conditions along the $\hat{\mathbf{x}}$ (horizontal) direction, while the lattice is open along the $\hat{\mathbf{y}}$ direction. The initial configuration in this case consists in two horizontal stripes of height, respectively, $(1-\alpha)L$ (upper part of the cylinder), in which all spins are set $s_i = +1$, and $\alpha L$, in which all spins are set $s_i = -1$, with $\alpha = 0.15$. The interface moves upwards for the parameters in our simulations (remember, $T = 0.11T_C$, $h = -0.1$ and $p = 10^{-6}$). In order to simulate an infinite system in the interface movement direction, we perform a shift of the lattice in such a way that the interface does not *feel* the presence of the boundary and it advances indefinitely (see section 5.3.2 for more details). We choose $L = 53$, and thus $N = 2809$, very similar to the number of spins in the circular system. This system simulates the temporal evolution of a model's domain wall in an semi-infinite bulk.

Domain wall motion in this system proceeds also by avalanches (as defined

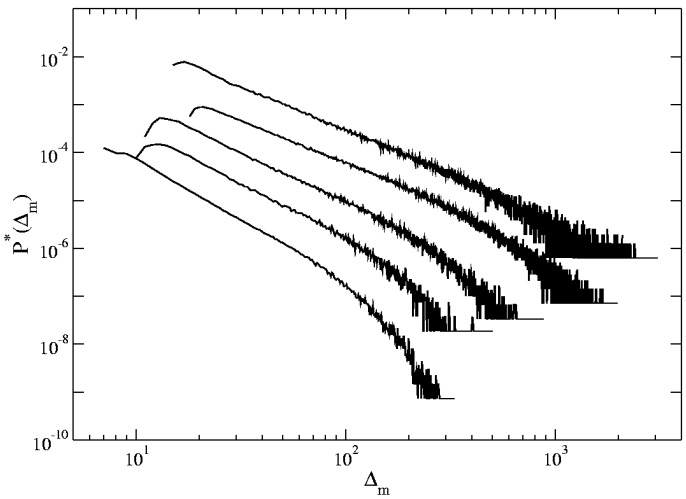


Figure 6.5: Large avalanche size distribution $P^*(\Delta_m)$ for the circular magnetic nanoparticle and for 5 different sizes. From top to bottom, $R = 120$, 84, 60, 42 and 30. Curves have been shifted in the vertical direction for visual convenience. The accumulated statistics goes from 15000 runs for the smallest size to 7000 experiments for the largest one.

above). Fig. 6.4 also shows the histogram $P(\Delta_m)$ for this semi-infinite system, where boundary effects are negligible. Comparing this histogram with the same curve for the circular particle, we observe that although the initial exponential regime is almost identical in both cases, the tail of $P(\Delta_m)$ corresponding to the second regime does not exist for the semi-infinite system. A similar result holds if we define our model in a square lattice with periodic boundary conditions, as we did in previous chapters, or if we set $p = 0$ in the circular nanoparticle. Thereby, the combined action of both free boundaries and impurities induces a new mechanism which is behind the large avalanches and essentially differs from the standard bulk noise driving the system and causing small, exponentially distributed avalanches only. It can be demonstrated analytically (see Appendix C for the details) that small events are *local* random fluctuations of a growing *flat* domain wall. It can be also shown that this small avalanches follow an exponential distribution of the form $P_{small}(\Delta_m) \sim \exp(-\Delta_m/\bar{\Delta}_{small})$, with a typical size,

$$\bar{\Delta}_{small} = \frac{1}{\ln\left[\frac{(1+p)(1+e^{2\beta|h|})}{p+e^{2\beta|h|}}\right]} \tag{6.1}$$

where $\beta = 1/k_B T$, and we set the Boltzmann constant $k_B = 1$. Fig. 6.4 also shows the analytical $P_{small}(\Delta_m)$ for comparison; the agreement with simulation is excellent.

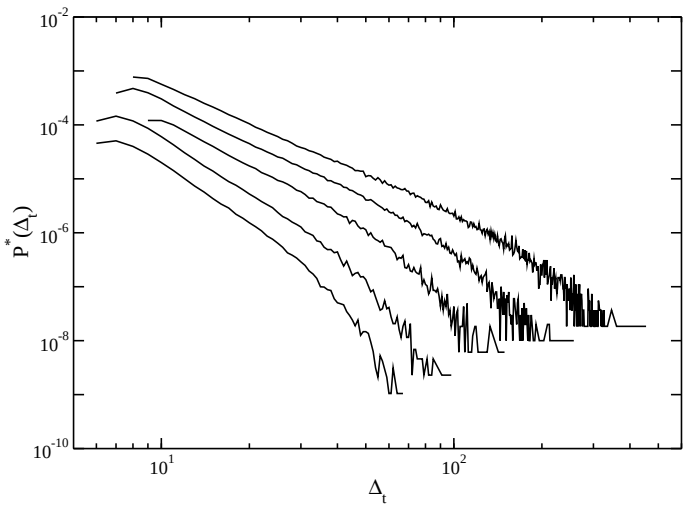


Figure 6.6: Large avalanche lifetime distribution $P^*(\Delta_t)$ for several different sizes of the circular magnetic nanoparticle. The sizes $R$ decrease from top to bottom, and take the same values as in the previous figure. Again, curves have been shifted in the vertical direction for visual convenience.

### 6.3.2 Large Avalanche Distributions

Our aim in this chapter is to analyze large avalanches in the circular magnetic nanoparticle, its distribution and its origin. In order to do so, we must filter in some way the trivial small avalanches (*extrinsic noise* [88]) reported above, since they soil the main signal. There are many different methods all over the literature to perform such filtering.[88, 97] In our case, we just subtract the fitted exponential behavior for small avalanches from the global histogram[1]. This process yields the distributions $P^*(\Delta_m)$ for large avalanches shown in Fig. 6.5. A power law behavior, followed by an (exponential) cutoff for very large avalanches, is thus clearly observed.

In particular, Fig. 6.5 shows large avalanche size distributions $P^*(\Delta_m)$ for 5 different sizes of the magnetic nanoparticle, namely $R = 30$, 42, 60, 84 and 120 spins. The measured power law exponents, $P^*(\Delta_m) \sim \Delta_m^{-\tau(R)}$, are shown in table 6.1. As observed, we find size-dependent corrections to scaling for the exponent $\tau$. Similar corrections have been also found in real experimental systems. [97] The observed finite−size corrections are compatible with a func-

[1]In practice, we must subtract two slightly different exponential distributions for small avalanches. As stated previously, small (trivial) avalanches are random local fluctuations of a growing flat domain wall. However, the critical droplet which appears as the circular nanoparticle demagnetizes shows different flat fronts (see Fig. 6.9). Trivial avalanches near the corner formed between two different flat domain walls have a slightly larger typical size due to surface tension effects. This subtle effect must be taken into account in order to obtain the clean power law distributions observed in Fig. 6.5

| R | 30 | 42 | 60 | 84 | 120 |
|---|---|---|---|---|---|
| $\tau$ | 2.76(2) | 2.24(2) | 2.06(2) | 1.77(2) | 1.77(2) |
| $\Delta_m^c$ | 27.9(7) | 56.3(14) | 123(3) | 300(9) | 675(16) |
| $\alpha$ | 3.70(2) | 3.52(2) | 2.85(2) | 2.61(2) | 2.39(2) |
| $\Delta_t^c$ | 5.92(20) | 9.3(3) | 16.1(6) | 26.7(7) | 48.6(12) |

Table 6.1: Here we show the size dependence of both the power law exponents, $P^*(\Delta_m) \sim \Delta_m^{-\tau(R)}$ and $P^*(\Delta_t) \sim \Delta_t^{-\alpha(R)}$, and the observed exponential cutoffs, $\Delta_m^c(R)$ and $\Delta_t^c(R)$.

tional dependence of the form $\tau(R) = \tau_\infty + a/R^2$, where $\tau_\infty = 1.71(4)$.[2] Analogously, we can perform a similar analysis for the avalanche lifetime distributions, $P^*(\Delta_t) \sim \Delta_t^{-\alpha(R)}$. Fig. 6.6 shows $P^*(\Delta_t)$ for large avalanches (once the extrinsic noise has been subtracted) and for the system sizes reported above. The measured exponents $\alpha(R)$ are also shown in table 6.1. Again, these are compatible with a law $\alpha(R) = \alpha_\infty + a'/R^2$, where $\alpha_\infty = 2.25(3)$. Hence we expect avalanche power law distributions $P^*(\Delta_m) \sim \Delta_m^{-\tau_\infty}$ and $P^*(\Delta_t) \sim \Delta_t^{-\alpha_\infty}$, with $\tau_\infty = 1.71(4)$ and $\alpha_\infty = 2.25(3)$, in the Thermodynamic Limit. At a first glance this result could seem unphysical, because we have proven before that large avalanches are due to the presence of free boundaries, whose importance diminish as the system grows (i.e. as the surface/volume ratio goes to zero). However we will prove later in this chapter that the mechanism responsible of large avalanches (which appears due to free boundaries) remains relevant in the Thermodynamic Limit.[3]

On the other hand, as stated previously, the power law behavior of both $P^*(\Delta_m)$ and $P^*(\Delta_t)$ lasts up to an exponential cutoff $\Delta_m^c$ and $\Delta_t^c$, respectively, which depends on system size. We measure these cutoff values (see table 6.1) fitting an exponential function of the form $\exp[-\Delta_{m(t)}/\Delta_{m(t)}^c]$ to the cutoff tails, and find a power law dependence with R, i.e. $\Delta_m^c \sim R^{\beta_m}$ and $\Delta_t^c \sim R^{\beta_t}$, where $\beta_m = 2.32(6)$ and $\beta_t = 1.53(3)$ (see Fig. 6.7). Analogous power law dependences of cutoff with system size have been found in real magnetic materials. [110] Typically, this power law dependence of cutoff with system size has been identified as a sign of genuine critical behavior. [102] However, as we will prove below, this is not the case here.

We can now wonder about the relation between the size and the lifetime of an avalanche. Moreover, we would like to know if there is any relation between them at all. With this aim we study the histogram $P(\Delta_t|\Delta_m)$, i.e. the probability of measuring an avalanche with lifetime $\Delta_t$ when its size is $\Delta_m$. Fig. 6.8 shows $P(\Delta_t|\Delta_m)$ for a circular magnetic nanoparticle of radius $R = 30$. The first rel-

[2]The fact that $\tau_\infty < 2$ involves that the mean value of the size power law distribution does not exist in the Thermodynamic Limit. [102]

[3]In fact, the importance of boundary conditions in the Thermodynamic Limit is not a new idea in Physics. For instance, for problems related with (thermal) conductivity, the boundary heat reservoirs play a fundamental role in order to understand the nonequilibrium physics in the Thermodynamic Limit.

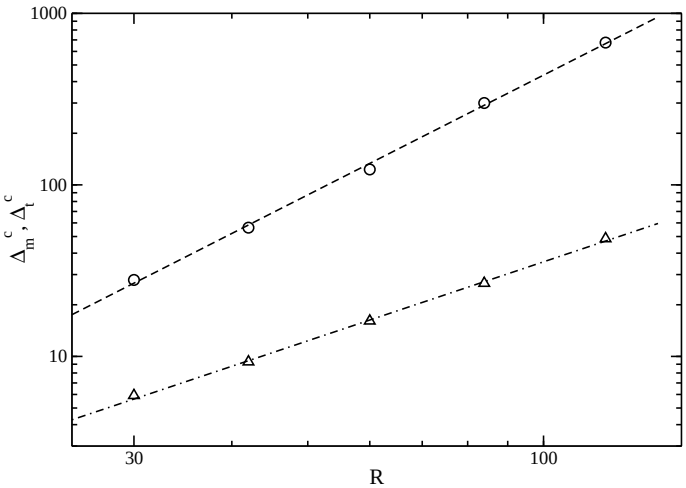


Figure 6.7: Log–log plot of the cutoff dependence with system size. In particular, we observe that $\Delta_m^c \sim R^{\beta_m}$ (◯) and $\Delta_t^c \sim R^{\beta_t}$ (△), with $\beta_m = 2.32(6)$ and $\beta_t = 1.53(3)$.

evant conclusion derived from this plot is that the distribution $P(\Delta_t|\Delta_m)$ is peaked. That is, for each value of $\Delta_m$, the marginal distribution $P(\Delta_t|\Delta_m)$ shows a narrow peak around certain typical value $\langle\Delta_t\rangle_{\Delta_m}$. This means that the relation between the lifetime and the size of an avalanche is rather deterministic in our model system, for both large and small events. Let us assume that the relation is completely deterministic, and that for large enough avalanches it can be written as $\Delta_m \sim \Delta_t^\gamma$. This equation defines the exponent $\gamma$.[4] Hence, taking into account the conservation of probability, i.e. $P^*(\Delta_m)d\Delta_m = P^*(\Delta_t)d\Delta_t$, and assuming that both $P^*(\Delta_m)$ and $P^*(\Delta_t)$ are pure power law distributions, we can write a scaling relation among the different avalanche exponents,

$$\gamma = \frac{1-\alpha}{1-\tau} \tag{6.2}$$

This scaling relation predicts a value $\gamma = 1.76(8)$ in our system. In order to corroborate such prediction, we should calculate from the marginal distribution $P(\Delta_t|\Delta_m)$ the mean value $\langle\Delta_t\rangle_{\Delta_m}$ for each $\Delta_m$ in the scaling region, thus obtaining a relation $\langle\Delta_t\rangle_{\Delta_m} = \mathcal{G}(\Delta_m)$ which should yield the value of $\gamma$. However, we do not know the distribution $P_{small}(\Delta_t|\Delta_m)$ for the extrinsic noise, and it soils the scaling region, so this way of measuring $\gamma$ does not yield any definite conclusion. Instead, we are able to measure $\gamma$ in an indirect way using the cutoff dependence with R. As we previously pointed out, $\Delta_m^c \sim R^{\beta_m}$ and $\Delta_t^c \sim R^{\beta_t}$. On the other hand, using the relation between $\Delta_m$ and $\Delta_t$ assumed

[4]Many references about Barkhausen Noise [108, 109, 111, 112] refer to $\gamma$ as $1/\sigma\nu z$, where $\sigma$, $\nu$ and $z$ are critical exponents. These references assume the existence of an underlying critical point in order to explain Barkhausen noise.

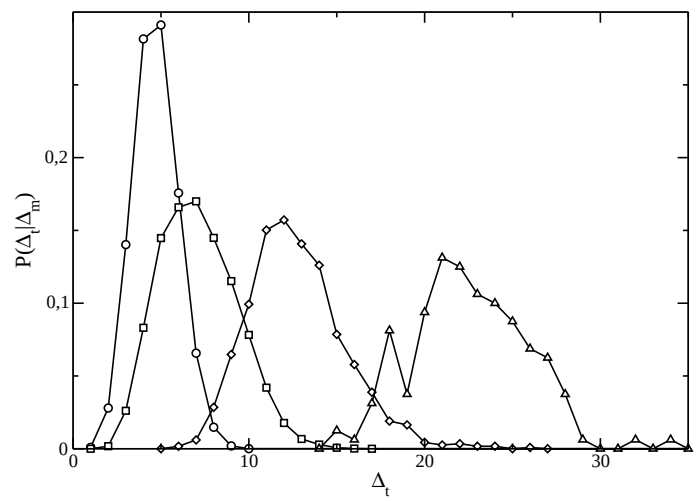


Figure 6.8: Normalized marginal distribution $P(\Delta_t|\Delta_m)$ for a circular nanoparticle of radius $R = 30$, after performing 15000 different experiments. In particular, we show $P(\Delta_t|\Delta_m)$ for $\Delta_m = 10$ (◯), 20 (□), 50 (◊) and 100 (△). Notice the peaked form of the distribution, and that larger avalanche sizes involve longer lifetimes.

above, we can write $\Delta_m^c \sim (\Delta_t^c)^\gamma$, and thus

$$\gamma = \frac{\beta_m}{\beta_t} \tag{6.3}$$

which yields $\gamma = 1.52(5)$. This indirectly measured value is similar, although not compatible, with the one predicted by the scaling relation (6.2). This is not a surprise, since the scaling relation (6.2) is based on the assumption that both $P^*(\Delta_m)$ and $P^*(\Delta_t)$ are pure power law distributions. However, as we will see later on in this chapter, these probability functions are not purely power-law distributed, but instead come from the superposition of many different exponential distributions. This observation breaks the above scaling relation, eq. (6.2); in fact we can prove (see Fig. 6.16 and complementary discussion) that the three measured exponents, $\tau$, $\alpha$ and $\gamma$, are related in the framework of a superposition of typical scales.

Studying the power spectrum of the avalanches time signal constitutes another way of measuring $\gamma$. Many avalanche systems have a power spectrum which shows two different power law regions, one for low frequencies and another one for high frequencies. The low frequency region reflects the correlations between avalanches, while the high frequency region reflects the dynamics within avalanches. For avalanche systems with $\tau_\infty < 2$ it has been shown that the high frequency power spectrum decays as $\mathcal{P}(\omega) \sim \omega^{-\gamma}$.[108] Hence we could also obtain the value of $\gamma$ in this way (this analysis will be done in a forthcoming work).

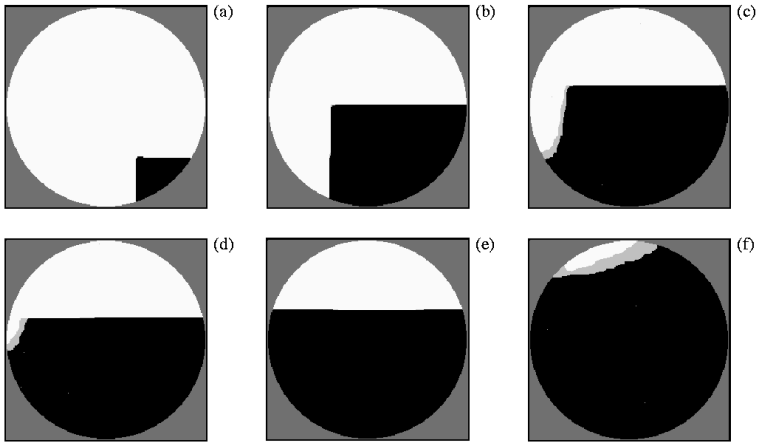


Figure 6.9: Some snapshots of a particular decay of a circular nanoparticle of radius $R = 120$. Avalanches are plotted in grey. Notice that large avalanches appear only for curved domain walls.

## 6.4 The Physical Origin of Scale Invariant Noise

Let us summarize our results up to now. We have observed that the presence of free boundaries and impurities in a magnetic system induces large avalanches in the demagnetization process from a metastable state. These large avalanches follow power law distributions for their sizes and lifetimes up to certain exponential cutoff, which depends algebraically on system size. Moreover, the power law distributions converge in the Thermodynamic Limit to size independent power laws, $P^*(\Delta_m) \sim \Delta_m^{-\tau_\infty}$ and $P^*(\Delta_t) \sim \Delta_t^{-\alpha_\infty}$ with $\tau_\infty = 1.71(4)$ and $\alpha_\infty = 2.25(3)$. We have also found that the relation between the size and the lifetime of an avalanche is rather deterministic. In fact, this relation can be quantified with an exponent $\gamma = 1.52(5)$.

A physicist trained in critical phenomena would say that these results strongly support the existence of an underlying continuous phase transition or second order critical point responsible of the observed scale invariance. This critical point would induce macroscopically large correlation lengths, and thus all scales in the system should be equally relevant. Moreover, the response to a small (microscopic) perturbation should appear at any scale (even at macroscopic ones). The characterization of this critical point should depend only on the symmetries and conservation laws present in the system, and not on the specific microscopic details. However, as we will see below, the observed power law behavior is *effective*, in the sense that the system is not really critical (i.e. the system does not present any singularity for our parameters). Instead, we will show that a finite (but large) number of different, gap−separated typical scales appear superposed in such a way that the global distributions exhibit several decades of power law behavior, as shown in Figs. 6.5 and 6.6.

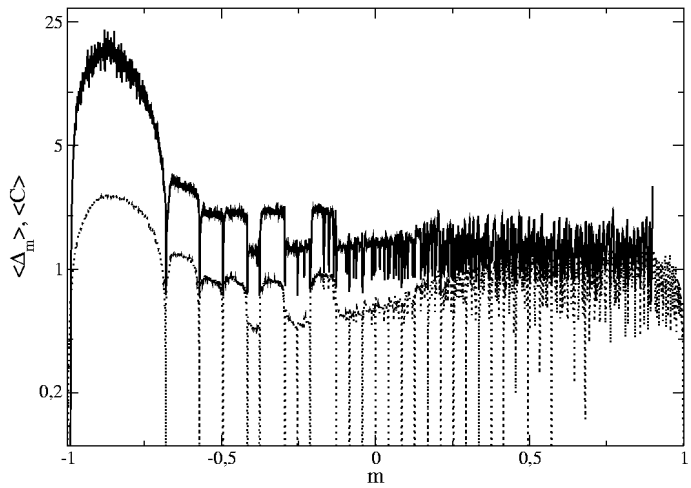


Figure 6.10: Semilog plot of the mean avalanche size (solid line) and the mean curvature (dashed line), $\langle \Delta_m \rangle$ and $\langle \mathcal{C} \rangle$ respectively, as functions of magnetization, after averaging over 3500 different runs. It is clear from this plot that, in average, large avalanches appear in the final part of the evolution. There are also some values of magnetization characterized by a very small mean avalanche size. In any case, this function shows clearly non–trivial structure. The same is true for $\langle \mathcal{C} \rangle(m)$. Also noticiable is the high degree of correlation between $\langle \Delta_m \rangle(m)$ and $\langle \mathcal{C} \rangle(m)$

### 6.4.1 Avalanches and Domain Wall Curvature

First of all, let us understand the origin of large avalanches in the circular magnetic nanoparticle. Fig. 6.9 shows some snapshots of the temporal evolution of a magnetic particle of radius $R = 120$. Due to the low temperature of simulations, the dynamics is restricted to the interface, the bulk being almost completely frozen. Hence the evolution of the system will be determined by the interface and its interplay with the open boundaries. It can be also shown that for our parameter values, configurations with only flat domain walls are metastable[5]. In fact, there are free energy barriers which impede flat domain walls to advance. In this way, the system presents many different metastable states. On the other hand, in Fig. 6.9 we observe again two different types of avalanches (plotted in grey): small, local avalanches associated with a flat domain wall, and large, global avalanches involving curved regions of the domain wall. In this latter case large avalanches appear because curvature increases domain wall interfacial energy, thus giving rise to large events towards configurations with less interfacial energy (i.e. less curvature).

In order to understand more deeply the relation between avalanches and domain wall curvature, let us study both the mean avalanche size and the mean domain wall curvature as a function of system magnetization, $\langle \Delta_m \rangle(m)$ and

[5]The stable phase shrinkage rate is larger than the stable phase growth rate for these configurations (see Chapter 3).

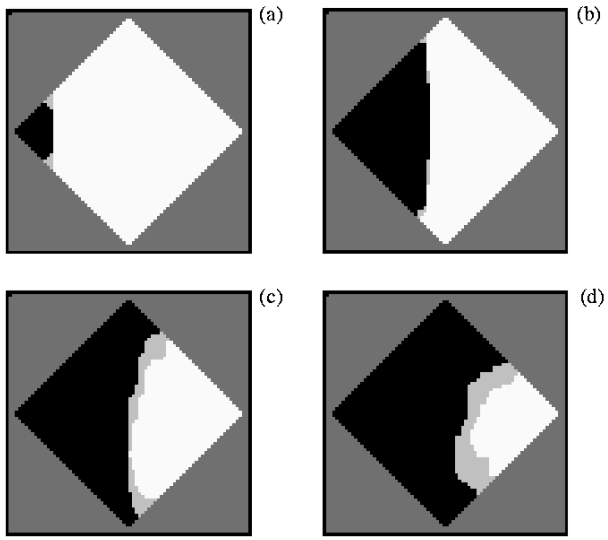


Figure 6.11: Some snapshots of the rhombus demagnetization process. Again, avalanches are plotted in grey. Notice that the domain wall remains flat when the contact angle with the open boundary is greater that $90^o$, and then only small avalanches appear. On the other hand, the domain wall gets curved when the contact angle is less that $90^o$, and large avalanches do appear.

$\langle \mathcal{C} \rangle(m)$ respectively. We will take as a measure of curvature $\mathcal{C}$ the number of step–like up spins in the interface between the stable phase and the metastable one, where step–like up spins are interfacial spins in class 3 (see Table 3.1), i.e. up spins with two up neighbors and two down neighbors[6]. Fig. 6.10 shows $\langle \Delta_m \rangle$ and $\langle \mathcal{C} \rangle$ as a function of magnetization $m$ for a particle of radius $R = 30$, after averaging over 3500 different demagnetization experiments. Here we observe that both $\langle \Delta_m \rangle(m)$ and $\langle \mathcal{C} \rangle(m)$ are highly non-homogeneous functions of magnetization, showing a non-trivial structure. In particular, we observe that there are certain well-defined magnetization values for which avalanches are typically very small. These magnetization values correspond to configurations where domain walls are flat, as can be deduced from the curvature plot. On the other hand, we observe that there are other magnetization values where typical avalanches involve many spins. In particular, we observe in Fig. 6.10 that for magnetizations in the range $m \in [-1, -0.75]$ the avalanche mean size is much larger than for other magnetizations (compare these results with the snapshots shown in Fig. 6.9). A main conclusion derived from Fig. 6.10 is the high correlation existing between the typical avalanche size and the domain wall curvature, as defined above. Large curvature implies large avalanches and reversely. Hence the size of an avalanches is perfectly determined by the

[6]This way of measuring curvature is valid only for low temperatures, since in this case clusters are very compact.

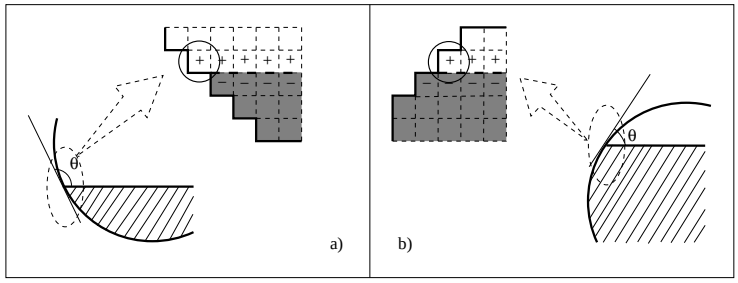


Figure 6.12: Sketch of the contact angle effect described in the text. In (a) the contact angle $\theta$ is larger than $90^o$, and microscopically border up spins near the interface have a low probability of being flipped if selected. On the other hand, in (b) the contact angle $\theta$ is smaller than $90^o$, and border up spins near the interface have probability one of being flipped if selected.

curvature of the interface when this avalanche starts.

Our next question concerns the origin of domain wall curvature. As it can be easily guessed, its origin underlies on the interplay between the interface and the open boundaries. However, in order to understand better the mechanism which gives rise to curved interfaces as the critical droplet grows, we study now demagnetization from a metastable state in our model system defined on a rhombus with free boundary conditions. Fig. 6.11 shows some snapshots of the rhombus demagnetization process. For our parameter values this system demagnetizes through the nucleation of a single critical droplet. As predicted in recent theoretical studies, [27] this critical droplet always appears in one of the four corners of the rhombus geometry. It is clear from Fig. 6.11 that while the domain wall advances forming a convex angle ($\theta > 90^o$) with the open boundary the interface remains flat, and only small avalanches appear. However, when the contact angle is concave ($\theta < 90^o$), the interface gets curved, as a consequence of the faster growth of the domain wall near the concave open borders, and large avalanches towards configurations with less interfacial energy develop. Microscopically, the interface gets curved because for concave contact angles the unflipped border spins near the interface have a probability one of being flipped if selected. This is shown in Fig. 6.12, where this mechanism is sketched for the circular particle. In this way, as the interface advances subject to concave boundary conditions, it gets curved.

### 6.4.2 Avalanche Statistics for Constant Domain Wall Curvature

We have shown that large avalanches originate due to domain wall curvature, and that the size of the avalanche is intimately related to the specific curvature of the interface. Now we want to know the distribution of avalanches for a given curved domain wall. That is, we wonder what is the probabil-

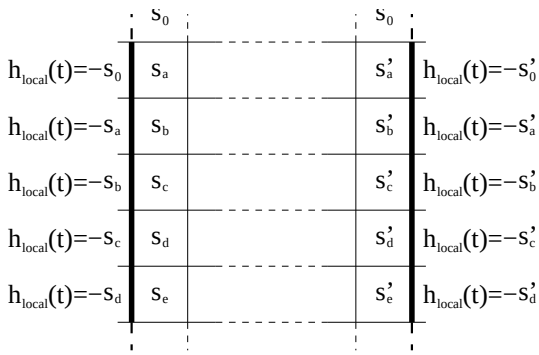


Figure 6.13: Sketch of the dynamic boundary conditions in the $\hat{x}$–direction used in the new system explained in the text. Here we represent the first and last columns of the system, and the local, dynamic magnetic field that each spin in these columns suffers as the system evolves in time. The effect of these dynamic boundary conditions is equivalent to eliminate the interaction of each border spin with its up neighbor, i.e. concave boundary conditions.

ity of finding an avalanche of a given size $\Delta_m$ if the domain wall has certain constant curvature. In order to find out which is this relationship we have designed an (unrealistic) modification of our basic system, where an interface with constant (up to small fluctuations) non-zero curvature develops, evolving via avalanches. Let us define again our system in a $L_x \times \infty$ lattice, with concave open boundary conditions in the $\hat{x}$ direction. This is done in practice in the following way. The system is set on a $L_x \times L_y$ square lattice, with very particular boundary conditions. The lattice is open in the $\hat{y}$ direction. Spins in the upper row are fixed to $+1$, and spins in the lower row are fixed to $-1$. On the other hand, boundary conditions in the $\hat{x}$ direction are *dynamic*: the lattice is also open in the $\hat{x}$ direction, although each spin in the first and last column suffers an additional dynamic magnetic field, equal at any time to the negative value of its up neighbor. This is sketched in Fig. 6.13. For each spin in the first and the last columns, the effect of these dynamic boundary conditions is to effectively decouple this spin with its up neighbor. In this way we emulate a concave, step–like border (as the one found by the interface in the rhombus system in the second part of its evolution), with a fixed distance between both concave borders. The initial configuration is identical to the one exposed for the semi–infinite system described previously, and we shift the system in a similar way in order to get an infinitely evolving domain wall. Thus, we simulate a semi–infinite system subject to open concave boundary conditions with a fixed distance $L_x$ between the concave borders.

After a short transient, the initially flat domain wall reaches an stationary state, with an almost constant (up to small fluctuations) non–zero curvature, which depends on the size $L_x$. Measuring curvature as stated previously, we notice that the steady domain wall curvature in this system is proportional to the system size $L_x$. On the other hand, this system evolves through avalanches,

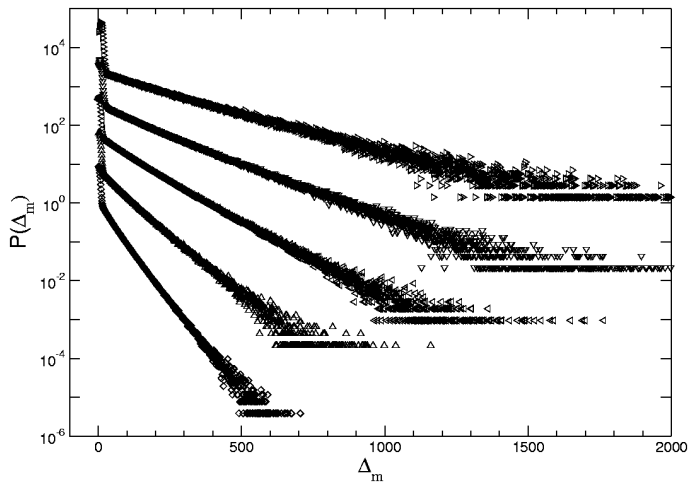


Figure 6.14: Avalanche size distribution $P(\Delta_m)$ for the semi–infinite system with concave open boundary conditions described in text. Here we show $P(\Delta_m)$ for different system sizes, namely (from bottom to top) $L_x = 20$, 25, 30, 35 and 40. The large avalanche tails are stretched exponentials, with well defined typical size. Distributions have been shifted in the vertical direction for visual convenience.

whose distribution we can measure. Fig. 6.14 shows the avalanche size distribution $P(\Delta_m)$ for this system and several values of $L_x$ (i.e. several different curvatures). As for the circular nanoparticle, we observe that $P(\Delta_m)$ shows two different well defined regions, the first one being related with the exponentially distributed extrinsic noise, explained before. The second regime is compatible with a stretched exponential function of the form

$$P_2(\Delta_m) = e^{-(\Delta_m/\bar{\Delta}_2)^\eta} \tag{6.4}$$

where we measure $\eta \approx 0.89$, independent of system size for large enough values of $L_x$. This stretched exponential function is characterized by a *typical* size $\bar{\Delta}_2$, which depends on $L_x$ (i.e., on curvature) in an exponential fashion. These results clarify what is going on in the circular magnetic nanoparticle. First, we observe that an interface with a given curvature evolves through large avalanches of a well defined typical size. Moreover, this typical size $\bar{\Delta}_2$ strongly (i.e. exponentially) depends on domain wall curvature. On the other hand, as we observed in Fig. 6.9, the interface of the growing critical droplet in the circular magnetic nanoparticle gets curved as the droplet grows. Furthermore, interfacial curvature, as defined above, takes a wide range of different values as the particle demagnetizes. Thus, the large avalanche distributions observed in the circular particle are just superpositions of distributions with well defined typical sizes.

The above results have another interesting implication. We have observed that the large avalanche typical size grows *exponentially fast* with the system

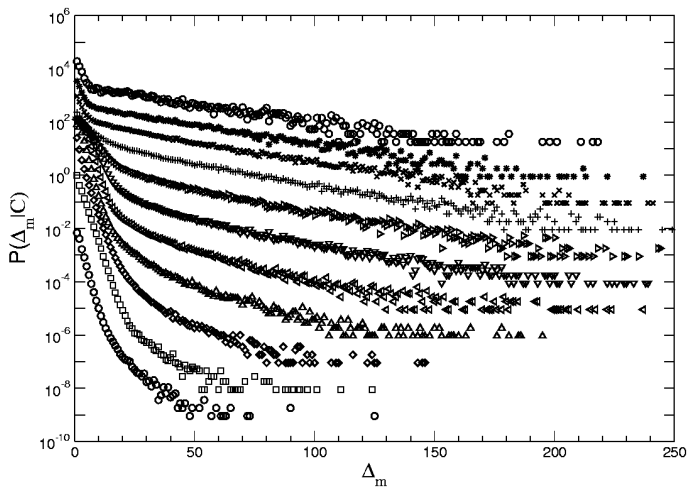


Figure 6.15: Avalanche size distribution for several fixed curvatures (measured as explained in the text) for a circular nanoparticle of radius $R = 30$, after performing 15000 different demagnetization experiments. Curvature grows from bottom to top. Notice that, as curvature increases, the large avalanche distribution for this curvature, which is an stretched exponential, increases its typical size. Curves have been shifted in the vertical direction for visual convenience.

size $L_x$. Hence, although the origin of large avalanches is connected to the presence of an open boundary (which is a surface effect), the mechanism which gives rise to large avalanches will be relevant in the Thermodynamic Limit, and large (infinite) avalanches will appear in this limit.

The above results suggest us to study avalanche distributions in the circular nanoparticle as a function of domain wall curvature (as defined previously). Fig. 6.15 shows $P(\Delta_m|\mathcal{C})$ for the circular nanoparticle, which is the probability of measuring an avalanche of size $\Delta_m$ when the interfacial curvature is $\mathcal{C}$. Here we note that the domain wall takes many different curvature values as demagnetization proceeds. For each constant curvature, the tail of the avalanche size distribution follows again an stretched exponential law, whose typical size grows with curvature.

This confirms what we previously stated, i.e. that large avalanches in the circular magnetic nanoparticle have a large (but finite) number of different, gap–separated typical sizes. Hence, the power law observed initially for the avalanche size distribution (see Fig. 6.5) is *effective*: our system is not critical. Although we observe an effective scale invariance, the system's correlation lengths are non–divergent, but finite. Moreover, if we slightly perturb the system, its response will be equally small.

### 6.4.3 Power Law Behavior as a Consequence of Superposition of Many Different Typical Scales

There is still an annoying remaining question: how can a finite superposition of distributions with well defined different typical scales give rise to a scale invariant power law global distribution ?. In order to answer this question we solve a mathematical exercise. Let us assume that we have a system that evolves via burst-like events of magnitude $x$. The state of this system is characterized by an observable $A$, in such a way that the probability of finding an event of magnitude $x$ when the system is in a state characterized by $A$ is $\mathcal{P}(x|A) = A\exp(-Ax)$. Therefore the observable $A$ fixes the typical scale of burst-like events. If $\mathcal{Q}(A)$ is the probability of finding the system in a state characterized by $A$, the probability of finding an event of size $x$ is,

$$\mathcal{P}(x) = \int_0^\infty \mathcal{Q}(A)\mathcal{P}(x|A)dA \tag{6.5}$$

where we have assumed that the observable $A$ varies continuously from $0$ up to $\infty$. Hence, due to the exponential form of $\mathcal{P}(x|A)$, $\mathcal{P}(x)$ is just the Laplace transform of $A\mathcal{Q}(A)$. If we now assume the simplest case, namely that the distribution $\mathcal{Q}(A)$ is flat so all possible values of $A$ are equally probable, we obtain $\mathcal{P}(x) \sim x^{-2}$. Hence, an *infinite* superposition of exponential distributions with well-defined typical scales (defined by $A$) yields a power law (scale free) probability function with exponent $-2$. This result is not surprising. Power law behavior is a consequence of the lack of any typical scale in the system. However, we can interpret this lack of typical scale in the opposite way, saying that in a system exhibiting power law behavior all possible scales are present, so there is no *typical* scale. This is what eq. (6.5) says.

However, avalanches in our magnetic nanoparticle show a *finite* set of well-defined typical scales[7]. In this case the continuous sum in eq. (6.5) must be substituted by a discrete sum over the the typical scales present in the system. In order to explicitely perform the calculation, let us assume that we have $N+1$ different typical scales $A_n$, with $n \in [0, N]$, all of them in a finite interval, $A_n \in [A_{min}, A_{max}]\ \forall n \in [0, N]$. We further assume that these typical scales are equally spaced in this interval, so $A_n = A_{min} + n\Delta$, where $\Delta = (A_{max} - A_{min})/N$. Therefore, assuming again that $\mathcal{Q}(A)$ is a constant function, we now write,

$$\begin{aligned}\mathcal{P}(x) &= \sum_{n=0}^{N} A_n e^{-A_n x}\Delta = \frac{\Delta e^{-A_{min}x}}{1-e^{-\Delta x}}\Big[A_{min} - A_{max}e^{-(N+1)\Delta x} \\ &- \Delta\frac{1-e^{-N\Delta x}}{1-e^{\Delta x}}\Big]\end{aligned} \tag{6.6}$$

[7]We assume for the following calculation that these typical scales are characterized by exponential distributions, instead of stretched exponentials, as we found in previous sections. We think that this simplification, which makes easy the calculation, does not involve any fundamental difference in the consequent physical discussion.

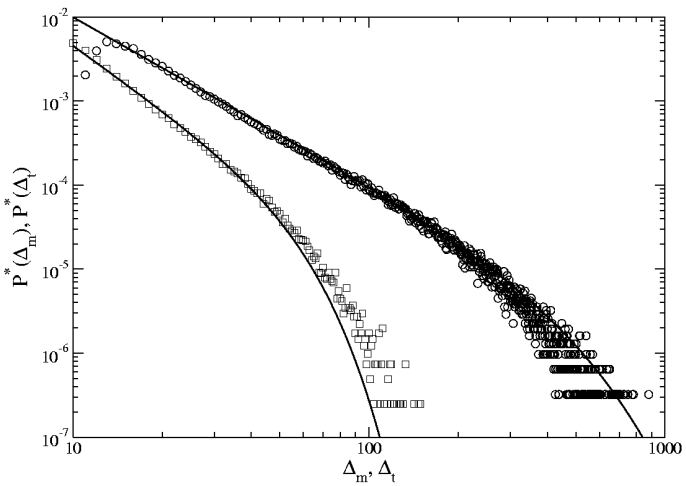


Figure 6.16: Large avalanche size (◯) and lifetime (□) distributions for a circular nanoparticle with radius $R = 60$ (these results are the same than those plotted in Figs. 6.5 and 6.6). The upper line corresponds to the prediction derived from eq. 6.6 for $N = 200$, $A_{min} = 0.007$ and $A_{max} = 1$. The lower line is derived from eq. 6.6 assuming that $\Delta_m \sim \Delta_t^{\gamma}$, where we use $\gamma = 1.52(5)$, the value we previously measured.

where we have used eqs. (4.29) and (4.33). Fig. 6.16 shows the event size distribution $\mathcal{P}(x)$ obtained from eq. (6.6) for $N = 200$, $A_{min} = 0.007$ and $A_{max} = 1$. As we can observe in this figure, the curve follows power law behavior up to an exponential cutoff given by $\exp(-A_{min}x)$. Fig. 6.16 also shows for comparison the avalanche size distribution measured for a circular particle with $R = 60$. The agreement between the theoretical curve based on a finite superposition of different typical scales and the measured distribution is very good. Moreover, assuming that eq. (6.6) represents the avalanche size distribution, and using the relation $\Delta_m \sim \Delta_t^{\gamma}$ between the size and the lifetime of an avalanche, we can obtain the avalanche lifetime distribution via the conservation of probability. Thereby, if $\mathcal{P}(\Delta_m)$ is the probability of finding an avalanche with size $\Delta_m$, the probability of finding an avalanche with lifetime $\Delta_t$ is $\gamma\Delta_t^{\gamma-1}\mathcal{P}(\Delta_t^{\gamma})$. This curve, also shown in Fig. 6.16 for the same parameters described above, agrees with the measured avalanche lifetime distribution for the $R = 60$ magnetic particle when we use the previously measured value $\gamma = 1.52(5)$. This agreement confirms the measured value for the exponent $\gamma$, and on the other hand it also strengthens our conclusion about the origin of the scale invariance in this problem. Hence the superposition of a finite (but large) number of exponential distributions with different typical rates results in a global distribution which shows several decades of power law behavior, together with an exponential cutoff corresponding to the slowest exponential typical rate.

## 6.5 Conclusions and Outlook

In this chapter we have studied how an impure ferromagnetic nanoparticle evolves from the metastable phase towards the stable one. Under the combined action of both impurities (which involve nonequilibrium conditions) and free borders, the formation of a nucleus of the stable phase turns out to proceed by avalanches. This burst-like evolution characterizes the dynamics of many nonequilibrium system.[102] In addition to small events, which show up as a completely random, thermal effect (extrinsic noise[88]; see Appendix C), we have described *critical avalanches*. These are typically much larger than the extrinsic noise, while they *apparently* show no temporal and spatial scale. We find for these large avalanches size and lifetime distributions which follow power laws, $P(\Delta_m) \sim \Delta_m^{-\tau}$ and $P(\Delta_t) \sim \Delta_t^{-\alpha}$ with $\tau \to 1.71(4)$ and $\alpha \to 2.25(3)$ for large enough systems. This scale free behavior holds up to exponential cutoffs, which grow as a power law of the system size, $\Delta_m^c \sim R^{\beta_m}$ and $\Delta_t^c \sim R^{\beta_t}$, with $\beta_m = 2.32(6)$ and $\beta_t = 1.53(3)$ respectively. In addition, the size and lifetime of an avalanche are related via $\Delta_m \sim \Delta_t^{\gamma}$, with $\gamma = 1.52(5)$. A detailed analysis of these scale free avalanches reveals that they are in fact the combined result of many avalanches of different well-defined *typical* size and duration. That is, the simplicity and versatility of our model system allows us to identify many different types of avalanches, each type characterized by a probability distribution with well defined typical size and duration, associated with a particular *curvature* of the domain wall. Due to free borders and the microscopic impurity the system visits a broad range of domain wall configurations, and thus the combination of these avalanches generally results (see section 6.4.3) in a distribution which exhibits several decades of power law behavior and an exponential cutoff. However, this apparent scale-free behavior does not mean that avalanches are critical, in the sense of a second order phase transition where diverging correlation lengths appear. Instead, we find that avalanches in the magnetic nanoparticle have a large (but finite) number of different, gap-separated typical sizes and durations. In this way we have proposed in this chapter a new mechanism to obtain power law distributions not related to any underlying critical dynamics.[113]

However, the proposal of this new mechanism is not so important on its own. The deep insight derived from this analysis comes when we extrapolate the conceptual framework here developed to the understanding of Barkhausen Noise in particular and $1/f$ Noise in general. As we previously stated, Barkhausen Noise is the noise by which an impure ferromagnet responds to a slowly varying external magnetic field. This response is not continuous, but burst-like. In particular, magnetization jumps are observed as a function of the applied field which are called *avalanches*. Experimentalists are able to measure the size and lifetime of these avalanches, finding that both magnitudes follow power law distributions with well-defined exponents. In order to obtain these exponents they must filter out the extrinsic noise which soils the main signal. A main feature characterizing Barkhausen Noise is that the scale-free behavior codified by the observed power law avalanche distributions appears with-

| Ref. | $\tau$ | $\alpha$ | $\gamma$ |
|---|---|---|---|
| [111] | 1.46(5) | ———— | 1.70(5) |
| $[114]_1$ | 1.27(3) | 1.5(1) | 1.77(12) |
| $[114]_2$ | 1.50(5) | 2.0(2) | ———— |
| [88] | 1.77(9) | 2.25(8) | 1.51(1) |
| Our simulation | 1.71(4) | 2.22(3) | 1.52(5) |

Table 6.2: In this table we show results on *critical* exponents for different experiments on Barkhausen Noise. As it is clear from direct inspection, universality is not observed. The last row shows our results for the magnetic noise in the circular nanoparticle.

out any need of fine tuning. For many years[8] theoretical physicist have been wondering about the origin of this *spontaneous* or *self-organized* scale invariant behavior. Different theoretical approaches have been proposed as explanation of Barkhausen Effect (most of these approaches are incompatible among them[88]). All these theories are based on assuming the existence of an underlying critical point, responsible of the observed scale invariance. The main theoretical approaches are divided in three different branches:

- The Random Field Ising Model (RFIM) has been proposed as a possible theoretical framework in order to explain Barkhausen Noise.[91, 108] In this model a second order phase transition driven by the disorder is observed. The calculated critical exponents are similar to those measured in some Barkhausen experiments. This phase transition is a plain old one, in the sense that fine tuning of parameters is needed in order to reach the critical region, as opposed to observations in Barkhausen materials.

- Another theoretical approach is based on disordered interfaces and the pinning-depinning transition.[90, 109, 114] As above, here an underlying critical point is assumed. Barkhausen Noise is analyzed in this case in terms of the domain wall motion in a bulk with quenched disorder. This theoretical approximation is the most popular in the scientific community.

- Some SOC models have been also proposed as possible explanation to Barkhausen Noise. Nowadays, this theoretical approach is almost neglected.

All these theoretical models reproduce some aspects of Barkhausen experiments. The assumption these approaches make about the existence of an underlying critical point responsible of the observed scale invariance involves that Barkhausen experiments must show *universality*. That is, if the scale invariance observed in Barkhausen Noise is derived from an underlying critical point, it is expected that the critical exponents measured for the avalanches will

[8] In fact, Barkhausen Noise was discovered a century ago, and since then its origin remains mysterious.

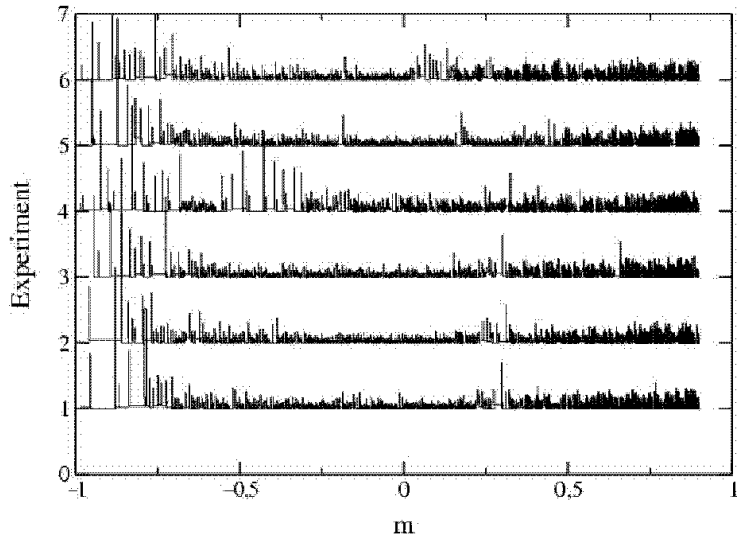


Figure 6.17: Avalanche sizes as a function of magnetization for several different runs. Large avalanches appear in the final part of the evolution ($m \approx -1$). Notice also that, in general, large avalanches appear for approximately the same values of magnetization for each run (see, for instance, the large avalanche appearing for $m \approx 0.3$ in the four first runs).

be universal, i.e. independent of the microscopic details of the material. These critical exponents should only depend on the symmetries and conservation laws which characterize the material. However, this is not observed in practice. Table 6.2 compares *critical* exponents measured in different Barkhausen experiments, and the exponents we have measured in our simple model. A comparison among the different experimental results shown in Table 6.2 clearly proves the lack of universality in Barkhausen materials. This fact contradicts the assumption about the existence of an underlying critical point in Barkhausen materials. Furthermore, the power of most practical applications of Barkhausen Noise is based on the sensitivity of Barkhausen emission to microstructural details in the material.[87, 89] Such sensitivity is incompatible with the concept of universality derived from a critical point, where by definition the behavior of the system is not sensitive to details, but only to symmetries and conservation laws.

Let us now analyze the relation between our results for the magnetic nanoparticle and Barkhausen Noise. In Table 6.2 we observe that the exponents we have obtained for the avalanches in the magnetic nanoparticle are almost equal to those measured by Spasojević et al[88] in Barkhausen experiments. In particular, we have obtained exponents $\tau_\infty = 1.71(4)$, $\alpha_\infty = 2.25(3)$ and $\gamma = 1.52(5)$, while Spasojević et al have performed experiments on quasi-bidimensional VITROVAC, measuring exponents $\tau = 1.77(9)$, $\alpha = 2.22(8)$ and $\gamma = 1.51(1)$. The results of our simulations are perfectly compatible with these experimental

measures. These observations led us to suspect that Barkhausen Noise might also come from the superposition of more elementary events. In fact, the $1/f$ noise behavior in this case is assumed to reflect topological rearrangements of domain walls,[104] which result in practice in a series of jumps between different metastable states, which is the basic process in our model.

Our system also reproduces some other phenomena observed in real materials, which support the above hypothesis about the origin of Barkhausen Noise. For instance, our system shows *reproducibility*. It is observed during the demagnetization process in the ferromagnetic nanoparticle that large avalanches are reproducible from one experiment to another. This means that large avalanches usually appear at the same stages of evolution, independently of the observed experiment. Fig. 6.17 shows the avalanche size as a function of magnetization for several demagnetization experiments in our magnetic nanoparticle. It is clear from this figure that there are certain magnetizations for which large avalanches usually appear (see for instance avalanches for magnetization $m \approx 0.3$ or $m \in [-1, -0.75]$). On the other hand, extrinsic noise (i.e. small avalanches) shows high variability. The reproducibility phenomenon points out the existence of a dynamic correlation in the system. The same property has been observed in experiments with Perminvar and a Fe-Ni-Co alloy.[105] In these experiments the hysteresis loop associated to the material is studied, and it is observed that some (large) avalanches are almost perfectly reproducible from one hysteresis loop to another, while other (small) avalanches show no reproducibility. That is, measuring the size of the avalanches as a function of the applied magnetic field it is found that there are certain values of the external field for which very large avalanches develop, and this property is observed for many different hysteresis loops.

In order to investigate the origin of reproducibility in our system, let us come back to Fig. 6.10. There we plotted the mean avalanche size $\langle \Delta_m \rangle(m)$ and the domain wall mean curvature $\langle \mathcal{C} \rangle(m)$ as a function of magnetization for a system with radius $R = 30$, after averaging over 3500 different runs. The highly inhomogeneous (non-trivial) shape of $\langle \Delta_m \rangle(m)$ confirms the above conclusion, i.e. our magnetic nanoparticle shows reproducibility. Moreover, the mean curvature $\langle \mathcal{C} \rangle(m)$ is also reproducible from one experiment to another. As we previously discussed, the high correlation between $\langle \Delta_m \rangle(m)$ and $\langle \mathcal{C} \rangle(m)$ implies that the typical scale of an avalanche is completely determined by the curvature of the domain wall when this avalanche starts. Hence the reproducibility observed in avalanches is due to the reproducibility of the domain wall curvature. The observed domain wall curvature reproducibility points out that the system evolves from the metastable phase to the stable one through certain *typical* configurations, each one characterized by a typical droplet shape and a typical domain wall curvature. Fig. 6.9 shows an example of this typical evolution (we came to this conclusion after looking at many different particular evolutions). Different experiments evolve approximately in the same way because, on one hand, the system is very efficient selecting the most energetically favorable configurations during the evolution due to the low temperature of simulations (in this case the free energy minima are very deep), and on the

other hand the presence of the free boundaries involves that the droplet always nucleates at the border. In experiments showing reproducibility it is concluded that the presence of quenched disorder in these real systems is essential for the observed reproducibility.[105] In our case, the presence of the border (together with the low temperature) is the responsible of the reproducibility phenomenon. In this sense we could interpret the open boundary in our system as a quenched disorder distributed in a very particular way.

Summarizing, we observe that the exponents characterizing the avalanche distributions in our system reproduce some experimental results on Barkhausen Noise. Moreover, our ferromagnetic nanoparticle also shows reproducibility, which is observed in real Barkhausen materials. In addition, the avalanche size and lifetime distributions show exponential cutoffs which depend algebraically on system size. This behavior has been also reported in real materials [110]. Finally, the measured exponents $\tau$ and $\alpha$ show finite size corrections similar to those found in experiments with avalanche systems[97]. All these similarities, together with the fact that experimental observations do not support the existence of universality[9] in Barkhausen Noise, led us to suspect that Barkhausen Noise might also come from the superposition of more elementary events with well-defined typical scales.

The chances are that our observation that scale invariance originates in a combination of simple events, which we can prove in our model cases, is a general feature of similar phenomena in many complex systems [91]. This should explain why distributions exhibiting power law, exponential or stretched exponential behavior have been identified in different but related experimental situations and in different regimes of the same experiment.

Finally, let us mention that the analysis method introduced in this chapter in order to identify the origin of different avalanches and the superposition of different typical scales can be easily exported to many experimental situations, simplifying the investigation about the origin of Barkhausen emissions in particular, and $1/f$ Noise in general.

[9]Saying that universality is not observed is equivalent to affirm that there is no phase transition underlying Barkhausen Noise.

# Part II

# Nonequilibrium Phase Separation, Absorbing States and Heat Conduction

# Chapter 7

# Kinetics of Phase Separation in the Driven Lattice Gas: Self-Similar Pattern Growth under Anisotropic Nonequilibrium Conditions

## 7.1 Introduction

The first part of this thesis has been devoted to the study of metastability and avalanches in a nonequilibrium magnetic model. There we have investigated the dynamic process by which a nonequilibrium spin system subject to a nonzero magnetic field evolves from a metastable phase towards the truly stable one. There are other dynamical phenomena in nonequilibrium systems which involve transformations between different phases. In particular, a very interesting phenomenon is the segregation process that emerges when a nonequilibrium (conserved) system evolves from a disordered phase towards the ordered one. The aim of this chapter is to investigate the effects that nonequilibrium anisotropic conditions induce on this phase separation phenomenon.

Many alloys such as Al-Zn, which are homogeneous at high temperature, undergo phase separation after a sudden quench into the miscibility gap (for details, see the reviews [115]-[119], for instance). One first observes nucleation in which small localized regions (*grains*) form. This is followed by "spinodal decomposition". That is, some grains grow at the expense of smaller ones, and eventually coarsen, while their composition evolves with time. In addition to theoretically challenging, the details are of great practical importance. For example, hardness and conductivities are determined by the spatial pat-

tern finally resulting in the alloy, and this depends on how phase separation competes with the progress of solidification from the melt.

A complete kinetic description of these highly non-linear processes is lacking. [119] Nevertheless, the essential physics for some special situations is now quite well understood. This is the case when nothing prevents the system from reaching the equilibrium state, namely, coexistence of two thermodynamic phases. The simplest example of this is the (standard) lattice gas evolving from a fully disordered state to segregation into *liquid* (particle-rich phase) and *gas* (particle-poor phase). (Alternatively, using the language of the isomorphic lattice binary alloy, [120] the segregation is into, say Al-rich and Zn-rich phases.) As first demonstrated by means of computer simulations,[121, 115, 116] this segregation, as well as similar processes in actual mixtures exhibit time *self-similarity*. This property is better defined at sufficiently low temperature, when the thermal correlation length is small. The system then exhibits a *single* relevant length, the size $\ell(t)$ of typical grains growing algebraically with time. Consequently, any of the system properties (including the spatial pattern) look alike, except for a change of scale, at different *times*.

This interesting property is revealed, for example, by the sphericalized structure factor $S(k,t)$ as observed in scattering experiments. After a relatively short transient time, one observes that $S(k,t) \sim J(t) \cdot F[k\,\ell(t)]$. Taking this as a hypothesis, one may interpret $J$ and $\ell$ as phenomenological parameters to scale along the $S$ and $k$ axes, respectively. The hypothesis is then widely confirmed, and it follows that $J(t) \sim \ell(t)^d$ where $d$ is the system dimension. It also follows that $F(\varkappa) = \Phi(\varkappa) \cdot \Psi(\sigma\varkappa)$ where $\Phi$ and $\Psi$ are universal functions. In fact, $\Phi$ describes the diffraction by a single grain, $\Psi$ is a grain interference function, and $\sigma$ characterizes the point in the (density−temperature) phase diagram where the sample is quenched. It then ensues that $\Psi \approx 1$ except at small values of $k$, so that, for large $\varkappa$, $F(\varkappa)$ becomes almost independent of density and temperature, and even the substance investigated.[121, 122, 119]

The grain distribution may also be directly monitored. A detailed study of grains in both microscopy experiments and computer simulations confirms time scale invariance. More specifically, one observes that the relevant length grows according to a simple power law, $\ell(t) \sim t^a$, and one typically measures $a = 1/3$ at late times. This is understood as a consequence of diffusion of monomers that, in order to minimize surface tension, evaporate from small grains of high curvature and condensate onto larger ones (*Ostwald ripening*). In fact, Lifshitz and Slyozov, and Wagner independently predicted $\ell \sim t^{1/3}$,[123] which is often observed, even outside the domain of validity of the involved approximations.[124] In some circumstances, one should expect other, non-dominant mechanisms inducing corrections to the Lifshitz-Slyozov-Wagner one. [115, 117, 119] For instance, effective diffusion of grains (*Smoluchowski coagulation*) leads to $a = 1/6$, which may occur at early times;[125] interfacial conduction leads to $a = 1/4$;[126, 127] and, depending on density and viscosity, a fluid capable of hydrodynamic interactions may exhibit crossover with time to viscous ($a = 1$) and then inertial ($a = 2/3$) regimes.[118]

Extending the above interesting picture to more realistic situations is an open question. The assumption that the system asymptotically tends to the coexistence of two *thermodynamic* (equilibrium) phases is often unjustified in Nature. This is the case, for example, for mixtures under a shear flow, whose study has attracted considerable attention, e.g.[128]-[132]. The problem is that sheared flows asymptotically evolve towards a *nonequilibrium* steady state and that this is highly anisotropic. Studying the consequences of anisotropy in the behavior of complex systems is in fact an important challenge (see, for instance, [51, 133, 134]). Another important example is that of binary granular mixtures under horizontal shaking. The periodic forcing causes in this case phase separation and highly anisotropic clustering.[152]

In this chapter, we study in detail the kinetics of the driven lattice gas (DLG) [134] following a deep quench. Our motivation is twofold. On one hand, the DLG is recognized to be an excellent microscopic model for nonequilibrium anisotropic phenomena.[51] On the other, the DLG is not affected by hydrodynamic interactions, which makes physics simpler. Our goal is timely given that the asymptotic state of the DLG is now rather well understood, and previous studies of kinetics altogether reveal an intriguing situation.[134]-[141] Following this pioneering effort, we here present a new theoretical description of the essential physics during anisotropic, nonequilibrium pattern growth. This is compared with new extensive computer simulations.[142]

## 7.2 Model and Simulation Details

The DLG consists in a $d-$dimensional, e.g., simple-cubic lattice with configurations $\mathbf{n} = \{n_i; i = 1, ..., N\}$. The variable at each lattice site has two possible states, $n_i = 1$ (*particle*) or $0$ (*hole*). As for the standard lattice gas, dynamics is a stochastic process at temperature $T$ consisting in nearest-neighbor (NN) particle/hole exchanges. This conserves the particle density, $\rho = N^{-1} \sum_i n_i$, and depends on $\mathbf{n}$.

A distinguishing feature of the DLG is that exchanges are favored in one of the principal lattice directions, say $\vec{x}$. Therefore, assuming periodic (toroidal) boundary conditions, a net current of particles is expected to set in along $\vec{x}$. This is accomplished in practice by defining a biased transition rate. We shall refer here to the *energy* function $H = -4J \sum_{NN} n_i n_j$, which describes attractive interactions between particles at NN sites, and to the transition rate (per unit time):[51]

$$\omega(\mathbf{n} \to \mathbf{n}^*) = \min\left\{1, e^{-(\Delta H + E\delta)/T}\right\}. \tag{7.1}$$

$\mathbf{n}^*$ stands for configuration $\mathbf{n}$ after jumping of a particle to a NN hole; $\Delta H = H(\mathbf{n}^*) - H(\mathbf{n})$ is the *energy* change brought about by the jump; and units are such that both the coupling strength $J$ and the Boltzmann constant are set to unity. One further defines $\delta = (\mp 1, 0)$ for NN jumps along $\pm\vec{x}$ or along any of the transverse directions, say $\vec{y}$, respectively. Consistent with this, $\vec{E} = E\vec{x}$ may be interpreted as a field driving particles, e.g., an electric field if one assumes

that particles are charged. (One may adopt other interpretations, e.g., the binary alloy one.[120] Dynamics then consists in interchanges between particles of different species, one of them favored along $\vec{x}$.)

The DLG was described as modeling surface growth, fast ionic conduction and traffic flow, among a number of actual situations of practical interest.[51] A common feature in these situations is anisotropy, and that steady states are out of equilibrium. Both are essential features of the DLG induced by the rate (7.1). The only trivial case is for $E = 0$, which reduces (7.1) to the Metropolis algorithm. In this case, detailed balance holds, and one simply has the familiar lattice gas with a unique (equilibrium) steady state. For any, even small $E$, qualitatively new behavior emerges. In fact, detailed balance breaks down for $E > 0$ and, consequently, the steady state depends on $\omega(\mathbf{n} \to \mathbf{n}^*)$. Increasing $E$, one eventually reaches *saturation.* That is, particles cannot jump backwards, i.e., $-\vec{x}$, which formally corresponds to an *infinite field* $(E = \infty)$.

The way in which the microscopic anisotropy (7.1) conveys into macroscopic behavior is amazing.[51] Consider, for simplicity, $d = 2$, $\rho = \frac{1}{2}$ and $E = \infty$. The system then exhibits a critical point at $T = T_C^\infty \simeq 1.4T_C\,(E = 0)$, where $T_c(E = 0) \approx 2.2691 \equiv T_{ons}$, with novel critical behavior.[140, 141] Furthermore, the asymptotic, steady states below $T_C^\infty$ do not comprise equilibrium phases. Instead, one observes a particle *current* and fully *anisotropic* phases; both are nonequilibrium features. The intensity of the current increases with $T$, and suddenly changes slope at $T_C^\infty$ (in fact, this property may serve to accurately locate the critical point). The stable ordered configurations consist of one stripe, to be interpreted as a *liquid* (rich-particle) phase of density $\rho_L\,(T)$. The *gas* (poor-particle) phase of density $\rho_G\,(T)$ fills the remainder of the system. Except for some microscopic roughness, the interface is linear and rather flat, in general[1].

The computer evolutions reported here always begin with a completely disordered state to simulate the system at infinite temperature. We then model a sudden quench and the subsequent time evolution. With this aim, one proceeds with rate (7.1) that involves the temperature $T$ at which the system is quenched. The run is followed until one stripe is obtained (eventually, in order to save computer time, the run was sometimes stopped before reaching the final stationary state). The code involves a list of $\eta\,(t)$ particle-hole NN pairs from where the next move is drawn. Time is then increased by $\Delta t = \eta\,(t)^{-1}$, so that its unit or *MC step* involves a visit to all sites on the average[2].

The lattice is rectangular, $L_\parallel \times L_\perp$, with sides ranging from 64 to 256 and, in a few cases, 512. Results concern an average over around thousand inde-

[1]Some partial, inconclusive studies about interfaces in the Driven Lattice Gas[154] have reviewed in Ref. [51].

[2]This corresponds to the standard Monte Carlo method only if the time increment $\Delta t$ is drawn from a Poisson distribution. Taking constant $\Delta t = \eta(t)^{-1}$ involves some approximation. However, if the number of particle-hole pairs in the system is sufficiently large, the approximation is excellent. In particular, for a half filled system subject to an *infinite* drive (our model case), the minimum amount of particle-hole pairs present in the system will be of order $2L_\parallel$, which is large for large lattices.

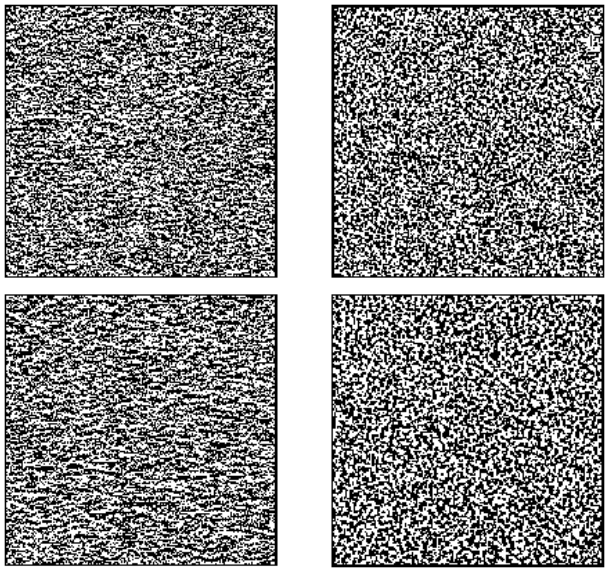

Figure 7.1: A series of MC snapshots comparing very early patterns for the DLG (with an infinite horizontal field) and for the standard lattice gas, i.e., zero field (LG) at the same time. This corresponds to a 256x256 lattice at $T \simeq 0.6T_C^{\infty}$. The time (in MC steps) is here $t = 4$ and 10 (from top to bottom) for the DLG (left column) and for the LG (right column).

pendent runs. Due to the great computational effort which is consequently involved, this chapter describes simulations concerning a single point of the two-dimensional DLG phase diagram. That is, most of our evolutions are for $\rho = \frac{1}{2}$ and $E = \infty$, and simulate a quench at $T = 0.8T_C\,(E = 0) \simeq 0.6T_C^{\infty}$. This choice is motivated by the fact that clustering is then reasonably compact, which helps to obtain good statistics, while it proceeds fast enough, so that one can observe full relaxation to the steady state. In spite of this restriction, brief investigation of other points, together with some of our observations below, led us to believe that the validity of our results extends to a large domain around the center of the miscibility gap; in fact, such generality of behavior has been reported for $E = 0$.[116, 121, 125, 119]

## 7.3 Growth of Order

The DLG exhibits different time regimes during phase separation. Though they parallel the ones for $E = 0$, the *peculiarities* induced by the anisotropic condition are essential.

Starting from complete disorder, there is a very short initial regime in which small grains form. The novelty is that typical grains are now fully anisotropic,

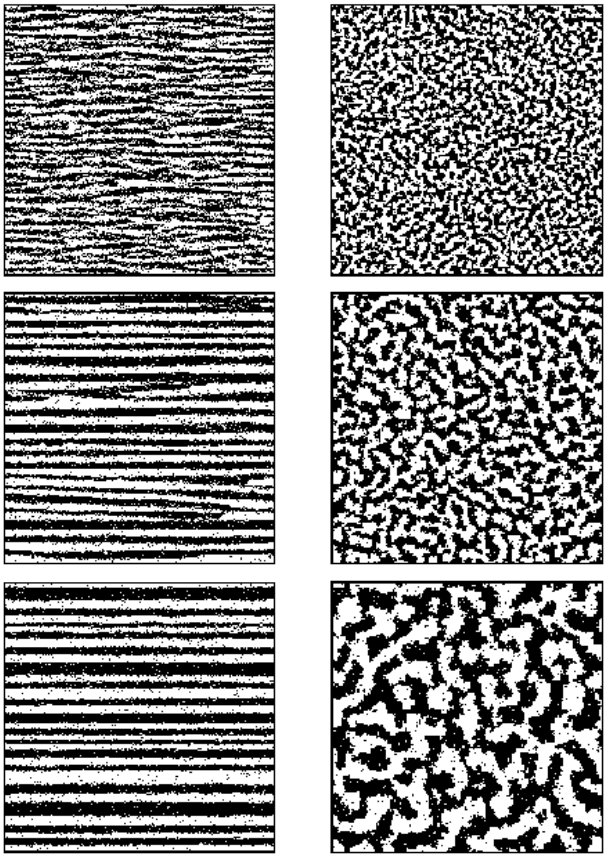

Figure 7.2: The same as Fig. 7.1 but at late time, namely, $t = 100$, 1000 and 10000 MC steps (from top to bottom) for the DLG (left column) and for the LG (right column).

stretched along $\vec{x}$. The grains then rapidly coarsen to form macroscopic strings, as illustrated in Fig. 7.1. Sheared fluids (an experimentally accessible situation that also involves both nonequilibrium physics and anisotropy) seem to exhibit similar initial regimes.[130, 132] That is, during a short time interval, they show larger growth rate along the flow than in the other directions, which is assumed to correspond to the initial formation of anisotropic regions. Afterwards, sheared fluids develop string-like macroscopic domains similar to the ones in the DLG.

Figs. 7.1 and 7.2 include a comparison with the zero-field case, i.e., the standard, isotropic lattice gas (LG). This clearly illustrates the strong anisotropy of nucleation and early phase separation for the DLG. Close inspection of these and similar graphs also seems to indicate relatively small but significant differences in the degree of segregation between the two cases at a given time. That is, at small distances, there is a more homogeneous distribution of parti-

cles, both longitudinally and transversely, in the DLG than in the LG. The latter shows up more segregated at the same time, which is already rather evident by direct inspection of graphs for $1 < t \leq 100$ in Figs. 7.1 and 7.2. We believe this reveals the different role played by surface tension as the degree of anisotropy is varied: Typical DLG grains are rather linear except at their longitudinal ends, where curvature may be even stronger than for the spherical clusters in the LG at comparable times. This seems to be at the origin of a smother transverse distribution of particles in the DLG at early times. On the other hand, the field also tends to smooth things longitudinally.

In order to quantify the aforementioned observation, we evaluated the number of broken bonds in the direction of (perpendicular to) the field, $n_{\|}(t)$ ($n_{\perp}(t)$) as a function of time during the early evolution stage. Then $A(t) \equiv [n_{\perp}(t) + n_{\|}(t)]/2N$ is the density of broken bonds. The higher the degree of segregation at time $t$, the smaller is $A(t)$. For instance, we observe in a large $256 \times 256$ lattice that $A(t = 10) = 0.295$ and $A(t = 10) = 0.38$ for the LG and DLG respectively, confirming the above observation. On the other hand, let $B(t) \equiv [n_{\perp}(t) - n_{\|}(t)]/2N$. One would expect $B(t) \approx 0$ (up to fluctuations) only for the isotropic system. In fact, we measured $B(t) \approx 0$ for the LG, while $B(t)$ rapidly converges to a nonzero value $B(t) \approx 0.05$ for the DLG at early times (again for a large $256 \times 256$ lattice). We take this number, $B(t) = 0.05$, as characterizing the anisotropic shape of DLG clusters at early times.

The difference of segregation between the DLG and the LG at early times merits further study. This will need to take into account the anisotropy of surface tension. In any case, this concerns a regime very near the initial, melt state that only bears minor practical importance, given that it extends extremely shortly on the macroscopic time scale. We are interested in the rest of this chapter on the subsequent evolution, to be described on the assumption of a simple flat interface, which holds in Fig. 7.2 for $t > 100$.

The DLG strings coarsen with time until well defined, relatively-narrow longitudinal (i.e., directed along $\vec{x}$) stripes are formed. (For periodic boundary conditions, the case of our simulations, each stripe forms a ring.) This results into a multi-stripe state, as illustrated in Figs. 7.2 and 7.3. The ordering time in the DLG, defined as the time the system needs to form the stripes, scales with the system size in the direction of the field, $L_{\|}$, since in this case ordered clusters (stripes) percolate along the field direction (see below).[139] This is not the case for the equilibrium LG, where the ordering time depends exclusively on system intensive parameters such as temperature and density.

The multi-stripe states are not stable, however. They are only partially segregated and, in fact, a definite tendency towards a fully segregated state with a single stripe is generally observed in computer simulations. One may also develop simple arguments indicating that, in general, a multi-stripe state will monotonically evolve until forming a single stripe.[51, 143] It is true that, in practice, the complete relaxation may take a very long time. More specifically, a macroscopic system may take to decay into the true stable state a long, *macroscopic* time interval, namely, a time that may show up as mathematically *infinite* in some time scales. In fact, the complete relaxation time is observed to

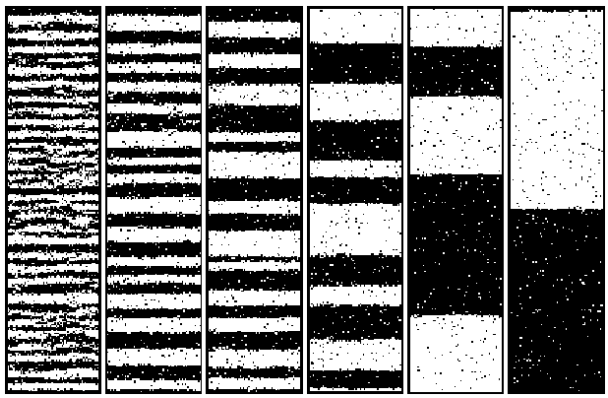

Figure 7.3: A series of MC snapshots that illustrate (late) growth at $T \simeq 0.6T_C^{\infty}$. This is for a rectangular lattice of size $L_{\perp} \times L_{\parallel} = 256 \times 64$ and $t = 10^2, 10^4, 10^5, 10^6, 10^7$ and $1{,}1\text{x}10^8$ MC steps, respectively, from left to right.

increase with system size, as first demonstrated in [139]. It should also be remarked that this property is not a nonequilibrium feature but occurs already in the equilibrium ($E = 0$) case; see, for instance, [116, 118] and references therein. Slow relaxation is a consequence of the conservation of particle density $\rho$ implied by the particle-hole exchange dynamics; this induces scale invariance, namely, slow (power-law) evolution of correlations so that, once enough order sets in, all but very small pattern modifications during a single MC step are precluded. Consequently, certain individual runs sometimes block for a long time in a state with several stripes; however, this does not correspond to the average behavior. As illustrated by Fig. 7.3, which shows a typical evolution, and demonstrated below by our averages corresponding to thousand evolutions, the number of stripes monotonically decreases with time (see also section 7.5), and the whole relaxation can easily be observed in computer simulations if one waits long enough.

We next attempt a theoretical description of the relaxation process. Our interest is on the *anisotropic spinodal decomposition* by which the earliest state with many well-defined stripes decays into a single stripe.We shall assume that relaxation is a consequence of monomer events causing effective diffusion of liquid stripes. (Note that assuming gas stripes here would be completely equivalent.) That is, due to single particle processes, liquid stripes move transversely as a whole, and may collide and eventually coalesce with one of the neighboring stripes; see the late evolution depicted in Fig. 7.3. We notice that coalescence implies evaporation of the gas stripe between the two involved liquid stripes. Therefore, given the particle/hole symmetry, our assumption is in a sense equivalent to assuming that growth is due to evaporation of stripes;[139] however, the view adopted here allows for a more detailed description below.

In order to evaluate the implications of stripe effective diffusion via monomer

events, lets assume that stripes are well defined, compact and exhibit a (linear) interface which is rather flat. This is perfectly justified at sufficiently low temperature (the case analyzed in detail here),[51] and it might hold more generally, in a wide region including the center of the miscibility gap but excluding the critical region. Under this assumption, consider a stripe of mean width $\ell(t)$ that consists of $M$ particles whose coordinates along the transverse (vertical) direction are $y_j(t)$; $j = 1, \ldots, M$. We characterize the stripe position by its center of masses, $Y_{cm}(t) \equiv M^{-1} \sum_j y_j(t)$.

Let us evaluate the *mobility* coefficient $\mathcal{D}_\ell \equiv N_{me}\langle(\Delta Y_{cm})^2\rangle$ which depends on the stripe width $\ell(t)$. Here $N_{me}$ is the number of monomer events per unit time, and $\langle(\Delta Y_{cm})^2\rangle$ is the mean squared displacement of the stripe associated to one of the monomer events. We think of two possible types of events, each giving a different contribution to $\mathcal{D}_\ell$ :

(A) Evaporation-condensation of particles and holes in the stripe surface. Here particles (holes) at the stripe interface evaporate to the hole (particle) gas, and condensate later at the same interface. The evolution of the evaporated particle (hole) in the bulk can be seen as a one dimensional random walk with two absorbing walls, the left and right interfaces, respectively. According to standard random walk theory,[144] the evaporated particle (hole) will go again with unit probability to one of the (two) possible interfaces, Moreover, the random walker will stick again to its original interface with high probability, so trapping a particle (hole) from the opposite interface is unlikely. Consequently, in this case (A), $N_{me}$ is simply the evaporation rate. That is, $N_{me,A} = \nu \sum_j' \exp(-2T^{-1}\Delta_j)$, where $\nu$ is the *a priori* frequency, the sum is over the surface particles and $\Delta_j$ is the number of resulting broken bonds. For a flat linear interface, particles can only jump transversely away the surface, $\nu$ equals the inverse of the lattice coordination number, $q$, and one may write $N_{me,A} \approx 4q^{-1}L_\parallel \exp(-2\bar{\Delta}/T)$ where $\bar{\Delta}$ is the mean number of broken bonds per evaporation event. We multiplied here by 2 to take into account evaporation of surface holes that travel within the stripe to reach the (same) surface again. On the other hand, evaporation processes induce changes $\Delta Y_{cm} = M^{-1}\delta y$, where $\delta y$ is the net particle (transverse) displacement, and $M \approx L_\parallel \times \ell(t)$ for compact stripes. Therefore,

$$\mathcal{D}_\ell^{(A)} \sim 4q^{-1}\langle\delta y^2\rangle\, e^{-2\bar{\Delta}/T}\, L_\parallel^{-1}\ell^{-2}. \tag{7.2}$$

(B) A hole jumps one lattice spacing away within the stripe interior. This induces $\Delta Y_{cm} = 1/M$ or 0, depending on the jump direction. One may write $N_{me,B} = 2\nu\rho_h(T)\, L_\parallel \ell p_h(T)$, where $\rho_h$ is the density of holes, $L_\parallel \ell$ is the *volume* or total number of sites within the liquid stripe, and $p_h$ is the jumping probability per unit time. The factor 2 here comes from the fact that a hole modifies $Y_{cm}$ when jumping to any of the two directions $\pm\vec{y}$. At low T, $\rho_h$ is small; holes are then rather isolated from each other, so that jumps do not modify the number of broken bonds, and $p_h \approx 1$. It ensues

$$\mathcal{D}_\ell^{(B)} \sim 2q^{-1}\rho_h L_\parallel^{-1}\ell^{-1}. \tag{7.3}$$

Note that a different dependence of (7.2) and (7.3) on $\ell$ is a consequence of the fact that the rates $N_{me,A}$ and $N_{me,B}$ involve processes consisting in evaporation on the interface and diffusion on the bulk, respectively.

For $\rho = \frac{1}{2}$, one has on the average stripes of width $\ell$ that are separated a distance $\ell$ from each other. Therefore, a given stripe takes a mean time $\tau_\ell = \ell^2/\mathcal{D}_\ell$ to find (and thus to coalesce with) another one, and this causes its width to increase by $\Delta\ell = \ell$. Consequently, $d\,\ell/d\,t \sim \Delta\ell\ \tau_\ell^{-1} = \mathcal{D}_\ell \ell^{-1}$. Together with (7.2) and (7.3), respectively, this implies that mechanism A is characterized by a power law $\ell \sim t^{1/4}$, and that mechanism B is to be associated with $\ell \sim t^{1/3}$. Furthermore, assuming that pattern growth in the DLG is the result of competition between the two mechanisms, and that they are independent of each other, $\mathcal{D}_\ell = \mathcal{D}_\ell^{(A)} + \mathcal{D}_\ell^{(B)}$, it follows that

$$\frac{d\,\ell}{d\,t} \sim \frac{1}{L_\parallel}\left(\frac{\alpha_A}{\ell^3} + \frac{\alpha_B}{\ell^2}\right), \tag{7.4}$$

where $\alpha_A = 4\nu\langle\delta y^2\rangle\, e^{-2\bar{\Delta}/T}$ and $\alpha_B = 2\nu\rho_h$. This is our general result for the DLG as far as the field $E$ is large, e.g., infinite, and the temperature $T$ is low enough so that the interfaces, and mechanisms A and B, are sufficiently simple as assumed. This is to be compared with the Lifshitz-Slyozov-Wagner behavior $d\,\ell/d\,t \sim \ell^{-2}$ which assumes spatial isotropy and diffusion directly governed by surface tension. Formally, (7.4) is similar to an equation obtained before by assuming isotropic conditions; see section 7.1.[126]

The consequences of (7.2)–(7.4) are as follows. Both (7.2) and (7.3) imply independently that

$$\ell \sim (\varphi\theta)^{1/\varphi}\left(t/L_\parallel\right)^{1/\varphi}. \tag{7.5}$$

The difference is that $\theta = \alpha_A$ and $\varphi = 4$ from (7.2) while one obtains $\theta = \alpha_B$ and $\varphi = 3$ from (7.3). On the other hand, for sufficiently late times, $\ell$ becomes large and equation (7.4) simply solves into

$$\ell(t) \sim \alpha t^{1/3} + \zeta, \tag{7.6}$$

where $\alpha^3 = 3\alpha_B L_\parallel^{-1}$ and $\zeta = \alpha_A/2\alpha_B$. That is, the prediction is that hole diffusion within the stripe (mechanism B) will be dominant at late times. A different hypothesis, based on the stripe evaporation picture, was shown in [139] to imply $\ell \sim \left(t/L_\parallel\right)^{1/3}$. This coincidence is not surprising since, as argued above, the coalescence of two particles stripes implies the evaporation of the intermediate hole stripe and due to the particle/hole symmetry in our system, both mechanisms (stripe diffusion/coalescence and stripe evaporation) correspond to the same physical process yielding the same behavior. In order to uncover the close analogy between the two pictures, one may notice that, to evaporate a particle stripe, many of its particles must cross the surrounding hole stripes and stick on the neighboring particle stripes (this is so since the particle density in the gas phase remains almost constant). This particle migration process through the surrounding hole stripes is in fact what we have called 'hole diffusion within the stripe' in the presence of particle/hole symmetry. Hence the

fundamental mechanism involved in a stripe evaporation is the diffusion of its constituents through the neighboring stripes. This observation is a key one to understand the relation between stripe's evaporation and hole (particle) diffusion.

The effect of mechanism A —surface evaporation and subsequent condensation— on growth is more subtle. In fact, our theory predicts a crossover from the $t^{1/4}$ regime to the $t^{1/3}$ regime as time is increased. That is, the two mechanisms will have a comparable influence at $t \sim \tau_{\text{cross}}$ with

$$\tau_{\text{cross}} = \frac{(4\alpha_A)^3}{(3\alpha_B)^4} L_{\parallel}. \tag{7.7}$$

For times $t < \tau_{\text{cross}}$, mechanism A is dominant and the $t^{1/4}$ behavior is expected, while mechanism B is dominant for $t > \tau_{\text{cross}}$ and the asymptotic $t^{1/3}$ growth law is then observed. The crossover time $\tau_{\text{cross}}$ is a macroscopic, observable time. Further, we may define the time $\tau_{ss}$ at which a single stripe is reached by the condition that $\ell(t) \approx \frac{1}{2}L_{\perp}$. One obtains

$$\tau_{ss} = \frac{L_{\parallel}}{\alpha_B}\left\{\frac{L_{\perp}^3}{24} - \frac{\zeta L_{\perp}^2}{4} + 2\zeta^2 L_{\perp} - 8\zeta^3\left[\ln\frac{\alpha_B\left(2\zeta + \frac{1}{2}L_{\perp}\right)}{L_{\parallel}} - \ln\frac{2\zeta\alpha_B}{L_{\parallel}}\right]\right\}. \tag{7.8}$$

Hence our system is characterized by two different time scales, namely, $\tau_{\text{cross}}$ and $\tau_{ss}$. They depend on system size in a different way. For large systems one generally obtains $\tau_{ss} \gg \tau_{\text{cross}}$, so that the system converges, after a short, perhaps unobservable transient time, to the relevant $t^{1/3}$ behavior. However, there are small systems for which $\tau_{ss} < \tau_{\text{cross}}$. These systems will reach the stationary (single-striped) state before having time to enter into the asymptotic $t^{1/3}$ regime. For these small systems, the only relevant behavior is the $t^{1/4}$ one. Therefore, there is a *size* crossover between $t^{1/4}$ asymptotic behavior for small systems and $t^{1/3}$ asymptotic behavior for large ones. The condition $\tau_{\text{cross}}(T, L_{\parallel}) = \tau_{ss}(T, L_{\parallel}, L_{\perp})$ defines the crossover size.

Consider now the parameter $\gamma \equiv \tau_{\text{cross}}\left(T, L_{\parallel}\right)/\tau_{ss}\left(T, L_{\perp}, L_{\parallel}\right)$. It follows that the $t^{1/3}$ behavior is dominant for $\gamma \ll 1$. However, one also has that $\gamma\left(T, L_{\perp}, L_{\parallel}\right) \to 0$ for finite T in the thermodynamic limit ($L_{\perp}, L_{\parallel} \to \infty$, $L_{\perp}/L_{\parallel} = \text{const}.$). Consequently, the $t^{1/3}$ growth law is the general one, namely, the only one we should expect to observe in a macroscopic system. Corrections to this should only occur at early times in small systems. This is fully confirmed below.

One may also define a longitudinal length,[140, 139] say $\ell_{\parallel} \sim t^{a_{\parallel}}$, where one expects $a_{\parallel} > 1/3$ (given that the growth is more rapid longitudinally than transversely). This length is only relevant during the initial regime, until stripes become well-defined, all of them extending the whole length $L_{\parallel}$. This condition may be taken as defining the onset of the multi-stripe state, which may be characterized by $\ell_{\parallel}(\tau_{ms}) = L_{\parallel}$, from where it follows that $\tau_{ms} \sim L_{\parallel}^{1/a_{\parallel}}$. Interesting enough, this is on the macroscopic time scale, as for both $\tau_{\text{cross}}$ and

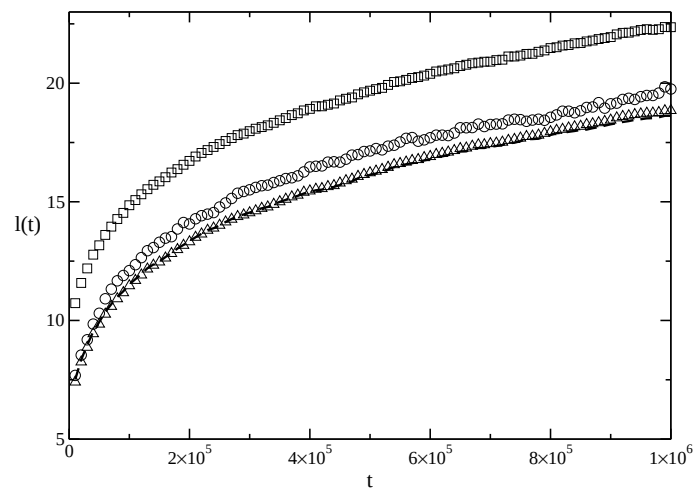


Figure 7.4: Time evolution of the relevant length, $\ell(t)$, as obtained by different methods, namely, from the number $N_s$ of stripes (dashed line), from the maximum width, $\ell_{max}$ (□) from the mass, $\ell_M$ (△), and from the peak of the structure function, $\ell_S \equiv 2\pi/k_{\perp,max}$ (◯); these quantities are defined in the main text. The graphs here correspond to an average over 600 independent runs for the 128x128 lattice.

$\tau_{ss}$ (more precisely, $\tau_{cross} \sim L_{\|}$ and $\tau_{ss} \sim L_{\|} L_{\perp}^3$). The fact that all these relevant times are on the macroscopic, observable time scale confirms that, as argued above, the single-stripe (and not the multi-stripe) state is the only stable one in general. It is also to be remarked that, once the multi-stripe state sets in, the only relevant length is the transverse one, $\ell$. Of course, this is compatible with the possible existence of two correlation lengths describing thermal fluctuations at criticality.

In order to test our predictions, several measures of the relevant length in computer simulations were monitored, namely:

- the maximum width of the stripe, $\ell_{max}$, averaged over all stripes in the configuration. This maximum width is defined as the distance in the direction perpendicular to the field between the leftmost and the rightmost particles within the stripe;
- $\ell_M \equiv M/L_{\|}$, where $M = M(t)$ is the *mass*, or number of particles belonging to the stripe, averaged over all stripes in the configuration. This mass width is defined as the width of a perfectly dense stripe with $M$ particles.
- $\ell_s \equiv L_{\perp}/2N_s$, where $N_s$ is the number of stripes in the configuration.

After averaging over many independent evolutions, all these quantities happen to behave similarly with time. Further measures of the relevant length that we define in the next section behave in the same way. We shall refer to

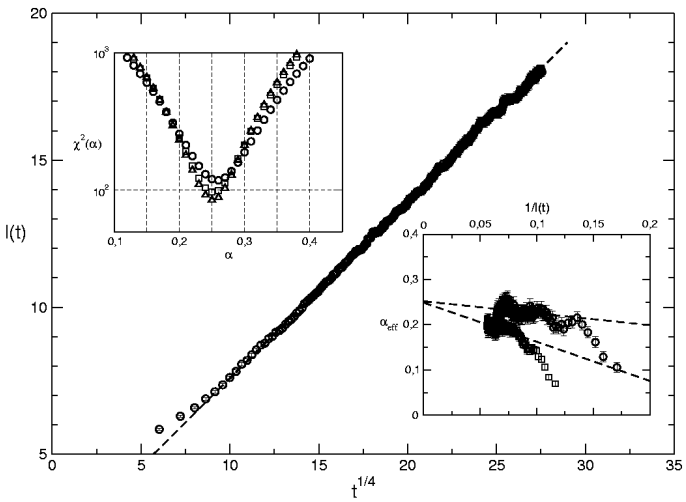


Figure 7.5: The main graph shows $\ell(t) = \ell_S(t)$ versus $t^{a_\perp}$ for $a_\perp = 1/4$ in the case of the "small" 64x64 lattice. A similar behavior is obtained for any of the studied measures of $\ell$ (see the main text for definitions), which are represented in the insets by different symbols, namely, $\ell_{max}$ (□), $\ell_S$ (◯), and $\ell_M$ (△). The upper inset shows the chi square function for varying $a_\perp$ as obtained from a series of fits; a well-defined minimum is exhibited indicating that $a_\perp \simeq 1/4$ in this case. The lower inset shows the *effective exponent*, $d\log_2 \ell \,/\, d\log_2 t$, as a function of $1/\ell(t)$; this extrapolates to the same value of $a_\perp$.

this common behavior, which is illustrated in Fig. 7.4, as $\ell(t)$. (It is noticeable that, before showing a common behavior, Fig. 7.4 reveals some significant differences between our measures of $\ell(t)$ at early times. This confirms the more difficult description —not attempted here— which is required by the initial regime.)

In Figs. 7.5 and 7.6 we illustrate our analysis and main results concerning the (late) time evolution of $\ell(t)$. The predictions above are confirmed and, in particular, "small" lattices —Fig. 7.5— happen to behave differently than "large" lattices —Fig. 7.6. In both cases we plotted $\ell(t)$ versus $t^{a_\perp}$ for varying $a_\perp$, looking for the best linear fit $\ell(t) = \alpha t^{a_\perp} + \zeta$, excluding the initial time regime. The upper insets in the figures show the chi square function associated to each fit, namely,

$$\chi^2(a_\perp) = \sum_{i=1}^{\eta} \frac{[\ell(t_i) - (\alpha t_i^{a_\perp} + \zeta)]^2}{\alpha t_i^{a_\perp} + \zeta}, \tag{7.9}$$

for a least-squares fit to $\eta$ data points using parameters $a_\perp$, $\alpha$ and $\zeta$. The graphs confirm the existence of a common behavior for all the monitored measures of $\ell(t)$ (indicated by different symbols). These graphs also demonstrate that $\ell(t) = \alpha t^{a_\perp} + \zeta$, with small $\zeta$, during the whole time regime of consideration.

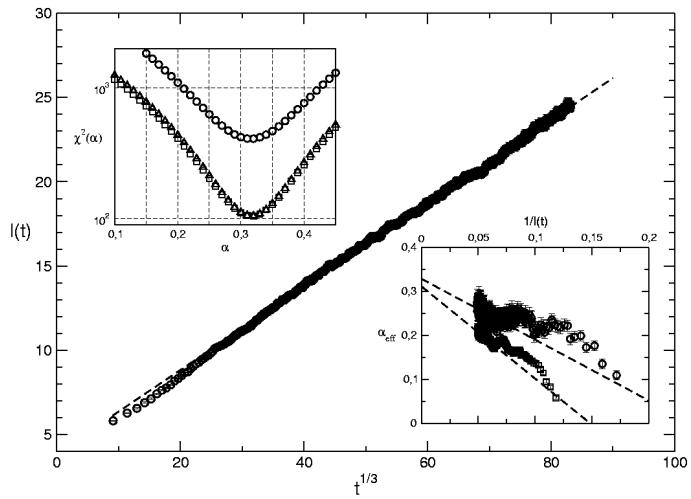


Figure 7.6: Same as Fig. 7.5 but demonstrating that $a_\perp = 1/3$ for the "large" $L_\perp \times L_\parallel =$ 256x64 lattice (one obtains a similar result for larger $L_\parallel$).

On the other hand, the upper insets indicate that $a_\perp$ is very close to $\frac{1}{4}$ for "small" systems (in fact, for $L_\perp \leq 128$) while $a_\perp \simeq \frac{1}{3}$ as the system becomes larger, say $L_\perp \geq 256$ that corresponds to a "large" lattice according to familiar MC standards. As an alternative method to analyze $\ell(t)$, one may evaluate

$$\overline{a}(t) \equiv \frac{d \log_n \ell(t)}{d \log_n t}. \tag{7.10}$$

Our prediction is that $\overline{a}(t) = a_\perp - \zeta a_\perp / \ell(t)$, i.e., this should provide the exponent $a_\perp$ by extrapolating to large $\ell(t)$ (late time). The insets at the bottom of Figs. 7.5 and 7.6 show the results for $n = 2$. They are in agreement with the other method, and again confirm our predictions.

As indicated above, the size crossover between the $t^{1/4}$ and $t^{1/3}$ asymptotic regimes is expected for a system size $(L_\parallel, L_\perp)$ such that $\tau_{\text{cross}}\left(T, L_\parallel\right) = \tau_{\text{ss}}\left(T, L_\perp, L_\parallel\right)$. In order to make this condition explicit, we need to estimate the amplitudes $\alpha_A$ and $\alpha_B$ in (7.4); see equations (7.7) and (7.8). These amplitudes, which state the relative importance of surface evaporation/condensation versus bulk hole-diffusion, are given respectively by $\alpha_A = 4q^{-1}\langle \delta y^2 \rangle e^{-2\bar{\Delta}/T}$ and $\alpha_B = 2q^{-1}\rho_h$. We note that, for a sufficiently flat interface (i.e., one that involves microscopic –but not macroscopic– roughness), $\langle \delta y^2 \rangle \sim \mathcal{O}(1)$ and $\bar{\Delta} \simeq 5$. On the other hand, the excess energy associated to an isolated hole is 16, so that $\rho_h \sim \exp(-16/T)$ is a rough estimate of the hole density. As depicted in Fig. 7.7, it follows numerically, in full agreement with our observations, that $a_\perp = \frac{1}{4}$ is to be observed only at early times, earlier for larger systems; to be more specific, the crossover for $L_\parallel = 64$, for instance, is predicted for $L_\perp \sim 140$, which confirms the above; see also Figs. 7.5 and 7.6.

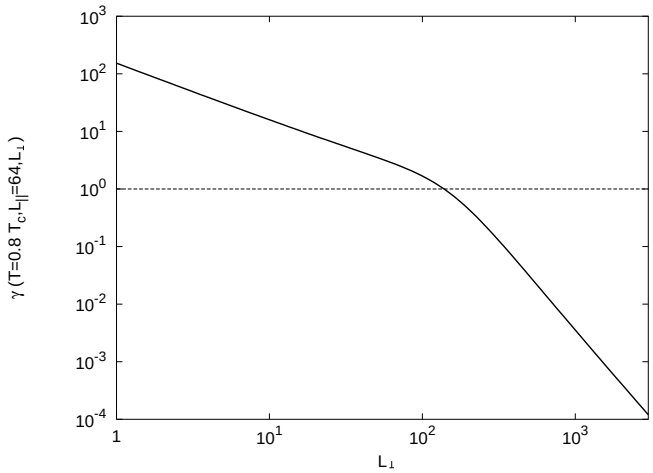


Figure 7.7: The parameter $\gamma = \tau_{\text{cross}}(T, L_{\parallel})/\tau_{\text{ss}}(T, L_{\perp}, L_{\parallel})$, with the characteristic times $\tau_{\text{cross}}$ and $\tau_{\text{ss}}$ defined in the main text, as a function of $L_{\perp}$ for $L_{\parallel} = 64$, using our estimates for the amplitudes $\alpha_A$ and $\alpha_B$. This confirms our distinction between "small" and "large" lattices, as explained in the main text.

This behavior may be understood on simple grounds. The surface/volume ratio is large initially and, consequently, mechanism A (based on surface events) is then dominant. This is more dramatic the smaller the system is. That is, the surface is negligible for macroscopic systems, in general, and, as illustrated in Fig. 7.3, even if the surface is relevant at very early times, its ratio to the volume will monotonically decrease with time. This causes hole diffusion in the bulk (mechanism B) to become dominant, more rapidly for larger systems, as the liquid phase is trying to exhibit only two surfaces. On the other hand, ref. [139] studies the stripe coarsening process in the infinitely driven lattice gas. Pure $t^{1/3}$ behavior is reported assuming the stripe evaporation mechanism. This result is perfectly compatible with our results, given that the systems in ref. [139] correspond to very large values of $L_{\perp}$ (800 and 960) and small values of $L_{\parallel}$ (8, 16 and 32). For these shapes our theory also predicts the (simple) $t^{1/3}$ asymptotic behavior.

## 7.4 Correlations and the Structure Factor

Consider now the Fourier transform of the pair correlation function $C(x, y; t) = \langle n_{0,0}(t)\ n_{x,y}(t)\rangle$, where $n_{x,y}$ stands for the occupation variable at lattice site $\vec{r} = (x, y)$. This is the so-called structure factor, $S(\vec{k}, t)$, where $\vec{k} = (k_{\parallel}, k_{\perp})$. Given that the $k_{\parallel}$ dependence is only relevant at early times, before the multi-stripe state sets in, i.e., for $t < \tau_{\text{ms}}$, we shall set $k_{\parallel} = 0$ in the following. That is,

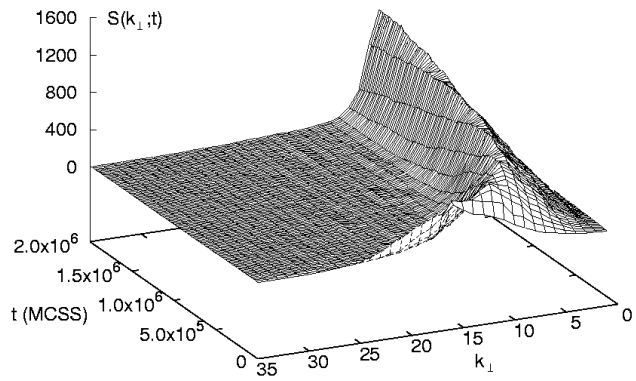


Figure 7.8: Time development of the structure factor $S(k_\perp; t)$, as defined in the main text, for a "large" lattice $L_\perp \times L_\parallel = 256 \times 256$ during early and intermediate phase segregation. A peak grows with time as it shifts towards the small values of $k_\perp$.

our interest here is on

$$S(k_\perp; t) = \frac{1}{L_\parallel L_\perp} \left| \sum_{x,y} n_{x,y}(t) \exp[ik_\perp y] \right|^2 . \tag{7.11}$$

As illustrated in Fig. 7.8, this function develops a peak at $k_\perp = k_{max}(t)$ immediately after quenching. The peak then monotonically shifts towards smaller wave numbers with increasing t; in fact, one expects $k_\perp \to 0$ as $t \to \infty$ in a macroscopic system. The wave length $\ell_S \equiv 2\pi/k_{max}$ turns out to be an excellent characterization of the relevant order, namely, it measures both the stripe width and the stripe separation during phase segregation. In particular, we confirm that $\ell_S(t)$ has the common behavior discussed above for length $\ell(t)$; see Figs. 7.4, 7.5 and 7.6.

The fact that the DLG shows a unique *time-dependent* relevant length, $\ell_\perp = \ell(t)$, has some important consequences. For example, extrapolating from the equilibrium case (see section 7.1),[121] one should probably expect dynamical scaling, i.e.

$$S(k_\perp; t) \propto \ell(t) F[k_\perp \ell(t)] \tag{7.12}$$

for the anisotropic DLG in two dimensions. This is indeed observed to hold during most of the relaxation and, in particular, during all the segregation process after formation of well-defined stripes. This is illustrated in Fig. 7.9 depicting the scaling function F. A time-dependent mean-field model of a binary mixture in shear flow has recently been demonstrated to exhibit a similar

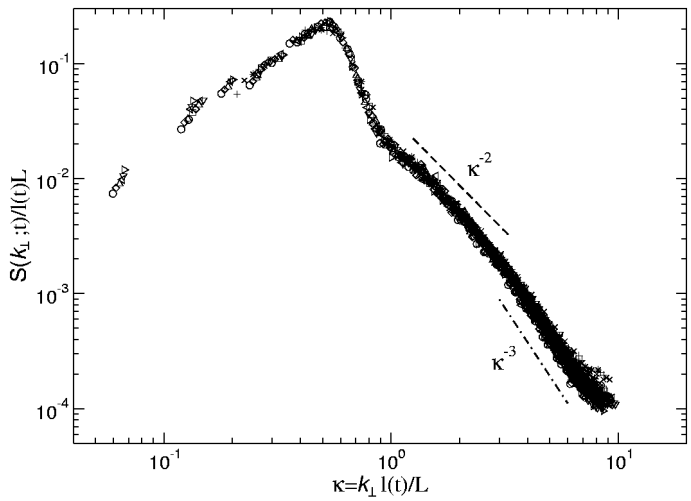


Figure 7.9: The scaling with both time and size of the structure function to show that $\Phi(\kappa) \equiv S(k_\perp;t)/\ell L$, with $\kappa = k_\perp \ell L^{-1}$, is well-defined and universal, i.e., the same at any time (excluding some early evolution) and for any square lattice of side $L$. This plot includes all data for $t \geq 10^4$ MC steps and 64x64, 128x128, and 256x256 lattices. The broken lines illustrate the different kinds of behavior of $\Phi(\kappa)$ that are discussed in the main text.

property, though involving two lengths both behaving differently from $\ell(t)$ above.[132]

The structure factor may be obtained by scattering, which makes it an important tool in many studies. Analyzing further the details of functions $S(k_\perp;t)$ and $F(\varkappa)$ or, alternatively, the universal function $\Phi(\varkappa) \equiv S/\ell L$, as observed in computer simulations is therefore of great interest (the extra $L$ factor in the definition of $\Phi(\varkappa)$ is our finite size scaling ansatz). Experimental studies often refer to the mean 'radius of gyration' of the grains as the slope of the straight portion in a plot of $\ln[S(k,t)]$ *versus* $k^2$.[145] We checked the validity under anisotropic conditions of this concept, which is in fact quite useful in equilibrium even outside the domain of validity of its approximations.[121] We confirm that $S(k_\perp;t)$ exhibits the Guinier Gaussian peak, namely,

$$\Phi(\varkappa) \sim \exp\left[-\text{const.}\,(\varkappa - \varkappa_{\max})^2\right] \tag{7.13}$$

around the maximum $\varkappa_{\max}$. More intriguing is the behavior of $\Phi(\varkappa)$ before the peak, $\varkappa < \varkappa_{\max}$. Fig. 7.9 indicates that scaling does not hold in this region even at the end of our (otherwise long enough) simulations. This is so because $\Phi(\varkappa)$ goes as $\rho^2 L/\ell(t)$ at $k_\perp = 0$, and thus depends on time for very small values of $\kappa$, breaking the scaling observed for larger values of $\kappa$. However, a detailed study of data reveals that the scaling function near the origin tends with time towards a common envelope $\Phi(\varkappa) \sim \varkappa^{1+1/3}$ for $\varkappa_0 < \varkappa < \varkappa_{\max}$; we do not

have a simple explanation of this. In any case, this behavior breaks down close to the origin, $\varkappa \lesssim \varkappa_0$, where $\Phi(\varkappa) \to 0$ as $\varkappa \to 0$ and $t \to \infty$ for the infinite system.

The behavior after the peak, $\varkappa > \varkappa_{\max}$, may be predicted on simple grounds. The (sphericalized) structure factor for (equilibrium) isotropic binary mixtures is known to satisfy the Porod's law, $S \sim k^{-(d+1)}$ at large enough $k$, where $d$ is the system dimension,[121] i.e., $S \sim k^{-3}$ in two dimensions. The main contribution to the large-$k$ tail comes from the short-distance behavior of $C(x, y; t)$. That is, the Porod's region for the DLG may be taken to correspond to $\lambda_\perp \ll k_\perp^{-1} \ll \ell(t)$, where $\lambda_\perp$ stands for a (transverse) thermal length that characterizes the smallest, thermal fluctuations. Let two points, $\vec{r}_0$ and $\vec{r}_0 + \vec{r}$, $\vec{r} = (x, y)$. For any $x$ such that $\lambda_\perp \ll x \ll \ell(t)$, one roughly has that the product $n_{\vec{r}_0}(t)\ n_{\vec{r}}(t)$ equals $+1$ if the two points are on the stripe, and $0$ otherwise, i.e., if either an interface exists between them or else the two points belong to the gas between stripes. Since $x \ll \ell(t)$, the probability that $\vec{r}$ crosses more than one interface is negligible. For a half-filled system, the probability that $\vec{r}_0$ lies at a particle stripe is $\frac{1}{2}$, and the probability that both $\vec{r}_0$ and $\vec{r}_0 + \vec{r}$ belong to the same stripe is roughly $\frac{1}{2}(\ell(t) - x)/\ell(t)$. Hence,

$$C(x, y; t) \simeq \frac{1}{2}\left(1 - \frac{x}{\ell(t)}\right), \qquad x \ll \ell(t). \tag{7.14}$$

By power counting, this implies the *anisotropic Porod law* (in two dimensions):

$$S(k_\perp; t) \sim \frac{1}{\ell(t)\ k_\perp^2}, \qquad \lambda_\perp \ll k_\perp^{-1} \ll \ell(t). \tag{7.15}$$

Therefore, $\Phi(\varkappa) \sim \varkappa^{-2} L^{-1}$, which is confirmed in Fig. 7.9. This is in contrast with the (isotropic) Porod's result. The difference is a consequence of the fact that the DLG clusters are stripes that percolate in the direction of the field, instead of the isotropic clusters of the LG. The short-distance pair correlation function for the latter is $C(\vec{r}; t) \simeq \frac{1}{2}(1 - |r|/\ell(t))$, from which one has that $\Phi(\varkappa) \sim \varkappa^{-3}$. It follows that anisotropy may easily be detected by looking at the tail of the structure factor.

The detailed analysis of $S(k_\perp; t)$ also reveals that, as $L_\parallel$ is increased in computer simulations, the anisotropic behavior $\Phi \sim \varkappa^{-2}$ crosses over to $\Phi \sim \varkappa^{-3}$ for larger $\varkappa$; see Fig. 7.9. We believe this reflects the existence of standard thermal fluctuations. That is, very small clusters of particles occur in the gas in the asymptotic regime whose typical size in the direction perpendicular to the field is of order $\lambda_\perp$. These very-small asymptotic clusters are rather isotropic, namely, they do not differ essentially from the corresponding ones in equilibrium binary mixtures. More specifically, for $x \sim \lambda_\perp$, one may approximate $C(\vec{r}; t) \sim 1 - |r|/\lambda_\perp(t)$, which implies the $\varkappa^{-3}$ power-law tail for large $\varkappa$. On the other hand, according to (7.5), the mean stripe width grows as $\ell(t) \sim (t/L_\parallel)^a$ with $a = 1/4$ or $a = 1/3$, depending on the value of $L_\perp$. Therefore, the number of stripes at time $t$ is proportional to $L_\perp L_\parallel^a / t^a$ and, for a given time, the number of stripes increases with $L_\parallel$ as $L_\parallel^a$. We also know that, at a given time, the

number of small, fluctuating clusters is proportional to $L_{\|}$. Hence the relative importance of small clusters due to thermal fluctuations as compared to stripes is proportional to $L_{\|}$. In fact, the $\varkappa^{-3}$ tail is observed for large enough values of $L_{\|}$ but not for small lattices.

## 7.5 A Continuum Description

The rigorous derivation of a general continuum analog of the driven lattice gas is an open problem.[51] Recent studies led to the following proposal for a coarse-grained density, $\phi(\mathbf{r}, t)$ :[147]

$$\partial_t \phi(\mathbf{r}, t) = \tau_\perp \nabla_\perp^2 \phi - \nabla_\perp^4 \phi + \frac{\lambda}{6} \nabla_\perp^2 \phi^3 + \tau_\| \nabla_\|^2 \phi + \nabla_\perp \xi(\mathbf{r}, t). \tag{7.16}$$

Here, the last term stands for a conserved Gaussian noise representing the fast degrees of freedom, and $\tau_\perp$, $\tau_\|$ and $\lambda$ are model parameters. Compared to previous proposals,[148, 137] this Langevin type of equation amounts to neglect a non-linear current term, $-\alpha \nabla_\| \phi^2$, that was believed to be essential (*relevant*) at criticality. However, one may show that, at least in the limit $E \to \infty$, the coefficient $\alpha$ cancels out (due in this case to a subtle saturation effect).[147] In fact, recent scaling analysis has unambiguously confirmed that a particle current is not relevant and that equation (7.16) captures the correct critical behavior of the DLG.[140, 141] Consequently, an important question is now whether (7.16) reproduces also the kinetic behavior of the DLG as described in previous sections. We present here a first confirmation that, as compared with other approaches,[137] (7.16) is indeed a proper continuum description of the DLG kinetic relaxation.

In order to numerically integrate (7.16), let us introduce the indexes $i, j = 1, \ldots, N$ to represent, respectively, the two components of $\mathbf{r} \equiv (x_\perp, x_\|)$ . One thus makes a trivial discretization of the space, and then of the time by Cauchy-Euler method.[149] The result is a set of $N^2 - 1$ coupled nonlinear equations, namely,

$$\begin{aligned} \phi(i, j; t + \Delta t) &= \phi(i, j, t) \\ &+ \Delta t \left[ \tau_\perp \widetilde{\nabla}_\perp^2 \phi - \widetilde{\nabla}_\perp^4 \phi + \frac{\lambda}{6} \widetilde{\nabla}_\perp^2 \phi^3 + \tau_\| \widetilde{\nabla}_\|^2 \phi \right] + \sqrt{\Delta t} \widetilde{\nabla}_\perp \xi(i, j; t). \end{aligned} \tag{7.17}$$

This equation is to be solved by the computer. With this aim, we may write $\widetilde{\nabla}_\perp \xi(i, j; t) = [\xi(i+1, j; t) - \xi(i-1, j; t)] / 2\Delta x_\perp$ and $\phi(i, j; t) \equiv \phi(i\Delta x_\perp, j\Delta x_\|; t)$ where $\Delta x_\perp = L_\perp / N$ and $\Delta x_\| = L_\| / N$. The maximum value of $\Delta x_\perp$ is thus limited by the interface width. For Fig. 7.10, which concerns a $256 \times 256$ lattice $(N = 256)$ we —rather arbitrarily— used $\Delta x_\perp = \Delta x_\| = 1.7$, and $\Delta t = 0.05$, which produce a locally stable solution. The parameters $\tau_\perp$, $\tau_\|$ and $\lambda$, are fixed on the basis of its physical meaning. The *mass* terms $\tau_\|$ and $\tau_\perp$ represent temperatures along the longitudinal and transverse directions, respectively, relative to the critical temperature, i.e., $\tau_\perp \sim (T_\perp - T_C^\infty)$. Given the anisotropy of

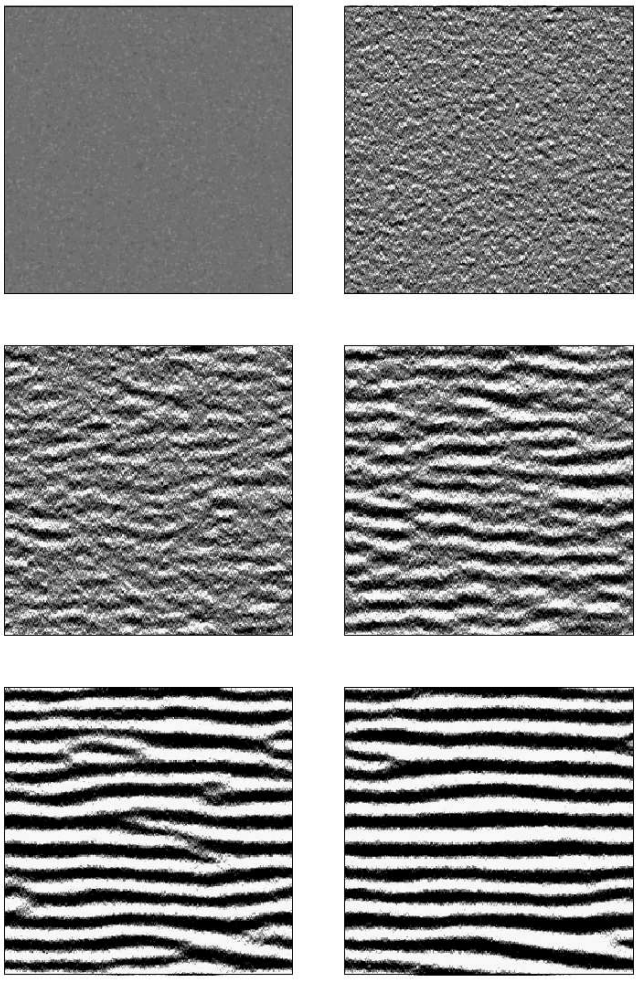

Figure 7.10: Series of snapshots as obtained from equation (7.17) for the $256 \times 256$ lattice with parameters as given in the main text. Time (arbitrary units) is $t = 0, 10, 100, 200, 500$, and $1000$ respectively, from left to right and from top to bottom.

phase segregation, with longitudinal interfaces only, $\tau_\perp < 0$ and $\tau_\parallel > 0$. On the other hand, $|\tau_\perp|$ should be small enough to allow for a relatively fast evolution. Our choices for Fig. 7.10 are $\tau_\perp = -0.25$, $\tau_\parallel = 0.5$ and $\lambda = 1$.

It is remarkable that, in spite of some apparent similarity, the problem here differs from the one in the study of (standard) spinodal decomposition by means of the isotropic ($E = 0$) Cahn-Hilliard equation. In equilibrium,[150] one usually assumes that the influence of noise on growth, which is then assumed to be directly driven by surface tension, is negligible far from criticality. The noise term in (7.17) may be expected to be important in a more general context, however. That is, as described in section 7.3, the DLG develops striped patterns in which surface tension smooths the interfaces but has no other dominant role on the basic kinetic events. Consequently, neglecting the noise in (7.17) would turn metastable any striped geometry after coarsening of strings, which is not acceptable (see section 7.3).

Finally, it is interesting to notice that if a one-dimensional structure is assumed, and the gradient in the direction parallel to the field in Eq. 7.16 is eliminated, then this equation reduces to the one-dimensional time-dependent Ginzburg-Landau model in [153]. There it was found a $\ln(t)$ growth at zero temperature and a crossover from $\ln(t)$ to $t^{1/3}$ at finite temperatures.

## 7.6 Conclusion

This chapter presents a theoretical description of spinodal decomposition in the DLG, and compares it with new data from a kinetic Monte Carlo study. This is also compared with the kinetic implications of a Langevin, continuum equation that had previously been shown to capture correctly the critical behavior of the DLG. The resulting picture from these three approaches, which is summarized below, should probably hold for a class of highly-anisotropic phase segregation phenomena. In fact, our results provide a method for analyzing experiments that could be checked against laboratory realizations of the DLG, i.e., the case of phase segregation under biased fields or other influences such as electric fields, gravity and elastic stresses.

Immediately after a deep quench, there is an early regime in which anisotropic grains develop. They tend to coarsen to form small strings that then combine into well-defined thin stripes. Such nucleation and early coarsening (Figs. 7.1 and 7.2) seem governed by surface tension at the string ends competing with other both surface and bulk processes. This complicated situation typically extends less than $10^3$ MC steps in computer simulations, which corresponds to a very short macroscopic time, so that it would be hardly observable in experiments. As a matter of fact, most of the system relaxation proceeds by coarsening of stripes until full segregation (Fig. 7.3). Surprisingly enough, this regime, which has been studied for more than a decade now,[135]-[139] happens to be theoretically simpler than the corresponding one for the isotropic case.[115]-[125]

The evolution from many stripes to a single one mainly proceeds by compe-

tition of two mechanisms: (A) evaporation of a particle (hole) from one stripe surface and subsequent deposition at the same surface, and (B) diffusion of a hole within the bulk of the stripe. The first one dominates initially (and lasts more for smaller systems), when the surface/volume ratio is relatively large. Mechanism A implies that the relevant length (as defined in Fig. 7.4) increases with time according to $\ell(t) \sim t^{1/4}$. The surface/volume ratio decreases with time, however, and mechanism B soon becomes dominant. This implies $\ell(t) \sim t^{1/3}$ which is the general prediction for a macroscopic system (cf. Figs. 7.5, 7.6 and 7.7)[3]. This was obtained before by assuming coarsening of two (liquid) stripes by evaporation of the gas stripe placed between them;[139] see also [135]. Note that the $t^{1/3}$ law is precisely the behavior which is acknowledged to be dominant under isotropy, but this has a different origin in the equilibrium case.[118, 119] Note also that surface tension determines evaporation rates but has no other influence on mechanisms A and B.

The $t^{1/3}$ growth law, (7.6), is perfectly confirmed by the DLG data (Fig. 7.6). This indicates time-scale invariance. In fact, such invariance was demonstrated for the isotropic case, in which the situation is somewhat more involved (section 7.1). The invariance property may be better analyzed by looking at the structure factor transversely to the drive, $S(k_\perp, t)$ (Fig. 7.8). This exhibits *dynamic scaling*, i.e., it remains self-similar during phase segregation[4]. More specifically, $\Phi(\varkappa) \equiv S(k_\perp; t)/\ell L$, with $\varkappa = k_\perp \ell L^{-1}$, is universal, namely, the same at any (sufficiently late) time $t$ and for any square lattice of side $L$. Furthermore, the function $\Phi(\varkappa)$ has a well-defined shape. In particular, it exhibits the Guinier Gaussian peak, and this is followed by the *anisotropic Porod* decay, $\Phi(\varkappa) \sim \varkappa^{-2}$ and then by a *thermal tail* $\Phi(\varkappa) \sim \varkappa^{-3}$ (Fig. 7.9). Also noticeable is the fact that the the parameter to scale along the $S$ axis is $J(t) = \ell$ and not $\ell^2$ as under isotropy.

Our results in this chapter have two main restrictions, both due to the great computational effort required by this problem.[51] Firstly, they follow from an extensive analysis of only one phase-diagram point, namely, $\rho = \frac{1}{2}$, $E = \infty$, and $T = 0.8T_C^0$. However, our own observations (including brief investigation of other points), together with an extrapolation of the many results known for the isotropic case, strongly suggest that the picture in this chapter holds within a large domain around the center of the miscibility gap[5]. In fact, the scaled structure factor for isotropic systems was shown to be almost independent of density and temperature, and even the substance investigated, in a wide region below the coexistence line.[124] Our consideration of only a two-dimensional system does not seem a real restriction neither. That is, adding an extra (transverse) dimension should not essentially modify the picture here[6].

[3]The $t^{1/3}$ behavior here is in contrast with the logarithmic growth that is assumed to govern a class of lattice models in which coarsening is not a direct consequence of surface tension.[151]

[4]More properly, one should speak here of "self-affinity", given the underlying anisotropy.[133]

[5]Extending some of our arguments to $\rho \neq \frac{1}{2}$ needs some care but the whole picture should still be valid, at least not far from $\rho = \frac{1}{2}$.

[6]Note that the Lifshitz-Slyozov-Wagner behavior is known to be valid in some cases in both $d = 2$ and $d = 3$.[119]

It would be interesting to look next in the laboratory for both time-scale invariance and $t^{1/3}$ growth under highly anisotropic conditions. In fact, there are some evidences of such behavior in sheared fluids (section 7.1), and one may think of some more direct experimental realizations of the driven lattice gas. In particular, coarsening striped patterns very similar to those observed in our system are found in some intriguing experiments on granular binary mixtures under shaking.[152] We think that the mechanisms we propose in this chapter should help the understanding of such experimental results. In general, we hope our observations will motivate both experiments and future more complete theories.

# Chapter 8

# Dynamic Phase Transitions in Systems with Superabsorbing States

## 8.1 Introduction

Dynamic phase transitions separating active from fluctuation-free absorbing phases appear in a vast group of physical phenomena and models as, for instance, directed percolation [155, 156], catalytic reactions [157], the pining of surfaces by disorder [158], the contact process [159], damage spreading transitions [160], nonequilibrium wetting [161], or sandpiles [162, 163]. See [155] and [156] for recent reviews. Classifying these transitions into universality classes is a first priority theoretical task. As conjectured by Janssen and Grassberger [164] some time ago and corroborated by a huge number of theoretical studies and computer simulations, systems exhibiting a continuous transition into a unique absorbing state with no extra symmetry or conservation law belong to one and the same universality class, namely that of directed percolation (DP). At a field theoretical level this class is represented by the Reggeon field theory (RFT) [165].

This universality conjecture has been extended to include multicomponent systems [166] and systems with infinitely many absorbing states [167, 168]. On the other hand some other, less broad, universality classes of systems with absorbing states have been identified in recent years. They all include some extra symmetry or conservation law, foreign to the DP class. For example, if two symmetric absorbing states exist (which in many cases is equivalent to having activity parity-conservation [169]), the universality class is other than DP, and the corresponding field theory differs from RFT [170]. A second example is constituted by systems with absorbing states in which fluctuations occur only at the interfaces separating active from absorbing regions, but not in the bulk of

compact active regions (examples of this are the *voter model* or compact directed percolation [171]). In this case the exponents are also non DP. A third and last example is that of systems with many absorbing states in which the activity field is coupled to an extra conserved field. This type of situation appears, for example, in conserved sandpile models, and has been recently shown to define a new universality class [162, 172]. Apart from these and some few other well known examples[1], systems with absorbing states belong generically into the DP universality class.

Recently, it has been proposed a very simple, biologically motivated model, exhibiting a continuous transition into an absorbing phase,[176] and claimed that this model shows a sort of "superuniversality", i.e. in both one and two dimensions the model has the same critical exponents, namely those of one-dimensional DP. Consequently, the system has been hypothesized to show a rather strange *dimensional reduction*[2] in two dimensions. This conclusion, if confirmed, would break the Janssen-Grassberger conjecture, since it is not clear that any new symmetry or extra conservation law is present in this model. In what follows we show what are the physical reasons why this model does not show directed percolation behavior: the presence of what we called *superabsorbing sites* is at the basis of this anomalous behavior. We will discuss also how DP can be restored by changing the geometry of the lattice on which the model is defined.

## 8.2 The Model

The model (called from now on Lipowski model) is defined operationally as follows: let's consider a square d-dimensional lattice. At a bond linking neighboring sites, $i, j$, a random variable $w = w_{ij}$ is assigned. Different bonds are uncorrelated, and $w$ is distributed homogeneously in the interval $[0, 1]$. At each site $i$ one defines $r_i$ as the sum of the four bonds connecting this site to its four nearest neighbors. If $r_i$ is larger that a certain threshold, $r$ (that acts as a control parameter) the site is declared active, otherwise the site is inactive or absorbing. Active sites are considered unstable; at each step one of them is chosen randomly and its four associated $w_{ij}$ bond variables are replaced by four freshly chosen independent random values (extracted from the same homogeneous probability distribution), and time is incremented by an amount $\Delta t = 1/n(t)$, where $n(t)$ is the number of active sites at that time. Critical exponents are defined as it is customary in the realm of absorbing phase transitions [155].

It is clear that for small values of $r$, for instance $r = 0$, the system will always be active, while for large enough values of $r$ an absorbing configuration

[1]For example, long range interactions do also change the universality.[173]

[2]Dimensional reduction is not a new concept in statistical physics. For example, quenched disordered magnetic systems were some time ago claimed to behave in d dimensions as their corresponding pure counterparts in $d - 2$ dimensions [174]. However, this results, is at odds with simple domain wall arguments, and has recently proven to fail [175].

(with $r_i < r$ for all sites $i$) will be eventually reached. Separating these two regimes we observe a critical value of $r$, $r_c$, signaling the presence of a continuous phase transition. In $d = 1$ $r_c \approx 0.4409$ [176], while for $d = 2$ we find $r_c = 1.38643(3)$. As bond variables are continuous it is obvious that there is a continuous degeneracy of the absorbing state (i.e. infinitely many absorbing configurations).

In the one dimensional case, all the measured critical exponents take the expected DP values [176], compatible with theoretical predictions for systems with many absorbing states [168, 177]. The only discrepancy comes from the fact that the spreading exponents $\eta$ and $\delta$ (see section 8.3.2 for definitions) appear to be non-universal, but the combination $\eta + \delta$ coincides with the DP expectation. This non-universality in the spreading is however generic of one-dimensional systems with an infinite number of absorbing states [178, 177], and therefore it does not invalidate the conclusion that the system behaves as DP.

In two dimensions the only measured critical exponent in [179] is the order parameter one, $\beta$, which has been reported to take a value surprisingly close to the one dimensional DP expectation, $\beta \approx 0.27$ [179]. Based on this observation it has been claimed that the system exhibits a sort of dimensional reduction. This possibility would be very interesting from a theoretical point of view and elucidating it constitutes the main original motivation of what follows.

Finally let us mention that for spreading experiments it was found that, as happens generically in two-dimensional systems with many absorbing states [177, 180], the critical point is shifted, and its location depends on the nature of the absorbing environment the initial seed spreads in. In particular, the annular type of growth described in [179] in the case of spreading into favorable media is typical of spreading in two-dimensional systems with many absorbing states, and it is well known to be described by dynamical percolation [177, 180].

## 8.3 Model Analysis

In order to obtain reliable estimations for $\beta$ and determine other exponents, we have performed extensive Monte Carlo simulations in $d = 2$ combined with finite size scaling analysis, as well as properly defined spreading experiments.

### 8.3.1 Finite Size Scaling Analysis

We have considered square lattice with linear dimension $L$ ranging from 32 to 256. Averages are performed over a number of independent runs ranging from $10^2$ to $10^5$ depending on the distance to the critical point and on system size. The first magnitude we measure is the averaged density of active sites, $\rho(L, r, t)$, which for asymptotically large times converges to a stationary value $\rho(L, r)$. Observe that for small system sizes the system always reaches an absorbing configuration in finite time and therefore the only truly stationary state is $\rho = 0$. In order to extrapolate the right asymptotic behavior in the

active phase one has to determine $\rho(L, r)$ averaged over the runs which have not reach an absorbing configuration. A peculiarity of this system is that its convergence towards a well defined stationary state is very slow, fluctuations around mean values are extremely persistent and, therefore, a huge number of runs is needed in order to obtain smooth evolution curves. Owing to this fact, numerical studies are rather costly from a computational point of view. The reasons underlying such anomalously long lived fluctuations will be discussed in forthcoming sections. The maximum times considered are $8 \times 10^5$ Monte Carlo steps per spin; this is one order of magnitude larger than simulations presented in [179]. Near the critical point the relaxation times are very large (larger than $10^5$) and, in order to compute stationary averages, transient effects have been cut off. We observe the presence of a continuous phase transition separating the active from the absorbing phase at a value of $r \approx 1.38$.

Assuming that finite size scaling holds [181] in the vicinity of the critical point point $r_c$, we expect for values of $r < r_c$ (i.e. in the active phase)

$$\rho(L, r) \sim L^{-\beta/\nu_\perp} \mathcal{G}(L/\Delta^{-\nu_\perp}) \tag{8.1}$$

where $\Delta = |r - r_c|$. Right at the critical point, this corresponds to a straight line in a double logarithmic plot of $\rho(L, r)$ vs. $L$. In Fig. 8.1 it can be seen that, in fact, we observe a straight line as a function of $\log(L)$ for $r = 1.38643(3)$ which constitutes our best estimation of $r_c$. This finite size analysis allows us to determine $r_c$ with much better precision than in the previous estimations [179]. From the slope of the previous log-log plot we measure $\beta/\nu_\perp = 0.57(2)$ which is quite far from both, the one-dimensional DP exponent $\beta/\nu_\perp = 0.2520(1)$, and the two-dimensional value $0.795(5)$.

We have considered the larger available system size, $L = 256$, and studied the time decay of a fully active initial state for values of $r$ close to $r_c$ in the active phase (see Fig. 8.2). The stationary values for large values of $t$ should scale as $\rho(L, r) \sim \Delta(L)^\beta$. From the best fit of our data (see Fig. 8.3) we determine both $r_c(L = 256) \approx 1.38645$ and $\beta = 0.40(2)$.

At the critical point, $\rho(r = r_c, t) \sim t^{-\theta}$. From the asymptotic slope of the curve for $r_c(L = 256)$ in Fig. 8.2, we measure $\theta = 0.275(15)$. In this way, we have already determined three independent exponents. From these, using scaling laws, we can determine others, as for example $\nu_\perp = \beta/(\beta/\nu_\perp) = 0.69(9)$ (to be compared with the DP prediction 1.09 in $d = 1$ and 0.733 in two dimensions [182]).

To further verify the consistency of our results we have considered $\rho(L, r)$ computed for different values of $r$ and $L$, and assumed that $\rho(L, r)L^{\beta/\nu_\perp}$, depends on $r$ and $L$ through the combination $L^{1/\nu_\perp}\Delta$ [155]. In Fig. 8.4, we show the corresponding data collapse which is rather good when the previously reported values of $\beta$ and $\nu_\perp$ are used. In the inset we verify that the data points are broadly scattered when one-dimensional DP exponent values are considered, showing that the dimensional reduction hypothesis is not valid. Data collapse is neither observed using two-dimensional DP exponents; this provides a strong evidence that we are in the presence of anomalous (non-DP) scaling

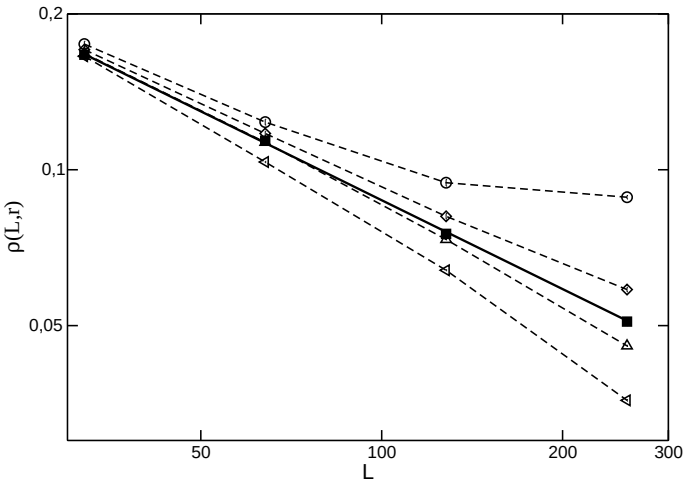


Figure 8.1: Log-log plot of the density of active sites as a function of $L$ (the linear system size) for different values of $r$: from top to bottom, 1.38630, 1.38640, 1.38643, 1.38645, and 1.38650 respectively. The straight solid line corresponds to the critical point $r_c = 1.38643(3)$.

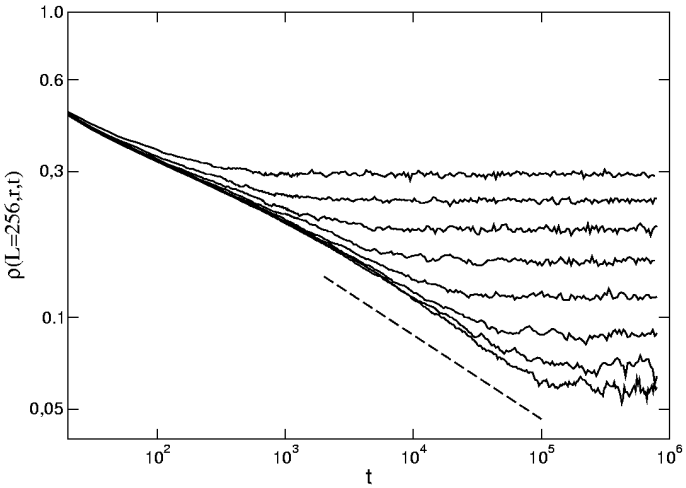


Figure 8.2: Log-log plot of the time evolution of the density of active sites for $L = 256$ and different values of $r$ in the active phase, namely, from top to bottom $r = 1.38143$, 1.38402, 1.38527, 1.38587, 1.38616, 1.38630, 1.38637, and 1.38640 respectively. From the slope of the straight dashed line we estimate $\theta = 0.275(15)$.

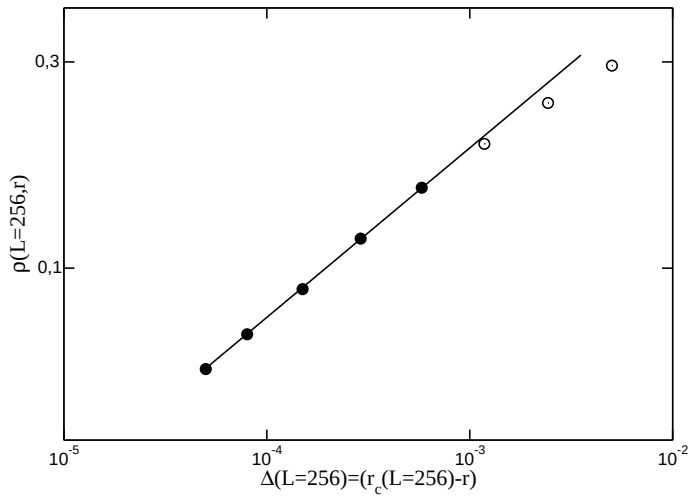


Figure 8.3: Log-log plot of the stationary density of active sites as a function of the distance to the critical point, for $L = 256$ and different values of $r$ in the active phase (the same values reported in Fig 8.2). The best fit gives $\beta = 0.40(2)$ and $r_c(L = 256) \approx 1.38645$. Filled (empty) circles are used to represent scaling (not scaling) points.

behavior. Finally, let us remark that the observed scaling does not extend over many decades for any of the computed steady state magnitudes. Much better scaling is observed for spreading exponents as will be shown in the following section.

### 8.3.2 Spreading Experiments and Superabsorbing States

In order to further verify and support our previous conclusion we have performed also spreading experiments as it is customarily done in systems with absorbing states [183, 155]. These consist in locating a seed of activity at the center of an otherwise absorbing configuration, and studying how it spreads on average in that medium [155]. In the absorbing phase the seed dies exponentially fast, propagates indefinitely in the active phase, while the critical point corresponds to a marginal (power law) propagation regime [155].

As said before, it is well established that two-dimensional systems with infinitely many absorbing states show some peculiarities in studies of the spreading of a localized activity seed. The absorbing environment surrounding the seed can either favor or un-favor the propagation of activity depending on its nature (see [177, 180] and references therein). For the, so called, *natural* initial conditions [155] the critical point for spreading coincides with the bulk critical point, and standard DP exponents are expected. In order to generate such natural configurations one could start the system with some highly active configuration and run the system right at the critical point; once it reaches an absorbing configuration it can be taken as a natural or self-generated en-

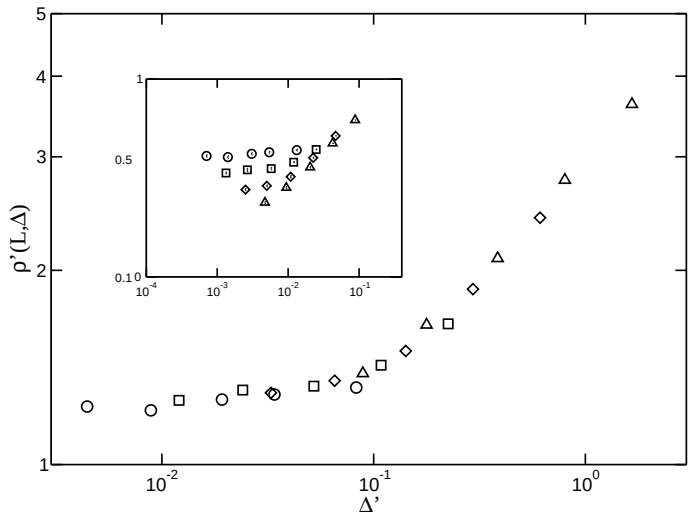


Figure 8.4: Log-log data collapse for the density of active sites: $\rho'(L,\Delta) = \rho(L,\Delta)L^{\beta/\nu_\perp}$ and $\Delta' = \Delta L^{1/\nu_\perp}$. Using the obtained exponent values, $\beta/\nu_\perp \approx 0.57$, and $\nu_\perp \approx 0.69$, a reasonably good data collapse is observed. In the inset we show an attempt to collapse data using one-dimensional DP exponent values. There is no evidence of scaling neither in this case nor using two-dimensional DP exponents.

vironment for spreading. An alternative, more efficient way of proceeding, inspired in sandpile systems [162], is as follows. One considers an arbitrary absorbing configuration and runs a spreading experiment. Once the epidemic (or "avalanche" in the language of self-organized criticality [162]) is over, one considers the newly reached absorbing configuration as initial state for a new spreading experiment avalanche. After iterating this process a number of times the system reaches a statistically stationary absorbing state: the natural one (see [162] and references therein). Using this absorbing state for spreading leads to DP exponent values (and critical point) in systems with many absorbing states as for example the pair contact process [178, 184].

By following this procedure we have found a very peculiar property of this model, that we believe to be at the basis of its deviating from DP. If the initial seed is located for all avalanches in the same site (or small group of localized sites), as is usually the case, after a relatively small number of avalanches the system reaches an absorbing configuration such that it is impossible to propagate activity for any possible forthcoming avalanche beyond a certain closed contour. For example, configurations as the one showed in Fig. 8.5.a are generated. The four sites at the center are the ones at which activity seeds are placed in order to start avalanches. White sites are active and grey ones are absorbing. At each marked-in-black site, the sum of the three (black) bonds connecting it to sites other than a central one is smaller than $r_c - 1 = 0.38643(3)$. In this way, regardless the value of the bond connecting the site to the central region the site

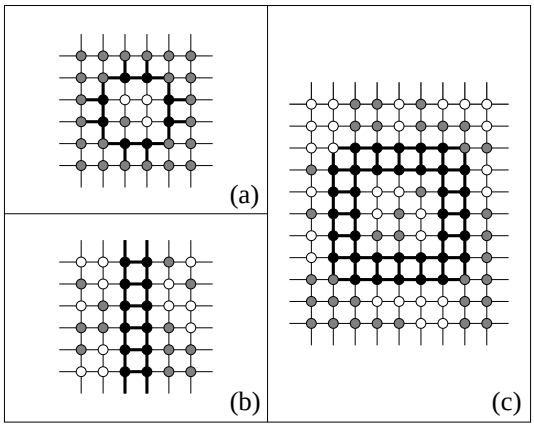


Figure 8.5: Different frozen configurations of superabsorbing (black) sites. White (grey) color stands for active (absorbing) sites. (a) Blocking configuration for spreading from the central cluster of four sites. Black sites cannot change their state whatever the state or dynamics inside the cluster might be. Black bonds remain also frozen. (b) Spanning frozen cluster of superabsorbing sites. (c) Almost-frozen cluster of superabsorbing sites. This, and analogous structures, can be destabilized from the outside corners.

remains inactive: it is a *superabsorbing site*. The existence of "inactive forever" sites have been already pointed out in [179, 185]. In the configuration showed in Fig. 8.5.a activity cannot propagate out of the "fence" of superabsorbing sites: the cluster of superabsorbing sites will remain frozen indefinitely, and activity cannot possibly spread out. All avalanches will necessarily die after a few time steps. This type of blocking structure is quite generic, and appears in all experiments after some relatively short transient.

In conclusion, this way of iterating spreading experiments leads always to blocking closed configurations of superabsorbing sites instead of driving the system to a natural absorbing configuration.

Observe that some activity put out of a blocking fence of sites in Fig. 8.5.a could well affect any of the external bonds of the superabsorbing sites (the dangling black bonds in Fig. 8.5.a), converting the corresponding site to an absorbing or even an active one. Therefore, in order to overcome this difficulty of the frozen blocking configurations and be able to perform spreading experiments in some meaningful way, we iterate avalanches by locating the initial seed at randomly chosen sites in the lattice. In this way there is always a non-vanishing probability of destroying blocking "fences" by breaking them from outside as previously discussed. Measurements of the different relevant magnitudes are stopped when the system falls into an absorbing configuration or alternatively whenever a linear distance $L/2$ from the avalanche origin is reached. Observe that in the second case the dynamics has to be run further in order to reach a new absorbing configuration at which launching the next avalanche.

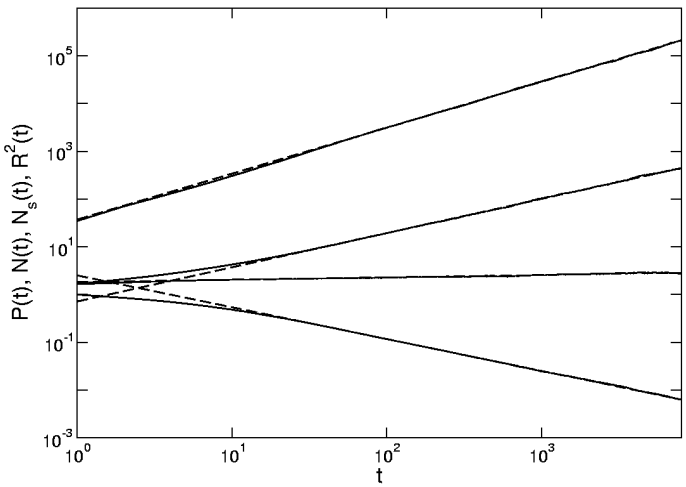


Figure 8.6: Numerical results for spreading experiments. $R^2(t)$ (topmost curve), $N_s(t)$ (second curve from above), $N(t)$ (third curve from above), and $P(t)$ (bottom curve). From the slopes we estimate $z = 0.96(1)$ and $\eta + \delta = 0.71(1)$, $\eta = 0.05(1)$ and $\delta = 0.66(1)$ respectively.

We monitor the following magnitudes: the total number of active sites in all the runs as a function of time $N(t)$ (we also estimate $N_s(t)$ defined as the average number of active sites restricted to surviving runs), the surviving probability $P(t)$, and the average square distance from the origin, $R^2(t)$. At the critical point these are expected to scale as $N(t) \sim t^{\eta}$, $P(t) \sim t^{-\delta}$ and $R^2(t) \sim t^{z}$. Results for this type of measurements are reported in Fig. 8.6.

We obtain rather good algebraic behaviors at the previously estimated critical point, $r_c$, confirming that the iteration-of-avalanches procedure leads the system to a natural absorbing environment. Slightly subcritical (supercritical) values of $r$ generate downward (upward) curvatures in this plot for all the four magnitudes. Our best estimates for the exponents at criticality are: $z = 0.96(1)$, $\eta = 0.05(1)$, $\delta = 0.66(1)$ (see Table 8.1). To double check our results we also plot $N_s(t)$, which is expected to scale with an exponent $\eta + \delta$. An independent measurement of its slope in the log-log plot gives $\eta + \delta = 0.71(1)$, in perfect agreement with the previously obtained results.

We can use these values to verify the hyperscaling relation [186, 177]

$$\eta + \delta + \theta = d\frac{z}{2}. \tag{8.2}$$

Substituting the found values for $z$ and $\eta + \delta$ we obtain $\theta \approx 0.25(2)$, compatible within error bars with the previously determined value $\theta = 0.275(15)$.

One more check of the consistency of our results by using scaling laws is the following. As $z = 2\nu_{\perp}/\nu_{\parallel}$ [182], we can estimate $\nu_{\parallel}$ from $z$ and $\nu_{\perp}$. Then, using $\nu_{\parallel}$ and the fact that $\theta = \beta/\nu_{\parallel}$ we obtain $\theta = 0.27(1)$, again in excellent agreement with the directly measured value.

| Model | $\beta$ | $\beta/\nu_\perp$ | $\theta$ | $\eta$ | $\delta$ | $z$ |
|---|---|---|---|---|---|---|
| Lipowski | 0.40(2) | 0.57(2) | 0.275(15) | 0.05(1) | 0.66(1) | 0.96(1) |
| DP, $d = 1$ | 0.276 | 0.252 | 0.159 | 0.313 | 0.159 | 1.265 |
| DP, $d = 2$ | 0.583 | 0.795 | 0.450 | 0.229 | 0.450 | 1.132 |

Table 8.1: Exponent values for the two dimensional Lipowski model and directed percolation in both one and two dimensions. Figures in parenthesis denote statistical uncertainty (note that error-bars are statistical errors coming from power-law fittings, and therefore do not include eventual systematic corrections to scaling).

In Table 8.1, we present the collection of exponents and compare them with DP values in both one and two dimensions [182]. There is no trace of dimensional reduction: this model does not behave, at least up to the scales we have analyzed, as any other known universality class.

### 8.3.3 More about Superabsorbing States

Let us recall our definition of superabsorbing states. A site, three of whose associated bonds take values such that the sum of them is smaller that $r - 1$, cannot be activated from the remaining direction by neighboring activity. We say that this site is superabsorbing in that direction (or it is in a superabsorbing state). A site can be superabsorbing in one or more than one directions. Still a site in a superabsorbing state can obviously be activated by neighboring activity in any of the remaining directions (if any).

Having stated the existence of frozen clusters in standard spreading experiments (when initialized from a fixed localized set of sites), one may wonder whether there are similar frozen structures in simulations started with an homogeneous initial distribution of activity, or in the modified type of spreading experiments we have just used (i.e. allowing the initial seed to land at a randomly chosen site) in the neighborhood of the critical point.

In principle, for any finite lattice, the answer to that question is affirmative. In Fig. 8.5.b we show the shape of a frozen cluster of superabsorbing sites: any of the sites in it is superabsorbing with respect to the corresponding outward direction, and it cannot be "infected" from any of the other directions as neighboring sites are similarly superabsorbing. If a cluster like that is formed (or put by hand on the initial state) it will remain superabsorbing forever. However the probability to form such a perfectly regular chain is extremely small for large system sizes. Observe also that in order to have a completely frozen two-site broad band structure it has to be unlimitedly long (or closed if periodic boundary conditions are employed). If instead it was finite, then sites at the corners would be linked to two external susceptible-to-change bonds and, therefore, themselves would be susceptible to become active: they would not be blocked forever. In this way any finite structure of superabsorbing sites in the square lattice is unstable: it can be eaten up (though very slowly) by the

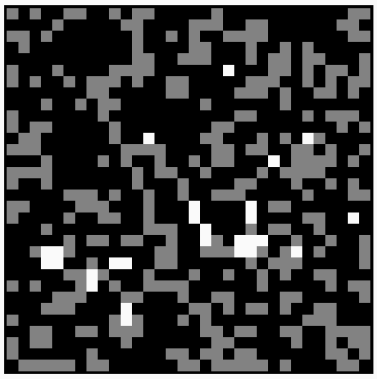

Figure 8.7: Snapshot of a configuration in a $32 \times 32$ lattice in the stationary regime for a value of $r$ close to the critical point. White color denotes activity, black corresponds to superabsorbing sites, while grey stands for absorbing sites. Observe that superabsorbing sites percolate through the lattice.

dynamics, and is therefore not fully frozen. For instance, the cluster of superabsorbing sites represented in Fig. 8.5.c is almost-frozen, but not really frozen as it may lose its superabsorbing character from the outside corners as previously described. Analogously, any other cluster shape of superabsorbing sites may be destabilized from its outside corners.

In conclusion, frozen clusters of superabsorbing sites do not appear spontaneously. However, almost-frozen regions do appear and may have extremely long life spans, specially close to the critical point where activity is scarce, and therefore the possibility of destabilizing them is small. In order to give an idea of how frequently superabsorbing sites appear we present in Fig. 8.7 a snapshot of a typical system-state near the critical point.

White corresponds to active sites, while the remaining sites are absorbing: in black we represent superabsorbing (in one or more than one directions) sites, while simple absorbing (not-superabsorbing) sites are marked in grey color. Observe that superabsorbing sites are ubiquitous; in fact they percolate through the system. Among them, about one forth are superabsorbing in all four directions.

Even though none of the clusters of superabsorbing sites is completely frozen, and in principle, activity could reach any lattice site, the dynamics is *glassy* [187] in some sense. For instance, imagine an active region separated from an absorbing region by a line of superabsorbing-in-the-direction-of-the-activity sites. In order to reach the absorbing region, activity has to circumvent the superabsorbing barrier. But near the critical point, where activity is scarce, barriers of superabsorbing sites are intertwisted among them forming structures that, even if not completely frozen, are very unlikely to be infected: activity has to overcome them progressively in order to reach the interior of superabsorbing regions. This resembles some aspects of glassy systems for which

degrees of freedom are hierarchically coupled and, at observable timescales, they may appear effectively frozen [187].

This phenomenology is certainly very different from DP, and it is the reason why the relaxation towards stationary states is so slow, and why deviations from mean values are so persistent in numerical simulations. In particular, as superabsorbing regions are long lived, the time required for the system to self-average is very large, and as near the critical point the probability of reaching an absorbing state is large, in practice, the system does not have the time to self-average. Consequently, a huge amount of independent initial states and runs have to be considered in order to measure smooth well behaved physical magnitudes [188]. We strongly believe that this type of pathological dynamics is responsible for the departure of the Lipowski model from the DP universality class in two dimensions.

At this point one might wonder whether the one-dimensional version of this model is essentially different. Or in other words, why (one-dimensional) DP exponents are observed in $d = 1$ [176]?. The answer to this question is not difficult if one argues in terms of superabsorbing sites. First of all notice that in $d = 2$, $r_c > 1$. This means that just by changing one bond, whatever the value of the output is, the site can stay below threshold if the other three bonds sum less than $r_c - 1$; this is to say superabsorbing states do exist at criticality. However in $d = 1$, $r_c = 0.4409 < 1$. In this case by changing one bond value it is always possible to activate the corresponding site: superabsorbing sites do not exist in $d = 1$ at the critical point[3]. Once the "disturbing" ingredient is removed from the model, we are back to the DP class as general principles dictate.

### 8.3.4 The Honeycomb Lattice

In order to further test our statement that superabsorbing states are responsible for the anomalous scaling of the two-dimensional Lipowski model, we have studied the following variation of it. We have considered the model defined on a honeycomb lattice (with three bonds per site), and performed Monte Carlo simulations. In this case there is the (geometrical) possibility of having completely frozen clusters of superabsorbing sites (see Fig. 8.8).

The main geometrical difference from the previous case comes from the fact that here cluster-corners are linked only to one external bond, and therefore are more prone to form frozen clusters. In principle, before performing any numerical analysis, there are two alternative possibilities: either the critical point is located at a value of $r$ smaller than 1 or larger than 1. In the first case, there would be no superabsorbing sites (in analogy with the one-dimensional case); in the second case pathologies associated with superabsorbing sites should be observed. The case $r_c = 1$ would be marginal. Finite size scaling analysis indicate the presence of a continuous phase transition located at $r \approx 1.0092$ (very

[3]Observe that for values of the control parameter $r > 1$, well into the absorbing phase, superabsorbing sites show up also in $d = 1$; but they do not affect the critical region.

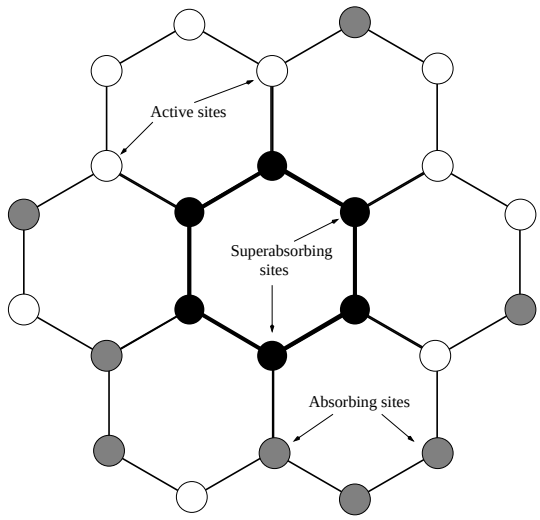


Figure 8.8: Frozen cluster in the honeycomb lattice. This type of frozen structure of superabsorbing sites remains indefinitely superabsorbing at the critical point. Black: superabsorbing sites. Grey: absorbing sites. White: active sites.

nearby the marginal case, but significatively larger than $r = 1$).

For Monte Carlo simulations, we have employed lattices of up to a maximum of $256 \times 256$ sites. All the observed phenomenology is perfectly compatible with two-dimensional DP behavior. The dynamics does not show any of the anomalies described for the square lattice case. In particular, from the dependence of the stationary activity density on system size we evaluate $\beta/\nu_\perp = 0.80(1)$; from the time decay at criticality $\theta = 0.45(1)$, and finally $\beta = 0.57(2)$; fully confirming consistency with two-dimensional DP behavior. This result seems to be in contradiction with the two alternative possibilities presented above. Let us now discuss why this is the case.

As the coordination number is 3 in this case, the sum of two bond-values has to be smaller than $r_c - 1 \approx 0.0092$ in order to have a superabsorbing site in the direction of the remaining bond at criticality. As the two bonds are independent random variables, the probability of creating a superabsorbing site if the two of them are changed, is fewer than 0.5%, and the probability to generate frozen clusters (composed by six neighboring superabsorbing sites as shown in Fig. 8.8), is negligible at the critical point. In fact, we have not been able to observe any of them in our simulations. This means that one should study extremely large system sizes and extraordinarily long simulations in order to see anomalies associated with superabsorbing sites, otherwise, for any feasible simulation the behavior is expected to be DP-like. The observation of DP exponents in this case strongly supports the hypothesis that superabsorbing states are at the basis of the anomalous behavior of the model on the square lattice.

However, strictly speaking, the system should exhibit a (unobservable) first-

order phase transition at $r = 1$ in the thermodynamic limit. Indeed, for values of $r$ larger than 1 there is a finite, though extremely small, probability of creating frozen clusters of superabsorbing sites (as the one in Fig. 8.8). As this is an irreversible process, after some (divergently long) transient there would be a percolating network of frozen clusters of superabsorbing sites, and the only possible stationary state would be an absorbing one with zero activity. On the other hand, for values of $r$ smaller than unity, the probability of creating superabsorbing sites is strictly zero, and there will be a non-vanishing density of activity. As the density at $r = 1$, almost independent of system size, is $\rho \approx 0.18$, the transition is expected to be discontinuous, and therefore the DP transition observed in our simulations is merely a finite size effect, and should disappear for large enough sizes and long times. In any case, this first order transition is unobservable computationally.

## 8.4 Conclusions and Outlook

Summing up, we have shown that the two-dimensional Lipowski model does not belong to any known universality class. We have measured different critical exponents by running Monte Carlo simulations started from homogeneous initial states and also by performing spreading experiments. In any case, we find absolutely no trace of dimensional reduction, and there is neither evidence for the system to behave as two-dimensional DP. Instead, a novel scaling behavior is observed. The main relevant physical ingredient of this class is the presence of superabsorbing sites, and almost-frozen clusters of superabsorbing sites which slow down enormously the dynamics.

The previous conclusion is strongly supported by two other observations: (i) the regular DP behavior observed in the one-dimensional version of the model for which superabsorbing states do not appear at criticality, and (ii) the two-dimensional DP behavior observed for the two-dimensional model defined on a honeycomb lattice, for which the probability of generating superabsorbing sites at criticality is almost negligible.

In general, superabsorbing sites can either arrange into completely frozen clusters or not depending on dimensionality, coordination number and other system details. Let us distinguish three main cases:

- When completely frozen clusters of superabsorbing sites appear below (or above) a certain value of the control parameter but not above (below), first order transitions are expected (as occurs in the multiplicative model discussed in Appendix D [185]).

- If completely frozen clusters do not appear at criticality, but instead almost-frozen clusters are present, we expect anomalous behavior (as occurs in the original Lipowski model [179]).

- If neither frozen nor almost-frozen clusters are observed at criticality (as is the case for the one dimensional version of the model [176]) we expect

standard directed percolation behavior.

There are two possible follow-ups of this work. First, it would be worth studying in more realistic situations as, for instance, in surface catalysis (dimer-dimer or dimer-trimer) models [167] whether effects similar to those described in this chapter play any relevant role. In particular, for those models depending upon lattice and particle geometry there are cases in which activity cannot propagate to neighboring regions, but is constrained to evolve following certain directions or paths. It would be rather interesting to sort out whether anomalies reported for those models [167] are related to the existence of superabsorbing states.

On the other hand, from a more theoretical point of view, an interesting question is: what is the field theory or Langevin equation capturing the previously described phase transition with superabsorbing states? and, how does it change with respect to Reggeon field theory?. Establishing what this theory looks like, would clarify greatly at a field theoretical level the effect of superabsorbing states on phase transitions, and would permit to shed some light on the degree of universality of this anomalous phenomenology. Our guess is that a Reggeon field theory [165, 164] with a spatio-temporal dependent anisotropic Laplacian term (which, for example, would enhance, un-favor or forbid diffusion from certain sites in certain directions) could be a good candidate to describe this new phenomenology. Analogously to what happens in field theoretical descriptions of other systems with many a absorbing states [167, 177], the inhomogeneous Laplacian-term coefficient should be described by a second physical field coupled to the activity field in such a way that its fluctuations would vanish upon local absence of activity. Further pursuing this line of reasoning is beyond the scope of the present chapter. As long as this program has not been completed, is not safe to conclude unambiguously that the anomalies described in this chapter are relevant in the limit of extremely large times and system sizes.

# Chapter 9

# Heat Conduction and Fourier's Law in One-Dimensional Systems

## 9.1 Introduction

A research on dynamics of nonequilibrium systems must include a reference to *transport phenomena*. These dynamic processes appear ubiquitously in Nature. Some classical examples are heat and mass transport in fluids (eg. boiling water), diffusion, electric conduction, etc. Many natural systems can be understood and analyzed using the transport phenomena jargon, as for instance atmospheric dynamics, oceanic currents, ion currents between cells, stellar convection, traffic flow, social migration, diffusion of information, etc. These initially so different systems share certain common features. In general, they are usually inhomogeneous, and typically show nonzero gradients of several magnitudes, together with non–zero net fluxes carrying energy, mass and/or momentum through the system.

Classically, transport phenomena have been studied by Irreversible Thermodynamics, where these processes are analyzed in terms of conservation laws, local entropy balance equations and the maximum entropy production postulate. [79] This theory builds up using a series of phenomenological macroscopic laws based upon the proportionality among the fluxes and the thermodynamical forces. Fick's law of diffusion, Fourier's law of heat conduction and Ohm's law of electric conduction, for instance, belong to this class of linear phenomenological laws. Such laws are completely defined once certain proportionality factors, called *transport coefficients*, are specified. Some of these transport coefficients are the diffusivity, and the thermal and electrical conductivity (related, respectively, to the above mentioned laws). It has been shown that the phenomenological laws of Irreversible Thermodynamics remain valid

(i.e. reproduce experimental results) as far as the system under study stays close enough to thermodynamic equilibrium, although the notion of "close enough to equilibrium" is not clear.

On the other hand, nonequilibrium Statistical Mechanics is a theory which aspire to describe macroscopic nonequilibrium phenomena (and, as a limiting case, the equilibrium ones) starting from the microscopic description of Nature. Therefore, a successful nonequilibrium statistical–mechanical theory should be able to calculate microscopically, among other things, the transport coefficients associated to the linear laws of Irreversible Thermodynamics, commonly observed in Nature. Moreover, this theory should be capable to define precisely the notion of "close enough to equilibrium" for a general system. Although great advances have been made in the field, up to now there is no closed theory for the mechanical–statistical description of nonequilibrium systems.

In order to further advance in the field, we must understand deeper the microscopic mechanisms underlying irreversible processes. In particular, in this chapter we want to investigate the microscopic basis of heat transport. The corresponding linear phenomenological law of Irreversible Thermodynamics associated to heat transport is Fourier's law, which in its more general form reads,

$$c_v(T)\frac{\partial}{\partial t}T(\vec{r},t) = \vec{\nabla}\cdot[\kappa\vec{\nabla}T(\vec{r},t)] \tag{9.1}$$

where $T(\vec{r},t)$ is the temperature measured by a probe at position $\vec{r}$ at time $t$, $c_v(T)$ is the specific heat per unit volume, and $\kappa$ is the thermal conductivity. Notice that, in order to write down this equation, one should assume that no mass transport and/or other mechanism different from heat conduction appears in the system. This diffusion–like equation describes the time evolution of a macroscopic system whose initial temperature profile $T(\vec{r},t=0) \equiv T_0(\vec{r})$ should be inhomogeneous. Alternatively, Fourier's law (eq. 9.1) can be applied to a homogeneous system in contact with heat reservoirs at time invariant temperatures $T_\alpha$. In the stationary state, the temperature profile should be solution of the equation,

$$\vec{\nabla}\cdot[\kappa\vec{\nabla}T(\vec{r},t)] = 0 \tag{9.2}$$

where $J \equiv -\kappa\vec{\nabla}T(\vec{r},t)$ is the stationary heat flux through the system. This law has been extensively tested in experiments in fluids and crystals. However, we do not understand yet many of its fundamental aspects. [190, 191]

In particular, derivation of Fourier's law from a microscopic Hamiltonian dynamics is still an open question. Moreover, writing eq. 9.1 we assume that the state of the system is completely defined, from the macroscopic point of view, by the local temperature field $T(\vec{r},t)$ at any time $t$. Such assumption implicitly involves that the Local Thermodynamic Equilibrium (LTE) property holds for the investigated system, which usually is far from clear. As a simple picture of what LTE means, let us imagine our system divided up into many *small* cells, large enough so each one contains a large (*quasi*–macroscopic) number of atoms, and at the same time small enough in order to be accurately described by an (equilibrium) Gibbs measure at temperature $T(\vec{r},t)$ for each cell

at position $\vec{r}$. Thus, although the system is macroscopically inhomogeneous, locally thermodynamic equilibrium holds (in the sense of Gibbs measures). This concept can be precisely defined using the Hydrodynamic Scaling Limit, where the ratio of micro to macro scales goes to zero. [190]

Thus, many fundamental questions arise related to the microscopic understanding of heat conduction, as for instance: which are the necessary and sufficient conditions in order to observe LTE in a system?, which is the interplay among LTE, energy equipartition and heat transport?, which are the minimum requirements a system must fulfill in order to obey Fourier's law?, etc. In order to answer all these question (and many other, equally interesting questions) we must study simplified mathematical models of real systems. The study of these simple models will give us a firm basis in order to understand the microscopic origin of heat conduction and the physical hypothesis underlying Fourier's law. As usual in Theoretical Physics, mathematical and computational simplicity drive us to consider low dimensional systems, namely one and two–dimensional systems, which are comparatively much easier to handle with than *real* three–dimensional ones.[1] On the other hand, there is also experimental motivation for studying heat conduction in low dimensional systems. As an example, let us mention anisotropic crystals, solid polymers, single walled nanotubes, quantum wires, etc. [191]

In particular, heat transport in one–dimensional systems is nowadays a highly interesting problem in the context of both non-linear dynamics and non–equilibrium statistical physics. Its study has added new insights to the understanding of the microscopic origin of normal heat conduction, as we will see below. Long ago, Peierls was the first one to identify a mechanism which gives rise to a finite thermal conductivity. He proposed a successful perturbative theory, based on a phonon scattering mechanism, in order to explain thermal conductivity in solids. [192] In electrically insulating solids, heat is transmitted by lattice vibrations. In that case, it is useful to visualize the solid as a gas of interacting phonons. These phonons (elementary lattice excitations) store and transport energy through the system. In a perfect harmonic crystal, phonons behave as a gas of non–interacting particles. Hence, energy flow through the system without any loss, so the energy current (assuming that the system is subject to a temperature gradient) does not decrease with crystal length. Therefore, a perfect harmonic crystal should have an infinite thermal conductivity. However, a real crystal presents anharmonicities which give rise to phonon interactions, i.e. phonons scatter among them. In these collisions momentum is conserved modulus a vector of the reciprocal lattice. We thus can classify phonon collisions in two distinct classes: those which perfectly conserved momentum (*normal process*), and those where the difference between the initial and the final momentum is a vector $\vec{k}$ of the reciprocal lattice (*umklapp process*). Peierls theory shows that, in absence of umklapp processes, the thermal con-

[1] In spite of their apparent simplicity, low dimensional systems present some unusual features which usually do not appear in their three–dimensional counterparts. For instance, transport coefficients in low dimensional systems may not even exist.

ductivity of a solid is infinite. Consequently, this theory predicts that we do not expect a finite thermal conductivity in monoatomic one–dimensional lattices with nearest neighbor interactions. However, as we will see below, other mechanisms are possible which give rise to normal heat conduction in these one–dimensional chains. More generally, it has been shown that any integrable Hamiltonian system must have a divergent thermal conductivity, since its associated normal modes behave as a gas of non–interacting phonons, carrying energy from the hot to the cold sources without any loss.[191] On the other hand, there are one–dimensional non–integrable systems, to which Peierls theory does not apply directly, which also show a divergent thermal conductivity, as for instance the Fermi–Pasta–Ulam–$\beta$ model [193].

Many recent studies have focused their attention on heat transport in several one–dimensional systems, with the hope of identifying the relevant mechanisms underlying normal (finite) heat conduction. Some of these models yield a finite thermal conductivity, while others yield an infinite $\kappa$. Nowadays, the general belief is that integrability,[2] total momentum conservation and total pressure are the relevant ingredients which define whether a systems presents normal heat transport or, instead, anomalous thermal conductivity. In particular, it has been shown that the non–integrability is a sufficient condition in order to obtain a non–trivial temperature profile, although this property is not sufficient to guarantee normal heat conduction. [194] Furthermore, there are one–dimensional systems with zero total pressure and translational invariant Hamiltonian which show normal heat conduction. On the other hand, it has been shown that the effect of local potentials, which break the Hamiltonian translational invariance and simulate interactions of the one–dimensional system with its embedding higher–dimensional space, is crucial in order to guarantee normal heat transport. Local potentials break total momentum conservation, thus identifying this symmetry as a relevant one in the heat transport problem. It is actually believed that one should not expect in general a finite thermal conductivity in one–dimensional systems with momentum conserving interactions and non–zero pressure. [195]

The last statement has been formally established in a recent theorem due to Prosen and Campbell [196], which affirms that "in 1D systems, conservation of total momentum implies anomalous conductivity provided only that the average pressure is non-vanishing in thermodynamic limit". The goal of this chapter is to show a counterexample to the above theorem. We introduce a system that, although its particle interaction conserves momentum and it exhibits a nonzero pressure, the energy behavior has a diffusive character and Fourier's law holds, thus implying a finite thermal conductivity. Therefore, we think that in one dimensional systems with nonzero pressure, the conservation of momentum does not seem to be a key factor to find anomalous heat transport. We think that there are other cooperative mechanisms that can do the job of the local potentials. As we will see below, maybe systems having degrees

[2] A system with N degrees of freedom is integrable if there exists a canonical transformation such that the system can be described by N conjugated action–angle canonical coordinates. Hence, an integrable system with N degrees of freedom will have N constants of motion.

of freedom that acquire easily energy but release it in a very long times scale have, in general, normal thermal conductivity. On the other hand, and supporting our results, there are strong evidences (which we will describe later) pointing out that Prosen and Campbell's theorem is empty, in the sense that all the calculations are correct, but they do not predict anything about system's thermal conductivity.

The structure of this chapter is as follows. In section 9.2 we present our one–dimensional model, together with the boundary heat baths used, explaining carefully their properties and the reasons underlying our choices. In Section 9.3 we describe the numerical results obtained. There we study the system from several perspectives, all of them pointing out the finiteness of thermal conductivity in the model in thermodynamic limit, and thus the validity of Fourier's law in this system. Finally, in Section 9.4 we summarize our results and present the conclusions, paying special attention to the fundamental implications that our observations have on the microscopic understanding of heat conduction.

## 9.2 One Dimensional Model of Heat Conduction

Our model consists in a one–dimensional chain of interacting particles subject to a temperature gradient, which induces a heat flux from the hot extreme to the cold one. In a line of length $L$, there are $N$ point particles of different masses interacting exclusively via elastic collisions. In order to minimize the finite size effects, the particles have only two different masses and they alternate along the line, *i.e.* $m_{2l-1} = 1$ and $m_{2l} = (1+\sqrt{5})/2$ with $l = 1, ..., N/2$. We have chosen the masses of the even particles to be the most irrational number (golden number) in order to minimize possible periodicities, resonances or non-ergodic behaviors. At the extremes of the line there are thermal reservoirs at fixed (time invariant) temperatures $T_1 = 1$ and $T_2 = 2$ at $x = 0$ and $x = L$, respectively.

We simulate the reservoirs by using the following deterministic process: each time particle 1 (L) hits the boundary at $x = 0$ ($x = L$) with velocity $v$, the particle is reflected with the velocity modulus

$$v' = \left[\frac{-2}{m_{1(L)}\beta_{1(2)}} \ln\left(1 - e^{-\frac{\beta_{1(2)}}{2} m_{1(L)} v^2}\right)\right]^{1/2} \tag{9.3}$$

where $\beta_{1(2)} = 1/T_{1(2)}$ (see Fig. 9.1). This reversible and deterministic heat bath is due to H. van Beijeren (private communication). This map emulates a true heat bath. Other mechanisms exist that emulate the presence of true heat baths, as for example stochastic thermal reservoirs, where the particle colliding with the end wall returns with a velocity modulus randomly extracted from a Maxwellian distribution for the corresponding temperature. In general the correct, rigorous procedure should require studying infinite systems, but this is usually not feasible, and hence one must look for alternative, effective implementations of a thermal reservoir, as the one chosen. These effective

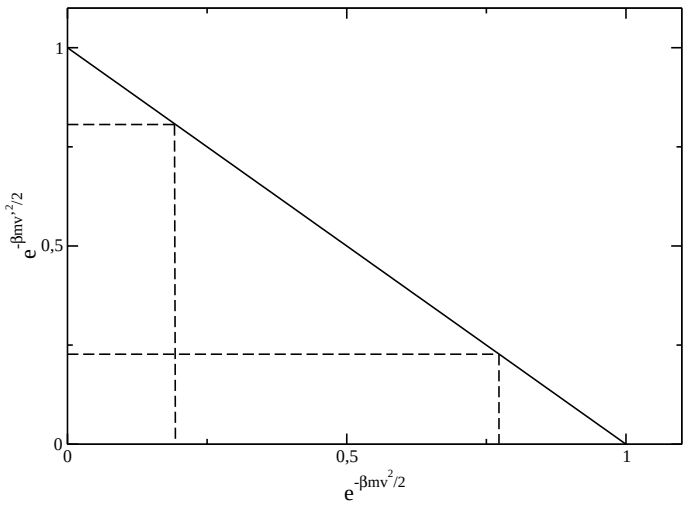


Figure 9.1: Graphic representation of the deterministic heat bath scheme. Notice that when the particle reaches the end wall with a large velocity, it is reflected with low velocity, and reciprocally. This thermal reservoir generates thermal equilibrium.

heat baths must thermalize the system exactly as a real semi–infinite heat bath should do, since it has been shown [197] that the coupling between the system and the thermal reservoirs dramatically affects the physical properties of the system, even in the Thermodynamic Limit. Needless to say that we tested, as a preliminary step, that our deterministic heat bath generates an equilibrium distribution (Gibbs measure) starting from a completely random state, and thus correctly simulates a true thermal source. On the other hand, the deterministic thermal reservoir shows a very interesting property: it is time reversible. Hence, dissipation and irreversibility appear intrinsically in the system, and not as a consequence of the randomness introduced by stochastic thermal reservoirs. Furthermore, this type of heat bath guarantees that our system is completely deterministic, and thus the tools from non-linear system analysis can be used. Let us mention that, in order to check the influence of the type of reservoir into the measured system properties, we have also used the more conventional stochastic boundary conditions described above, but only different finite size effects and no other relevant behavior has been observed.

For $T_1 \neq T_2$, due to the temperature gradient, there is a flow of energy from the high temperature reservoir to the low one, and the system then evolves to a nonequilibrium stationary state. This properties (nonzero temperature gradient and nonzero net heat flux) are typical of nonequilibrium systems. On the other hand, numerical studies of our model are rather complex, since there relaxation times are very long.[3] This problem restricts simulations to relatively

[3]Very often low dimensional systems show very large relaxation times. This is due to the restrictions induced by its low dimensionality in phase space flow.

small systems, where finite size effects are very important. We will notice this problem in the forthcoming analysis. In spite of these difficulties, several authors have studied this model before. [198, 199, 200] For instance, in [199] special attention is payed to the existence of a non–trivial temperature profile. There it is observed that the temperature profile does not change under rescaling of masses. Moreover, it is found that $T(x; \nu T_1, \nu T_2) = \nu T(x; T_1, T_2)$. This involves that the independent variables of the system are $M/m$, $T_1/T_2$ and $N$. Furthermore, as the number of particles $N$ increases, the temperature profile get closer to a limiting profile, similar to that predicted by kinetic theory. A version of this model in which the masses are randomly placed was already studied in [198]. In this work, the system Thermodynamic Limit behavior was not considered but the Local Thermodynamic Equilibrium (LTE) property was demonstrated. This property guarantees the existence of a well–defined local temperature. Moreover, LTE has been numerically observed in the alternating masses model for large enough system sizes (otherwise, we couldn't define local temperatures). [199] Some of these works [199, 200] have also studied the thermal conductivity as a function of system size, arriving to the conclusion that $\kappa$ slowly diverges in the Thermodynamic Limit. As we will see below, this type of analysis is strongly affected by finite size effects, and thus any conclusion derived from it about thermal conductivity could be wrong. In fact, as we will demonstrate, the thermal conductivity $\kappa$ is finite in the Thermodynamic Limit for this system, and hence Fourier's law holds here.

## 9.3 Numerical Analysis

Our goal in this chapter is to check whether the system has a finite thermal conductivity in the Thermodynamic Limit, $N, L \to \infty$ with $N/L = 1$, or instead it exhibits a divergent $\kappa$. With this aim we performed a detailed numerical analysis along several different, complementary lines.

### 9.3.1 The Existence of a Non-trivial Thermal Profile

Before going on the analysis of conductivity, we have to check whether this system shows a nontrivial temperature profile. This would indicate that LTE holds in the system, and then it makes sense to wonder whether Fourier's law holds or not. As a first step, we must give a working definition of local temperature. We define the local temperature by measuring the mean kinetic energy of each particle and its mean position $\bar{x}_i$ at the stationary state. Assuming that energy equipartition holds at least locally (we checked this point), this mean kinetic energy is proportional to the local temperature at position $\bar{x}_i$. There are many other methods to measure local temperature, almost all of them based on the Virial theorem. Strictly speaking, the only correct method to measure temperature profiles consists in dividing the system in cells, each one with a large enough number of particles, and measuring the velocity distribution in every cell. If local equilibrium holds, one expects a Maxwellian distribution for each

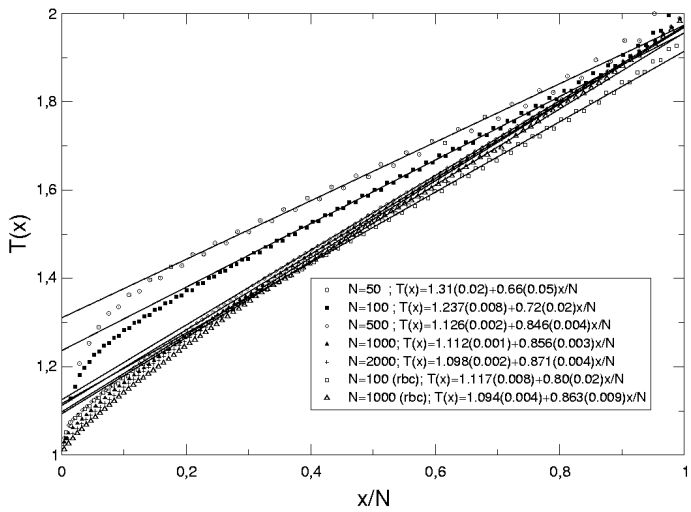


Figure 9.2: Temperature profile at the stationary state for N particles. Lines are the best fits of the data in the interval $x/N \in [0.4, 0.6]$. The corresponding equations are shown in the box. Errors in the coefficients are in brackets. We have also included, for direct comparison, temperature profiles obtained using stochastic boundary conditions (noted as rbc).

cell, with local temperatures proportional to the variance of this distribution [198]. The method we use, and those based on Virial theorem, are just (numerically efficient) approximations. These approximations are effective as far as they confirm the existence of a non–trivial temperature profile in the Thermodynamic Limit. This is the important conclusion here, and not the exact shape of the temperature profile, which of course depends somehow on the thermal baths used and the definition of local temperature.

We computed the profiles for $N = 50, 100, 500, 1000, 2000$ particles, with fixed $N/L = 1$, $T_1 = 1$ and $T_2 = 2$. Fig.9.2 shows the local temperature as a function of $x/N$ (by seeking clearer figures, we have performed local averaging of the temperatures and positions to draw only 100 points; no difference is found by drawing all the points). We see in Fig.9.2 that the temperatures follow linear profiles in the interval $x/N \in [0.4, 0.6]$ with slopes depending on the system size. This slope apparently tend to converge to unity but we find that the convergence is very slow. On the other hand, the temperature profile get curved near the boundary heat baths. This *surface resistance* [201], which is consistent with previous studies [199, 201], tends to diminish as the system grows. In any case, a non–flat profile is clearly expected in the Thermodynamic Limit.

### 9.3.2 The Averaged Heat Current

We now pay attention to the heat flux through the system. If Fourier law holds and the heat conductivity is finite, the mean heat current, defined as $J = N^{-1}\sum_{i=1}^{N} m_i v_i^3/2$, should go to zero as $1/N$ whenever $T_{1,2}$ and $N/L$ are kept fix. This is so because in the steady state we have $J = -\kappa\nabla T(\vec{r},t) \approx \kappa(T_2 - T_1)/N$. If instead $J \sim N^{-\alpha}$ with $\alpha < 1$ then we should have a divergent thermal conductivity, $\kappa = JN/(T_2 - T_1)$. [193] In our case, the data does not give us a conclusive answer. In fact we fitted our experimental points (J corresponding up to seven different N's) to behaviors like $J = aN^{-0.71}$, $J = aN^{-1}(1 + b\ln N)$, both yielding a divergent conductivity, and $J = aN^{-1}(1 + bN^{-1})$ and $J = aN^{-1}(1+b/\ln N)$, both yielding a finite conductivity. All these four fits had regression parameters of order 0.999. Thus we cannot conclude nor convergence nor divergence of thermal conductivity from this point of view. Moreover, our fits reflect that finite size corrections to the leading order are dominant and that we are far from the asymptotic regime for the observable heat current. Therefore, the direct use of the Fourier's law $\kappa = JN/(T_2 - T_1)$ does not clarifies (from the numerical point of view) the existence of a finite heat conductivity in the Thermodynamic Limit. Some authors find for the same model that the heat current goes like $N^{-0.83}$[199] or $N^{-0.65}$[200]. These results are similar to our direct fit to power law behavior. However, in contrast with them, we conclude that such fits are done in a non-asymptotic regime.

### 9.3.3 The Current-current Self Correlation Function

It is clear from the previous section that direct use of Fourier's law does not yield any definite conclusion about system's thermal conductivity in the Thermodynamic Limit, due to the strong finite size effects affecting our data. Hence we must look for other different methods in order to conclude about $\kappa$. One of these methods is based upon the Green–Kubo formulae. The heat conductivity is connected to the total energy current–current time correlation function evaluated at equilibrium via its time integral (Green-Kubo formula[79]). It can be written as,

$$\kappa = \lim_{\tau\to\infty}\lim_{L\to\infty}\int_{-\tau}^{\tau} < J(0)J(t) >_\beta \, dt \tag{9.4}$$

where we can write,

$$< J(0)J(t) >_\beta \equiv C(t) = \frac{\int\prod_n dp_n dq_n J(0)J(t) exp(-\beta H)}{\int\prod_n dp_n dq_n exp(-\beta H)} \tag{9.5}$$

Hence $C(t)$ is the equilibrium canonical average of $J(0)J(t)$ at inverse temperature $\beta$ for a system with Hamiltonian $H$. The order of limits in eq. (9.4) is crucial in order to precisely define $\kappa$. The integral has some meaning (i.e. yields a finite $\kappa$) whenever the correlation function decays as $< J(0)J(t) >_\beta \sim t^{-1-\Delta}$ with $\Delta > 0$. Thus, we have to measure the long time tail of the total energy current–current correlation function $C(t)$ in order to conclude about sys-

tem's thermal conductivity. As Green–Kubo formula states, this autocorrelation function must be measured in equilibrium. The fact that the equilibrium average should be taken using the canonical ensemble is related with one of the fundamental hypothesis underlying Green-Kubo formula: Local Thermodynamic Equilibrium. As previously explained, this hypothesis implies that one can define locally a temperature, in such a way that the system behaves locally as an equilibrium system with this temperature. This hypothesis implicitly involves the use of the canonical ensemble, since in this ensemble the temperature is defined precisely, being the energy a fluctuating observable. In order to measure $C(t)$ one thus should simulate our system with heat reservoirs at the borders at equal temperatures $T = (T_1 + T_2)/2$. However, this procedure is not practical, due to the strong finite size effects affecting $C(t)$ as a consequence of the open boundaries. In practice, this finite size corrections impede any definite analysis of the self correlation function. In order to avoid such difficulties related to the presence of the open borders, we measure $C(t)$ in the microcanonical ensemble with total energy $E$ defined by the temperature $T = (T_1 + T_2)/2$ via the equipartition theorem. In this way, we substitute open boundaries by periodic boundary conditions, recovering translational symmetry. Using the microcanonical ensemble, where finite size effects are minimized in some sense, we are able to successfully analyze the long time behavior of the self correlation function $C(t)$. However, as we will see below, some easily identifiable finite size effects related with the system's finite length remain. One could wonder whether this ensemble change is plausible. The equivalence of equilibrium ensembles is well known fact in Equilibrium Statistical Mechanics, although it has not been rigorously proved in all cases. Hence one should interchange microcanonical and canonical averages arbitrarily, expecting invariant results (up to very small –logarithmic– finite size corrections) under such modifications. However, in order to gain confidence in our results, we will also present evidences pointing out the validity of this interchange.

Writing eq. (9.4) we have assumed that the total momentum is set to zero in the system. Otherwise, if a non–zero net momentum exists, one should use the connected part of the autocorrelation function $C(t)$ in eq. (9.4), defined as,

$$C_c(t) \equiv < J(0)J(t) >_\beta - < J >_\beta^2 \tag{9.6}$$

in order to precisely calculate the thermal conductivity. [190] This is an important point, because if there is a net momentum in the system and one uses the non–connected self correlation function $C(t)$ in the Green–Kubo formula the result won't have nothing to do with the real thermal conductivity. This subtle technicality has not been taken into account in a recent theoretical work [196], which in principle proves that "...for classical many–body lattice Hamiltonians in one dimension, total momentum conservation implies anomalous conductivity in the sense of divergent Kubo expression ...". However, in their derivation, which is *not* restricted to a zero total momentum ensemble, these authors have used the non–connected self correlation function $C(t)$, and thus the divergence of the Green–Kubo formula does not implies anything on the system's thermal conductivity, contrary to author's claim. Moreover, in this

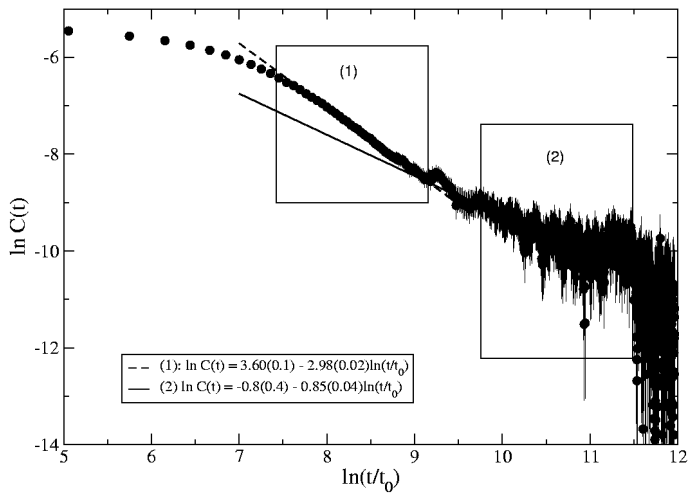


Figure 9.3: Total energy current–current time correlation function $C(t)$ for the different masses system with $N = 1000$. The inset shows the results of a power law fit for the time decay in regions (1) and (2). In region $(1)$ we observe $C(t) \sim t^{-1.3}$. Notice large error-bars and strong fluctuations for $\ln(t/t_0) > 10$. $t_0$ is the mean collision time.

chapter we show a counterexample to the above affirmation, i.e. we show a one–dimensional system, which conserves momentum and has non–zero pressure, whose thermal conductivity is finite in the Thermodynamic Limit, as we will see below.

We hence have measured $C(t)$ using periodic boundary conditions and setting total momentum equal to zero, with total energy defined through the equipartition relation, $E = NkT/2$, where $T$ is the arithmetic average of $T_1$ and $T_2$. In Fig. 9.3 we show our results on $C(t)$ for a system with $N = 1000$ particles. Here we can study two different regions:

1. Region $(1)$, defined for $\ln(t/t_0) \in [8, 9]$, where a power law fit yields $C(t) \sim t^{-1.3}$.

2. Region $(2)$, defined for $\ln(t/t_0) > 10$, where the same algebraic fit yields $C(t) \sim t^{-0.85}$.

The observed slight difference in the time decay exponent of $C(t)$ depending on the fitting region is crucial in order to conclude about the convergence or divergence of thermal conductivity of our model in the Thermodynamic Limit. Thus we must develop a set of physically well–motivated criteria that help us to distinguish the true bulk asymptotic behavior from spurious finite size corrections. As we will explain below, we think that only region $(1)$ corresponds to the infinite system bulk behavior, which involves a finite thermal conductivity in the Thermodynamic Limit, and thus that Fourier's law holds for our total–momentum–conserving one–dimensional model. The bump observed in

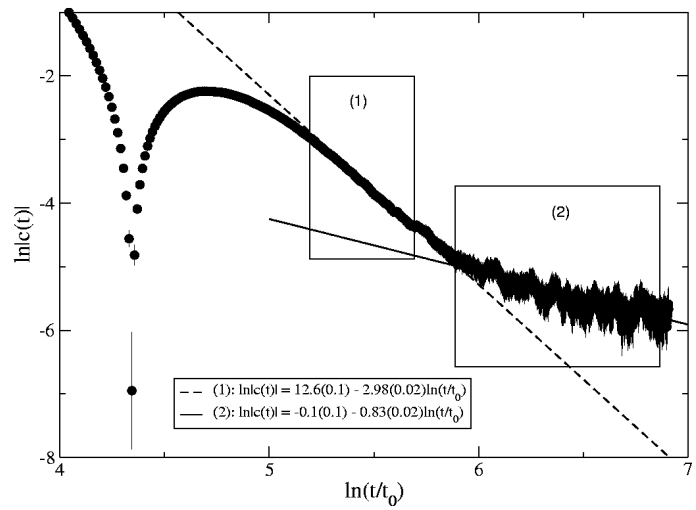


Figure 9.4: Local energy current–current time correlation function $c(t)$ for the equal masses system with $N = 500$. The inset shows the results of a power law fit for the time decay in regions (1) and (2). Here $|c(t)| \sim t^{-3}$ in region $(1)$, and we observe a $t^{-0.83}$ tail in region $(2)$.

$C(t)$ for very long times (namely $\ln(t/t_0) > 9.5$) is typical of system autocorrelations due to finite size effects [4].

As an example of the previous statement, let us study the asymptotic behavior of the local energy current–current time correlation function $c(t) =< j_i(0)j_i(j) >_\beta$ for the equal masses version of our model, where $j_i = m_i v_i^3/2$. Making equal the particle's masses (i.e. $M = m$) has strong implications on system's properties. As a first fact, let us mention that the equal masses version of our model is not ergodic. Once we define the set of initial velocities for the particles, these velocities will remain invariant during the whole evolution. This is due to the elastic collisional kinematics, which implies that the equal masses system effectively behaves as a gas of identical non–interacting particles. Hence the total energy current J is a constant of motion for the equal masses case, and thus $C(t)$. Furthermore, this system is integrable (i.e. it has a macroscopic number of constants of motion), and thus it shows an infinite thermal conductivity. Long time ago, Jepsen [203] proved that, for this equal masses system, $< v_i(0)v_i(t) >_\beta \sim t^{-3}$, where the average should be taken over the canonical ensemble. Following the steps stated by Jepsen, it can be shown analytically, after a lengthly calculation[5], that also $c(t) \propto< v_i(0)^3 v_i(t)^3 >_\beta \sim t^{-3}$ for this system. In order to learn how system's finiteness affect current–current time correlation functions, we have measured $c(t)$ for equal masses

[4] As an example, autocorrelation functions of financial time series show this finite size behavior.[202]

[5] Pedro L. Garrido, private communication.

in a finite system. We have performed such simulation using the canonical ensemble and with a Maxwellian initial velocity distribution, in order to reproduce the previous exact result. Thus we use our deterministic heat baths at the boundaries, with both ends at the same temperature (for completeness, we simulated also this system using stochastic thermal reservoirs, obtaining the same results). Notice that, for the equal masses case, we cannot interchange freely the canonical and the microcanonical ensembles. The underlying reason is the non-ergodic behavior of this system. The presence of the boundary heat reservoirs restores ergodicity, while averages in the microcanonical ensemble depend on initial conditions. Hence, since Jepsen calculation is done in the canonical ensemble, we must simulate the equal masses system also in this ensemble in order to recover the analytical result. Fig. 9.4 shows the numerical computation of $c(t)$ for $N = 500$. It is remarkable that we can also define here two different regions: (1) one for $\ln(t/t_0) \in [5.1, 5.8]$, where a power law fit yields $|c(t)| \sim t^{-3}$, and (2) one for $\ln(t/t_0) > 6$, where a power law fit yields $|c(t)| \sim t^{-0.83}$. We recover the theoretically predicted asymptotic bulk behavior in region (1), while region (2) should be due to finite size effects. Moreover, it is intriguing that the finite size time decay exponent ($\sim 0.83$) is almost the same both in the different masses case and the equal masses one, being these systems very different in essence, and for two different time correlation functions –namely $C(t)$ and $c(t)$. This fact points out the existence of an underlying common finite size mechanism, responsible of this spurious long time decay. We think that autocorrelation effects as those provoked by perturbations which travel all around the system and come back to their origin are at the basis of the observed long time finite size corrections. In conclusion, coming back to the different masses case, in our opinion the above example indicates that only region (1) of Fig. 9.3 represents the asymptotic bulk behavior. Hence, any conclusion about system's conductivity derived from region (2) should be misleading. This result involves a finite Green–Kubo thermal conductivity, and hence that Fourier's law holds in our one–dimensional system.

In order to confirm such result we computed the local energy current-current time correlation function $c(t)$ at equilibrium for the different masses case. It has much better averaging properties than $C(t)$, and thus its asymptotic behavior is much easier to distinguish. The obvious question is whether $c(t)$ has something to do with the total energy current–current self correlation function $C(t)$ entering Green–Kubo formula, both calculated for the different masses model. In general, we can write $C(t) \sim \sum_{i,l} < j_i(0)j_l(t) >= \sum_i < j_i(0)j_i(t) > + \sum_{i \neq l} < j_i(0)j_l(t) >= Nc(t) + \sum_{i \neq l} c_{i,l}(t)$, where $c_{i,l}(t) \equiv < j_i(0)j_l(t) >$. Hence, for *regular* systems, where non–local time correlation functions $c_{i,l}(t)$ decay fast enough with distance, one expects a similar time decay for both $C(t)$ and $c(t)$. However, there are *anomalous* systems for which $c_{i,l}(t)$ decays very slowly, or does not decay at all. One of these anomalous systems is the equal masses version of our model. As explained before, this system is not ergodic; $C(t)$ is constant here. Furthermore, as previously stated, it can be analytically proved that $c(t) \sim t^{-3}$ there. Hence, the behaviors of $C(t)$ and $c(t)$ are clearly different for the equal masses case. Moreover, since $C(t)$ is the cor-

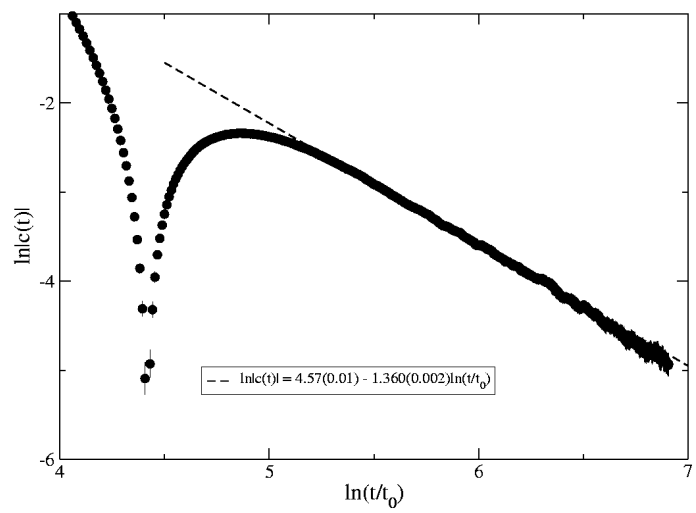


Figure 9.5: Local energy current–current time correlation function $c(t)$ for the alternating masses system with $N = 1000$. The inset shows the results of a power law fit for the long time decay of $c(t)$. Here $|c(t)| \sim t^{-1.36}$. This result is very similar to the observed asymptotic behavior of $C(t)$, and thus reinforces our previous analysis. The number of independent averaged histories is of order $10^9$.

relation function entering the Kubo formula for conductivity, in this case the fact that $c(t) \sim t^{-3}$ implies nothing about the system's conductivity. We measure $c(t)$ for the alternating masses case using the canonical ensemble, i.e. we simulate the system subject to thermal reservoirs at the borders, both at equal temperature $T_1 = T_2 = 1.5$. This measurement yields $c(t) \sim t^{-1-\Delta}$, where $\Delta$ is again very close to 0.3 (see Fig. 9.5), which is very similar to the observed time decay of $C(t)$. This may be thought as an indication that our system is *regular*, in the sense stated above. Moreover, since the averaging properties of $c(t)$ are much better, the observation of a $t^{-1.3}$ tail in $c(t)$ confirms our analysis for $C(t)$, reinforcing our conclusion, i.e. that Fourier's law holds for this unidimensional system. On the other hand, assuming that our different masses system is regular, the fact that $C(t)$, measured using the microcanonical ensemble, and $c(t)$, measured using the canonical ensemble, show very similar behavior supports our previous hypothesis about the equivalence of microcanonical and canonical ensemble averages for the alternating masses model.

In our opinion the decay of correlations is so slow that it explains the strong finite size effects observed in the temperature profile and in the mean heat current. In fact we can argue that $JN/(T_2 - T_1) = \kappa - AN^{-\Delta}$ which explains why we do not see a clear behavior of $J$ with $N$ with system sizes of order $10^3$ (the corrections are of order unity for those sizes).

### 9.3.4 The Energy Diffusion

The above facts imply that Fourier's law holds for our one–dimensional alternating masses system, which conserves total momentum and has a non–zero pressure. However, this conclusion depends critically on data analysis. We have exposed above our analysis, which we think is physically well motivated and coherent. In spite of this, there is always a possibility that an analysis focused in only one observable may drive to the wrong conclusions. Hence, we have attempted to obtain a global, consistent vision of the problem by measuring several magnitudes. With this aim in mind we also studied the dynamical aspects of Fourier's law (see eq. (9.1)). Particularly, we studied the propagation of energy in the system. We prepared the system with zero energy (all particles at rest) and positions $x(i) = i - 1/2$, $i = 1, \ldots, N$. Then, we give to the light particle $i = N/2 + 1$ a velocity chosen from a Maxwellian distribution with temperature $T = 1.5$. That is, we introduced an energy pulse in an otherwise frozen system, and monitored how the energy flows through the system until any boundary particle moves. Finally, we average over many initial conditions (changing the initial velocity of the central light particle). If the system follows Fourier's law we should see a diffusive type of behavior (if the thermal conductivity is constant). This is due to the Local Thermodynamic Equilibrium (LTE) property: if LTE holds in the system, local temperature and local energy are proportional (due to local equipartition of energy, involved by LTE), and thus a diffusive behavior of energy implies a diffusive behavior of local temperature, which is exactly what Fourier's dynamical law, eq. (9.1), states. Figure 9.6 shows the energy distribution for $N = 100$ and different times measured in units $t_0 = 0.032$, where $t_0$ is the mean free time between consecutive particle collisions. Let us remark here again that to apply eq. (9.1) the temperature should have a smooth variation in the microscopic scale to guarantee that local equilibrium holds. In Figure 9.6 we see that, for times larger than $t = 200t_0$, the average variation in the local temperature is of order $0.001$. Therefore, we may assume that we are in a regime where eq. (9.1) holds. Initially, the energy of the light particle is transfered to the neighbors very fast and then the particle stays very cold, much colder than its neighbors. In fact, in this initial regime, the energy maxima are moving outwards at constant velocity. This behavior ends at around $t = 100t_0$. The system then begins to slow down and, at $t \simeq 300t_0$, the structure of the energy distribution changes, and one can then differentiate the behavior corresponding to light particles and heavy ones at least around the maxima of the distribution. We measured the mean square displacement of the energy distribution at each time,

$$s(t) = \sum_n (n - 51)^2 e(n, t) \tag{9.7}$$

We found that we can fit $\ln s(t) = -6.39(0.04) + 2.05(0.01) \ln t$ for $t/t_0 \in (30, 100)$, which is a ballistic behavior that changes smoothly until we reach $t > 400t_0$, where we find a diffusive behavior $\ln s(t) = -1.00(0.01) + 1.005(0.002) \ln t$ (see Fig. 9.7). This last result confirms that our system follows even the dynam-

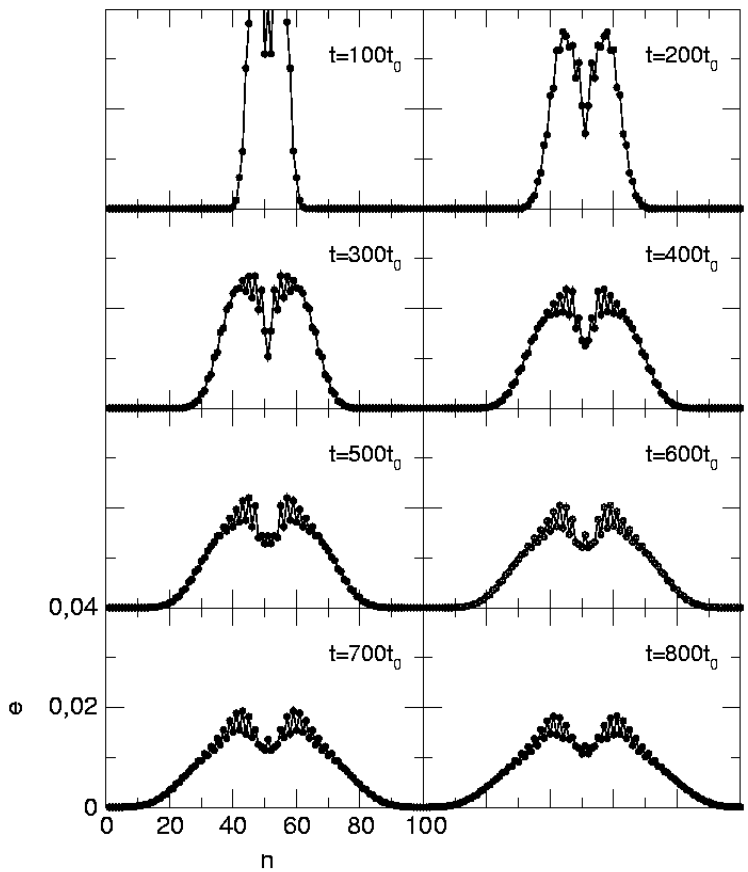


Figure 9.6: Evolution of the energy distribution for an initial condition in which all particles, $N = 100$, are at rest except particle 51 which has an averaged energy corresponding to temperature 1.5. The figure shows averages over $10^7$ independent realizations and $t_0 = 0.032$.

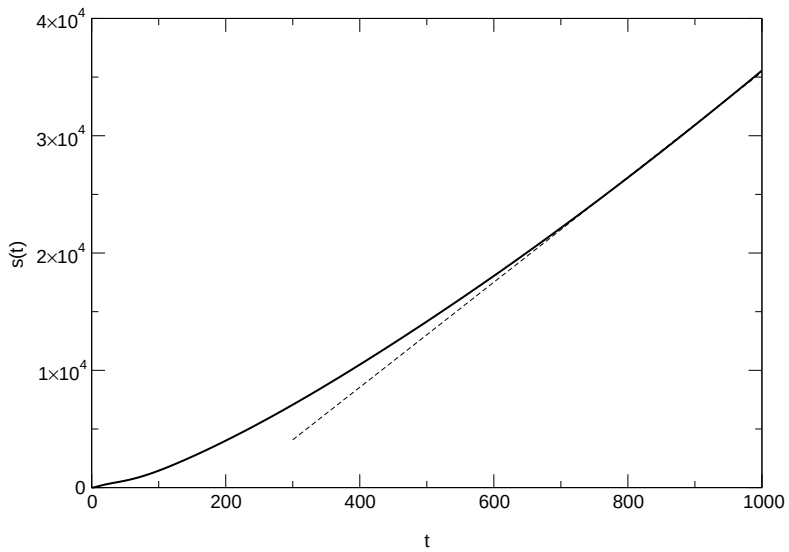


Figure 9.7: Time evolution of $s(t)$ (see the text for definition). A linear behavior $s(t) \sim t$ is clear for long enough times, thus indicating a diffusive propagation of energy. For shorter times we observe $s(t) \sim t^2$, i.e. ballistic propagation.

ical aspects of Fourier's law.

As we noticed above, in Fig. 9.6 we see that the light and heavy particles seem to follow different energy distributions, at least for times longer than $t = 300t_0$. In order to get some more insight about such behavior, we computed the evolution of the total energy stored in the light (heavy) particles. The result is shown in Fig. 9.8 where we can detect five different time regions:

1. $t/t_0 \in (0, 16)$; only the light particle and the two heavy nearest neighbors have a nonzero velocity.

2. $t/t_0 \in (16, 23)$; the five central particles (three light and two heavy ones) are moving. The total energy stored in the light particles reaches a minimum.

3. $t/t_0 \in (23, 233)$; the heavy particles begin to release energy (on the average) until, at $t = 233t_0$, both types of particles have the same amount of energy.

4. $t/t_0 \in (233, 600)$; light particles keep getting energy until we reach the next region,

5. $t > 600t_0$; where the total energy stored in the light particles reaches a constant value that exceeds to the one corresponding to the heavier ones.

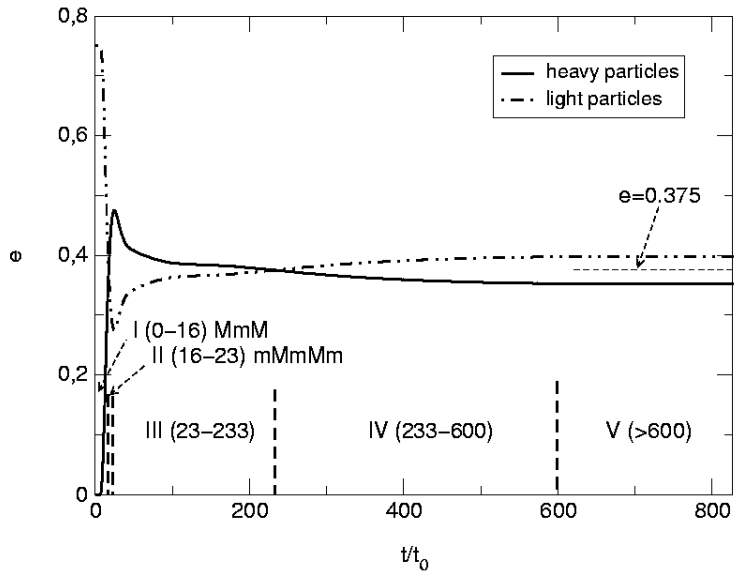


Figure 9.8: Evolution of the total energy stored in the heavy and light particles. The conditions are the same as in Fig.9.6. MmM indicates that only the central light particle and the nearest heavy ones are moving in region I.

Let us remark that, in the asymptotic regime $t > 600t_0$, the energy distribution is still evolving and, therefore, this partition of energy between both degrees of freedom is an asymptotic *dynamical* (non–stationary) property of the system, i.e. it does not appear once we reach the steady state.

In order to discard any non–ergodic behavior of our system we included reflecting boundary conditions at the extremes of the chain and we did much longer simulations. We saw that the isolated system tends to the equilibrium in which equipartition of energy between all degrees of freedom holds. That is, the total mean energy stored in the light particles is equal to the one stored in the heavy ones once the stationary state has been reached. Moreover, we have checked that the system at any stationary state (equilibrium or non–equilibrium) does not present the property of non–equipartition of the energy. This is not incompatible with the dynamical non–equipartition observed above. If due to fluctuations a light particle gains energy over the mean particle energy, it will release this energy excess very slowly, thus effectively trapping energy for a long time, as a local potential would do, although finally this particle should converge to the mean particle energy. We think that this dynamical non-equipartition of the energy between degrees of freedom is responsible for the normal thermal conductivity. In fact, we see that, around the distribution max-

ima, the particles arrange in the form that hot light particles are surrounded by cold heavy ones. The energy is then trapped and released in a diffusive way. However, we also see that the release is diffusive when a large enough number of those hot-cold structures develop. Therefore we think that the mechanism for the thermal resistance is somehow cooperative.

## 9.4 Conclusions

In this chapter we have studied the microscopic foundations of normal heat conduction, which is a dynamic phenomenon very interesting nowadays in the context of nonequilibrium Statistical Mechanics. In order to do so, we have numerically investigated a simple one-dimensional model where point particles of alternating masses elastically collide. When this system is subject to a temperature gradient, a net heat flux emerges from the hot reservoir to the cold one, together with a non-trivial, non-linear steady temperature profile.

An evaluation of the system thermal conductivity from the observed energy current does not yield any conclusive answer about its convergence nor divergence, due to the strong finite size effects affecting our measurements. We thus use the Green-Kubo formula in order to evaluate $\kappa$ in the Themodynamic Limit, for which we measure the total energy current self correlation function, $C(t)$. A careful analysis of the long time behavior of $C(t)$, together with some other related measurements, allow us to conclude that our model system, in spite of being a one-dimensional momentum-conserving system with nonzero pressure, exhibits a finite thermal conductivity in the Thermodynamic Limit, and thus Fourier's law holds in this limit. We further check this conclusion measuring how energy propagates through the system, finding a diffusive kind of propagation, compatible with the dynamic version of Fourier's law.

In conclusion, Peierls arguments have successfully explained the observed thermal conductivity in solids by applying a perturbative scheme around the lattice harmonic interaction. The actual belief is that strong anharmonicity is not enough to guarantee a normal thermal conduction in one dimensional systems. Moreover, it has been proposed that the key lacking ingredient is that the dynamics of the system should not conserve linear momentum via the existence of local potentials through the line (think about particles attached to the one dimensional substrate through some kind of non-linear springs). In this way, local potentials should act as local energy reservoirs that slow down the energy flow. These properties, anharmonicity and non-conservation of momentum, are in some way the ones used on the original Peierls argument. We have shown a model that does not follow such clean picture. Although our one dimensional model is non-linear and it conserves linear momentum (with non-zero pressure), we find that it follows Fourier's law. We think that there are other cooperative mechanisms that can do the job of the local potentials. Maybe, systems having degrees of freedom that acquire easily energy but release it in a very long times scale have, in general, normal thermal conductivity. In any case, we think that it is worth to explore such possibility.

# Chapter 10

# Summary, Conclusions and Outlook

In this thesis we have studied the dynamical aspects of some nonequilibrium systems. They are open, hysteretic systems, subject to density and/or temperature gradients, energy and/or mass fluxes, under the action of external agents and different sources of non-thermal noise, etc. Nonequilibrium systems abound in Nature. In fact, they are the rule, being equilibrium systems an unlikely exception. Examples of out-of-equilibrium systems can be found for instance in biology (e.g. living organisms), economy (e.g. traded stocks), geology (e.g. earthquakes), quantum and molecular physics (e.g. magnetic nanoparticles), hydrodynamics (e.g. turbulent fluids), astrophysics (e.g. star evolution and structure), sociology (e.g. opinion spreading), and so on. Moreover, it seems that nonequilibrium conditions are essential for the observed complex structure in Nature.[1]

In spite of their importance, up to now nobody has been able to formulate a complete theory connecting the microscopic properties of nonequilibrium systems with their macroscopic phenomenology. This connection has been rigorously established only for equilibrium systems in terms of the partition function.[2] The search for a statistical-mechanical description of nonequilibrium systems is one of the main aims of modern Physics. Nowadays there is only a set of *ad hoc* techniques which describe in a partial and approximate way some particular problems in nonequilibrium statistical physics. In particular, most of the studies and theoretical developments in nonequilibrium physics have been centered on nonequilibrium steady states, which constitute the simplest situation in nonequilibrium phenomena. On the other hand, the dynamical aspects of nonequilibrium systems have been poorly studied, and the aim of this thesis consists in enlarging a bit our understanding of such processes.

Dynamical phenomena in complex systems are usually related to transformations between different phases. Thus we have investigated how nonequilibrium conditions affect such transitions. In particular, we have studied the ef-

fects that nonequilibrium conditions induce on the dynamic problem of metastablity, where a system set in a metastable phase eventually evolves towards the stable one. We have also studied how a system under nonequilibrium anisotropic conditions and with conserved number of particles evolves from an initially disordered phase via segregation towards an ordered phase. In addition to their intrinsic interest due to their ubiquity in Nature, these two examples are very interesting because they have equilibrium counterparts. That is, both metastability and phase segregation are dynamic processes observed in equilibrium systems, and they have been deeply investigated. This fact allows us to deduce, comparing both the equilibrium and nonequilibrium cases, the net effects induced by nonequilibrium conditions, which yields many hints about the relevant ingredients that must be taken into account in order to build up a general formalism for nonequilibrium systems. On the other hand, there are dynamic processes intrinsic to nonequilibrium systems. This is the case, for example, of dynamic phase transitions between an active phase, characterized by a non-trivial dynamics, and an absorbing phase, where the system is frozen. This phase transition is irreversible, and hence it is a pure nonequilibrium phenomenon. In this thesis we have investigated the effects that a new, hidden symmetry has on the universality observed in these absorbing phase transitions. Another dynamic processes with no equilibrium counterparts are transport phenomena in general, and heat conduction in particular. We have also investigated the microscopic origins of normal heat conduction and Fourier's law. Of course, there are many nonequilibrium dynamic phenomena that have not been studied in this thesis. As an example, just mention all the rich, complex and yet not fully understood phenomenology observed in fluids: convection, turbulent flow, etc.[8] However, we think that the nonequilibrium dynamic phenomena studied here yield a comprehensive overview of the richness and diversity of new effects that nonequilibrium conditions induce on dynamic processes in complex systems.

The thesis has been divided into two different parts. The first part, which comprises chapters 2, 3, 4 and 5, is devoted to the study of the metastability problem and its associated dynamics in nonequilibrium systems with short-range interactions. In particular, we have studied a nonequilibrium ferromagnet defined on a two-dimensional lattice. On the other hand, in the second part, which comprises chapters 7, 8 and 9, we have studied respectively the kinetics of phase separation in an anisotropic nonequilibrium lattice gas, an absorbing (dynamic) phase transition in a biological inspired model, and the microscopic foundations of normal heat conduction and Fourier's law in a one-dimensional particle chain. In what follows we summarize the results obtained in each chapter, and the possible follow-ups of this work.

In **chapter 2** we present our motivation for studying metastability in magnetic systems, which is two-fold. On one hand, this problem is very interesting from the technological point of view, since impure (i.e. nonequilibrium) magnetic particles are at the basis of many modern and incipient technologies, as for instance dense recording magnetic materials, possible quantum computers, etc. On the other hand, the study of metastability in short-range nonequilib-

rium magnets yields much information about the link between microscopic and macroscopic physics in nonequilibrium systems. In this chapter we also present the model we study in the first part of the thesis, paying special attention to the model properties and the way in which nonequilibrium conditions enter the model. In brief, the model is defined on a lattice with binary spins at the nodes interacting via the Ising Hamiltonian, and subject to a competing dynamics where two different Glauber rates (one at finite temperature, $T$, and the other at "infinite" temperature) compete weighted by a nonequilibrium parameter $p$. This impure dynamics, generically observed in real materials, drives the system towards a nonequilibrium steady state.

The first approach to the problem of metastability in this bidimensional nonequilibrium magnet is presented in **chapter 3**, where a first-order mean field approximation is implemented. This approximation, which allows us to study both the static and dynamic properties of metastable states, is based on three main hypothesis: absence of fluctuations, kinetic isolation of domains, and homogeneity. Using these hypothesis on the general master equation we are able to calculate the system phase diagram, $T_c(p)$, and both the stable and metastable state magnetizations. On the other hand, studying the intrinsic coercive magnetic field, which is the field for which metastable states become unstable, we find that under strong nonequilibrium conditions (in particular, $p > \pi_c \approx 0.0315$) a *non-linear cooperative phenomenon* between the thermal noise (parameterized by $T$) and the non-thermal noise (parameterized by $p$) emerges: although both noise sources independently add disorder to the system, which implies the attenuation, or even destruction of existing metastable states, the combination of both noises parameterized in the microscopic dynamics does not always involves a larger disorder, giving rise to parameter space regions where there are no metastable states for low and high temperatures, but they appear for intermediate temperatures. All these predictions are confirmed via Monte Carlo simulations. In order to investigate the dynamics of the metastable-stable transition using mean field approximation, we extend this theory to include fluctuations, since they are at the basis of the metastable state exit mechanism. In this way we build up a mean field stochastic dynamics based on the mean field predictions for the stable phase growth and shrinkage rates. In spite of including fluctuations, the extended mean field theory fails to describe the metastable-stable transition. This is so because this transition is fully inhomogeneous (it proceeds via droplet nucleation and growth), and hence cannot be described by the homogeneous mean field theory. In order to describe this inhomogeneous dynamic process the properties of the interface separating the stable and metastable phases must be studied. Two possible continuations of the research presented in this chapter should be the following:

- It should be desirable to understand in a deeper way the mechanism which gives rise to the non-linear cooperative phenomenon between the thermal and non-thermal noise sources for $p > \pi_c$.

- It should be also worthy to study in depth the mean field stochastic dy-

namics proposed in this chapter as a natural way to include fluctuations in mean field theory. A more rigorous justification of this method, which seems natural, must be developed. Also a comparison of the predictions associated to fluctuations derived from this method with Monte Carlo results should be welcome.

**Chapter 4** is devoted to the study of the properties of the interface separating the metastable and stable phases in the nonequilibrium ferromagnet. In this chapter we develop a generalization of the Solid-On-Solid approximation [59] in order to understand the effects that nonequilibrium conditions induce on the microscopic and macroscopic properties of the interface. The generalization is based on the concept of effective temperature. It is found that different spin classes suffer different effective temperatures for the nonequilibrium case, the more ordered spins suffering the higher effective temperatures. In this way interfacial spins suffer different effective temperatures for $p \neq 0$, depending on the spin class to which they belong to. Using this observation, and neglecting the presence of overhangs in the interface and the interactions between the interface and bulk fluctuations, we build up the generalization of the SOS theory. The microscopic structure codified in the step probability function and predicted by the generalized SOS approximation matches almost perfectly Monte Carlo results, finding that the larger $p$ is, the rougher the interface is. On the other hand, the macroscopic structure is captured by the surface tension. We find in this case that while the equilibrium surface tension monotonously increases as temperature decreases, the nonequilibrium surface tension exhibits a maximum at certain nonzero temperature, converging towards zero in the low temperature limit. Such low temperature anomalous behavior is a consequence of the dominant character of the non-thermal (nonequilibrium) noise source in this limit, as can be deduced from the interface effective temperature, which becomes independent of $T$ in the low temperature limit. The non-monotonous behavior of surface tension in the nonequilibrium case will be fundamental when understanding the properties of the metastable-stable transition in the nonequilibrium ferromagnet, since this anomalous behavior will be inherited by most of the relevant observables in this problem. Using the explicit expression derived for the nonequilibrium surface tension via the generalized SOS theory, we also study in this chapter the shape and form factor of a nonequilibrium spin droplet using Wulff construction. The non-zero interfacial effective temperature induced by nonequilibrium conditions in the low temperature limit implies that the droplet shape is no more a square in this limit for $p \neq 0$ (as opposed to what happens in equilibrium systems), but a differentiable curve in between a square and a circle. In order to extend the investigations developed in this chapter, we propose the following lines:

- The generalized SOS approximation must be further tested against Monte Carlo simulations, both on its microscopic and macroscopic aspects. In particular, one should study the interfacial roughness derived from this theory, since it is a relevant observable in many surface problems. Also the importance of overhangs and interactions between the interface and

bulk fluctuations should be addressed.

- The effects that the suppression of the surface tension at low temperature in the nonequilibrium case induce on many natural phenomena controlled by an interface must be investigated, since many real interfaces are subject to nonequilibrium conditions as those captured by our competing dynamics.

In **chapter 5** we present a nonequilibrium extension of nucleation theory.[75, 76, 26] We hypothesize the existence of a nonequilibrium potential associated to a spin droplet, equivalent to the equilibrium free energy, which controls the exit from the nonequilibrium metastable state. Moreover, we assume that such droplet nonequilibrium potential can be written as a competition between a surface term, proportional to the (nonequilibrium) surface tension and which hinders the droplet growth, and a volume (bulk) term, which favours droplet growth and depends on the spontaneous magnetization. Using the results obtained in previous chapters for both the nonequilibrium surface tension and the nonequilibrium spontaneous magnetization, we build up our nonequilibrium generalization of nucleation theory. This extended approximation yields correct predictions for the relevant observables in this problem, namely the critical droplet size, the droplet radial growth velocity, the metastable state mean lifetime, etc. All these magnitudes inherit the anomalous, non-monotonous behavior of the nonequilibrium surface tension. In particular, we observe that the critical droplet size and the metastable state mean lifetime exhibit a maximum as a function of temperature for any $p \neq 0$, decreasing for lower temperatures. On the other hand, the droplet radial growth velocity shows a minimum as a function of temperature. Thereby a main conclusion of our analysis is that the properties of the interface separating the metastable and stable (nonequilibrium) phases determine in a fundamental way the metastable state exit dynamics. All these results are verified by extensive Monte Carlo simulations. On the other hand, the morphology of the metastable-stable transition is also highly affected by nonequilibrium conditions, mainly at low temperatures. In particular, it is found that finite nonequilibrium systems may demagnetize from the metastable state through the nucleation of multiple critical droplets both at high and low temperatures, while there is an intermediate temperature range where this process proceeds through the nucleation of a single critical droplet, as opposed to equilibrium systems, where the multidroplet mechanism only emerges at high temperatures, being the single droplet nucleation process the relevant one at low temperatures. This is in fact checked in Monte Carlo simulations. A principal conclusion derived from the results presented in this chapter is that the hypothesis of existence of a nonequilibrium potential which controls the metastable-stable transition dynamics accurately describes this nonequilibrium dynamic phenomenon. Hence, although we do not know how to construct such nonequilibrium potential from the microscopic point of view, this result points out possible paths in order to build up such potential. In addition to their theoretical interests, these results might also be relevant from the technological point of view, since a main technological concern is to retain

for as long as possible the actual (possibly metastable) states of impure magnetic particles in storage magnetic materials. In order to continue investigating the lines developed in this chapter, we propose:

- Investigate in depth the validity of the hypothesis of existence of a nonequilibrium potential controlling the exit from the metastable state. From a formal point of view, we do not know even whether this potential exists.
- It should be worthwhile to compare our theoretical results with experiments in real magnetic materials. The chances are that the phenomenology here described can be in fact observed in actual magnets.
- It should be also interesting to investigate metastability in one-dimensional nonequilibrium systems with ordered phase at low temperatures. Here the characterization of the interface is trivial, and the analysis of the metastability problem and the effects of nonequilibrium conditions on it should be much simpler.

In **chapter 6** we study the effects that circular free borders induce on the properties of the metastable-stable transition studied in previous chapters. This transition proceeds now through the heterogeneous nucleation of droplets near the border, due to obvious energetic effects. With this exception, all the nucleation properties found in previous chapters remain qualitatively valid when free boundaries are present. However, under the combined action of both open borders and nonequilibrium conditions, the evolution of a stable phase nucleus inside the parent metastable phase proceeds by avalanches. These burst-like events characterize the dynamics of many complex nonequilibrium systems. Once subtracted the extrinsic noise, the measured avalanche size and lifetime distributions show power law behavior, up to an exponential cutoff which depends algebraically on system size. In addition, the size and lifetime of an avalanche are also power-law related. A detailed analysis of these scale free avalanches reveals that they are in fact the combined result of many avalanches of different well-defined *typical* size and duration. That is, the simplicity and versatility of our model system allows us to identify many different types of avalanches, each type characterized by a probability distribution with well defined typical size and duration, associated with a particular *curvature* of the domain wall. Due to free borders and the microscopic impurity the system visits a broad range of domain wall configurations, and thus the combination of these avalanches generally results in a distribution which exhibits several decades of power law behavior and an exponential cutoff. However, this apparent scale-free behavior does not mean that avalanches are critical, in the sense of a second order phase transition where diverging correlation lengths appear. The deep insight derived from this chapter comes when we compare our results with experiments on Barkhausen Noise in particular and $1/f$ Noise in general. In fact, our measured exponents are almost identical to those measured by Spasojević et al[88] in Barkhausen experiments in quasi-bidimensional VITROVAC. Moreover, the exponents we measure exhibit finite

size corrections similar to those observed in real avalanche systems, and the algebraic dependence of cutoffs with system size is also a main feature of real systems. Avalanches in our model show also some properties, as for instance reproducibility, observed in real Barkhausen materials. On the other hand, all actual theoretical approaches to Barkhausen Noise are based on the assumption of the existence of an underlying critical point (plain old one or SOC one), responsible of the observed scale invariance. However, all these explanations imply that universality must hold in Barkhausen experiments, which is not observed in practice. Therefore, all the similarities found between avalanche properties in our model and Barkhausen experiments, together with the fact that experimental observations do not support the existence of universality in Barkhausen Noise, led us to suspect that Barkhausen Noise might also come from the superposition of more elementary events with well-defined typical scales, which is the underlying mechanism in our model. The chances are that our observation that scale invariance originates in a combination of simple events, which we can prove in our model cases, is a general feature of similar phenomena in many complex systems. Several follow-ups of the work developed in this chapter can be proposed:

- It should be desirable to export the analysis method introduced in this chapter in order to identify the origin of different avalanches and the superposition of different typical scales to many experimental situations, simplifying in this way the investigation about the origin of Barkhausen emissions in particular, and $1/f$ Noise in general.

- A general mathematical framework and a more complete theoretical approach to our observation that scale invariance originates in a combination of simple events is needed in order to generalize this idea.

In **chapter 7** we perform a theoretical and computational study of phase segregation under anisotropic nonequilibrium conditions. In particular, we study the driven lattice gas (DLG) in two dimensions, since it is a good microscopic metaphor of many real situations. The resulting picture holds for a class of highly anisotropic nonequilibrium phenomena in Nature: ionic superconductors, fluids under shear flow, or subject to external electric fields or gravity, vibrated granular materials, etc. The methods developed in this chapter help in the analysis of such situations. Coarsening in DLG evolves as follows. After a quench from an initially fully disordered state, anisotropic grains develop, which quickly give rise to strings. These strings further coarsen until well-defined narrow stripes form which percolate in the field direction. While the grain and string coarsening stages last for very short as compared to the total evolution time, the stripe coarsening process involves most of the system evolution. In fact this is due to the hydrodynamic slowing down appearing as a consequence of particle conservation and local dynamics. Hence this last stage is the relevant (observable) one from the experimental point of view. The stripe coarsening proceeds through the effective diffusion and coalescence of stripes. The effective diffusion of stripes can be understood in terms of two different

single-particle processes: hole (particle) diffusion within the stripe (HD), and surface evaporation/condensation (EC) of particles and holes. The EC mechanism is dominant at the beginning of the stripe coarsening process, due to the large surface/volume ratio at these stages, yielding a growth law for the stripe mean width of the form $\ell(t) \sim t^{1/4}$. However, as time goes on, the stripe surface/volume ratio decreases, and eventually the HD mechanism becomes dominant, implying a $t^{1/3}$ growth law. The temporal crossover between both growth trends appears for a time $\tau_{cross}(L_{\|})$. This temporal crossover implies the appearance of a size crossover, since both $\tau_{cross}(L_{\|})$ and the time the system needs to reach the final steady state, $\tau_{ss}(L_{\perp}, L_{\|})$ depend on system size. It is found that, for small enough values of $L_{\perp}$, $\tau_{cross}(L_{\|}) > \tau_{ss}(L_{\perp}, L_{\|})$, and therefore only 1/4-behavior is expected at long times. On the other hand, the $t^{1/3}$ growth law is the general one expected for macroscopic systems. All these theoretical results are perfectly checked in Monte Carlo simulations. A relevant experimental observable is the structure factor. We have studied such function in our system, due to its experimental importance. Since during the stripe coarsening stage there is only one relevant scale, namely the mean stripe width, then dynamical scaling, i.e. time self-similarity during the segregation process, is expected for the structure factor. This is in fact confirmed in Monte Carlo simulations. Furthermore, the shape of the scaling function shows the Guinier gaussian region, followed by the anisotropic Porod's region, $k_{\perp}^{-2}$, for large $k_{\perp}$ and a thermal tail $k_{\perp}^{-3}$ for very large $k_{\perp}$. The shape of the structure function, and in particular the anisotropic extension of Porod's law and the thermal tail, are perfectly understood from the anisotropic, striped character of DLG clusters. Moreover, the anisotropy present in DLG is the key ingredient needed in order to understand the whole coarsening process. Two possible extensions of the research carried out in this chapter are:

- The application of the theoretical analysis here developed to recent experiments on horizontally vibrated granular materials[152] which show striped patterns very similar to those observed in our system should shed light on the physical mechanisms behind such morphogenesis.
- It should be also worthy to study phase separation from the field theoretical point of view, using a recently proposed field equation which correctly describes the critical behavior of DLG for infinite field.

**Chapter 8** is devoted to the study of an absorbing (dynamic) phase transition in a biologically inspired lattice model, called Lipowski model. Phase transitions separating an active, fluctuating phase from a frozen one are ubiquitously observed in Nature. Some examples are catalytic chemical reactions, disease and damage spreading, forest fires, pinning of surfaces, nonequilibrium wetting, sandpiles, etc. In particular, our motivation for studying Lipowski model is to study the anomalous critical behavior reported for this system.[179] It has been claimed that this model shows a sort of *dimensional reduction* or *superuniversality*, in such a way that both the one- and two-dimensional versions of the model should belong to the one-dimensional directed percolation (DP)

universality class. In this chapter we perform a finite size scaling analysis of the critical behavior of the bidimensional system together with spreading experiments in order to address this question. Using these methods we calculate up to six different critical exponents, showing that the two-dimensional Lipowski model does not belong to any known universality class. In particular, we do not find any trace of dimensional reduction. Instead, a completely novel scaling is observed. We identify as the relevant ingredient for the observed novel scaling the presence of *superabsorbing sites* (and cluster composed by them) in the system. A site in the lattice that cannot be activated from some direction(s) by neighboring activity is called a superabsorbing site. A site can be superabsorbing in one or more directions. The presence of superabsorbing sites in the system enormously slow down the dynamics. The relevance of superabsorbing sites for the observed novel scaling behavior is strongly supported by two facts. First, one-dimensional DP behavior is observed in the one-dimensional version of Lipowski model, where no superabsorbing sites are found at criticality. On the other hand, the two-dimensional Lipowski model defined on a honeycomb lattice shows 2d DP behavior, while for this lattice coordination number the probability of finding superabsorbing sites at criticality is negligible. Hence superabsorbing sites are at the basis of the novel scaling found. Depending on the system dimension, the lattice coordination number and other details, we identify different phenomenology. For instance, if complete frozen superabsorbing clusters exist above (below) certain threshold, and not below (above) such threshold, then a first order transition is expected just at the threshold point. On the other hand, if *almost* frozen clusters of superabsorbing sites appear at criticality, we expect anomalous scaling as the one reported in this chapter. Finally, if superabsorbing sites are not observed at the critical point, usual DP scaling must be observed. There are still some open questions which might be addressed in future works:

- We might study in more realistic systems, as for instance catalytic dimer-dimer systems, whether effects similar to those uncovered in the present chapter play a relevant role.

- It should be also interesting from the theoretical point of view to look for a field theoretical Langevin equation describing from a coarse-grained point of view (in the spirit of the Reggeon Field Theory for the DP universality class) the novel scaling emerging due to the presence of superabsorbing sites.

- Other interesting questions are related to the relevance of the new symmetry induced by the presence of superabsorbing sites in the Thermodynamic Limit.

In **chapter 9** we study another nonequilibrium dynamic phenomenon, related now with transport phenomena. In particular, we investigate the microscopic foundations of normal heat conduction and Fourier's law. In order to do so we study a one-dimensional chain of point particles, interacting via

elastic collisions, which are subject to a temperature gradient induced by two deterministic heat baths at the extremes of the chain, working at different temperatures. This problem is very important from the theoretical point of view, since an understanding of the microscopic mechanisms governing heat conduction should shed much light on the connection between the microscopic fundamental physics and some macroscopic properties of many nonequilibrium systems, as for instance Local Thermodynamic Equilibrium, that are far from being understood. The general belief nowadays is that a one-dimensional system as the studied here, which conserves the total momentum and has a non-zero pressure, must exhibit an anomalous heat conductivity in the Thermodynamic Limit (TL). However, we show in this chapter that, on the contrary to the popular belief, the system investigated here exhibits a finite conductivity in the TL. In order to prove such result, we analyze the problem from several different, complementary points of view. First, we prove the existence of a non-trivial thermal profile in the TL, indicating that Local Thermodynamic Equilibrium (LTE) holds in the system, and thus it makes sense to ask about the validity of Fourier's law. The thermal profile shows a linear central region, and gets curved near the heat reservoirs (*surface resistance*). In order to verify whether Fourier's law holds or not for this system, we measure in a first step the heat flux $J$ through the system. If Fourier's law holds, $J$ should decrease as a function of the inverse number of particles in the system. However, finite size effects on $J$ are so strong that this analysis does not yield any definite conclusion about the system conductivity. A different method, based on the energy current self-correlation function $C(t)$, from which thermal conductivity can be derived via the Green-Kubo formulae, is then used. The thermal conductivity $\kappa$ should be finite in the TL if $C(t)$ decays as $t^{-1-\Delta}$, with $\Delta > 0$. The long time analysis of $C(t)$ shows that it presents two different asymptotic behaviors, namely $t^{-1.3}$ and $t^{-0.85}$. However, we show that the $t^{-0.85}$ tail comes from system autocorrelations due to finite size effects, and hence the $t^{-1.3}$ is the true asymptotic one in the TL. Therefore, the thermal conductivity, as derived from the Green-Kubo formula, is finite in our system, so Fourier's law holds in this case. The previous result depends critically on data analysis, and due to the slow decay of correlations and the strong finite size effects observed in this system, such analysis becomes very difficult. Hence further tests and a global consistent vision of the problem are needed in order to ensure about the validity of Fourier's law in this system. For this reason we also study in this chapter the dynamical aspects of Fourier's law. In particular we study the energy diffusion through the system, finding that an initially localized energy pulse propagates in a diffusive manner through the system, thus confirming that Fourier's law holds even in its dynamical aspects. Moreover, the energy diffusion study allows us ti identify the mechanism responsible of normal heat conduction in the system. We observe that light particles tend to dynamically absorb much more energy than heavy ones. In this way, the light degrees of freedom acquire energy easily, but release it at very long time scales, thus giving rise to *hot-cold structures*. Furthermore, energy propagates in a diffusive way when many of those hot-cold structures are formed, thus indicating the

cooperative character of the phenomenon. Cooperative phenomena as the one here described can do the job of local potentials, giving rise to normal heat conduction. In spite of our results, there are still many open question associated to the conductivity problem. Some ideas are:

- The analysis of the energy current self-correlation function has provoked an exciting discussion among the experts in the field. It should be desirable to obtain a clearer picture of the finite size effects which give rise to the measured $t^{-0.85}$ spureous tail in $C(t)$.

- Even simpler models must be proposed in order to study the problem of conductivity from a microscopic point of view. In this sense, a model similar to the one studied here but with significant smaller finite size effects should be welcome. A good candidate is a one-dimensional ring with charged point particles subject to an electric field.

- There are many more fundamental open question, as for instance: which are the necessary and sufficient conditions in order to observe LTE in a system ?, which is the relation among LTE, energy equipartition and heat transport ?, etc.

As the reader will surely have realized, this thesis is highly heterogeneous. We have studied here many different systems, and what is more significant, we have used many different theoretical methods and approximations in order to understand what is going on in each problem. This fact points out one of the main problems of actual nonequilibrium physics: the lack of a general formalism, equivalent in some sense to equilibrium Statistical Mechanics, in order to describe in a unified way nonequilibrium phenomena. On the other hand, we have been able to understand all the observed phenomenology in all the nonequilibrium dynamic problems studied here using these incomplete theoretical approaches, many of them based on concepts derived from equilibrium statistical physics. In order to do so, we have done many *reasonable* approximations, but which we are not able to prove. For these reasons we think that theoretical physicists must put their effort nowadays on the rigorous connection between the microscopic physics of nonequilibrium systems and the meso-macroscopic assumptions which allow us to develop semi-phenomenologic theoretical approaches to nonequilibrium phenomena, such as the Local Thermodynamic Equilibrium hypothesis, the existence of nonequilibrium potentials controlling the system dynamic and static properties, etc. I think in this connection underlies the missing link of nonequilibrium statistical physics.

Granada, November $6^{th}$, 2002

# Appendix A

# Monte Carlo with Absorbing Markov Chains Simulations and Rejection-Free Algorithms. Projective Dynamics and the Slow Forcing Approximation

In this appendix we present the foundations of Monte Carlo with Absorbing Markov Chains (MCAMC) algorithms, as well as the method of projective dynamics and the slow forcing approximation.[43, 45, 46]

In general, Monte Carlo methods, first introduced by Metropolis, Rosenbluth, Rosenbluth, Teller and Teller[47] and mainly characterized by the use of random numbers, are useful to study the static and dynamic properties of stochastic systems. A Monte Carlo algorithm generates stochastic trajectories in the system's phase space, in such a way that the properties of the system are derived from averages over the different trajectories. If we want to study the static properties of a system, there is a considerable freedom to choose the way in which we move through the phase space with the Monte Carlo algorithm. However, if we want to study dynamic properties there is no such freedom, since the physical meaning of the dynamics is an essential part of the model. Since we want to understand here a dynamic process as metastability in ferromagnetic systems, the advanced simulation algorithms we will use must respect the system dynamics. This is the case for the Monte Carlo with Absorbing Markov Chains algorithms that we summarize in this appendix.

Let's summarize the steps of an standard Monte Carlo algorithm for the

Ising model with spin flip dynamics before going into the functioning of MCAMC algorithms.[42] For a dynamics $\omega(\beta\Delta\mathcal{H})$, which yields the transition probability per unit time between two configurations which differ in the state of a single spin, and which depends on the inverse temperature $\beta$ and the energy increment between both configurations, $\Delta\mathcal{H}$, the steps the standard algorithm follows are:

- Increase the time from $t$ to $t + 1/N$.
- Choose randomly a spin in the lattice.
- Calculate a random number $\bar{r}$ with an homogeneous distribution in the interval $(0, 1)$.
- Calculate, or look up in a previously stored table, the energy $E_{old}$ of the current configuration, and the energy $E_{new}$ of the configuration of the system if we flip the selected spin. From these values, we calculate the energy increment $\Delta\mathcal{H}$ involved by this spin flip.
- Accept the configuration change, i.e. flip the selected spin, if $\bar{r} \leq \omega(\beta\Delta\mathcal{H})$. Otherwise keep the same configuration.

A Monte Carlo Step per Spin (MCSS) is defined as $N$ spin flip trials as the above described, where $N$ is the number of spins in the lattice. As we explained in section 2.2, a MCSS corresponds to a physical time of order $10^{-13}$ seconds, which is roughly the inverse frequency of the associated heat bath phonons. The fundamental problem of the previously described Monte Carlo scheme is that, with some probability, the algorithm rejects a spin flip, which involves a waste of computer time. Furthermore, for low enough temperatures the probability of accepting a spin flip against the local magnetic field a spin suffers is extremely small (the local magnetic field the spin $i$ suffers is defined as $h_i = -J\sum_j s_j - h$, where the sum runs over the nearest neighbors of spin $i$). Hence most of the trials are rejected in this case. This problem makes the standard Monte Carlo algorithm inefficient in order to study the exit from a metastable state at low temperatures.

The advantage of MCAMC algorithms resides in that they are *rejection-free* algorithms: in this case, once we randomly select a spin in the lattice, it is flipped with unit probability, and time is incremented by the necessary amount for this spin flip to take place. Hence, as opposed to classic Monte Carlo algorithms, in MCAMC algorithms the time increments are variable (and stochastic, as we will see below).

MCAMC algorithms use the concept of absorbing Markov chains (as its name points out). Hence it is necessary to make a brief introduction to the most relevant properties of absorbing Markov chains. Following ref. [43], let's consider one of these chains, with $s$ transient states and $r$ absorbing states. The generic system starts its evolution in one of the transient states, and it remains in the transient state space up to it is trapped in one of the $r$ absorbing states. In

order to completely define the absorbing Markov chain we only need to write the Markov matrix,

$$\mathbf{M}_{(r+s)\times(r+s)} = \begin{pmatrix} \mathbf{I}_{r\times r} & \mathbf{0}_{r\times s} \\ \mathbf{R}_{s\times r} & \mathbf{T}_{s\times s} \end{pmatrix} \tag{A.1}$$

The elements of this matrix yield the probability of evolving from the state $i$ to the state $j$ in each clock tic, $M_{i,j} \equiv M(i \to j)$. We must notice that here we are using the *mathematical* notation, where the state vector is a row vector, on which the Markov matrix acts from the right. It is obvious that this matrix describes a Markov process, since the transition probabilities between states (the elements $M_{i,j}$) only depend on the initial state (given by $i$, the row index) and the final state ($j$, the column index). Furthermore, the sum of the elements on each row is unity.

The size of the sub-matrices defining the Markov matrix is explicitely shown in the above expression. The matrix $\mathbf{I}$ is the identity, $\mathbf{0}$ is a matrix with all its elements equal to zero, $\mathbf{T}$ is the transient matrix, which shows the transition probabilities among the states belonging to the transient space, and $\mathbf{R}$ is the recurrent matrix, which shows the transition probabilities among the $s$ transient states and the $r$ absorbing states. The matrix that governs the evolution of the system after $m$ time steps is,

$$\mathbf{M}^m_{(r+s)\times(r+s)} = \begin{pmatrix} \mathbf{I}_{r\times r} & \mathbf{0}_{r\times s} \\ (\mathbf{I}+\mathbf{T}+\ldots+\mathbf{T}^{m-1})_{s\times s}\mathbf{R}_{s\times r} & \mathbf{T}^m_{s\times s} \end{pmatrix} \tag{A.2}$$

The system must initially lie in the transient space, so the initial state is represented by a vector $(\vec{0}^T, \vec{v}_I^T)$, where the vector $\vec{v}_I^T$ has $s$ components and the super-index $^T$ denotes the vector transpose, i.e. a row vector. Applying the matrix $\mathbf{M}^m$ to this initial state vector, we obtain the $(r+s)$-dimensional vector,

$$\begin{pmatrix} \vec{0}^T & \vec{v}_I^T \end{pmatrix}\mathbf{M}^m = \begin{pmatrix} \vec{v}_I^T(\mathbf{I}+\mathbf{T}+\ldots+\mathbf{T}^{m-1})\mathbf{R} & \vec{v}_I^T\mathbf{T}^m \end{pmatrix} \tag{A.3}$$

The components of this vector yield the probability of being in each one of the $(r+s)$ states of the system after $m$ time steps. If we introduce the row vector $\vec{e}$, with dimension $s$, such the all its elements are equal to unity, the probability of still being in the space of transient states after $m$ time step is,

$$p_{\text{transient}} = \vec{v}_I^T\mathbf{T}^m\vec{e} \tag{A.4}$$

The probability that the system has exited to each one of the $r$ possible absorbing states is determined by the components of the following $r$-dimensional vector,

$$\vec{p}_{\text{abs. after m steps}} = \vec{v}_I^T(\mathbf{I}+\mathbf{T}+\ldots+\mathbf{T}^{m-1})\mathbf{R} \tag{A.5}$$

Here it is clearly observed that the probability that the system has exited to each one of the $r$ absorbing states after $m$ time steps is equal to the probability that the exit takes place in the first step (determined by the term $\mathbf{IR}$), plus the probability that the exit takes place in the second step ($\mathbf{TR}$), plus the probability

| Class | Central spin | Number of up neighbors | $\Delta\mathcal{H}$ |
|---|---|---|---|
| 1 | +1 | 4 | 8J+2h |
| 2 | +1 | 3 | 4J+2h |
| 3 | +1 | 2 | 2h |
| 4 | +1 | 1 | -4J+2h |
| 5 | +1 | 0 | -8J+2h |
| 6 | -1 | 4 | -8J-2h |
| 7 | -1 | 3 | -4J-2h |
| 8 | -1 | 2 | -2h |
| 9 | -1 | 1 | 4J-2h |
| 10 | -1 | 0 | 8J-2h |

Table A.1: Spin classes for the two-dimensional isotropic Ising model with periodic boundary conditions. The last column shows the energy increment associated to each spin class.

that the exit takes place in the steps $3, 4, \ldots, m$. Thus, the probability that the system exits to each one of the $r$ possible absorbing states, *given* that the exit takes place in the $m$-th time step is,

$$\vec{p}_{\text{abs. in step } m} = \frac{\vec{v}_I^T \mathbf{T}^{m-1} \mathbf{R}}{\vec{v}_I^T \mathbf{T}^{m-1} \mathbf{R} \vec{e}} \tag{A.6}$$

Eqs. (A.4) and (A.6) are the basic equations from which MCAMC algorithms are derived.

In order to apply our knowledge about absorbing Markov chains to the bidimensional Ising model we must introduce the concept of *spin classes*. For a spin in the lattice, the spin class to which this spin belongs to is defined by the spin orientation ($+1$ or $-1$) and the number of up nearest neighbors it shows. Hence, for the two-dimensional isotropic Ising model with periodic boundary conditions there are 10 different spin classes, schematized in Table A.1. All spins belonging to the same spin class involve the same energy increment when flipped (see Table A.1), so the transition rate for a spin depends exclusively on the class $i \in [1, 10]$ to which it belongs to, $\omega_i \equiv \omega(\beta\Delta\mathcal{H}_i)$, where $\Delta\mathcal{H}_i$ is the energy increment associated to class $i$. On the other hand, if we have an up (down) spin in class $i \in [1, 5]$ ($i \in [6, 10]$), when we flip this spin its class will change to $i + 5$ ($i - 5$). Equivalently its four nearest neighbor spins will change the class to which they belong to, increasing (decreasing) in one unit the class they were before the spin flip.

Let's assume that $n_i$ is the number of spins in class $i$. Then $N = \sum_{i=1}^{10} n_i$. Thus the probability of flipping in a time step any of the spins in class $i$ will be $n_i\omega_i/N$, since $n_i/N$ is the probability of selecting a spin in class $i$, and $\omega_i$ is the probability per unit time of flipping the spin, once it has been selected. In order to exit from a given state in the Ising system, one of the spins in the system, which belongs to some spin class, must be flipped. Consequently we

can interpret this process as an absorbing Markov chain where the current state is the only transient state, and where there are 10 different absorbing states, each one associated to a spin flip where the flipped spin belongs to one of the 10 possible spin classes. Thus the absorbing state 3 is the state to which the system exits if we flip in the current configuration a spin belonging to class 3.

Therefore the system is governed by a Markov matrix $\mathbf{M}_{(10+1)\times(10+1)}$, with $s = 1$ transient states and $r = 10$ absorbing states. The recurrent matrix $\mathbf{R}$ is now a row vector with 10 components,

$$\mathbf{R} = \begin{pmatrix} \frac{n_1\omega_1}{N} & \frac{n_2\omega_2}{N} & \dots & \frac{n_{10}\omega_{10}}{N} \end{pmatrix} \tag{A.7}$$

and the transient matrix $\mathbf{T}$ is now a scalar which yields the probability of remaining in the current configuration,

$$\mathbf{T} = 1 - \frac{1}{N}\sum_{i=1}^{10} n_i\omega_i \equiv \lambda \tag{A.8}$$

The next step consists in determining the number of time steps the system needs to exit the current configuration. The probability that the system is still in the same transient state (i.e. the current state) after $m$ time steps is $\lambda^m$. This probability does not depend on the absorbing state to which the system finally exits. The probability that the absorption occurs in the $m$-th step is $\lambda^{m-1}(1-\lambda)$. Since we are speaking about probabilities, the number of time steps the system needs to exit the current state will be a stochastic variable determined through the inequality $\lambda^{m-1} \geq \tilde{r} > \lambda^m$, where $\tilde{r}$ is a random number homogeneously distributed in the interval $(0, 1]$. From this inequality we obtain,

$$m = \lfloor \frac{\ln(\tilde{r})}{\ln\lambda} \rfloor + 1 \tag{A.9}$$

where $\lfloor x \rfloor$ is the integer part of $x$. Once we determine the time the system needs to exit the current state, we only have to decide to which absorbing state the system exits to. In order to do so we select randomly, with probabilistic weights determined by the elements of the recurrent matrix $\mathbf{R}$, to which class the spin to flip belongs to. We thus define 10 partial sums $Q_i = \sum_{j=1}^{i} n_j\omega_j$, with $i \in [1, 10]$. In order to decide the class to which the spin to flip belongs to, we generate another random number $\bar{r}$ homogeneously distributed in the interval $[0, 1)$ and we determine the index $k \in [1, 10]$ that fulfills the following condition,

$$Q_{k-1} \leq \bar{r}Q_{10} < Q_k \tag{A.10}$$

The index $k$ yields the class where we must flip the spin. If there are more than one spin in class $k$, we must use another random number to decide, completely at random, the spin to flip in this class.

Summarizing, the steps to follow in a simulation of the Ising model using this rejection-free algorithm are,

- Calculate three random numbers $\tilde{r}$, $\bar{r}$ and $\hat{r}$.

- Calculate the accumulated sums $Q_i = \sum_{j=1}^{i} n_j \omega_j$, with $i \in [1, 10]$.
- Using $\tilde{r}$, calculate from eq. (A.9) the number of time steps $m$ in order to exit the current configuration.
- Using $\bar{r}$, calculate the class $k$ which satisfies the condition $Q_{k-1} \leq \bar{r} Q_{10} < Q_k$.
- Using $\hat{r}$, randomly select one of the $n_k$ spins in class $k$, and flip this spin.
- If the flipped spin was up (down) before the change, add one unit to the number of spins in class $k+5$ ($k-5$), $n_{k+5} \to n_{k+5}+1$ ($n_{k-5} \to n_{k-5}+1$). In the same way, subtract one unit from the number of spins in class $k$, $n_k \to n_k - 1$.
- If the flipped spin was up (down) before the change, each one of its four nearest neighbors changes from the class $l$ to which it belonged to the class $l+1$ ($l-1$). We increase the number of spins in class $l+1$ ($l-1$) in one unit, and we decrease the number of spins in class $l$ in one unit.
- Increase the time from $t$ to $t + m/N$ (we divide by $N$, the number of spins in the lattice, because we measure time in MCSS).

This algorithm is rejection-free, because it accepts with unit probability all proposed spin flips, and time increases in stochastic intervals, depending on the system's current state. This algorithm, which is the one we have used when studying metastability, is called in literature *s-1 Monte Carlo with Absorbing Markov Chains algorithm*. The name s-1 points out the fact that this algorithm uses a single transient state. Using eqs. (A.4) and (A.6) it is possible to generalize this algorithm to transient subspaces with 2 (s-2 MCAMC) and 3 (s-3 MCAMC) states.[43] In general, these algorithms are many order of magnitude faster than standard Monte Carlo algorithms when simulating systems with discrete state space at low temperatures. The efficiency of these algorithms increments as we enlarge the transient subspace.

There is an efficient way to computationally implement MCAMC algorithms. It is based on the creation of four different lists. The vector `NCLS(k)`, with $k = 1, \ldots, 10$, contains the number of spins $n_k$ in each spin class. The vectors `ICLASS(i)` and `ICPOS(i)` inform us about the class to which a spin situated in a lattice site $i$ belongs to and the place that this spin occupies in the list of spins belonging to the same class, respectively. Finally, the matrix `LOC(j,k)` yields the lattice position of a spin in class $k$ situated in the $j$-th position in the list of spins belonging to this class. Hence we have that `LOC(ICPOS(i),ICLASS(i))=i`. Using these four vectors it is very simple to implement MCAMC algorithms, as well as to actualize the class populations after each spin flip.

When we want to study the problem of metastability in an Ising model at very low temperatures and weak magnetic fields, the local stability of the metastable state is so strong that simulations are not feasible even for MCAMC

algorithms. Therefore it is necessary to go one step beyond MCAMC algorithms and design more advanced techniques able to simulate *rare events* as the exit from the metastable state in these extreme conditions. In our case the solution underlies in the so-called *slow forcing approximation*.[45] In this approximation the system is forced to evolve towards the stable state by a moving magnetization wall. That is, we define an upper bound for magnetization, which depends on time, $m_{lim}(t) = 1 - \phi t$, and such that the system magnetization is forced to stay below this threshold at any time. This constraint imposed on magnetization clearly modifies the system's original dynamics. Hence, given the dynamic character of the problem of metastability, such modification on the dynamics would affect in principle the results of simulations performed with a nonzero forcing $\phi$. However, it has been shown that for small enough values of the forcing $\phi$, a slow forcing limit exists[45], such that in this limit the system observables are independent of the applied forcing, while the simulation is still significantly accelerated as compared to the non-forced system. In some sense, this slow forcing limit is an *adiabatic limit*: although the system is forced, if $\phi$ is small enough the system has enough time to thermalize and select the same *typical* configurations that a system without forcing should choose in its evolution from the metastable state to the stable one. In this way the phase space sampling in the slow forcing limit is almost indistinguishable from the sampling performed with non-forced algorithms, although in the first case the sampling can be done in a reasonable amount of time. It is important to realize that the forcing is only relevant in the neighborhood of the metastable state: once the energy barrier has been overcome, the system rapidly evolves towards the stable state via nonequilibrium (non-thermalized) configurations, being the magnetization wall irrelevant in this process. The combination of the s-1 MCAMC algorithm and the slow forcing approximation constitutes the basic computational scheme we have used to simulate our system.

If we now think, for instance, about the metastable state lifetime, it is obvious that the result obtained using the slow forcing approximation will be much smaller than the real one. Thus we must develop a method that allows us to extract information, as for instance the metastable state lifetime, from simulations performed using the slow forcing approximation. This method is based on the so-called *projective dynamics method*.[46] The idea behind the projective dynamics method is that one expects that a one-dimensional physical picture of the nonequilibrium potential which controls the process is valid even for a complicated process as that of metastability in our nonequilibrium model. In this approximation the dynamics of the (complex) system is projected on a one-dimensional system where the relevant variable is one of the *slow-evolving* observables of the original system. In particular, all states with the same magnetization are projected on a single state, defined by the value of magnetization. Therefore, instead of considering transitions among the $2^N$ possible states in the (complex) Ising system, which are captured by a Markov matrix with dimension $2^N \times 2^N$, we only consider transitions between projected states with well defined magnetization, giving rise in this case to a projected Markov matrix with dimensions $(N+1) \times (N+1)$. It has been mathematically proved that

the original Markov matrix with $2^N$ states is not even weakly lumpable[48], although it seems to be lumpable with respect to the states in the escape route from the metastable state. Thus the original master equation which governs the Ising dynamics, given by eq. (2.2) (see section 2.2) is projected on a master equation for the $(N+1)$ magnetization states,

$$\frac{dP(n_{up};t)}{dt} = \sum_{n'_{up}} \left[ W(n'_{up} \to n_{up}) P(n'_{up};t) - W(n_{up} \to n'_{up}) P(n_{up};t) \right] \tag{A.11}$$

The variable $n_{up}$ is the number of up spins which identifies the projected state, and it is completely equivalent to magnetization $m$, $n_{up} = N(1+m)/2$. Here the projected transition rates between magnetization states, $W(n'_{up} \to n_{up})$, naturally appear. Only transitions between states which differ in one up spin are allowed, since our dynamics is a single spin flip dynamics (see eq. 2.3). Hence the transition rates $W(n'_{up} \to n_{up})$ and $W(n_{up} \to n'_{up})$ will be zero always that $n'_{up} - n_{up} \neq \pm 1, 0$. This property implies that the associated projected Markov matrix is tridiagonal, and so very easy to treat analytically.

It is possible to measure these transition rates in a simple way in Monte Carlo simulations. We only have to notice that, for instance, $W(n_{up} \to n_{up}-1)$ is just the probability per unit time that an up spin flips. An up spin must be in a class $k \in [1,5]$, and we know that the probability per unit time of changing a spin in class $k$ is given by $n_k \omega_k / N$, where $n_k$ is the number of spins belonging to class $k$, and $\omega_k$ is the transition rate associated to this class. Therefore we can write,

$$\begin{aligned} W(n_{up} \to n_{up}-1) &\equiv \frac{g(n_{up})}{N} = \frac{1}{N} \sum_{k=1}^{5} n_k \omega_k \\ W(n_{up} \to n_{up}+1) &\equiv \frac{s(n_{up})}{N} = \frac{1}{N} \sum_{k=6}^{10} n_k \omega_k \\ W(n_{up} \to n_{up}) &\equiv 1 - \frac{g(n_{up})}{N} - \frac{s(n_{up})}{N} \end{aligned} \tag{A.12}$$

These equations help us to define growth rate, $g(n_{up})$, and the shrinkage rate, $s(n_{up})$, of the stable phase in the state with magnetization $n_{up}$. Using the s-1 MCAMC algorithm is very simple to measure both $g(n_{up})$ and $s(n_{up})$, since we know the classes populations at any time. We can obtain much information about the metastable-stable transition from these stable phase growth and shrinkage rates. For instance, if we perform $K$ demagnetization experiments with $h < 0$ from the metastable state (with positive magnetization) to the stable one (with negative magnetization), we can write the following balance equation, valid for all values of $n_{up}$,

$$N(n_{up} \to n_{up}-1) = K + N(n_{up}-1 \to n_{up}) \tag{A.13}$$

where $N(n_{up} \to n_{up}-1)$ and $N(n_{up}-1 \to n_{up})$ are, respectively, the number of times that, in these $K$ experiments, we go from a state with $n_{up}$ up spins to

other state with $n_{up} - 1$ up spins, and the number of times we go from $n_{up} - 1$ to $n_{up}$. If $\eta(n_{up})$ is the total time we spend in a state with magnetization $n_{up}$ in one experiment, we can write, $N(n_{up} \to n_{up} - 1) = K\eta(n_{up})g(n_{up})$, and $N(n_{up} - 1 \to n_{up}) = K\eta(n_{up} - 1)s(n_{up})$. We can now write the following recurrence relation,

$$\eta(n_{up}) = \frac{1 + \eta(n_{up} - 1)s(n_{up} - 1)}{g(n_{up})} \tag{A.14}$$

which relates the time we spend in states with $n_{up}$ up spins to the time we spend in states with $n_{up} - 1$ up spins. On the other hand, we must give a threshold in order to define the metastable state lifetime, such that the first passage time through this threshold will yield the definition of the metastable lifetime. For lattice spin system as the one we study this threshold is usually defined by the zero magnetization condition. In this way we define the lifetime of the metastable state for the ferromagnetic spin system as the first passage time to $m = 0$ (or, equivalently, $n_{up} = N/2$). We can calculate this mean lifetime using the above recurrence relation. In order to do so we must fix an initial condition for the recurrence. We can think in this process as a one-dimensional random walk, which starts at $n_{up} = N$ and finishes at $n_{up} = N/2$. Thus we have that $\eta(N/2) = 0$ so,

$$\tau = \sum_{n_{up}=\frac{N}{2}+1}^{N} \eta(n_{up}), \quad \eta(n_{up}) = \frac{1 + \eta(n_{up} - 1)s(n_{up} - 1)}{g(n_{up})}, \quad \eta(\frac{N}{2}) = 0 \tag{A.15}$$

In this way we can obtain the metastable state mean lifetime from the stable phase growth and shrinkage rates, $g(n_{up})$ and $s(n_{up})$, respectively. An estimation of the error for $\tau$ can be obtained by a simple quadratic error propagation procedure, from the errors associated to the times $\eta(n_{up})$, whose error derive from the statistical errors in the measure of $g(n_{up})$ and $s(n_{up})$. The mean lifetime obtained from (A.15) is exact up to statistical errors, as compared to the mean lifetime of the real system.[43] Finally, the projected growth and shrinkage rates, $g(n_{up})$ and $s(n_{up})$, allow us to study the shape of the nonequilibrium potential (or the fee energy in the equilibrium system) during the escape from the metastable state. Thus the points $n^*_{up}$ for which $g(n^*_{up}) = s(n^*_{up})$ identify the local extremes of this nonequilibrium potential. This fact allows us to measure, as explained in Chapter 3, the magnetization of the stable and metastable states with high precision, as well as the magnetization which defines the critical droplet. We also are able to calculate from $g(n_{up})$ and $s(n_{up})$ the system's magnetic viscosity[31].

# Appendix B

# Calculation of the Probability $\Pi_2(T, p)$ of Finding an Interfacial Spin in Class 2

In this appendix we present in detail the calculation of $\Pi_2(T, p)$, the probability of finding an interfacial spin belonging to class 2, in our generalized Solid-On-Solid approximation for the nonequilibrium interface.

As explained in section 4.3, the probability $\Pi_2(T, p)$ is defined by the average (see eq. (4.26)),

$$\Pi_2(T, p) = \sum_{\delta,\epsilon=-\infty}^{+\infty} \pi_2(\delta, \epsilon) p(\delta, \epsilon) \tag{B.1}$$

where $\pi_i(\delta, \epsilon)$ is the probability of finding a spin of class $i$ in an interfacial spin column characterized by a left step with magnitude $\delta$ and a right step with size $\epsilon$, and where $p(\delta, \epsilon)$ is the probability of finding an interfacial spin column in such configuration $(\delta, \epsilon)$. The two-body probability function $p(\delta, \epsilon)$ depends on the relative signs (including zero) of the steps $\delta$ and $\epsilon$. Table 4.1 shows the different functions $p(\delta, \epsilon)$ for each one of the 9 possible typical configurations for a interfacial spin column in the generalized SOS approximation. On the other hand, as explained in section 4.3, the probability function $\pi_2(\delta, \epsilon)$ can be written as,

$$\pi_2(\delta, \epsilon) = \frac{n_2(\delta, \epsilon)}{N(\delta, \epsilon)} \tag{B.2}$$

where $n_2(\delta, \epsilon)$ is the number of spins in class 2 for an interfacial spin column characterized by $(\delta, \epsilon)$, and where $N(\delta, \epsilon)$ is the total number of interfacial spins associated to this column. Table 4.2 shows the different values of $n_2(\delta, \epsilon)$ and $N(\delta, \epsilon)$ for each typical column configuration. Attending to the entries of

both tables, we can write for $\Pi_2(T,p)$,

$$\begin{aligned}
\Pi_2(T,p) &= \frac{1}{\mathcal{Q}}\Big\{\sum_{\delta=1}^{+\infty}\sum_{\epsilon=1}^{+\infty}(1-\frac{1}{\delta})Y^{\delta+\epsilon}X_3^3X_2^{\delta+\epsilon-2}+\sum_{\delta=1}^{+\infty}(1-\frac{1}{\delta})Y^{\delta}X_2^{\delta-1}X_3^2 \\
&+ \sum_{\delta=1}^{+\infty}\sum_{\epsilon=-\infty}^{-1}(1-\frac{\alpha}{\lambda})Y^{\delta+\epsilon}X_4^3X_3^{2(\alpha-1)}X_2^{\lambda-\alpha}+\sum_{\epsilon=1}^{+\infty}Y^{\epsilon}X_3^2X_2^{\epsilon-1}+X_2 \\
&+ \sum_{\epsilon=-\infty}^{-1}(1-\frac{1}{|\epsilon|})Y^{\epsilon}X_3^2X_2^{|\epsilon|-1}+\sum_{\delta=-\infty}^{-1}\sum_{\epsilon=1}^{+\infty}Y^{\delta+\epsilon}X_4^3X_3^{2(\alpha-1)}X_2^{\lambda-\alpha} \\
&+ \sum_{\delta=-\infty}^{-1}Y^{\delta}X_3^2X_2^{|\delta|-1}+\sum_{\delta=-\infty}^{-1}\sum_{\epsilon=-\infty}^{-1}(1-\frac{1}{|\epsilon|})Y^{\delta+\epsilon}X_3^3X_2^{|\delta|+|\epsilon|-2}\Big\} \qquad \text{(B.3)}
\end{aligned}$$

where $X_i = e^{-2J\beta_{eff}^{(i)}}$ and $Y = e^{\gamma_p(\phi)}$. Writing the above equation we have used the equalities $X_9 = X_2$, $X_8 = X_3$ and $X_7 = X_4$, and we have defined $\alpha = \min(|\delta|,|\epsilon|)$ and $\lambda = \max(|\delta|,|\epsilon|)$. The factor $\mathcal{Q}$ is the normalization constant, already calculated in section 4.3, see eq. (4.25).

We must use the classic results for the geometric sum and the geometric series, as well as some other results that can be easily derived from them, see eqs. (4.28)-(4.33), in order to perform the sums involved in the calculation of $\Pi_2(T,p)$. It is convenient to summarize again these results,

$$\sum_{k=0}^{\infty}x^k = \frac{1}{1-x} \quad , \quad |x|<1 \qquad \text{(B.4)}$$

$$\sum_{k=0}^{n}x^k = \frac{1-x^{n+1}}{1-x} \quad , \quad x\neq 1 \qquad \text{(B.5)}$$

$$\sum_{k=1}^{\infty}\frac{x^k}{k} = \ln(\frac{1}{1-x}) \quad , \quad |x|<1 \qquad \text{(B.6)}$$

$$\sum_{k=1}^{n}\frac{x^k}{k} = \ln(\frac{1}{1-x})-\int_0^x dy\frac{y^n}{1-y} \quad , \quad |x|<1 \qquad \text{(B.7)}$$

$$\sum_{k=1}^{\infty}kx^k = \frac{x}{(1-x)^2} \quad , \quad |x|<1 \qquad \text{(B.8)}$$

$$\sum_{k=1}^{n}kx^k = \frac{x(1-x^n)}{(1-x)^2}-\frac{nx^{n+1}}{1-x} \quad , \quad x\neq 1 \qquad \text{(B.9)}$$

Using these expressions we can complete satisfactorily the calculation of $\Pi_2(T,p)$. To see in detail this calculation, let's solve in a first step, as a simple case, the double sum appearing in the first term of the right hand side of eq. (B.3). This term is associated to an interfacial spin column characterized by $\delta,\epsilon>0$ (type

A in Table 4.1). If we denote this sum as $S_A$, then $S_A$ is written as,

$$\begin{aligned} S_A &= \sum_{\delta=1}^{+\infty}\sum_{\epsilon=1}^{+\infty}(1-\frac{1}{\delta})Y^{\delta+\epsilon}X_3^3X_2^{\delta+\epsilon-2} \\ &= \frac{X_3^3}{X_2^2}\sum_{\epsilon=1}^{+\infty}(X_2Y)^{\epsilon}\sum_{\delta=1}^{+\infty}(1-\frac{1}{\delta})(X_2Y)^{\delta} \end{aligned}$$

Up to now we have only re-written the sum $S_A$. Applying eq. (B.4) to the sum over $\epsilon$, decomposing the sum over $\delta$ in two different sums, and using for these sums the solutions expressed in eqs. (B.4) and (B.6), we find the solution,

$$S_A = \frac{X_3^3Y^2}{(1-X_2Y)^2} - \frac{X_3^3X_2^{-1}Y}{1-X_2Y}\ln(\frac{1}{1-X_2Y}) \tag{B.10}$$

In the same way we have calculate this first sum, we can calculate the rest of terms on the right hand side of eq. (B.3), being most of the calculations as simple as the one we have solved previously. The only sum which shows some degree of complexity is that associated to an interfacial spin column of type C (see Table 4.1), i.e. $\delta > 0$ and $\epsilon < 0$. This sum, called from now on $S_C$, corresponds to the third term on the right hand side of eq. (B.3),

$$S_C = \sum_{\delta=1}^{+\infty}\sum_{\epsilon=-\infty}^{-1}(1-\frac{\alpha}{\lambda})Y^{\delta+\epsilon}X_4^3X_3^{2(\alpha-1)}X_2^{\lambda-\alpha}$$

where we must remember that $\alpha = \min(|\delta|,|\epsilon|)$ and $\lambda = \max(|\delta|,|\epsilon|)$. This sum can be written as,

$$\begin{aligned} S_C &= \frac{X_4^3}{X_3^2}\sum_{\delta=1}^{+\infty}\Big\{(X_2Y)^{\delta}\sum_{\epsilon=1}^{\delta}(1-\frac{\epsilon}{\delta})(\frac{X_3^2}{X_2Y})^{\epsilon} \\ &\quad +(\frac{X_3^2Y}{X_2})^{\delta}\sum_{\epsilon=\delta+1}^{+\infty}(1-\frac{\delta}{\epsilon})(\frac{X_2}{Y})^{\epsilon}\Big\} \end{aligned} \tag{B.11}$$

Using eqs. (B.4)-(B.9) we can perform the sum over $\epsilon$, yielding,

$$\begin{aligned} S_C &= \frac{X_4^3}{X_3^2}\sum_{\delta=1}^{+\infty}\Big\{(X_2Y)^{\delta}\big[\frac{X_3^2X_2^{-1}Y^{-1}}{1-X_3^2X_2^{-1}Y^{-1}} - \frac{1}{\delta}\frac{X_3^2X_2^{-1}Y^{-1}-(X_3^2X_2^{-1}Y^{-1})^{\delta+1}}{(1-X_3^2X_2^{-1}Y^{-1})^2}\big] \\ &+ (\frac{X_3^2Y}{X_2})^{\delta}\big[\frac{(X_2Y^{-1})^{\delta+1}}{1-X_2Y^{-1}} - \delta\int_o^{X_2Y^{-1}}dy\frac{y^{\delta}}{1-y}\big]\Big\} \end{aligned} \tag{B.12}$$

At this point we can perform easily the sums over $\delta$, taking into account that we can interchange the sum and the integral (the Riemann integration is a linear

application). Summing over $\delta$ we arrive to,

$$\begin{aligned} S_C &= \frac{X_4^3}{X_3^2}\Big\{\frac{X_3^2}{(1-X_3^2X_2^{-1}Y^{-1})(1-X_2Y)} + \frac{X_3^2X_2^{-1}Y^{-1}}{(1-X_3^2X_2^{-1}Y^{-1})^2}\ln(\frac{1-X_2Y}{1-X_3^2}) \\ &+ \frac{X_3^2X_2Y^{-1}}{(1-X_2Y^{-1})(1-X_3^2)} - \int_0^{X_2Y^{-1}} dy \frac{X_3^2YX_2^{-1}y}{(1-y)(1-X_3^2YX_2^{-1}y)^2}\Big\} \end{aligned} \tag{B.13}$$

In order to finish the calculation of $S_C$ we only have to evaluate the integral. This integral is of the type,

$$zI \equiv z\int_0^x dy \frac{y}{(1-y)(1-zy)^2}$$

where in this case $z = X_3^2X_2^{-1}Y$ and $x = X_2Y^{-1}$. Integrating I by parts, choosing $u = y/(1-y)$ and $dv = dy/(1-zy)^2$, we obtain,

$$I = \frac{x}{z(1-x)(1-zx)} - \frac{1}{z}\int_0^x dy \frac{1}{(1-zy)(1-y)^2} \tag{B.14}$$

We call $I_2$ to the integral appearing in the second term on the right hand side of the above equation. This last integral can be solved analytically, knowing that generically[64],

$$\begin{aligned} \int dy \frac{1}{(a+by)^n(\alpha+\beta y)^m} &= -\frac{1}{(m-1)(a\beta-\alpha b)}\frac{1}{(a+by)^{n-1}(\alpha+\beta y)^{m-1}} \\ &- \frac{(m+n-2)b}{(m-1)(a\beta-\alpha b)}\int dy \frac{1}{(a+by)^n(\alpha+\beta y)^{m-1}} \end{aligned}$$

Applying this expression to $I_2$, taking into account that in this case $a = 1$, $b = -z$, $\alpha = 1$, $\beta = -1$, $m = 2$ and $n = 1$, we arrive to,

$$I_2 = \frac{x}{(1-z)(1-x)} + \frac{z}{(1-z)^2}\ln(\frac{1-x}{1-zx})$$

where we have already analytically solved the last remaining integral. Using this result in the expression for I, eq. (B.14), and applying the result of this substitution to the previously calculated expression for $S_C$, eq. (B.13), and taking into account that $z = X_3^2X_2^{-1}Y$ and $x = X_2Y^{-1}$, we finally obtain the sum $S_C$,

$$\begin{aligned} S_C &= \frac{X_4^3}{X_3^2}\Big\{\frac{X_3^2}{(1-X_3^2X_2^{-1}Y^{-1})(1-X_2Y)} + \frac{X_3^2X_2^{-1}Y^{-1}}{(1-X_3^2X_2^{-1}Y^{-1})^2}\ln(\frac{1-X_2Y}{1-X_3^2}) \\ &+ \frac{X_3^2X_2Y^{-1}}{(1-X_2Y^{-1})(1-X_3^2)} + \frac{X_2Y^{-1}}{(1-X_2Y^{-1})(1-X_3^2X_2^{-1}Y)} \\ &+ \frac{X_3^2X_2^{-1}Y}{(1-X_3^2X_2^{-1}Y)^2}\ln(\frac{1-X_2Y^{-1}}{1-X_3^2}) - \frac{X_2Y^{-1}}{(1-X_2Y^{-1})(1-X_3^2)}\Big\} \end{aligned} \tag{B.15}$$

In a similar way we are able to calculate the rest of sums involved in the expression for $\Pi_2(T,p)$, finally obtaining the result shown in eq. (4.34). The calculations needed in order to evaluate $\Pi_4(T,p)$ are even simpler, so we do not include them in this appendix.

# Appendix C

# Avalanche Size Distribution for a Flat Domain Wall

In this appendix we calculate the avalanche size distribution associated to a flat domain wall in our nonequilibrium ferromagnetic system (see Chapter 6). These (small) avalanches characterize the so-called *extrinsic noise*[88] that appears in the avalanche size distributions associated to the ferromagnetic circular nanoparticle. In order to perform the calculation we need again the concept of spin class. Remembering from section 3.3.4, if we have a spin $s$ in our lattice, the spin class to which this spin belongs to is defined once we know the spin orientation, $s = +1$ or $s = -1$, and its number of up nearest neighbors, $n \in [0, 4]$. Therefore, for the two-dimensional isotropic Ising model subject to periodic boundary conditions there are 10 different spin classes (see Table C.1). The last column in Table C.1 shows the Glauber transition rate, see eq. (2.3), for each spin class once fixed the parameter values to $T = 0.11T_{Ons} \approx 0.25$, $p = 10^{-6}$ and $h = -0.1$. Remember also that $J = 1$ and $\beta = 1/T$.

Let us assume now that we have our nonequilibrium magnetic system defined on a square lattice with size $L \times L$, subject to periodic boundary conditions along the horizontal direction and open boundary conditions in the vertical direction. The initial condition consists in a stripe of down spins with height $L/2$ situated in the lower part of the system, and a complementary up spins stripe situated in the upper part of the system. That is, the initial condition comprises two bulk phases (up and down) and a perfectly flat interface between them. Under the action of a negative magnetic field the interface moves upwards on average. This system corresponds to the semi-infinite system introduced in sections 5.3.2 and 6.3.1 when studying the interface growth velocity and the extrinsic noise respectively. The probability per unit time of changing a spin in class $i$ is,

$$r_i(t) = \frac{n_i(t)}{N}\omega_i \tag{C.1}$$

where $n_i(t)$ is the number of spins in class $i$ at time $t$, $\omega_i$ is the transition rate

| Class | Central spin | Number of up neighbors | Transition rate |
|---|---|---|---|
| 1 | +1 | 4 | $\sim 10^{-6}$ |
| 2 | +1 | 3 | $\sim 1.24 \times 10^{-6}$ |
| 3 | +1 | 2 | $\sim 0.69$ |
| 4 | +1 | 1 | $\sim 1$ |
| 5 | +1 | 0 | $\sim 1$ |
| 6 | -1 | 4 | $\sim 1$ |
| 7 | -1 | 3 | $\sim 1$ |
| 8 | -1 | 2 | $\sim 0.31$ |
| 9 | -1 | 1 | $\sim 1.05 \times 10^{-6}$ |
| 10 | -1 | 0 | $\sim 10^{-6}$ |

Table C.1: Spin classes for the two-dimensional isotropic Ising model with periodic boundary conditions. The last column shows the approximate value of the Glauber transition rate, eq. (2.3), for $T = 0.11T_{ons}$, $p = 10^{-6}$ and $h = -0.1$.

associated to class $i$ (see section 3.3.4) and $N = L^2$ is the total number of spins in the system. For our initial condition the only occupied classes are class 1 (up bulk spins), class 2 (up interfacial spins), class 9 (down interfacial spins) and class 10 (down bulk spins). For low temperatures and $-2J \leq h \leq 0$ the $\omega_i$ values for these four spin classes are very small (see Table C.1). In fact, we have that $\omega_{1,10} \sim 10^{-6}$, $\omega_2 \sim 1.24 \times 10^{-6}$ and $\omega_9 \sim 1.05 \times 10^{-6}$. Since for the initial condition we have that $n_1, n_{10} \gg n_2, n_9$, there will be many bulk fluctuations before a fluctuation in the interface appears.

However, when an interfacial fluctuation appears a lateral avalanche takes place. Let us assume that an interfacial fluctuation appears in the form depicted in Fig. C.1.a, where one up interfacial spin has been flipped. Now this spin belongs to class 7, and its two nearest neighbor spins in the direction of the interface belong to class 3. Since $\omega_3 \approx 0.69$ and $\omega_7 \approx 1$, in this case we have that $r_3 \approx 2 \times 0.69/N$ and $r_7 \approx 1/N$. These probabilities must be compared with $r_1 \approx N^{-1}[(L/2-1)L-1] \times 10^{-6}$, $r_2 \approx 1.24 \times N^{-1}(L-2) \times 10^{-6}$, $r_9 \approx 1.05 \times N^{-1}(L-1) \times 10^{-6}$ and $r_{10} \approx N^{-1}[(L/2-1)L+1] \times 10^{-6}$. Hence, for feasible system sizes as those we use in our simulations, and for our fixed set of parameters, the probability of lateral growth of the initial fluctuation ($2 \times 0.69/N$) and the probability of destroying the fluctuation ($1/N$) are much larger than the probability of finding any other spin flip in the system. This argument allows us to safely assume that once the interfacial perturbation has appeared, the system dynamics can be reduced to the growth and shrinkage dynamics of the interfacial perturbation. Under this assumption, the most probable process to be observed consists in the growth of the interfacial fluctuation via the flipping of the lateral spins in class 3 which surround the fluctuation, until one of the two spins in class 8 which delimit the lateral size of the interfacial fluctuation flips, stopping in this way the fluctuation growth. We call this process and *avalanche*, and our aim now consists in calculating the size

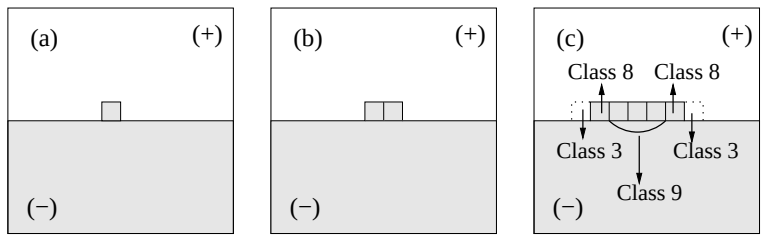


Figure C.1: Schematic plot of a flat interface and the origin and growth mechanism of a lateral interfacial avalanche, as described in the main text. Notice in (c) that during the lateral avalanche evolution the only relevant spins are the two spins in class 8 and the two spins in class 3.

distribution for these lateral interfacial avalanches.

Therefore we suppose that the system is in a state as that shown in Fig. C.1.b, with two up interfacial spins flipped, and we want to know the probability of finding a lateral avalanche as the one described above with size $\Delta_m < 0$ (it is an avalanche *in the direction* of the magnetic field, $h < 0$), where the size of the avalanche is defined as the number of spins it involves. Following our assumptions, the only way an avalanche can grow is through the flip of any of the two spins in class 3 adjacent to the cluster forming the avalanche (see Fig. C.1.c). This avalanche will stop once any of the two spins in class 8 at the lateral border of the avalanche cluster flips. All other spin flip processes in the system have a negligible probability of being observed as compared to these two processes.

The restricted dynamics we propose here only involves four different spins (two of class 3 and two of class 8). Hence the probabilities of flipping a spin in class 3 or 8 are now, respectively,

$$r_3 = \frac{1}{2}\left[p + (1-p)\frac{e^{2\beta|h|}}{1+e^{2\beta|h|}}\right] \tag{C.2}$$

$$r_8 = \frac{1}{2}\left[p + (1-p)\frac{e^{-2\beta|h|}}{1+e^{-2\beta|h|}}\right] \tag{C.3}$$

where we have used the general form of Glauber rate for arbitrary values of $T$, $p$ and $h$, once specified for classes 3 and 8. Since we have modified the system original dynamics, we must normalize again these probabilities. Applying the normalization condition, we obtain the avalanche growth and stop probabilities,

$$p_{grow} = \frac{1}{1+p}\left[p + (1-p)\frac{e^{2\beta|h|}}{1+e^{2\beta|h|}}\right] \tag{C.4}$$

$$p_{stop} = \frac{1}{1+p}\left[p + (1-p)\frac{e^{-2\beta|h|}}{1+e^{-2\beta|h|}}\right] \tag{C.5}$$

The probability of finding a lateral avalanche of size $\Delta_m < 0$ is $P(\Delta_m) =$

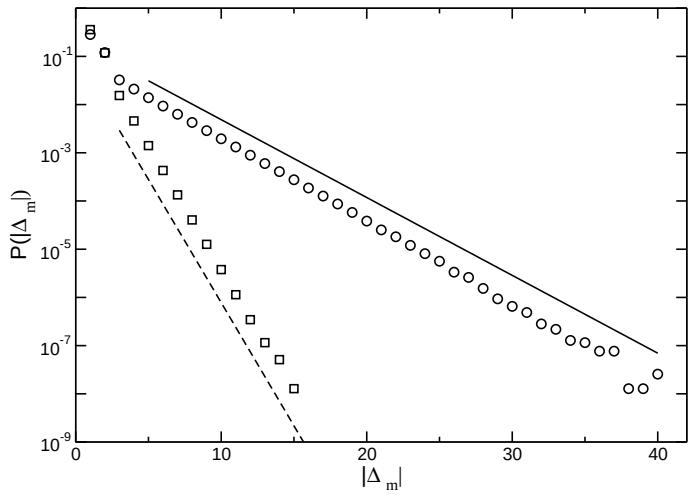


Figure C.2: Semilog plot of the avalanche size distributions $P(\Delta_m > 0)$ (dashed line) and $P(\Delta_m < 0)$ (continuous line) as obtained from our calculations for $T = 0.11T_{ons}$, $p = 10^{-6}$ and $h = -0.1$. The points are Monte Carlo results for the avalanche size distributions $P(\Delta_m > 0)$ (□) and $P(\Delta_m < 0)$ (◯) for the semi-infinite system described in the main text with $L = 53$. The agreement between the theoretical prediction and Monte Carlo results is excellent.

$p_{grow}^{|\Delta_m|} p_{stop}$, that is,

$$\begin{aligned} P(\Delta_m < 0) &= \frac{\left[p + (1-p)\frac{e^{-2\beta|h|}}{1+e^{-2\beta|h|}}\right]}{1+p} \times \left\{\frac{1}{1+p}\left[p + (1-p)\frac{e^{2\beta|h|}}{1+e^{2\beta|h|}}\right]\right\}^{|\Delta_m|} \\ &= \frac{1}{1+p}\left[p + (1-p)\frac{e^{-2\beta|h|}}{1+e^{-2\beta|h|}}\right] \times e^{-|\Delta_m|/\bar{\Delta}_m^{(-)}} \end{aligned} \tag{C.6}$$

where the typical size characterizing avalanches in the field direction can be written as,

$$\bar{\Delta}_m^{(-)} = \frac{1}{\ln\left[\frac{(1+p)(1+e^{2\beta|h|})}{p+e^{2\beta|h|}}\right]} \tag{C.7}$$

In a similar way we can calculate the size distribution and the typical size of positive avalanches, $P(\Delta_m > 0)$ and $\bar{\Delta}_m^{(+)}$ respectively. In this case the avalanche growth probability is given by eq. (C.5) and the avalanche stop probability is given by eq. (C.4). The result for the typical size is,

$$\bar{\Delta}_m^{(+)} = \frac{1}{\ln\left[\frac{(1+p)(1+e^{-2\beta|h|})}{p+e^{-2\beta|h|}}\right]} \tag{C.8}$$

Fig. C.2 shows the avalanche size probability distributions $P(\Delta_m < 0)$ and $P(\Delta_m > 0)$ as obtained from the previous calculations, see eq. (C.6) and its

equivalent for $\Delta_m > 0$, for $T = 0.11T_{ons}$, $p = 10^{-6}$ and $h = -0.1$. This figure also shows Monte Carlo results for the avalanche size distribution in the semi-infinite system described above with size $L = 53$. As we observe in this figure, the agreement between the predictions and Monte Carlo results is excellent.

This agreement allows us to state the origin of the extrinsic noise in our nonequilibrium magnetic system. As we have deduced previously in this appendix, the small avalanches which define the extrinsic noise are just local random fluctuations of an advancing flat domain wall. The extrinsic noise is thus an intrinsic property of the magnetic system, and it has nothing to do with the presence of free boundaries, as opposed to large avalanches in the circular nanoparticle defined in Chapter 6, whose origin is intimately related to the presence of free borders and its interplay with the domain wall.

# Appendix D

# Variations of Lipowski Model

In this appendix we briefly discuss some variations of Lipowski model not studied in Chapter 8. In particular, we introduce some results obtained for Lipowski model with parallel updating dynamics, and we also comment on a multiplicative version of this model.

## D.1 Lipowski Model with Synchronous Updating

As an alternative attempt to speed up the dynamics, and examine further some properties of the two-dimensional model, we have implemented the microscopic dynamics replacing the original sequential updating by a synchronous or parallel one, i.e. all active sites are "deactivated" simultaneously at each Monte Carlo step, and all their associated bonds are replaced by new random variables simultaneously. In this way, as random numbers do not have to be extracted to sequentially select sites, the dynamics is largely accelerated. For this modified dynamics, we have examined some relatively large system sizes, $L = 256$, and concluded that the nature of the transition is changed with respect to the sequential updating case: in this case the transition is first order and critical exponents cannot be defined. To show that this is the case, in figure 9 we present the stationary activity curve. The upper curve corresponds to simulations performed taking an initial activity-density equal to unity. On the other hand, the lower curve is obtained by starting the system with a natural absorbing configuration, and activating on the top of it a small percentage of sites (about a ten percent).

For values of $r$ in the interval $[\approx 1.545, \approx 1.555]$ the system reaches different states depending upon the initial condition. The presence of a hysteresis loop is a trait of the transition first-order nature. First order absorbing state transitions have been observed in other contexts [189]. However, we caution the reader that, as the transition is found to occur at a value of $r$ for which the probability of creating superabsorbing sites is very large (much larger than in the sequential case), and the dynamics is therefore extremely anomalous and

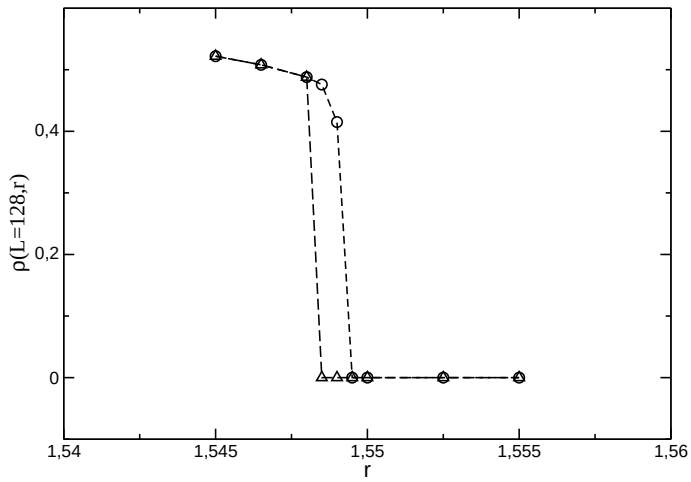


Figure D.1: Order parameter as a function of $r$ in the case of parallel updating. The transition appears to be discontinuous in this case, exhibiting also a hysteresis loop.

slow, it could be the case that the first order character of the transition is only apparent. Extracting clean, conclusive results in the critical zone is a computationally very expensive task, that we have not pursued.

## D.2 Multiplicative Version of Lipowski Model

Very recently, Lipowski has introduced a multiplicative version of his model on the square lattice in which sites are declared active if the product of the four adjacent bonds is smaller than a certain value of the control parameter $r$ [185]. Bonds take uncorrelated values in the interval $[-0.5, 0.5]$ extracted from a homogeneous distribution. For values of $r$ smaller than $r = 0$ there is a finite (not small) probability to generate superabsorbing sites. In this case, it is not difficult to see that isolated superabsorbing sites remain frozen forever. In analogy with the discussion of the honeycomb-lattice model, a first order transition is expected at $r_c = 0$ (as discussed also in [185]). However, in this case, as the probability to create superabsorbing sites is not negligible, the first order transition is actually observable. Based on a numerical measurement of $\beta$ Lipowski concludes that the model shares first-order properties with second-order features. In particular, the transition is clearly shown to be discontinuous, there is no diverging correlation length, but $\beta$ is claimed to be however in the two-dimensional DP class. Our guess is that this apparent puzzle is simply due to a numerical coincidence, and that in fact there is no trait of any second-order phase transition feature (observe that the fit for beta in [185] spans for less than half a decade in the abscise of the log-log plot).

# Bibliography


[1] N. Goldenfeld and L.P. Kadanoff, Science **284**, 87 (1999).

[2] R. Balescu, *Equilibrium and Nonequilibrium Statistical Mechanics*, John Wiley & Sons (1975).

[3] J. Biel Gayé, *Formalismo y Métodos de la Termodinámica*, vols. 1 and 2, Editorial Reverté (1998).

[4] P. Umbanhowar, Nature **389**, 541 (1997).

[5] M.C. Cross and P.C. Hohenberg, Rev. Mod. Phys. **65**, 851 (1993).

[6] J.P. Gollub and J.S. Langer, Rev. Mod. Phys. **71**, S396 (1999).

[7] J. Cardy, *Scaling and Renomalization in Statistical Physics*, Cambridge Lecture Notes in Physics, Cambridge University Press (1996).

[8] G. K. Batchelor, *An Introduction to Fluid Dynamics*, Cambridge University Press (2000).

[9] D.P. Landau and K. Binder, *A Guide to Monte Carlo Simulations in Statistical Physics*, Cambridge University Press, Cambridge (2000).

[10] W. Kob, J. Phys.:Condens. Mat. **11**, R85 (1999).

[11] G. Isidori, G. Ridolfi and A. Strumia, Nuc. Phys. B **609**, 387 (2001).

[12] R.L. Jaffe et al, Rev. Mod. Phys. **72**, 1125 (2000).

[13] E.E. Zabrodin et al, Phys. Rev. C **59**, 894 (1999).

[14] J. Páramos, O. Bertolami and T.A. Girard, e-print hep-ph/0206212 (2002).

[15] Unknown author, *A Metastability Primer*, internal document from Philips Semiconductors (1989).
Web site: http://www.philipslogic.com/support/appnotes/an219.pdf

[16] Richard P. Sear, J. Chem. Phys. **111**, 4800 (1999).

[17] M.A. Novotny and P.A. Rikvold, in *Encyclopedia of Electrical and Electronics Engineering* **12**, 64 (1999), editor J.G. Webster, (John Wiley & Sons, New York).

[18] Nils Berglund and Barbara Gentz, e-print physics/0111110 (2001).

[19] S. Banik and D. Bandyopadhyay, Phys. Rev. C **63**, 035802 (2001).

[20] A. Strumia and N. Tetradis, J. High Energy Phys. **11**, 023 (1999).

[21] See, for instance, R. Mélin, J. Mag. Mag. Mat. **162**, 211 (1996); M. Kolesik, M.A. Novotny and P.A. Rikvold, Int. J. Mod. Phys. C, in press (2002).

[22] L. Onsager, Phys. Rev. **65**, 117 (1944).

[23] J.S. Langer, in *Solids Far from Equilibrium*, edited by C. Godrèche, Cambridge University Press (1992).

[24] R.H. Schonmann, Commun. Math. Phys. **147**, 231 (1992).

[25] R.A. Ramos, P.A. Rikvold and M.A. Novotny, Phys. Rev. B **59**, 9053 (1999).

[26] P.A. Rikvold et al, Phys. Rev. B **49**, 5080 (1994).

[27] E.N.M. Cirillo and J.L. Lebowitz, J. Stat. Phys. **90**, 211 (1998).

[28] H.L. Richards et al, Phys. Rev. B **55**, 11521 (1997); D. García-Pablos, P. García-Mochales and N. García, J. Appl. Phys **79**, 6019 (1996).

[29] M. Kolesik et al, J. Appl. Phys. **81**, 5600 (1997).

[30] H.L. Richards, M.A. Novotny, and P.A. Rikvold, Phys. Rev. B **54**, 4113 (1996).

[31] J. Marro and J.A. Vacas, Phys. Rev. B **56**, 1 (1997).

[32] J. Tejada, X.X. Zhang and Ll. Balcells, J. Appl. Phys. **73**(10), 6709 (1993).

[33] E. Ising, Z. Physik **31**, 253 (1925).

[34] Pedro L. Garrido, *Cambios de fase en sistemas reticulares fuera del equilibrio en régimen estacionario*, Ph.D. thesis, University of Granada (1988).

[35] Pedro L. Garrido and Joaquín Marro, Phys. Rev. Lett. **62**, 1929 (1989).

[36] P.L Garrido and M.A. Muñoz, Phys. Rev. E **48**, R4153 (1993).

[37] R.J. Glauber, J. Math. Phys. **4**, 294 (1963).

[38] Ph.A. Martin, J. Stat. Phys. **16**, 149 (1977).

[39] P.C. Hohenberg and B.I. Halperin, Rev. Mod. Phys. **49**, 435 (1977).

[40] P. Tamayo, F.J. Alexander and R. Gupta, Int. J. Mod. Phys. C **7**, 389 (1996).

[41] A. Achahbar, J.J. Alonso and Miguel A. Muñoz, Phys. Rev. E **54**, 4838 (1996).

[42] See, for instance, K. Binder and D. W. Heermann, *Monte Carlo Simulation in Statistical Physics : An Introduction*, Springer Series in Solid-State Sciences, 80, Springer-Verlag, 1998; see also ref. [9].

[43] M.A. Novotny, *Annual Reviews of Computational Physics IX*, edited by D. Stauffer, (World Scientific, Singapore, 2001), p. 153-210. See also M.A. Novotny, Comp. in Phys. **9**, 46 (1995).

[44] A.B. Bortz, M.H. Kalos and J.L Lebowitz, J. Comput. Phys. **17**, 10 (1975).

[45] M. Kolesik, M.A. Novotny and P.A. Rikvold, Phys. Rev. Lett. **80**, 3384 (1998); see also M.A. Novotny, M. Kolesik, and P.A. Rikvold, Comp. Phys. Comm. **121-122**, 303 (1999).

[46] M. Kolesik, M.A. Novotny, P.A. Rikvold, and D.M. Townsley, in *Computer Simulation Studies in Condensed Matter Physics X*, editors D.P. Landau, K.K. Mon, and H.-B. Schttler, Springer Verlag, Heidelberg (1997), p. 246-251.

[47] N. Metropolis et al, J. Chem. Phys. **21**, 1087 (1953).

[48] A.M. Abdel-Moneim and F.W. Leysieffer, J. Appl. Prob. **19**, 685 (1982).

[49] R. Kikuchi, Phys. Rev. **81**, 988 (1951).

[50] R. Dickman, Phys. Lett. A **122**, 463 (1987).

[51] J. Marro and R. Dickman, *Nonequilibrium Phase Transitions in Lattice Models*, Cambridge University Press, Cambridge (1999).

[52] L. Elsgotz, *Ecuaciones Diferenciales y Cálculo Variacional*, editorial MIR (1992).

[53] Juan José Alonso, *Sistemas reticulares con difusión de desorden: Teoría cinética de campo medio y deducción de ecuaciones hidrodinámicas*, Ph.D. thesis, University of Granada (1992).

[54] William H. Press et al, *Numerical Recipes in Fortran: the Art of Scientific Computing*, Cambridge University Press (1993).

[55] Hilda W.F. Sung and C. Rudowicz, e-print cond-mat/0210657 (2002).

[56] Miguel A. Muñoz and Pedro L. Garrido, J. Phys. A: Math. Gen. **26**, 3909 (1993).

[57] M.F. Thorpe and D. Beeman, Phys. Rev. B **14**, 188 (1976).

[58] W. Genovese, M.A. Muñoz and P.L. Garrido, Phys. Rev. E **58**, 6828 (1998).

[59] W.K. Burton, N. Cabrera and F.C. Frank, Phil. Trans. Roy. Soc. (London), Ser. A **243**, 299 (1951).

[60] S. Miracle-Sole and J. Ruiz, in *Micro, Meso and Macroscopic Approaches in Physics*, edited by A. Verbeure, Plenum Press, New York (1993).

[61] P.A. Rikvold and M. Kolesik, J. Stat. Phys. **100**, 377 (2000).

[62] H.N.V. Temperley, Proc. Cambridge Phil. Soc. **48**, 683 (1952).

[63] J.E. Avron et al, J. Phys. A **15**, L81 (1982).

[64] I.S. Gradshteyn and I.M. Ryzhik, *Table of Integrals, Series and Products*, Academic Press (1980).

[65] Pablo I. Hurtado and Pedro L. Garrido, unpublished.

[66] D. Frenkel and B. Smit, *Understanding Molecular Simulation: From Algorithms to Applications*, $2^{nd}$ Edition, Academic Press (2002).

[67] C. Rottman and M. Wortis, Phys. Rev. B **24**, 6274 (1981).

[68] G. Wulff, Kristallogr. Mineral. **34**, 448 (1901); C. Herring, Phys. Rev. **82**, 87 (1951); *ibid*, in *Structure and Properties of Solid Surfaces*, edited by R. Gomer and C.S. Smith, University of Chicago, pp. 5-72 (1953).

[69] See Appendix D in reference [59].

[70] L. Neél, Ann. Géophys. **5**, 99 (1949); W.F. Brown, Jr. Phys. Rev. B **130**, 1677 (1963).

[71] J.D. Gunton and M. Droz, *Introduction to the Theory of Metastable and Unstable States*, Springer, Berlin (1983).

[72] C.K. Harris, J. Phys. A **17**, L143 (1984); M.J. Lowe and D.J. Wallace, J. Phys. A **13**, L381 (1980).

[73] C.C.A. Gunter, P.A. Rikvold and M.A. Novotny, Phys. Rev. Lett. **71**, 3898 (1993).

[74] A. Perini, G. Jacucci and G. Martin, Phys. Rev. B **29**, 2689 (1984); *ibid*, Surf. Sci. **144**, 53 (1984).

[75] J.S. Langer, Phys. Rev. Lett. **21**, 973 (1968).

[76] J.S. Langer, Ann. Phys. (N.Y.) **41**, 108 (1967); N.J. Günther, D.A. Nicole and D.J. Wallace, J. Phys. A **13**, 1755 (1980).

[77] J.J. Binney, N.J. Dowrick, A.J. Fisher and M.E.J. Newman, *The Theory of Critical Phenomena: An Introduction to the Renomalization Group*, Oxford University Press (1993).

[78] M. Avrami, J. Chem. Phys. **7**, 1103 (1939); *ibid*, J. Chem. Phys. **8**, 212 (1940); W.A. Johnson and P.A. Mehl, Trans. Am. Inst. Min. Metall. Ing. **135**, 416 (1939); A.N. Kolmogorov, Bull. Acad. Sci. USSR, Phys. Ser. **1**, 355 (1937).

[79] S.R. de Groot and P. Mazur, *Non-Equilibrium Thermodynamics*, Dover Publication, Inc., New York (1984).

[80] H. Tomita and S. Miyashita, Phys. Rev. B **46**, 8886 (1992).

[81] M.A. Novotny et al, J. Non-Crystalline Solids, **274**, 356 (2000).

[82] O. Penrose and J.L. Lebowitz, in *Fluctuation Phenomena* (2nd edition), edited by E. Montroll and J.L. Lebowitz, North−Holland, Amsterdam (1987).

[83] J.L. Simonds, Phys. Today **48** (No. 4), 26 (1995).

[84] J. Shi *et al.*, Science **271**, 937 (1996).

[85] W. Wernsdorfer, Adv. Chem. Phys. **118**, 99 (2001).

[86] V.L. Safonov and H.N. Bertram, J. Appl. Phys. **91**, 7279 (2002).

[87] L. Sipahi, J. Appl. Phys. **75**(10), 6978 (1994).

[88] D. Spasojević et al, Phys. Rev. E **54**, 2531 (1996).

[89] L. Sipahi et al, J. Appl. Phys. **75**(10), 6981 (1994).

[90] S. Zapperi et al, Phys. Rev. B **58**, 6353 (1998).

[91] J.P. Sethna et al, Nature **410**, 242 (2001).

[92] T. Antal et al, Phys. Rev. Lett. **87**, 240601 (2001).

[93] D.L. Gilden et al, Science **267**, 1837 (1978).

[94] F. Lillo and R.N. Mantegna, Phys. Rev. E **62**, 6126 (2000).

[95] J. Davidsen and H.G. Schuster, Phys. Rev. E **65**, 026120 (2002).

[96] S. Field et al, Phys. Rev. Lett. **74**, 1206 (1995).

[97] V. Frette et al, Nature **379**, 49 (1996).

[98] K.L. Schick and A.A. Verveen, Nature **251**, 599 (1974).

[99] P.A. Houle and J.P. Sethna, Phys. Rev. E **54**, 278 (1996).

[100] R.F. Voss and J. Clarke, Nature **258**, 317 (1975).

[101] P. Bak, C. Tang and K. Wiesenfeld, Phys. Rev. Lett. **59**, 381 (1987).

[102] H.J. Jensen, *Self-Organized Criticality. Emergent Complex Behavior in Physical and Biological Systems*, Cambridge Lecture Notes in Physics, Cambridge University Press (1998).

[103] J. Tejada et al, J. Appl. Phys. **73**(10), 6709 (1993).

[104] See, for instance, X. Che and H. Suhl, Phys. Rev. Lett. **64**, 1670 (1990); K.L. Babcock and R.M. Westervelt, Phys. Rev. Lett. **64**, 2168 (1990).

[105] J.S. Urbach et al, Phys. Rev. Lett **75**, 4694 (1995).

[106] A. Rikvold et al, Phys. Rev. E **49**, 5080 (1994).

[107] M.A. Novotny, Phys. Rev. Lett. **74**, 1 (1994).

[108] M.C. Kuntz and J.P. Sethna, Phys. Rev. B **62**, 11699 (2000).

[109] G. Durin and S. Zapperi, J. Mag. Mag. Mater. **242**, 1085 (2002).

[110] M. Bahiana et al, Phys. Rev. E **59**, 3884 (1999).

[111] A.P. Mehta et al, Phys. Rev. E **65**, 046139 (2002).

[112] A. Travesset, R.A. White and K.A. Dahmen, Phys. Rev. B **66**, 024430 (2002).

[113] D. Sornette, Int. J. Mod. Phys. C **13**, 133 (2002).

[114] G. Durin and S. Zapperi, Phys. Rev. Lett. **84**, 4705 (2000).

[115] K. Binder, M.H. Kalos, J.L. Lebowitz, and J. Marro, Adv. Colloid. Interface. Sci. **10**, 173 (1979); K. Binder, Rep. Progr. Phys. **50**, 783 (1987).

[116] J.D. Gunton, M. San Miguel, and P.S. Shani, in *Phase Transitions and Critical Phenomena*, Vol. 8, eds. C. Domb and J.L. Lebowitz, Academic Press, N.Y (1983).

[117] H. Furukawa, Adv. Phys. **34**, 703 (1985).

[118] A.J. Bray, Adv. Phys. **43**, 357 (1994).

[119] K. Binder, and P. Fratzl, *Spinodal Decomposition*, in *Phase Transformations in Materials*, G. Kostorz Ed., Wiley-VCH, Weinheim (2001), pp. 409-480.

[120] S.K. Ma, *Statistical Mechanics*, World Sci., Philadelphia (1985).

[121] J. Marro, J.L. Lebowitz, and M. Kalos, Phys.Rev. Lett. **43**,282(1979); ibid, Acta metall. **30**, 297 (1982); P. Fratzl, J.L. Lebowitz, J. Marro, and M.H. Kalos, Acta metall. **31**, 1849 (1983).

[122] J. Marro, R. Toral, and A.M. Zahra, J. Phys. C: Solid State Phys. **18**, 1377 (1985).

[123] I.M. Lifshitz and V.V. Slyozov, J. Phys. Chem. Solids **19**, 35 (1961); C. Wagner, Z. Elektrochem. **65**, 58 (1961).

[124] G.F. Mazenko and R. Wickham, Phys. Rev. E **51**, 2886 (1995).

[125] R. Toral and J. Marro, Phys. Rev. Lett. **54**, 1424 (1985).

[126] D.A. Huse, Phys. Rev. B **34**, 7845 (1986).

[127] S. Puri, A.J. Bray, and J.L. Lebowitz, Phys. Rev. E **56** 758 (1997).

[128] D. Beysens and M. Gbadamassi, Phys. Rev. A **22**, 2250 (1980).

[129] C. Chan and L. Lin, Europhys.Lett **11**,13 (1990).

[130] A. Onuki, J.Phys.Condens.Matter **9**, 6119 (1997).

[131] N.P. Rapapa and A.J. Bray, Phys. Rev. Lett. **83**, 3856 (1999).

[132] F. Corberi, G. Gonnella, and A. Lamura, Phys. Rev. E **61**, 6621 (2000).

[133] B.B. Mandelbrot, *Multifractals and* 1/f *noise*, Springer, New York (1999).

[134] S. Katz, J.L. Lebowitz, and H. Spohn, J. Stat. Phys. **34**, 497 (1984).

[135] C. Yeung, T. Rogers, A. Hernandez–Machado, and D. Jasnow, J. Stat. Phys. **66**, 1071 (1992).

[136] S. Puri, K. Binder, and S. Dattagupta, Phys. Rev. B **46**, 98 (1992); S. Puri, N. Parekh, and S. Dattagupta, J. Stat. Phys. **75**, 839 (1994).

[137] B. Schmittman and R. Zia, *Statistical Mechanics of Driven Diffusive Systems*, in *Phase Transitions and Critical Phenomena,* Vol. 17, C. Domb and J.L. Lebowitz Eds., Academic Press, London (1995).

[138] F. Alexander, C.A. Laberge, J.L. Lebowitz, and R.K.P. Zia, J. Stat. Phys. **82**,1133 (1996).

[139] E. Levine, Y. Kafri and D. Mukamel, Phys. Rev. E **64**, 26105 (2001).

[140] A. Achahbar, P.L. Garrido, J. Marro, and M.A. Muñoz, Phys. Rev. Lett. **87**, 195702 (2001).

[141] E.V. Albano and G. Saracco, Phys. Rev. Lett. **88**, 145701 (2002).

[142] P.I. Hurtado, J. Marro, and E.V. Albano, Europhys. Lett. **59**(1), 14 (2002); P.I. Hurtado, J. Marro, P.L. Garrido and E.V. Albano, accepted for publication in Phys. Rev. B (2002).

[143] P.L. Garrido, J. Marro, and R. Dickman, Ann. Phys. (NY) **199**, 366 (1990).

[144] See, for instance, N.T.J. Bailey, *The Elements of Stochastic Processes*, John Wiley & Sons, N.Y. (1964).

[145] A. Guinier and G. Fournet, *Small Angle Scattering of X-Rays*, Wiley, N.Y. (1955).

[146] O. Penrose, J.L. Lebowitz, J. Marro, M.H. Kalos, and A. Sur, J. Stat. Phys. **19**, 243 (1978); see also O. Penrose, J.L. Lebowitz, J. Marro, M.H. Kalos, and J. Tobochnik, J. Stat. Phys. **34**, 399 (1984).

[147] F. de los Santos, P.L. Garrido, and M.A. Muñoz, Physica A **296**, 364 (2001); see also P.L. Garrido, M.A. Muñoz, and F. de los Santos, Phys. Rev. E **61**, R4683 (2000).

[148] H.K. Janssen and B. Schmittmann, Z. Phys. B **64**, 503 (1986); K. Leung and J.L. Cardy, J. Stat. Phys. **44**, 567, **45**, 1087 (1986).

[149] M. San Miguel and R. Toral, in *Instabilities and Nonequilibrium Structures VI*, E. Tirapegui, J. Martínez, and R. Tiemann eds., Kluwer Acad. Pub. (2001).

[150] A. Chakrabarti, R. Toral, and J.D. Gunton, Phys. Rev. B **39**, 4386 (1989).

[151] I. Dornic, H. Chaté, J. Chave, and H. Hinrichsen, Phys. Rev. Lett. **87**, 045701 (2001).

[152] T. Mullin, Phys. Rev. Lett. **84**, 4741 (2000); P.M. Reis and T. Mullin, e-print cond-mat/0207399 (2002).

[153] T. Kawakatsu and T. Munakata, Prog. Theor. Phys. **74**, 11 (1985).

[154] K.-t. Leung et al, Phys. Rev. Lett. **61**, 1744 (1988); K.-t. Leung, K.K. Mon, J.L. Valles, R.K.P. Zia, Phys. Rev. B **39**, 9312 (1989).

[155] G. Grinstein and M. A. Muñoz, in *Fourth Granada Lectures in Computational Physics*, Ed. P.L. Garrido and J. Marro, Lecture Notes in Physics, **493**, 223 (Springer-Verlag, Berlin, 1997).

[156] H. Hinrichsen *Critical phenomena in Nonequilibrium systems*, e-prit cond-mat/0001070.

[157] R. M. Ziff, E. Gulari and Y. Barshad, Phys. Rev. Lett. **56**, 2553 (1986); I. Jensen, H.C. Fogedby and R. Dickman, Phys. Rev. **41**, 3411 (1990).

[158] A. -L. Barabási and H. E. Stanley, *Fractal Concepts in Surface Growth*, Cambridge University Press, Cambridge (1995).

[159] T. M. Ligget, *Interacting Particle Systems*, Springer Verlag, New York, (1985).

[160] P. Grassberger, J. Stat. Phys. **79**, 13 (1995).

[161] H. Hinrichsen, R. Livi, D. Mukamel and A. Politi, Phys. Rev. E 61, R1032 (2000); *ibid*, Phys. Rev. Lett. 79, 2710-2713 (1997).

[162] A. Vespignani, R. Dickman, M. A. Muñoz, and S. Zapperi, Phys. Rev. E **62**, 4564 (2000); R. Dickman, M. A. Muñoz, A. Vespignani, and S. Zapperi, Brazilian J. of Phys. **30**, 27 (2000).

[163] M. Paczuski, S. Maslov, and P. Bak, Europhys. Lett. **27**, 97 (1994).

[164] P. Grassberger, Z. Phys. B **47**, 365 (1982); H.K. Janssen, Z. Phys. B **42**, 151 (1981).

[165] H. D. I. Abarbanel and J. B. Bronzan, Phys. Rev. D **9**, 2397 (1974).

[166] G. Grinstein, Z. -W. Lai and D. A. Browne, Phys. Rev. A **40**, 4820 (1989).

[167] J. Kohler and D. ben-Avraham, J. Phys. A **24**, L621 (1991); D. ben-Avraham and J. Kohler, J. Stat. Phys. **65**, 839 (1992); K. Yaldram, K. M. Khan, N. Ahmed, and M. A. Khan, J. Phys. A. **26**, L801, (1993). E. V. Albano, J. Phys. A **25**, 2557 (1992); I. Jensen, Int. J. Mod. Phys. B **8**, 3299 (1994).

[168] M. A. Muñoz, G. Grinstein, R. Dickman and R. Livi, Phys. Rev. Lett. **76**, 451, (1996).

[169] P. Grassberger, F. Krause, and T. von der Twer, J. Phys. A **17**, L105 (1984); H. Takayasu and A. Yu. Tretyakov, Phys. Rev. Lett. **68**, 3060 (1992); N. Menyhard and G. Ódor, J. Phys. A **29**, 7739 (1996); H. Hinrichsen, Phys. Rev. E **55**, 219 (1997); W. Hwang, S. Kwon, H. Park, and H. Park, Phys. Rev. E **57**, 6438 (1998).

[170] J. Cardy and U. C. Täuber, Phys. Rev. Lett. **77**, 4780 (1996).

[171] E. Domany and W. Kinzel, Phys. Rev Lett. **53**, 311 (1984); J. W. Essam, J. Phys. A **22**, 4927 (1989).

[172] M. Rossi, R. Pastor-Satorras and A. Vespignani, Phys. Rev. Lett. **85**, 1803 (2000).

[173] H. K. Janssen, K. Oerding, F. van Wijland, and H. J. Hilhorst, European Phys. J. B. **7**, 137 (1999).

[174] G. Parisi and N. Sourlas, Phys. Rev. Lett. **43**, 744 (1979).

[175] E. Brézin and C. De Dominicis, e-print cond-mat/9804266 (1998).

[176] A. Lipowski and M. Lopata, Phys. Rev. E **60**, 1516 (1999).

[177] M. A. Muñoz, G. Grinstein, and R. Dickman, J. Stat. Phys. **91**, 541-569 (1998).

[178] I. Jensen, Phys. Rev. Lett. **70**, 1465 (1993); I. Jensen and R. Dickman, Phys. Rev. E **48**, 1710 (1993).

[179] A. Lipowski, Phys. Rev. E **60**, 6255 (1999).

[180] P. Grassberger, H. Chaté and H. Rosseau, Phys. Rev. E **55**, 2488 (1997).

[181] *Finite Size Scaling*, in *Current Physics - Sources and Comments*, Edited by J. Cardy, North-Holland, Amsterdam, (1988).

[182] M. A. Muñoz, R. Dickman, A. Vespignani and S. Zapperi, Phys. Rev. E **59**, 6175 (1999).

[183] P. Grassberger and A. de la Torre, Ann. Phys.(N.Y.) **122**, 373 (1979).

[184] R. Dickman, A. Vespignani and S. Zapperi, Phys. Rev. E **57**, 5095 (1998).

[185] A. Lipowski, Phys. Rev. E **62**, 4401 (2000).

[186] J.F.F Mendes, R. Dickman, M. Henkel, and M. C. Marques, J. Phys. A **27**, 3019 (1994).

[187] See C. A. Angell, Science **267**, 1924 (1995); and M. A. Muñoz, A. Gabrielli, H. Inaoka and L. Pietronero, Phys. Rev. E. **57**, 4354 (1998), and references therein.

[188] Interesting references about the self averaging property in critical disordered systems are: A. Aharony and A. B. Harris, Phys. Rev. Lett. **77**, 2125 (1996). S. Wiseman and E. Domany, Phys. Rev. Lett. **81**, 22 (1998).

[189] See, for example: R. Dickman and T. Tomé, Phys. Rev. A **44**, 4833 (1991). R. A. Monetti, A. Rozenfeld and E. V. Albano, e-print cond-mat/9911040 (1999). See also [161]

[190] F. Bonetto, J.L. Lebowitz and L. Rey-Bellet, e-print cond-mat/0002052 (2000).

[191] S. Lepri, R. Livi and A. Politi, e-print cond-mat/0112193 (2001).

[192] R.E. Peierls, *Quantum Theory of Solids*, Oxford University Press, London (1955).

[193] S. Lepri, R. Livi and A. Politi, Europhys. Lett. **43**, 271 (1998); S. Lepri, Phys. Rev. E **58**, 7165 (1998).

[194] B. Hu, B. Li and H. Zhao, Phys. Rev. E **61**, 3828 (2000).

[195] O.V. Gendelman and A.V. Savin, Phys. Rev. Lett. **84**, 2381 (2000); C. Giardina, R. Livi, A. Politi and M. Vassalli, Phys. Rev. Lett. **84**, 2144 (2000).

[196] T. Prosen and D.K. Campbell, Phys. Rev. Lett. **84**, 2857 (2000).

[197] A. Dhar, Phys. Rev. Lett. **86**, 5882 (2001); e-print cond-mat/0105085 (2001).

[198] P.L. Garrido and J. Marro, J. Phys. A **22**, 1355 (1989).

[199] A. Dhar, Phys. Rev. Lett. **86**, 3554 (2001).

[200] T. Hatano, Phys. Rev. E **59**, R1 (1999).

[201] K. Aoki and D. Kusnezov, Phys. Rev. Lett. **86**, 4029 (2001).

[202] See, for instance, R.N. Mantegna and H.E. Stanley, *An Introduction to Econophysics: Correlations and Complexity in Finance*, Cambridge University Press (2000).

[203] D.W. Jepsen, J. Math. Phys. (N.Y.) **6**, 405 (1965).

# Published work

- Pablo I. Hurtado, Miguel A. Muñoz, *Systems with Superabsorbing States*, Phys. Rev. E **62**, 4633 (2000).
- Pedro L. Garrido, Pablo I. Hurtado, Bjoern Nadrowski, *Simple One-dimensional Model of Heat Conduction which Obeys Fourier's Law*, Phys. Rev. Lett. **86**, 5486 (2001).
- Pedro L. Garrido, Pablo I. Hurtado, *Reply to Comment on Simple One-dimensional Model of Heat Conduction which Obeys Fourier's Law by A. Dhar*, Phys. Rev. Lett. **88**, 249402 (2002).
- Pedro L. Garrido, Pablo I. Hurtado, *Reply to Comment on Simple One-dimensional Model of Heat Conduction which Obeys Fourier's Law by H. Li et al*, Phys. Rev. Lett. **89**, 079402 (2002).
- Joaquín Marro, Jesús Cortés, Pablo I. Hurtado, *Modeling Nonequilibrium Phase Transitions and Critical Behavior in Complex Systems*, Comp. Phys. Comm. **147**, 115 (2002).
- Pablo I. Hurtado, J. Marro, Ezequiel V. Albano, *Growth and Scaling in Anisotropic Spinodal Decomposition*, Europhys. Lett. **59**(1), 14 (2002).
- Pablo I. Hurtado, J. Marro, Pedro L. Garrido, Ezequiel V. Albano, *Coarsening under Anisotropic Conditions in a Lattice Gas Model*, in *Modeling complex systems: Seventh Granada Lectures on Computational Physics*, Pedro L. Garrido, Joaquín Marro (eds.), AIP Conference Proceedings (2002).
- Pablo I. Hurtado, J. Marro, Pedro L. Garrido, *Metastability and Avalanches in a Nonequilibrium Ferromagnetic System*, in *Modeling complex systems: Seventh Granada Lectures on Computational Physics*, Pedro L. Garrido, Joaquín Marro (eds.), AIP Conference Proceedings (2002).
- Pablo I. Hurtado, J. Marro, Pedro L. Garrido, Ezequiel V. Albano, *Kinetics of Phase Separation in the Driven Lattice Gas: Self-Similar Pattern Growth under Anisotropic Nonequilibrium Conditions*, accepted for publication in Phys. Rev. B (2002).

- Pablo I. Hurtado, J. Marro, Pedro L. Garrido, *Origin of the* 1/f *Noise in a Model of Disorder*, submitted to Phys. Rev. Lett. (2002).

IN PREPARATION

- Pablo I. Hurtado, Joaquín Marro, Pedro L. Garrido, *Metaestability in Ferromagnetic Systems under Nonequilibrium Conditions* (2003).
- Pablo I. Hurtado, Joaquín Marro, Pedro L. Garrido, *Generalization of the Solid-on-Solid Approximation to Nonequilibrium Interfaces: Microscopic Structure, Surface Tension and Crystal Shape* (2003).
- Pablo I. Hurtado, Joaquín Marro, Pedro L. Garrido, *Hysteresis and the Intrinsic Coercive Field in Nonequilibrium Ferromagnetic Systems* (2003).

ABSTRACTS

- Pablo I. Hurtado, Miguel A. Muñoz, *Systems with Superabsorbing States*, Proc. of the Workshop on Surface Science and Porous Media, San Luis, Argentina (2000).
- Pablo I. Hurtado, J. Marro, P.L. Garrido, *Impure Ferromagnetic Nanoparticles: on the 1/f Noise during Decay from Metastable States*, in *SIMU Conference: Bridging the Time Scale gap*, Abstract Book (2001).
- Pablo I. Hurtado, Miguel A. Muñoz, *Lipowski Model and Superabsorbing States*, in *Modeling complex systems: Sixth Granada Lectures on Computational Physics*, Pedro L. Garrido, Joaquín Marro (eds.), AIP Conference Proceedings **574** (2001).
- Pablo I. Hurtado, J. Marro, E.V. Albano, *Kinetics of Phase Separation in the Driven Lattice Gas: Pattern Gowth and Scaling Laws under Anisotropic Nonequilibrium Conditions*, in *CMD19CMMP 2002-Condensed Matter and Materials Physics*, Europhysics Conference Abstracts **26A** (2002).